



**HAL**  
open science

# Modeling of transfer phenomena in PEM fuel cells for the automotive application

Rémi Bligny

► **To cite this version:**

Rémi Bligny. Modeling of transfer phenomena in PEM fuel cells for the automotive application. Engineering Sciences [physics]. Université de Lorraine, 2023. English. NNT : 2023LORR0068 . tel-04205142

**HAL Id: tel-04205142**

**<https://hal.univ-lorraine.fr/tel-04205142>**

Submitted on 12 Sep 2023

**HAL** is a multi-disciplinary open access archive for the deposit and dissemination of scientific research documents, whether they are published or not. The documents may come from teaching and research institutions in France or abroad, or from public or private research centers.

L'archive ouverte pluridisciplinaire **HAL**, est destinée au dépôt et à la diffusion de documents scientifiques de niveau recherche, publiés ou non, émanant des établissements d'enseignement et de recherche français ou étrangers, des laboratoires publics ou privés.



**UNIVERSITÉ  
DE LORRAINE**

**BIBLIOTHÈQUES  
UNIVERSITAIRES**

## AVERTISSEMENT

Ce document est le fruit d'un long travail approuvé par le jury de soutenance et mis à disposition de l'ensemble de la communauté universitaire élargie.

Il est soumis à la propriété intellectuelle de l'auteur. Ceci implique une obligation de citation et de référencement lors de l'utilisation de ce document.

D'autre part, toute contrefaçon, plagiat, reproduction illicite encourt une poursuite pénale.

Contact bibliothèque : [ddoc-theses-contact@univ-lorraine.fr](mailto:ddoc-theses-contact@univ-lorraine.fr)  
*(Cette adresse ne permet pas de contacter les auteurs)*

## LIENS

Code de la Propriété Intellectuelle. articles L 122. 4

Code de la Propriété Intellectuelle. articles L 335.2- L 335.10

[http://www.cfcopies.com/V2/leg/leg\\_droi.php](http://www.cfcopies.com/V2/leg/leg_droi.php)

<http://www.culture.gouv.fr/culture/infos-pratiques/droits/protection.htm>



SIMPPE



## Ecole doctorale SIMPPE

Sciences et Ingénierie des Molécules des Produits des Procédés et de l'Énergie

## LEMTA

Laboratoire Energies & Mécanique Théorique et Appliquée

# Thèse

présentée et soutenue publiquement pour l'obtention du titre de

## **DOCTEUR DE L'UNIVERSITE DE LORRAINE**

Mention : Energie et Mécanique

---

# **Modélisation des phénomènes de transport dans les piles à combustible de type PEM pour l'application automobile**

---

par Rémi BLIGNY

le 29/03/2023 devant le jury présidé par Yann Bultel (Pr, LEPMI, Université Grenoble Alpes) :

Rapporteurs :	Anthony Thomas	Maitre de Conférences, HDR, Institut Pprime, Université de Poitiers
	Arnaud Morin	Directeur de Recherche, CEA-Liten, Grenoble
Examineurs :	Yann Bultel	Professeur, LEPMI, Université Grenoble Alpes
	Ulrich Sauter	Dr.-Ing., Chief Expert, Rober Bosch GmbH, Renningen
Encadrants :	Gaël Maranzana	Professeur, LEMTA, Université de Lorraine
	Sophie Didierjean	Professeure, LEMTA, Université de Lorraine
Invité :	Jérôme Dillet	Ingénieur de Recherche, LEMTA, Université de Lorraine

Laboratoire Energies & Mécanique Théorique et Appliquée – LEMTA  
UMR 7563, CNRS, Université de Lorraine – 54500 Vandœuvre-lès-Nancy

# Remerciements

La thèse est aussi un travail d'équipe et j'aimerais écrire un mot à toutes les personnes qui ont contribué, de près ou de loin, à cet aboutissement.

Tout d'abord, merci aux deux Directeurs du LEMTA que j'aurai connus, Pascal Boulet et Olivier Lottin. Je crois pouvoir dire que les doctorants du laboratoire sont écoutés et préservés.

Ensuite, je veux adresser un remerciement tout particulier à mes directeurs de thèse, Gaël Maranzana et Sophie Didierjean, qui ont été bien plus que cela à mes yeux. Gaël, tu as su m'éveiller à ce monde qu'est la Recherche. Que ce soit en tant que Professeur, Directeur de stage ou Directeur de thèse, tu as toujours réussi à stimuler ma curiosité. Plus qu'un encadrant, tu es devenu un mentor duquel j'ai appris énormément. Ta créativité et ton intuition nous ont permis de réaliser des manipulations « originales » et « élégantes ». Ton enthousiasme et tes encouragements ont été essentiels lorsque les difficultés me bloquaient la route. La liberté que tu m'as laissée et la confiance que tu m'as accordée m'ont permis de prendre pleinement confiance en moi, affrontant aussi bien les réussites que les échecs. Sophie, tu as toujours été présente dans les moments importants, pour m'aider à trouver le bon chemin. Ta clairvoyance et ta précision m'ont permis d'améliorer tout ce que je produisais. Toujours très juste, tu m'as beaucoup encouragé quand j'en avais besoin, félicité lors de réussites mais aussi mis en garde quand c'était nécessaire. Merci infiniment pour les petits mots émouvants pendant le pot d'après-thèse qui nous ont réchauffé le cœur à ma famille et moi. Toutes ces manipulations "élégantes" et "originales" n'auraient jamais vu le jour sans le savoir-faire de Jérôme. Merci pour tous les efforts que tu as faits pour ce banc, et indirectement pour moi. Tu es très précieux pour les doctorants du LEMTA.

Un grand merci et encore toute mes félicitations à mes deux acolytes de bureau Zarina et Feryal, avec qui nous avons traversé les vagues et orages du périple doctoral. Vous êtes des exemples d'abnégation et j'espère vous recroiser bientôt. Juan, remarquable pour ses méthodes mathématiques et expérimentales, ses réflexions de psychologie et son pragmatisme irréprochable. Sans blague, merci d'avoir partagé cette période avec moi, tu as été un vrai soutien. Justine, avec qui j'ai

partagé chaque année depuis les bancs de la fac. Je te souhaite le meilleur, et je sais qu'il est déjà là. Giuseppe, pour qui je ne sais pas par où commencer. D'abord le début de ma thèse avec la fin de la tienne, puis la fin de la mienne avec le début de ton poste. C'est à s'y perdre, comme s'il n'y avait jamais eu de début ou de fin. Le résumé de tout cela est que j'ai trouvé un vrai ami. Merci de ta présence quotidienne et de ta disponibilité, tu as été un vrai pilier et tu as annihilé beaucoup d'inquiétudes avant qu'elles n'apparaissent.

Je voudrais plus largement remercier l'intégralité des personnes que j'ai pu croiser pendant cette période riche : Axel, Julian, Mylène, Salah, Ludovic (notre Superman), Nicolas Q. (merci pour tous ces échanges), Christian, Michel, Virginie, Valérie, Jean-Christophe (qui m'a appris que c'est avec une lutte sans pardon que l'on produit une belle thèse), Hadrien, Bruno, Natalia, Olivier F., Tobias, Ulrich, Céline, Rachida, Valentin (à qui je souhaite le meilleur pour la suite) et évidemment Alice, la tunnelologue. Bien sûr, merci à tous ceux que je n'ai pas cités.

Pour terminer, un remerciement tout particulier à ma famille qui a su tenir le cap pendant les orages et qui m'a offert la stabilité dont j'avais besoin.

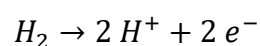
# Résumé élargi

Le système énergétique actuel doit se réinventer pour réduire ses émissions de polluants, notamment de gaz à effet de serre. En effet, les conséquences de cette pollution sont de plus en plus visibles et deviennent problématiques pour les écosystèmes et les humains. De plus, la raréfaction future des ressources fossiles nous oblige à trouver des alternatives aux technologies actuelles. L'hydrogène est un gaz déjà largement utilisé dans de nombreux domaines industriels. Comme l'électricité, il peut jouer le rôle de vecteur énergétique : un intermédiaire entre une source d'énergie et un mode de consommation. Le domaine de la mobilité a un long chemin à parcourir pour convertir le parc automobile en véhicules non émetteurs et l'hydrogène, s'il est produit sans émissions de carbone, est un très bon candidat pour la propulsion de véhicules respectueux de l'environnement.

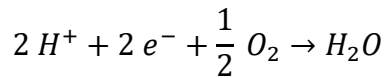
## **Les piles à combustible**

Une pile à combustible est un dispositif électrochimique dont le but est de convertir l'énergie chimique d'un combustible comme l'hydrogène en électricité, sans combustion directe. Toutes les technologies de piles à combustible partagent les mêmes éléments principaux (anode, cathode, électrolyte et circuit externe) et des avantages communs : (i) un rendement potentiellement élevé par rapport aux machines thermiques, (ii) certaines technologies sont facilement modulables, (iii) en cas d'utilisation d'hydrogène, les émissions nocives sont reportées au stade de sa production, (iv) aucune pièce mobile, hormis les dispositifs auxiliaires tels que les pompes ou les compresseurs, (v) grande variété de matières premières pour les carburants utilisés : pétrole, gaz, charbon, éthanol, ... (vi) temps de ravitaillement court par rapport aux systèmes à batteries.

Ce travail se focalise sur la technologie de piles à combustible à membrane échangeuse de protons (PEMFC) car elle est la plus adaptée aux applications de mobilité. Les deux demies-réactions mises en jeu sont les suivantes :



Oxydation - Anode



Réduction - Cathode

A l'anode, le dihydrogène  $H_2$  s'oxyde, libérant deux protons  $H^+$  et deux électrons  $e^-$ . A la cathode, protons, électrons et dioxygène  $O_2$  forment de l'eau  $H_2O$ . Le travail électrique produit par le mouvement des électrons est utilisé par le système extérieur. Le rendement de la cellule étant inférieur à 1, de la chaleur est également produite pendant le fonctionnement. Une cellule élémentaire de pile à combustible PEM est composée de plusieurs couches (Fig. 0-1).

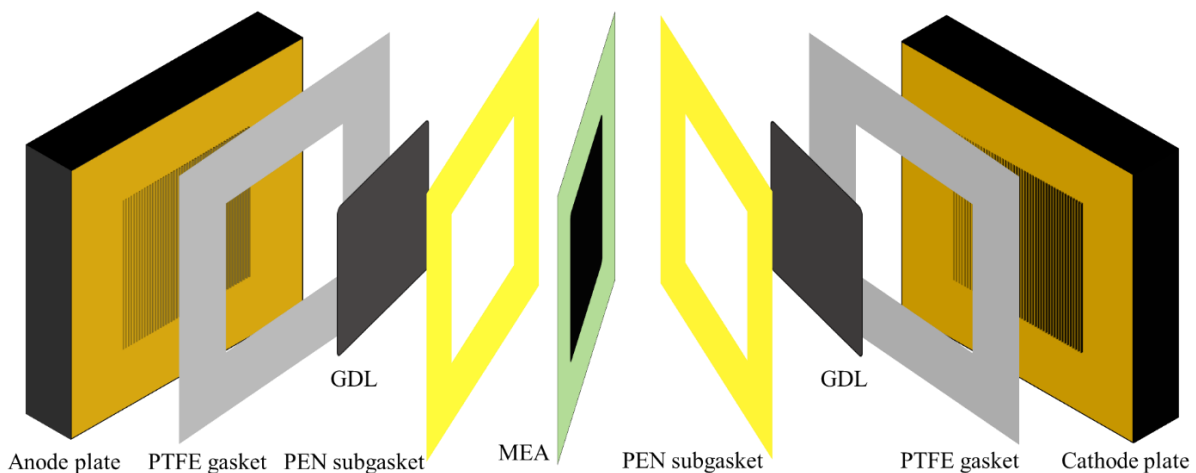


Figure 0-1 : Vue explosée d'une cellule élémentaire de pile à combustible

L'assemblage membrane-électrodes (AME ou *MEA* en anglais) est au centre de la cellule et est composé d'une membrane polymère conductrice de protons et de couches catalytiques qui ont été déposées de part et d'autre de la membrane. Le matériau le plus employé pour la membrane est le Nafion® (un ionomère à base d'acide sulfonique perfluoré – PFSA). Les couches catalytiques contiennent (i) un catalyseur, généralement du platine ou des alliages de platine, qui améliore la cinétique des réactions, (ii) un ionomère qui conduit les protons, (iii) une matrice à base de carbone qui est conductrice d'électrons et (iv) une porosité pour permettre le transport des gaz. L'AME est contenu entre deux couches de diffusion (GDL) qui remplissent une grande variété de fonctions dans la cellule en contrôlant le transport de la masse, de la chaleur et des électrons et en fournissant un support mécanique à la membrane et aux couches catalytiques. Ces couches sont majoritairement composées de fibres de carbone assemblées selon différentes configurations et sont

fortement poreuses. Enfin, les plaques d'alimentation (ou bipolaires, selon le contexte) ont plusieurs fonctions : (i) distribuer de manière homogène les réactifs par les canaux de circulation des gaz, (ii) collecter, conduire et distribuer le courant, (iii) assurer la stabilité mécanique de l'assemblage, (iv) évacuer la chaleur produite et (v) évacuer l'eau produite. Elles sont généralement fabriquées en métal, en graphite ou en matériaux composites.

La gestion de la chaleur et de l'eau sont primordiales pour le bon fonctionnement des cellules ainsi que pour leur durée de vie. D'une part, la membrane a besoin de suffisamment d'eau pour maintenir sa conductivité protonique et ainsi réduire autant que possible les pertes ohmiques. Pour cela, les gaz d'entrée sont généralement humidifiés. Cependant, l'eau peut s'accumuler dans la cellule et entraver le transport des gaz vers la couche catalytique. Cela conduit à une augmentation des pertes de transport de masse et donc à une perte de performance drastique aux densités de courant élevées. De plus, l'accumulation d'eau dans la cellule peut conduire à un manque de réactifs qui contribue à la corrosion du carbone et au vieillissement de la cellule. A l'inverse, si la membrane est trop sèche, des contraintes mécaniques sont susceptibles d'entraîner des dégradations irréversibles. Une température trop élevée augmente aussi les taux de dégradations et réduit la durée de vie des cellules.

La modélisation des mécanismes de transfert d'eau et de chaleur peut participer à l'amélioration des matériaux et de la conception, ainsi qu'à un meilleur contrôle des conditions de fonctionnement en temps réel. L'objectif principal de ce travail est de fournir un modèle d'ordre réduit pour les transferts couplés d'eau et de chaleur dans une pile à combustible. Tous les paramètres impliqués seront estimés, principalement à partir de données observables non électriques afin de supprimer le couplage entre les transferts et l'électrochimie. Un plan d'expériences original est développé, permettant d'estimer précisément les paramètres du modèle par des expériences *in-situ* uniquement.

## **Estimation de paramètres de transport de l'eau**

Le modèle développé ici vise à représenter le transfert d'eau en régime permanent dans une cellule sans production de courant et donc sans source d'eau ou de chaleur.

Ce modèle réduit 1+1D ne contient que deux paramètres à estimer : le coefficient de diffusion effectif de la vapeur d'eau en phase gazeuse  $D_{eff}$  et le coefficient de diffusion de l'eau sous forme adsorbée  $D_M$ . Ces coefficients effectifs dépendent des matériaux et de la géométrie mais sont très pratiques pour le contrôle en temps réel car le modèle associé est très simple et peut être résolu très rapidement.

Le banc expérimental, qui sert de base à toutes les expériences de ce document, est présenté en Fig. 0-2. L'estimation des paramètres repose sur un observable qui est l'humidité en sortie de cellule, étant donnés les débits de gaz et les humidités en entrée. Pour cela, un contrôle précis de l'humidité en entrée est assuré par deux humidificateurs à membrane, indépendamment réglés en température. Des mesures de température de rosée en entrée et en sortie sont effectuées par des hygromètres. Les températures des plaques de la cellule sont précisément régulées et les pertes de charges entre l'entrée et la sortie sont mesurées. Des déverseurs permettent de faire varier la pression totale.

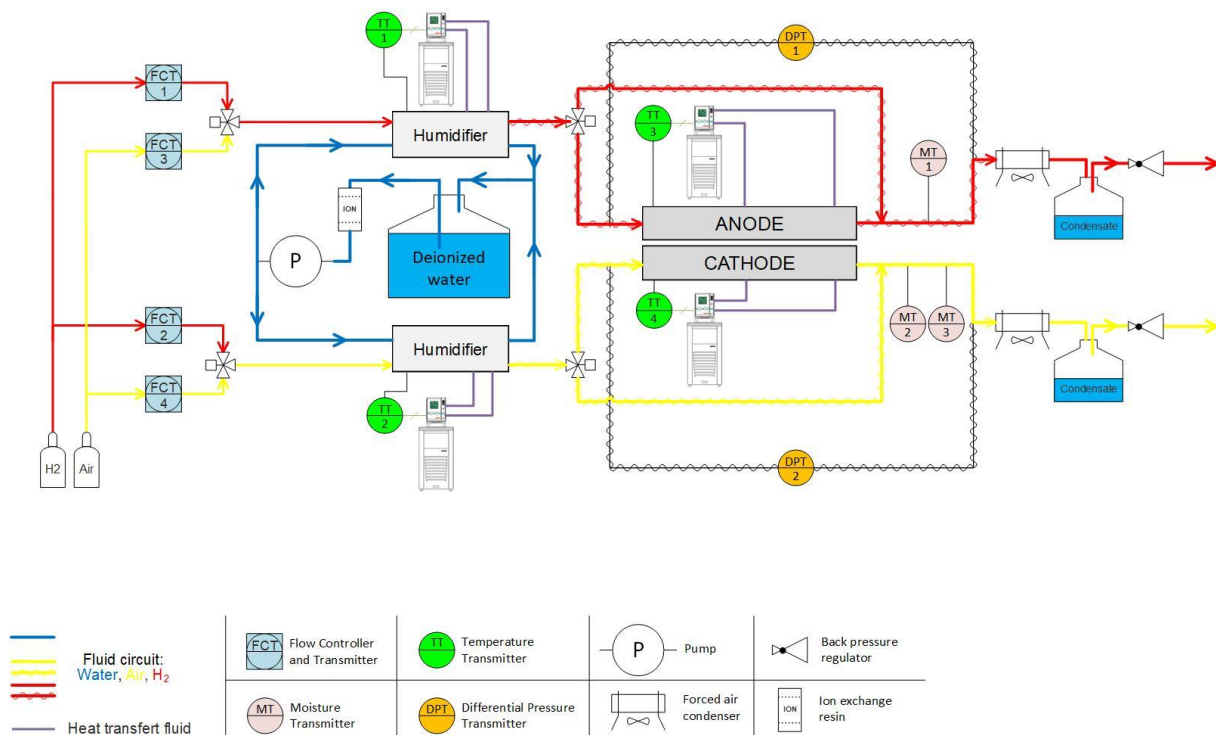


Figure 0-2 : Schéma du banc expérimental de base utilisé dans ce travail

Un plan d'expérience original est développé. La première série d'expériences, dénommée XP1, a pour but de mesurer les flux d'eau dans le plan de la membrane en

fonction de la différence de concentration, en maintenant constante la concentration moyenne d'eau dans la cellule. Cette hypothèse permet de fournir une estimation du coefficient de diffusion  $D_M$  pour une concentration moyenne en eau donnée, en considérant que la membrane est dans des conditions uniformes et que ses propriétés de transport sont similaires tant que la concentration moyenne en eau est constante. Deux gaz porteurs de la vapeur d'eau sont utilisés et le ratio des coefficients de diffusion associés  $D_{\text{eff}}$  est supposé égal à celui des coefficients de diffusion libres, documenté dans la littérature. La deuxième série d'expériences, dénommée XP2, consiste à faire varier la pression totale du système. Le coefficient de diffusion dans la phase gazeuse varie avec l'inverse de la pression comme :

$$\frac{pD_{AB}}{(p_{cA}p_{cB})^{1/3}(T_{cA}T_{cB})^{5/12}(1/M_A + 1/M_B)^{1/2}} = a \left( \frac{T}{\sqrt{T_{cA}T_{cB}}} \right)^b \quad (0-1)$$

Ainsi, en modifiant la pression totale de la cellule, les mécanismes de diffusion en phase gazeuse sont distingués des autres. En maintenant toutes les autres conditions expérimentales constantes, les mécanismes indépendants de la pression sont épargnés. Des résultats d'estimation sont présentés en Fig. 0-3. Le coefficient de diffusion effectif de la vapeur d'eau dans l'air  $D_{\text{eff}}^{\text{air}}$  est présenté en Fig. 0-3a, dans l'hydrogène  $D_{\text{eff}}^{\text{H}_2}$  en Fig. 0-3b et dans la membrane  $D_M$  en Fig. 0-3c. Les résultats des deux méthodes pour différents assemblages membrane-électrodes sont présentés.

L'hypothèse utilisée pour XP1 concernant le ratio des coefficients de diffusion entre les deux gaz n'est pas vérifiée par XP2, ce qui mène à des différences d'estimation entre les deux méthodes. Le modèle ne contenant que deux paramètres, certains mécanismes tels que la diffusion de Knudsen sont intégrés aux

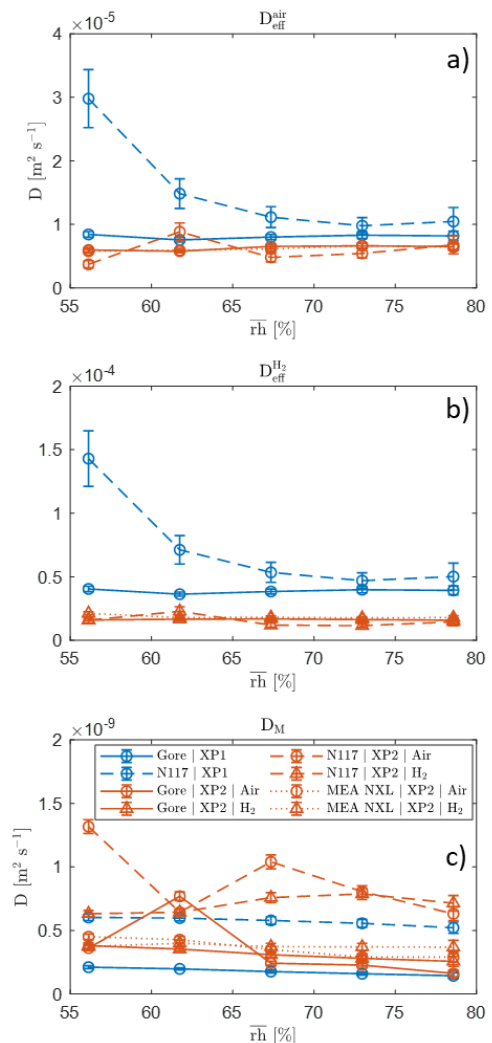


Figure 0-3 : Paramètres estimés pour tous les AME et par les deux méthodes

paramètres estimés. Selon les méthodes, ces contributions varient et créent des différences dans les estimations. Néanmoins, ces estimations sont reproductibles, cohérentes avec les valeurs de la littérature et peuvent être intégrées à des modèles réduits de transport de l'eau.

## Estimation de la résistance thermique entre l'AME et les plaques

La conductivité thermique effective de la GDL est d'une grande importance pour modéliser correctement le transfert de chaleur entre l'AME et les plaques bipolaires. Les valeurs expérimentales dans la littérature s'étalent dans une large gamme, en fonction des conditions de mesure. La grande variété de matériaux et de propriétés étend encore la gamme de valeurs.

La résistance thermique entre l'AME et une plaque peut être estimée en considérant que la chaleur est principalement transportée par conduction à travers la GDL. Le flux de chaleur  $\phi_{GDL}$ , la résistance thermique  $R_{th}$ , la température de l'AME  $T_M$  et les températures des plaques  $T_{pl}^{a,c}$  sont liés par l'expression suivante :

$$R_{th} = \frac{|T_M - T_{pl}^{a,c}|}{\phi_{GDL}} \quad (0-2)$$

Cette résistance thermique peut servir à estimer une conductivité thermique effective  $\kappa_{eff}$  de la GDL, qui prend en compte les effets géométriques, de compression et les résistances de contact :

$$R_{th}^{GDL} = \frac{t_{GDL}}{\kappa_{eff}} \quad (0-3)$$

La mesure de cette résistance thermique nécessite une mesure de flux de chaleur à travers la GDL ainsi que la mesure de la température de l'AME  $T_M$  et d'une des plaques. Cependant, la mesure de  $T_M$  est difficile étant donné le peu d'accessibilité dans une cellule.

Ainsi, une expérience originale est mise en place. Une différence de température est imposée entre les plaques : la cathode a une température de 5 °C supérieure à celle

de l'anode. Les gaz sont humidifiés à 100% par rapport aux températures des plaques. Le courant est progressivement augmenté, ce qui a pour effet d'augmenter la température de l'AME. En parallèle, les flux d'eau qui traversent l'anode et la cathode sont mesurés. Pour un certain point de fonctionnement, le flux d'eau côté cathode s'annule. La vapeur d'eau dans la GDL étant saturée, cela signifie que champ de température y est uniforme et donc que l'AME est à la même température que la plaque cathodique. Connaissant la tension de fonctionnement, le flux de chaleur produit, et évacué côté anode, est déterminé. La résistance thermique peut être estimée et avec elle la conductivité thermique effective. La Fig. 0-4 représente le point de fonctionnement à atteindre pour cette expérience.

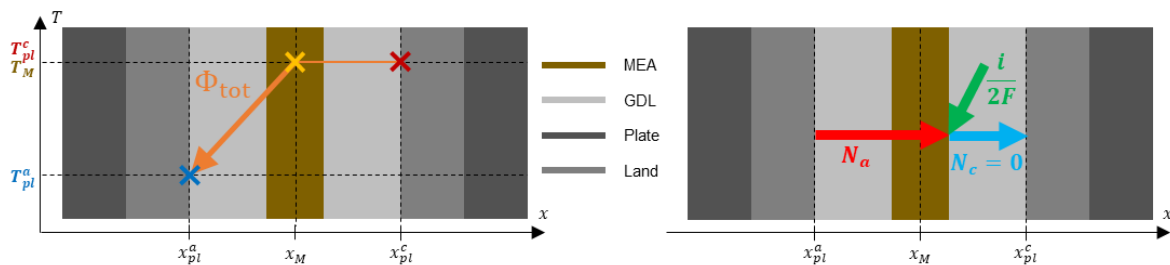


Figure 0-4: Schéma du champ de température et des flux d'eau dans la cellule pour l'estimation de la conductivité thermique effective

Plusieurs expériences sont menées en faisant varier la différence de température et en inversant les températures des plaques. Les valeurs estimées de conductivité thermique effective sont cohérentes avec la littérature et sont contenues dans l'intervalles  $[0.15 - 0.19] \text{ W m}^{-1}\text{K}^{-1}$ .

## Etude expérimentale et modélisation de cycles de charge

Un modèle transitoire est développé afin de représenter le transfert couplé de chaleur et d'eau pendant des cycles de charge. Les hypothèses, les lois de transfert et les paramètres associés sont décrits dans le manuscrit. Un point important est la modélisation de la saturation en eau du compartiment cathodique, qui joue le rôle de stockage d'eau liquide.

En parallèle, des expériences sont menées afin d'étudier le stockage de l'eau dans la cellule pendant des cycles de charge, définis comme des rampes croissantes et décroissantes entre un courant minimum et un courant maximum. Plusieurs vitesses de balayages sont imposées. La superposition d'oscillations de courant à 1 kHz permet la mesure de l'impédance de la cellule qui renseigne sur ses conditions d'humidification et de température. Les bilans d'eau sont réalisés en continu afin de déterminer à chaque instant la quantité d'eau stockée dans la cellule. La Fig. 0-5 représente quatre grandeurs d'intérêt dans cette expérience : le flux d'eau stocké  $n_{st}$ , le courant  $I$ , la saturation  $S^*$  et la résistance à 1 kHz  $R_{1kHz}$ . On y observe que le flux d'eau stocké est parfaitement synchronisé avec le courant, que la résistance est minimale lorsque le courant est maximal et que la saturation est désynchronisée des autres grandeurs. Aussi, la Fig. 0-6 suggère que l'AME est plus humidifié lorsque la vitesse de balayage est supérieure.

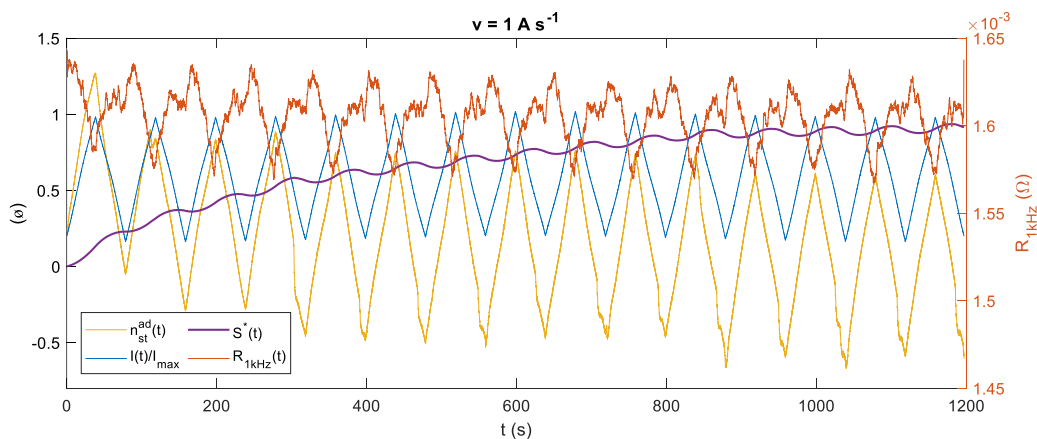


Figure 0-5: Flux d'eau stocké, courant, saturation et résistance à 1 kHz en fonction du temps

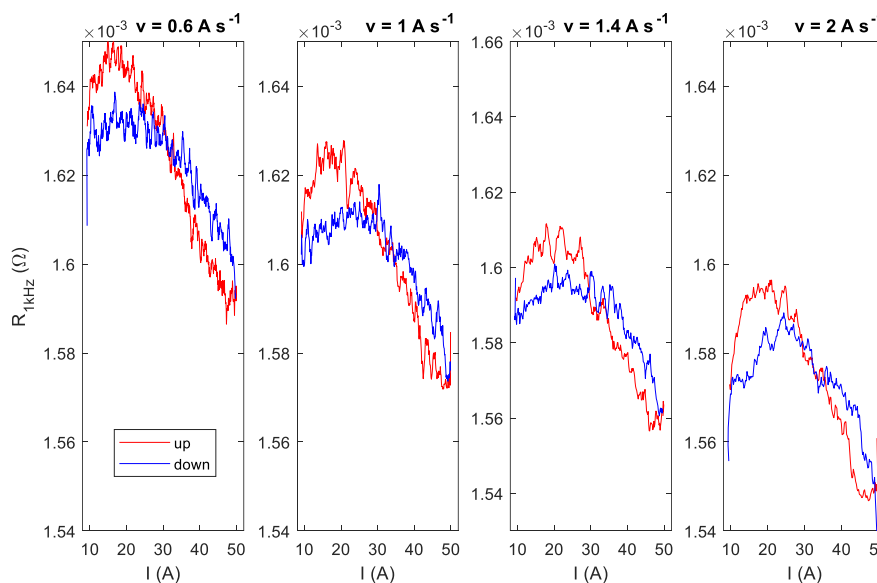


Figure 0-6: Résistance à 1 kHz en fonction du courant pour 4 vitesses de balayage

# **Preamble**

The current energy system needs to reinvent itself to reduce its emissions of pollutants, particularly greenhouse gases. Indeed, the consequences of this pollution are more and more visible and are becoming problematic for ecosystems and humans. Moreover, the future scarcity of fossil resources forces us to find alternatives to current technologies. Hydrogen is a gas already widely used in many industrial fields. Like electricity, it can play the role of an energy carrier: an intermediary between an energy source and a mode of consumption. The mobility field has a long way to go to convert the vehicle fleet to non-emitting vehicles. Hydrogen, provided it is produced without carbon emissions, is a very good candidate for the propulsion of ecofriendly vehicles. A fuel cell acts as an energy converter to produce hydrogen-based electricity to power an electric motor. This fuel cell is a multi-physical and multi-scale device, composed of innovative materials and which implements complex electrochemical reactions. The modeling of water and heat transport phenomena in the cell allows to better identify the mechanisms involved and thus to improve materials, designs and operating conditions. An optimized fuel cell is a system that will perform better, last longer and be less expensive.

The thesis work that is presented in this paper is divided into four parts. First of all, an overview of the energy and environmental system is drawn up. The current role of hydrogen in this system is presented, as well as the advantages it brings. Fuel cells, the cornerstone of hydrogen's automotive application, are introduced and the challenges to further improve the technology are detailed. Then, a chapter is dedicated to the modeling of water transport in a fuel cell. This modeling approach is coupled to a rich design of experiments in order to estimate crucial parameters for water transport. Different materials are characterized and two experimental methods are compared. Next, the thermal resistance between the MEA and the bipolar plates is estimated. Using the coupling between water transport and heat transport, an original experiment is set up to estimate the effective thermal conductivity of the porous layers of the cell. Finally, load cycles are applied to a cell to study transient water storage. A complex experiment is set up for this purpose. A preliminary modeling is performed and compared to the experimental results.

# Table of contents

<b>Remerciements</b>	<b>2</b>
<b>Résumé élargi</b>	<b>4</b>
<b>Preamble</b>	<b>12</b>
<b>Chapter I: Hydrogen, fuel cells and challenges</b>	<b>18</b>
<b>Introduction</b>	<b>18</b>
<b>I – Energy context</b>	<b>19</b>
I – 1. Current resources	19
I – 2. Hydrogen benefits	20
I – 3. Hydrogen sector	21
I – 3.1. Hydrogen production	21
I – 3.2. Hydrogen for industry	24
I – 3.3. Hydrogen for electric mobility	25
<b>II – Fuel cells</b>	<b>27</b>
II – 1. Technologies	27
II – 2. Fuel cell stack	29
II – 3. PEMFC structure	30
II – 3.1. Bipolar plates / feeding plates	30
II – 3.2. Gas diffusion layers (GDL)	31
II – 3.3. Catalyst layers (CL)	33
II – 3.4. Membrane	33
II – 4. Thermodynamics and performances	34
II – 4.1. Cell voltage	34
II – 4.2. Activation overpotential	36
II – 4.3. Ohmic overpotential	37
II – 4.4. Concentration overpotential	37
II – 4.5. Heat sources	38
<b>III – Challenges</b>	<b>39</b>
III – 1. Degradations	39
III – 1.1. Membrane	40
III – 1.2. Carbon support in the CL	41
III – 1.3. Catalyst	42
III – 1.4. GDL	42
III – 1.5. Ionomer in the electrode	42
III – 2. Water and heat management	43

III – 2.1. Strategies for water management	43
III – 2.2. Strategies for heat management	45
III – 2.3. Water and heat transport modeling	45
III – 2.4. Parameters, sensitivity and estimation	47
III – 3. Thesis objectives	48
<b>Chapter II: In-situ estimation of water transport parameters</b>	<b>51</b>
<b>Introduction</b>	<b>52</b>
<b>I – Overview of water transport modelling</b>	<b>53</b>
I – 1. In the membrane	53
I – 1.1. Fick’s diffusion	54
I – 1.2. Electroosmotic drag	56
I – 1.3. Sorption resistance	56
I – 2. In GDLS	57
I – 2.1. Water vapor transport laws	57
I – 2.2 Bulk diffusion coefficients	60
I – 2.3. Effective diffusion coefficients	61
I – 2.4. Liquid water	62
I – 3. In the CLs	64
I – 3.1. Knudsen diffusion	64
I – 3.2. Ionomer	64
I – 4. In channels	65
<b>II – 1+1D model</b>	<b>66</b>
II – 1. Through-plane direction	67
II – 2. Along the channel	69
<b>III – Design of experiment</b>	<b>70</b>
III – 1. Experimental set-up	70
III – 1.1. Bench	70
III – 1.2. Humidifiers	73
III – 1.3. Cell	77
III – 2. Set-up design optimization: definition of the optimal exchange surface	78
III – 3. XP1: constant average concentration	81
III – 4. XP2: pressure variation	83
III – 5. XP3: condensation	86
<b>IV – Parameters estimation</b>	<b>86</b>
IV – 1. Method for parameters estimation validation	88
IV – 2. Estimations by XP1	91
IV – 2.1. Gore MEA	91

IV – 2.2. N117 MEA _____	94
IV – 3. Estimation by XP2 _____	96
IV – 3.1. Gore MEA _____	96
IV – 3.2. N117 MEA _____	97
IV – 3.3. NXL membrane and MEA _____	98
IV – 3.4. Comparison between all materials _____	100
IV – 4. Comparison between XP1 and XP2 _____	100
IV – 5. Liquid sorption influence _____	104
<b>V – Conclusions and outlooks _____</b>	<b>107</b>
<b>Appendix _____</b>	<b>110</b>
<b>Chapter III: Estimation of thermal resistance between plates and MEA _____</b>	<b>112</b>
<b>Introduction _____</b>	<b>113</b>
<b>I – Heat sources _____</b>	<b>113</b>
I – 1. Reversible losses _____	115
I – 2. Activation losses _____	115
I – 3. Joule effect _____	116
I – 3.1. Protonic resistance _____	116
I – 3.2. Electronic resistance _____	116
I – 4. Concentration losses _____	117
I – 5. Conclusions about heat sources _____	117
<b>II – Overview of heat transfer mechanisms and modelling _____</b>	<b>118</b>
II – 1. Conduction in GDLs _____	118
II – 2. Thermal contact resistances _____	119
II – 3. Conduction in the membrane _____	120
II – 4. Coupling between heat and water _____	121
II – 4.1. Heat-pipe effect _____	121
II – 4.2. Evaporation/condensation _____	122
II – 4.3. Sorption/desorption _____	122
<b>III – Estimation of the thermal resistance between MEA and plates _____</b>	<b>122</b>
III – 1. Principle _____	122
III – 2. Materials _____	126
III – 3. Results _____	127
III – 3.1. Hot anode / cold cathode (“ha/cc”) _____	128
III – 3.2. Hot cathode / cold anode (“hc/ca”) _____	130
III – 4. Comparison with literature _____	134
<b>IV – Conclusions and outlooks _____</b>	<b>135</b>

<b>Chapter IV: Experimental and modelling study of heat and water transport during load cycling</b>	<b>137</b>
<b>Introduction</b>	<b>138</b>
<b>I – 1D transient model for coupled heat and water transport</b>	<b>139</b>
I – 1. Heat transport	139
I – 2. Water transport	140
I – 2.1 In the GDLs	140
I – 2.2. In the MEA	142
I – 3. Liquid water saturation	142
<b>II – Dynamic regime experiments</b>	<b>143</b>
II – 1. Materials	143
II – 2. Design of experiment	144
II – 2.1 Current profiles	144
II – 2.2. Procedure	145
II – 2.3. Feeding gases and stoichiometry	146
II – 2.4. Experimental conditions	149
II – 3. Processing method	150
II – 3.1. 1-kHz resistance	150
II – 3.2. Water balance	153
II – 4. Transient experiments – Results	154
II – 4.1. Voltage and 1-kHz resistance	154
II – 4.2. Water balance	160
II – 5. Pseudo-steady state experiments – Results	165
II – 5.1. Transient regime	166
II – 5.2. Voltage and 1-kHz resistance in pseudo-steady state	168
II – 5.3. Water balance in pseudo-steady state	170
<b>III – Comparison between model and pseudo-steady state experiments</b>	<b>172</b>
III – 1. Parametrization	172
III – 1.1. Electro-osmotic drag	173
III – 1.2. Polarization curve	173
III – 1.3. Wettable volume and limiting saturation	174
III – 2. Heat transfer	175
III – 3. Water storage	177
<b>IV – Conclusions and outlooks</b>	<b>179</b>
<b>Appendix</b>	<b>183</b>
<b>General conclusions and outlooks</b>	<b>189</b>

<b>References</b>	<b>192</b>
<b>Abstract / Résumé</b>	<b>207</b>

# **Chapter I: Hydrogen, fuel cells and challenges**

<b>Introduction .....</b>	<b>18</b>
<b>I – Energy context.....</b>	<b>19</b>
I – 1. Current resources .....	19
I – 2. Hydrogen benefits.....	20
I – 3. Hydrogen sector.....	21
<b>II – Fuel cells .....</b>	<b>27</b>
II – 1. Technologies.....	27
II – 2. Fuel cell stack .....	29
II – 3. PEMFC structure .....	30
II – 4. Thermodynamics and performances .....	34
<b>III – Challenges .....</b>	<b>39</b>
III – 1. Degradations.....	39
III – 2. Water and heat management .....	43
III – 3. Thesis objectives .....	48

## **Introduction**

This chapter briefly presents the energy context in which the hydrogen energy carrier is being developed. Fuel cells appear to be an essential tool in the hydrogen sector since they allow the conversion of hydrogen into electricity. Their applications can be multiple. The mobility sector, which must begin a conversion towards decarbonization, could largely benefit from the advantages of hydrogen thanks to fuel cells. Nevertheless, many challenges remain to be met, such as durability, performance and cost.

## I – Energy context

### I – 1. Current resources

The first highlighted sentence of the 2014 Intergovernmental Panel on Climate Change report synthesis [1] is the following: “Human influence on the climate system is clear, and recent anthropogenic emissions of greenhouse gases are the highest in history. Recent climate changes have had widespread impacts on human and natural systems”. In 2011, CO<sub>2</sub> emissions from fossil fuel combustion, cement production and flaring were 34.8 Gt per year and this figure is continuously increasing. A half of cumulative anthropogenic carbon emissions have occurred during the last 40 years. International Energy Agency published a Key World Energy Statistics report in 2020 [2] where one can find clues about world’s energy supply and consumption. The global energy supply was 6,098 Mtoe in 1973 and 86.7% were natural gas (16%), coal (24.5%) and oil (46.2%). In 2018, the same resources contribution slightly decreased to 81.3% (22.8% for natural gas, 26.9% for coal and 31.6% for oil) whereas the total energy supply increased up to 14,282 Mtoe. Thus, crude oil production went from 2,868 Mt in 1973 up to 4,439 Mt in 2019.

The consequence of anthropogenic carbon emissions is the global warming: the average temperature on Earth increased by 0.8 to 1.3 °C from the 1850-1900 period until 2010-2019 [3]. This climate change has many consequences, both on humans and ecosystems. As an example, a large majority of regions in the world experienced an increase in hot extremes since 1950’s. Physical, biological and human systems are all affected around the world by climate change.

The only way our society has to follow is the transition towards a non-carbon-based energy system where renewable energies represent a large majority of the total supply. In 2018, renewable energies represented 13.8% of the total supply (9.3% for biomass and waste, 2.5% for hydro and 2% for others, containing geothermal, solar, wind ocean for instance). Nuclear energy, which is not carbon-based, but not renewable, represented 4.9%. Even though the renewable part slowly increases, the absolute supply sharply enlarges. Hydroelectricity production has been multiplied by more than 3 between 1973 and 2018 (1,296 TWh to 4,325 TWh), 2018 wind electricity production

was 12 times higher than in 2005 (104 TWh to 1,273 TWh) and the solar photovoltaic (PV) production has been increased by a factor 138 during the same period (4 TWh to 554 TWh) [2]. Consequently, the price of renewable energy is continuously decreasing. PV electricity costed 600 USD(2020)/MWh in 2000 whereas it was around 55 USD(2020)/MWh in 2020. This strong price reduction enables an exponential adoption of PV since it is now competitive with fossil electricity production or even cheaper. The same adoption trends are observed for onshore and offshore wind electricity or for the number of electric vehicles on the roads, stimulated by the decreasing price of Li-ion batteries [4].

Transport sector was responsible of approximately 28% of the global carbon emissions in the atmosphere in 2014, with large variations regarding the regions: around 30% for Europe and US and less than 10% for China, India and Indonesia for instance [5]. In 2009, freight transport consumed almost 45% of total transport energy and half of this amount was used by heavy-duty vehicles. Passengers transport represents the remaining 55% and a large majority has been achieved with light-duty vehicles, representing itself half of the total energy transport [6]. Lots of efforts are needed to reduce the impact of transport sector on the global emissions. The transition towards cleaner vehicles but also the reduction of the total expended energy in transport are crucial.

## I – 2. Hydrogen benefits

One major drawback of renewable energy sources is that they are mainly intermittent: photovoltaic panels produce electricity with daylight and wind turbines work when wind is strong enough but not too much. However, the power system needs to be at equilibrium between production and consumption at every time. Even though the electric system has a capability to handle small unbalances, the addition of highly variable power sources such as renewables implies a need for a better system flexibility. Energy storage is one way to increase grid flexibility by time-shifting the delivery of power [7]. Production and storage of hydrogen is one way to store energy during grid unbalance. Hydrogen is produced by water electrolysis and then stored in adapted tanks. Then, the gas can be used for electricity production to fill power lacks on a grid (via a fuel cell) but others applications can be considered such as hydrogen

fueling stations, gas distribution, chemical and industrial processes [8]. Hydrogen can be produced from many renewable sources [9] and used as a clean energy carrier or feedstock for a large variety of sectors: transport, residential, chemical industry, steel industry, among others [5].

Transport sector is almost fully dependent on fossil fuels: 92% of the transport energy demand is currently met by petroleum oil [10]. To achieve the transition of this sector, deployment of eco-friendly solutions is highly needed. Fuel cell (FCEVs) and battery (BEVs) electric vehicles are seen as appropriate candidates to reduce to near zero the carbon emissions of the sector. Even though they are often compared, both have advantages that can make them coexist. BEVs are more efficient and can be easily recharged at home which make them more suitable for urban light-duty vehicles. FCEVs already have satisfying cruising range (> 500 km) and are refueled in minutes. Scale up of FCEVs is easier than for BEVs due to the significant batteries weight and the constraints on the electricity network that would be created by the widespread use of fast-charging. Thus, the prevailing opinion is that FCEVs are adapted to heavy-duty and long-distance transportation [11].

## I – 3. Hydrogen sector

### I – 3.1. Hydrogen production

Global hydrogen production is close to 70 Mt per year. 76% stem from natural gas, 23% from coal (exclusively in China) and 2% from other resources, of which a very small part comes from water electrolysis, which is a way to produce decarbonated hydrogen if the employed electricity is renewable or nuclear [12]. Depending on the process, colors are attributed to the produced hydrogen. Grey hydrogen is produced from steam methane reforming if carbon dioxide is released in the atmosphere. This process is the most established but contributes to the global emissions of carbon. Blue hydrogen production is similar to the grey, but carbon capture is added at the process end and then stored. Turquoise hydrogen is produced by methane pyrolysis, and the produced carbon is in solid state, preventing any carbon dioxide releasing. Finally, green hydrogen is produced by water electrolysis using renewable electricity. This process is carbon free (if the emissions associated with the production and operation

of renewable energy capture facilities are neglected) and is the most desirable way to produce hydrogen for the future [13]. Other colors exist depending on the origin of electricity, notably for nuclear source.

Two main processes are used for making hydrogen from hydrocarbons: steam reforming and partial oxidation.

Steam reforming uses steam and nickel-based catalysts to transform a raw material - generally natural gas - into synthesis gas (a mixture of hydrogen, carbon monoxide, carbon dioxide, etc.). These transformations take place between 840 and 920 °C and between 20 and 30 bar. In a steam reforming installation, two main chemical reactions are carried out:

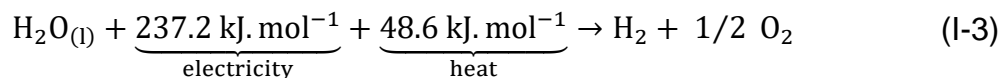


With the global reaction being:  $CH_4 + 2H_2O \leftrightarrow CO_2 + 4H_2$  ( $\Delta H = 165 \text{ kJ mol}^{-1}$ ).

The first reaction corresponds to steam reforming, while the second corresponds to water gas shift, allowing the recovery of hydrogen from the water molecule thanks to the carbon monoxide previously produced. These two reactions cannot be carried out in their entirety - they are governed by a thermodynamic equilibrium - which means that reagents can be found in the products, thus requiring a separation.

Partial oxidation can be carried out without a catalyst when the temperature is high enough. The working temperature lays between 900 and 1500°C and the pressure between 20 and 60 bar. It can use different raw materials such as natural gas, coal or biomass (biomass allows for negative carbon emissions when the carbon is captured as biochar or  $CO_2$ ) for instance. Its heavier investment can be amortized thanks to the great variety of origin of the resources used. Many chemical reactions can be involved, which makes this process more complex than steam reforming; this complexity being necessary to compensate for the diversity of resources. The two main steps remain, nevertheless, the same: creation of a synthesis gas and then use of the carbon monoxide. After the whole process, the gases produced must also be purified to extract the pure hydrogen.

Water electrolysis is one way to produce hydrogen without emitting or even producing carbon. High purity hydrogen come from this process, almost reaching 100%. The involved reaction at 25 °C is the following:



Several different technologies exist to carry out the electrolysis of water. Chronologically, the first of these is alkaline electrolysis. It uses two electrodes immersed in a solution of potash (KOH) concentrated between 20 and 30%. These electrodes are separated by a conductive diaphragm of hydroxide ions whose second role is to separate the gaseous species produced to prevent them from recombining. Several defects are inherent to this technology. The permeability of the diaphragm to gases does not allow an efficient separation of the produced gases, which reduces the efficiency of the production as well as its safety. The high ohmic losses in the liquid electrolyte do not allow the use of high currents and therefore the production of high gas flow rates, thus leading to a large footprint. It is not possible to operate at high pressure (above 30-50 bar). Highly concentrated potash is corrosive and creates muds by carbonating. However, this technology is the most developed today, benefiting from low costs and good durability.

Solid oxide electrolysis is a technology operating at a temperature higher than 800 °C for the major part. The cell efficiency is higher than low temperature cells, especially if a free heat source can be recovered, as the electrolysis of water is increasingly endothermic with increasing temperature. The unavoidable produced heat is used for the molecule splitting process and thus the required electric power is reduced [14]. The high temperature also implies that rare catalysts are not necessary to improve electrochemical reactions, lowering the potential total price and increasing the sustainability of such a technology. Finally, cells are reversible and can be switched from electrolysis to fuel cell mode, depending on the need. The major drawback of this technology is the intermittent operation, materials being damaged during startups and shutdowns due to thermal expansion and thus its durability.

PEM electrolysis, an acronym that stands for both Proton Exchange Membrane and Polymer Electrolyte Membrane, operates at low temperatures, generally below 100°C.

It was first developed by General Electric in the 1960s. Here, a polymer membrane is used both as an electrolyte and as a diaphragm, allowing the transport of protons and ensuring good impermeability to gases. Its advantages in terms of efficiency, response time and purity of the hydrogen produced make it one of the most studied technologies today. This research must succeed in finding solutions to its relatively low durability, its need for rare catalysts and corrosion-resistant materials [13]. This technology highly suffers from its need in rare catalyst such as iridium, whose annual production will not allow the upscaling to the terawatt range.

Anion Exchange Membrane water electrolyzers (AEMWE) bring together advantages of both alkaline and PEM electrolysis. The electrodes of AEMWE do not contain platinum-group metal or critical raw materials, which is an interesting potential for upscaling. Moreover, AEMWE use a membrane has an electrolyte, allowing to reach high current densities because of the lowered ohmic resistance. Compared to alkaline electrolysis, AEMWE are safer and can provide pressurized hydrogen [15].

At the end of the production step, hydrogen pressure is between 15 and 80 bars depending on the technology, materials or applications [5]. This pressure range is acceptable for pipelines but a variety of applications such as refueling stations (and thus automotive) expect higher pressure to increase energy density. Hydrogen station must be able to provide 700 bars hydrogen to refuel gas tanks of FCEV. To achieve such a pressure, a large diversity of hydrogen compressor technologies is available, from the most established mechanical compressors to the most innovative non-mechanical technologies [16].

### I – 3.2. Hydrogen for industry

Hydrogen has long been an important part of our industrial landscape, for reasons quite different from those for which it is currently famous. In 2012, hydrogen production amounted to 6 EJ (exajoules, or  $6 \times 10^{18}$  J) [17], representing nearly 470 billion cubic meters at room temperature and atmospheric pressure, and its use was evenly distributed over two main poles: the chemical industry (mainly for the production of ammonia) and petroleum product refining. The latter has largely increased its share over the last few decades because hydrogen is used in the desulfurization of petroleum

products, among other things. As environmental regulations are becoming increasingly restrictive with regard to the sulfur content of fuels, the use of hydrogen has increased significantly [18].

Ammonia is produced by the Haber-Bosch process, which was discovered in 1913 and which is today favored by all ammonia producers since it accounts for 90% of production [19]. It consists of the combination of hydrogen and nitrogen to form the ammonia molecule ( $\text{NH}_3$ ) thanks to a catalyst, high pressure and high temperature. The main application of ammonia is the fertilizer industry. All the hydrogen used in ammonia production comes from fossil resources [20]: 72% natural gas, 22% coal, 4% oil and 2% other fossil products. To transform these raw materials, many techniques and processes are used but their common major drawback is the fact that they release carbon in large quantities.

Hydrogen is present in a wide variety of fields thanks to its many qualities [18]. Its high reactivity with oxygen makes it indispensable in the metallurgical industry and in glassmaking where it is used as an oxygen scavenger. Oxygen molecules are responsible for the oxidation (corrosion) of materials when they are brought to high temperatures and must therefore be avoided as much as possible. Hydrogen is also used to treat fats and oils in order to reduce their tendency to oxidize and therefore to preserve them longer: this is the hydrogenation process used in food industry.

### I – 3.3. Hydrogen for electric mobility

In 2017, Toyota launched its first hydrogen vehicle: the Mirai. Its price was under \$59,000 and its platinum loading was  $0.365 \text{ mg cm}^{-2}$  (0.05 at the anode and 0.315 at the cathode). Its power density is  $2 \text{ kW kg}^{-1}$  and  $3.1 \text{ kW L}^{-1}$  for a total of 153 hp (114 kW). Several hydrogen vehicles now exist: Honda Clarity, Toyota Mirai, GM ZH2, Hyundai Nexu FCV. Honda and Hyundai vehicles offer a range of 366 miles or almost 600 km. Mercedes Benz will soon offer a hybrid hydrogen/battery vehicle that can carry 4.4 kg of hydrogen, for a total range of 300 miles or more than 480 km [21]. The United States has over 5,000 hydrogen vehicles and 30 stations. Germany had 64 stations in 2019 and plans to install 36 new ones, bringing the total number to 100 hydrogen stations. Japan plans to deploy 800,000 hydrogen vehicles on its territory by 2030.

Trucks show a very good potential for the use of fuel cells. Some heavy-duty vehicles can use batteries for short distances, but for longer distances the use of hydrogen is a good solution. Competition with battery technologies is strong, especially with the Tesla Semi, which offers 300 to 500 miles of range for \$200,000. Improved durability is necessary since the trucks are intended to be heavily used, with a target of 50,000 hours of operation. Good efficiency and low fuel costs are essential. Kenworth, Toyota, Hyundai and Nikola are developing hydrogen trucks [5].

In the field of aviation, fuel cells can be the main means of propulsion of unmanned aircraft. For such applications, the required characteristics are small size, high durability and high capacity. Fuel cell are also able to provide electrical energy for all the ancillary equipment of manned aircraft. They have the advantage of supplying a direct current, having a high-power density and a large energy capacity. Recently, electricity production with hydrogen and fuel cells is developed to be the main mean of propulsion for manned aircrafts. Zero Avia is developing passenger planes from a few seats up to several dozen seats in the near future. The Naval Research Lab has successfully completed a 48-hour flight using a 550 W stack and compressed hydrogen in a carbon/aluminum tank. In Spain in 2008, Boeing tested a two-person manned flight in a 16.3 m wingspan aircraft for 20 min at 100 km/h, powered only by a fuel cell. In 2016, a collaboration between an aircraft manufacturer (Pipistrel), a fuel cell producer (Hydrogenics), the University of Ulm, and the German Aerospace Center made it possible to fly an aircraft carrying two passengers using 9 kg of hydrogen. Boeing has integrated a fuel cell system into its 787-8 aircraft that provides energy for entertainment and for peak loads during takeoffs and landings.

There are many other applications for fuel cells. One of the first cost-effective is forklifts. More than 12,000 of these are deployed in the USA. The advantage of hydrogen in this situation is that no polluting gases are released, which allows the use of these devices in confined spaces, such as warehouses. Most of them are battery operated for the same reasons, but the hydrogen system allows a much faster recharge.

## II – Fuel cells

### II – 1. Technologies

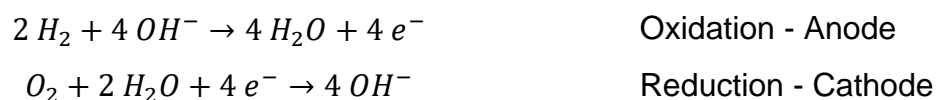
A fuel cell is an electrochemical device whose goal is to convert the chemical energy of a fuel into electricity, without direct combustion. The fuel and the oxidizer are kept separated and the global reaction is split into two reactions: an oxidation and a reduction. The cells tolerate several fuels such as hydrogen, methanol [22] or ammonia [23]. All fuel cells share the same main parts: anode, cathode, electrolyte and external circuit. At the anode, the fuel is oxidized, producing electrons that pass through the external circuit to create electrical work. At the cathode, in most applications, oxygen is reduced. All fuel cell types share common advantages [24]:

- Potentially high efficiency compared to thermal machines
- Some technologies are easily scalable,
- In case of hydrogen usage, harmful emissions are reported at the hydrogen production stage,
- No moving part besides ancillary devices such as pumps or compressors,
- Large variety of feedstocks for employed fuels: oil, gas, coal, ethanol, ...
- Short refueling time compared to battery systems.

Fuel cells can be separated in 5 main groups [25]:

- Alkaline FC (AFC)

The electrolyte conducts hydroxyl ions  $\text{OH}^-$ . If hydrogen is the fuel, the two half reactions are:



The first AFCs used liquid electrolyte based on potassium hydroxide (KOH) in water but recent progress led to usage of a polymer membrane. Such fuel cells are usually denoted as Anion Exchange Membrane FC (AEMFC). Their working temperature is below 100 °C.

- Phosphoric Acid FC (PAFC)

PAFCs are based on phosphoric acid ( $H_3PO_4$ ) as electrolyte. The involved ion is  $H^+$  since  $H_3PO_4$  is proton conductive. The working temperature is higher than AFCs – 150 to 220 °C – to find the optimal proton conduction of the electrolyte, avoid the production of liquid water and the leaching of the electrolyte. Half-reactions are as follows for a hydrogen fed cell:



- Solid Oxide FC (SOFC)

SOFC electrolyte is usually a metallic oxide ceramic that conducts  $O^{2-}$  ions. The working temperature is higher than 800 °C so that reactions kinetic is fast and cell efficiency is high. The involved reactions for hydrogen are the following:



- Molten Carbonate FC (MCFC)

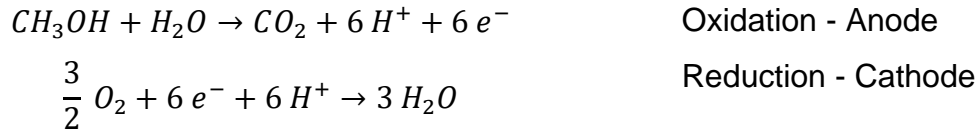
Using a molten carbonate salt mixture as electrolyte, MCFCs work at high temperature and tolerate a variety of fuels. The conducted ion is  $CO_3^{2-}$  and reactions are multiple: fuel is firstly reformed to produce hydrogen and carbon dioxide, and then, two steps are needed for the oxidation and one for the reduction, that needs  $CO_2$  to occur. This technology can also be used to extract diluted  $CO_2$  from flue gases.

- Proton Exchange Membrane FC (PEMFC)

PEMFC uses an ionomer as electrolyte, able to conduct protons. The complete structure is depicted in the following as it is the targeted technology of this study. When a PEMFC is fed with hydrogen, the following reactions occur:



Other fuels are usable in a PEMFC such as methanol. In this case, the cell is denoted as Direct Methanol FC (DMFC) and carbon dioxide is produced. The following reactions take place:



All FC technologies have their own features such as working temperature, electrolyte, fuel, efficiency, applications. High temperature FCs are preferred for stationary applications and even for cogeneration (usage of heat losses to produce hot water/vapor for instance) whereas low temperature FCs are well suited for portable applications or for mobility. PEMFC seems to be the more adapted technology since it uses a very convenient solid polymer electrolyte, works at low temperature and pressure, starts-up easily and has a satisfying power density. Consequently, the following work will focus on this technology.

## II – 2. Fuel cell stack

A typical laboratory PEM fuel cell generates power in the range of 10-100 W [26]. Indeed, as developed in *Thermodynamics and performances* part, the cell voltage is between 0.3-1 V while the current density is between 0 and 1.5-3 A cm<sup>-2</sup> depending on the working conditions. Thus, the order of magnitude of the delivered power is less than 2 W cm<sup>-2</sup>. One way to increase the total power supply of a PEMFC is to increase the total active surface. Nevertheless, this implies heterogeneities in gas supply, temperature, pressure and may lead to degradations. Moreover, the working voltage of the elementary cell, imposed by thermodynamics and the different irreversibilities is between 0.5 and 0.8 V. This low voltage is hardly usable for external devices such as electric motors or batteries. It is thus necessary to increase the voltage by assembling the cells in series in a stack. The stack voltage is the sum of each cell voltage whereas the total current is the same in all the cells. The stack is also a way to increase the volumetric power density of PEMFC.

Fig. I-1 schematizes a stack of two cells which are separated by bipolar plates, whose role is developed in the following. In a stack, all cells are connected in series for the

electric circuit whereas they are fed in parallel by the gas supply and cooling circuit to ensure the most homogeneous distribution possible between the cells.

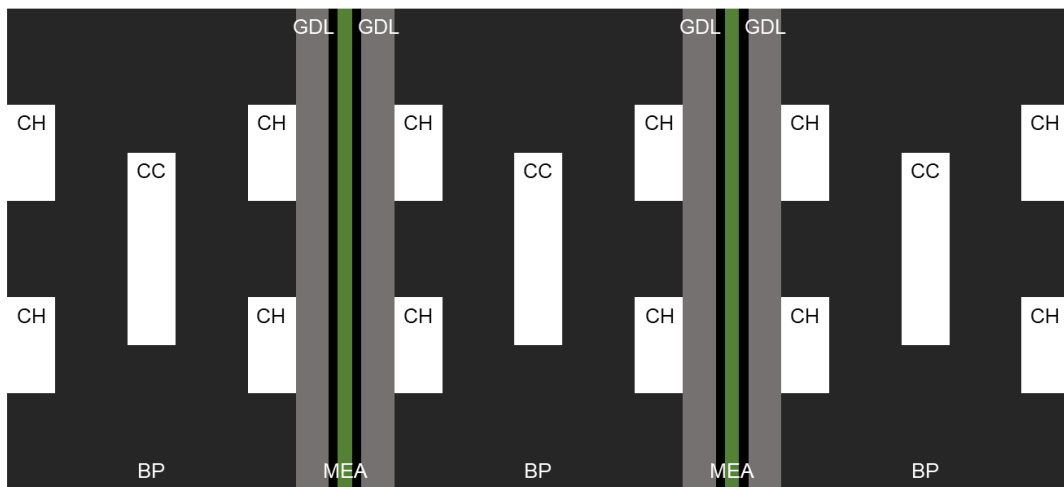


Figure I-1: Schematic of a stack of two cells separated by bipolar plates (CC: cooling circuit, CH: channel, BP: bipolar plate)

### II – 3. PEMFC structure

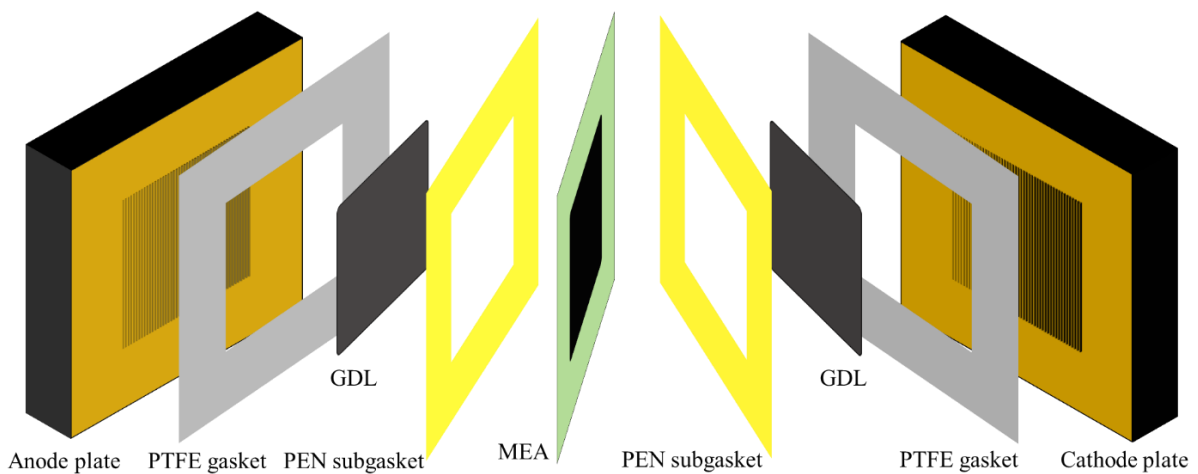


Figure I-2: Exploded view of a typical mono-cell assembly

Fig. I-2 represents an exploded view of a typical laboratory single cell assembly which is a stack of several layers, each one having its own role.

#### II – 3.1. Bipolar plates / feeding plates

The feeding plates are crucial parts of a fuel cell. Their functions are multiple [27]:

- To homogeneously distribute the reactants by the gas flow channels
- To collect, conduct and distribute current
- To assure mechanical stability of the assembly
- To remove produced heat
- To discharge produced water

In a fuel cell stack, the bipolar plates have two additional roles:

- To isolate anode and cathode reactants
- To electrically connect all the cells in series

Bipolar plates are usually made out of metal, graphite or composite materials. Metal materials benefit from relatively low price, easy manufacturing, mechanical resistance and good bulk electrical conductivity but their major drawbacks are the corrosion and the resulting interfacial electrical resistance with the GDL and cation contamination. On the contrary, graphite materials have low density in addition to a good corrosion resistance but suffer from low mechanical strength. This usually leads to thicker plates to ensure mechanical stability, thus reducing the power density of the stack. Moreover, graphite plates are more challenging to process and price is consequently higher. It should be noted, however, that some manufacturers, such as Ballard, are able to obtain very high performances in terms of power density, durability and costs from carbon plates.

An important feature of the plates is the channels that provide reactants to the cell and evacuate produced water. Channels are usually carved on the plate surface and three main geometry are commonly used: straight, serpentine and interdigitated [28]. Each geometry has its own particularity for pressure drop, gas distribution homogeneity or liquid water removal. Novel geometries are proposed to improve the overall performance of fuel cells [27], [28]. Industrialists tend towards geometries with straight parallel channels of very small dimensions (hydraulic diameter lower than 0.4 mm).

## II – 3.2. Gas diffusion layers (GDL)

The gas diffusion layers (GDL) are located between the plates and the electrodes. They fulfill a large variety of functions in the cell by controlling mass, heat and electrons

transport and by giving mechanical support for the membrane and the catalyst layers [29]. Reactants and products are transported to and from reaction sites through the GDL. Heat is conducted from the membrane and electrodes towards the plates to be evacuated. The GDL is often separated into two different layers: the macroporous substrate (MPS), on the channel side, and the microporous layer (MPL), on the catalyst layer side, even though stand-alone MPS can be used in a fuel cell.

The MPS is a carbon-based material made out of fibers (with a diameter of about 10  $\mu\text{m}$  [30]) which are woven (carbon clothes) or non-woven (carbon papers). Fig. I-3 [30] represents SEM images of three typical MPS. Carbon clothes are more complex to process, and thus more expensive, because of their special structure. Their main advantage is their high mechanical flexibility and compressibility. The carbon papers are more easily processed and consist in randomly stacked fibers bonded by PTFE to ensure cohesion. Some carbon papers contain straight fibers whereas some others are based on “spaghetti” fibers. Structure, PTFE loading and MPL influence GDL properties such as porosity, pore size distribution, tortuosity, hydrophobicity or electrical conductivity for instance [30].

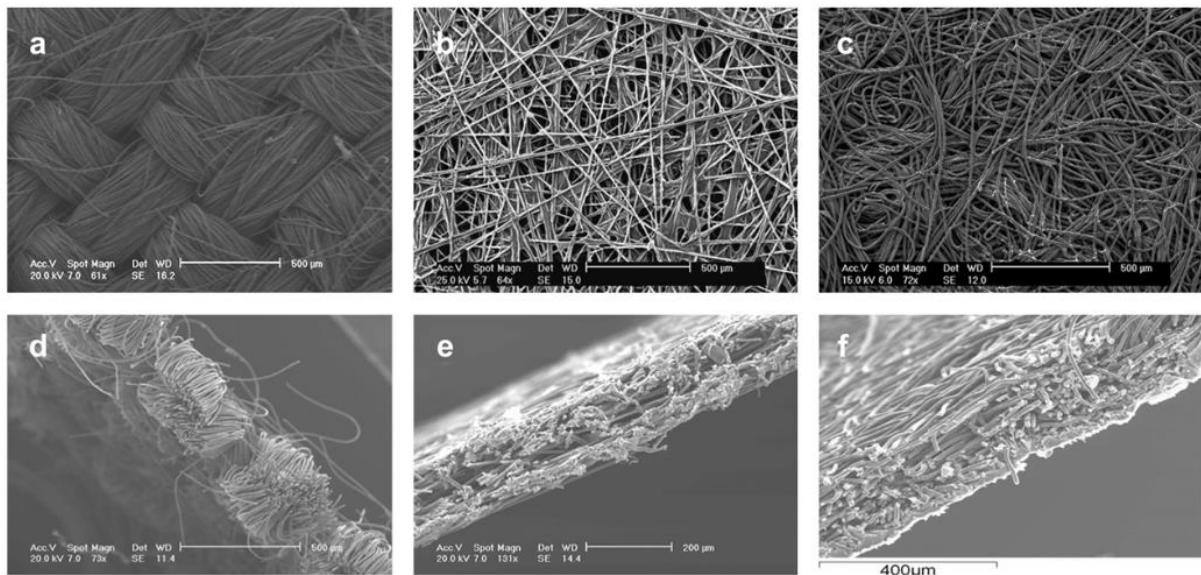


Figure I-3: SEM view of carbon cloth (a and d), straight fibers (b and e) and “spaghetti” (c and f) carbon papers [30]

The MPL is not literally a stand-alone layer because it is applied straight onto the MPS. It is composed of carbon powder and a hydrophobic agent which are sintered on the surface of the MPS. The pore size diameter (about 0.1  $\mu\text{m}$  [31]) is several orders of

magnitude lower than of the MPS, explaining that there is no clear limit between MPL and MPS [29]. It has been shown that the MPL was beneficial to the water management of a fuel cell by preventing the return of liquid water from the channels to the electrode and acting as a thermal resistance. It can also reduce the electronic contact resistance between the GDL and the electrodes and protect the MEA, from a mechanical point of view, against fiber intrusion by homogenizing the mechanical stresses.

### II – 3.3. Catalyst layers (CL)

The catalyst layer is placed between the GDL and the membrane. The basic functions of the catalyst layer are to (i) enable the fuel oxidation reaction or the oxidizer reduction, (ii) conduct ions from or to the reaction sites, (iii) conduct electrons from or to the reaction sites and (iv) facilitate reactant transport and product removal. In order to fulfill these roles, the layer contains (i) catalyst, usually platinum or platinum alloys, that improves the reactions kinetics, (ii) ionomer that conduct protons, (iii) a carbon-based matrix which is electron conductive and (iv) porosity to allow gas transport. Finally, the layer should be thin to reduce transport resistance and increase catalyst utilization [24], [32].

When the CLs are applied on the membrane, it is referred as a Catalyst Coated Membrane (CCM) whereas CLs sprayed onto the GDLs are named Gas Diffusion Electrode (GDE).

### II – 3.4. Membrane

The membrane is in the middle of the assembly, between the two CLs. All three of these layers are usually denoted as Membrane Electrodes Assembly (MEA). It has four main roles to fulfill [33]–[35]:

- Reactants separator to prevent direct reaction between fuel and oxidizer,
- Electrolyte to conduct protons from anode to cathode,
- Electrical insulator,
- Structural framework to support the catalyst, in the case of CCM.

Suitable materials for membrane must have specific properties such as:

- High ionic conductivity,
- Low fuel permeability,
- Thermal and hydrolytic stability,
- Chemical stability in aggressive environment,
- Morphological and dimensional stability,
- Mechanical strength in dry and hydrated states,
- Easy manufacturing
- Competitive low-cost and long-term durability

Nafion® (trademark of E. I. DuPont De Nemours & Co.) is regarded as the state-of-the-art material for membrane [36]. It belongs to the perfluorinated sulfonic-acid (PFSA) ionomer which is a copolymer composed of polytetrafluoroethylene (PTFE) associated to side-chains ended by ionic group  $SO_3^-$ . This structure results in natural phase separation that gives PFSAs their ion and solvent transport capabilities. Nevertheless, other materials are gaining interest, notably for higher temperature PEM fuel cells, where Nafion thermal properties are exceeded. For instance, short-side-chain PFSAs, such as Aquivion®, have the same PTFE backbone as Nafion but with shorter side-chains and exhibit higher temperature stability [37].

## II – 4. Thermodynamics and performances

### II – 4.1. Cell voltage

The voltage  $U$  of a working fuel cell is a function of the delivered current density  $i$ . Fig. I-4 presents a so-called polarization curve which represents the variation of the cell voltage with the current. The voltage  $E^{TH}$  is defined by assuming that all the chemical energy of hydrogen is converted into electrical work, thus using the reaction enthalpy variation  $\Delta H$  (depending on whether water is produced in liquid or vapor form, see Chapter III):

$$E^{TH} = -\frac{\Delta H}{nF} \quad (I-4)$$

Here,  $n$  and  $F$  are respectively the number of electrons involved in the oxidation of one mole of fuel ( $n = 2$  for  $H_2$ ) and the Faraday constant ( $F = 96485 \text{ C mol}^{-1}$ ). Nevertheless,  $E^{\text{TH}}$  never exists because the entropy of reaction is non-null and all the chemical energy is not available for electrical work. Thus, only the Gibbs energy can be converted into electrical work, the remaining part being heat. The reversible voltage  $E^0$  is defined by using the Gibbs energy variation  $\Delta G$ :

$$E^0 = -\frac{\Delta G^0}{nF} \quad (1-5)$$

While the reaction enthalpy only depends on the temperature, the Gibbs energy variation also depends on the pressure. For a generic reaction between reactants A and B, producing C and D species:



The Nernst equation expresses the variation of  $\Delta G$  with the species activities  $a_i$ :

$$\Delta G = \Delta G^0 - RT \ln \left( \frac{a_A^{\nu_A} a_B^{\nu_B}}{a_C^{\nu_C} a_D^{\nu_D}} \right) \quad (1-7)$$

By dividing the Gibbs energy variation by  $(-nF)$ , the reversible voltage is expressed:

$$E = E^0(T) + \frac{RT}{nF} \ln \left( \frac{a_A^{\nu_A} a_B^{\nu_B}}{a_C^{\nu_C} a_D^{\nu_D}} \right) \quad (1-8)$$

Considering ideal gases for reactants, the activity  $a_i$  is defined as the ratio between the partial pressure and the total pressure  $P_i/P^0$ . For concentrated species, the activity is assumed to be unity. In the case of a hydrogen/air fuel cell, the reversible voltage is:

$$E = E^0 + \frac{RT}{2F} \ln \left( \frac{\frac{P_{H_2}}{P^0} \times \left( \frac{P_{O_2}}{P^0} \right)^{0.5}}{\frac{P_{H_2O}}{P_{sat}}}} \right) \quad (1-9)$$

Where  $P_{\text{sat}}$  is the water saturation pressure. For a temperature of 353 K,  $E^0 = 1.176 \text{ V}$  and the final reversible voltage is  $E \approx 1.18 \text{ V}$ , depending on reactants concentrations and for water produced in vapor form.

The Open Circuit Voltage (OCV) is the cell voltage when no current is produced by the cell ( $i = 0$ ). An ideal system would deliver the reversible voltage  $E$  but real fuel cell suffers from several losses, lowering the OCV. This originates from gas crossover through the membrane, internal currents or parasitic reactions such as platinum or carbon oxidation and peroxide formation. In the end, a realistic OCV is around 0.95 - 1 V.

An ideal fuel cell would ensure a constant voltage for any current. However, as shown in Fig. I-4, voltage is a continuously decreasing function of cell current. Indeed, several losses occur and lead to voltage decrease and consequently to efficiency decrease. Three regions are highlighted in a polarization curve (Fig. I-4b). At low current densities, activation overpotential, due to kinetics, dominates. For intermediate current densities, ohmic resistance, mainly due to the membrane resistivity, is no longer negligible and leads to an almost linear variation of the voltage with current (as the logarithmic variation of the activation overvoltage is small). Note that for dry conditions the ohmic character of the volumetric electrode corresponding to the transport of the protons by the ionomer phase can be observed. Finally, for high current densities, reactant transport is less efficient and concentrations close to electrodes decrease, thus leading to important overpotential. The maximum current density, often denoted as  $i_{lim}$ , is the highest current density that can be delivered by the cell before the zero voltage.

Considering all overpotentials, the cell voltage  $U$  is expressed as follows:

$$U = E_{OCV} - \eta_{act} - \eta_{\Omega} - \eta_{conc} \quad (I-10)$$

## II – 4.2. Activation overpotential

The activation overpotential  $\eta_{act}$  rigorously contains the contribution of both electrodes although the anode term is often neglected due to its fast kinetic. Butler-Volmer relation links the cell current  $i_{cell}$  and the activation overpotential for one catalytic site:

$$i_{cell} = i_0 \left( \frac{C_s}{C^*} \right)^{\gamma} \left[ \exp\left( \frac{\alpha_a F \eta_{act}}{RT} \right) - \exp\left( - \frac{\alpha_c F \eta_{act}}{RT} \right) \right] \quad (I-11)$$

Here,  $i_0$ ,  $C_S$ ,  $C^*$  and  $\gamma$  respectively represent the exchange current density per membrane surface, the reactant concentration at the catalyst surface, the reference reactant concentration and the reaction order.  $\alpha_a$  and  $\alpha_c$  are the charge transfer coefficients relative to the oxidation and reduction respectively.

For high values of overpotential, one of the two terms dominates while the other one can be neglected, thus leading to an explicit relation between current and overpotential, known as the Tafel kinetics model:

$$\eta_{act} = b \ln\left(\frac{i}{i_0}\right) \quad (I-12)$$

Where  $b$  is the Tafel slope. Theoretically,  $b = \frac{RT}{\alpha F}$  but it is often experimentally estimated. Note that when this equation is applied to a volumetric electrode, parameters such as exchange current and charge transfer coefficients are no longer intrinsic to the oxygen reduction reaction but depend on the electrode structure, thickness, ionomer loading, among others, and include ohmic losses through the electrode.

### II – 4.3. Ohmic overpotential

The ohmic overpotential  $\eta_{\Omega}$  has two contributions: electrons and protons transport [38]. The first one is mainly due to contact resistances between all electron conductive layers of the cell and electrons conduction in the bulk of the materials. The second contribution originates from the protonic resistance of the ionomer which is a function of its hydration. From an experimental point of view, those two contributions are usually summed up and denoted as a high-frequency resistance  $R_{hf}$  when alternative current measurement are performed [39]. Consequently, the ohmic losses are modelled as a simple resistive loss:

$$\eta_{\Omega} = R_{hf} \times i \quad (I-13)$$

### II – 4.4. Concentration overpotential

Concentration overpotential  $\eta_{conc}$  is due to mass-transport limitations. At high current density, the reactants fluxes that are needed to achieve to electrochemical reactions

are large. However, the porous layers create diffusive resistances that limit the maximal gas flux capable to reach the active sites. In addition, at high current density, large amount of water is produced and condensation within porous layer further increases the diffusion resistances. Consequently, the reactant concentration within the CL decreases as the current increases, lowering the cell voltage. This phenomenon leads to the appearance of the limiting current density: reactants concentration in the CL is null and the cell voltage drops to zero.

The simplest way to model the transport losses is to assume that the exchange current density  $i_0$  is proportional to the oxygen concentration and that the oxygen concentration decreases linearly with the current density. Under these conditions, the concentration overvoltage is written as a function of the limiting current:

$$\eta_{conc} = b \ln \left( 1 - \frac{i}{i_{lim}} \right) \quad (I-14)$$

More complex models, containing more parameters, are able to describe mass transport limitations as a function of current and intrinsic transport properties of the different layers [40].

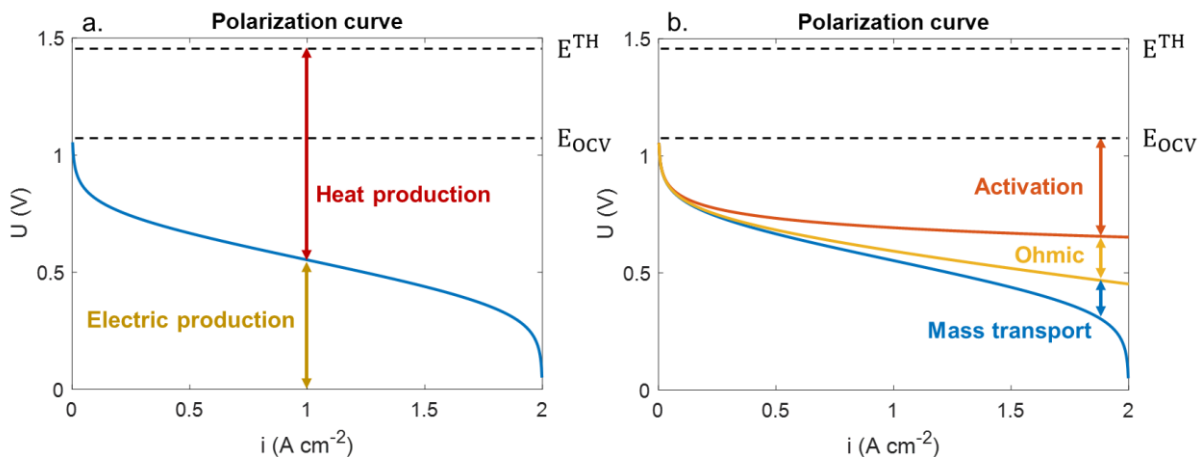


Figure I-4: Polarization curves representing a. heat and electricity production and b. different voltage losses

## II – 4.5. Heat sources

All the overpotentials decrease the electrical efficiency of the cell by lowering the working voltage. This efficiency loss results in heat production, as mentioned in Fig.

I-4a, originating from several sources [41]. Chapter III extensively describes the heat sources of a fuel cell and the link with the overvoltages.

## III – Challenges

### III – 1. Degradations

Lifetime of fuel cells is still to improve in order to allow widespread use of the technology in the domains where they are competitive, such as trucks [42]–[44]. This challenge is closely related to the cost: increasing platinum content of a stack will improve its lifetime but significantly increase its cost; increasing the membrane thickness will make it last longer but it increases the cost and decreases the efficiency of the system. The challenge is thus twofold: increasing lifetime while reducing costs. Aging mechanisms can be hindered by adjusting the material, their shaping, and also by adapting the system design/control to avoid degrading working conditions.

Degradations of PEMFC are of different nature. On the one hand, continuous aging results in smooth performance losses during the whole lifetime of the cell. On the other hand, abrupt aging can occur due to a snowballing mechanism and very quickly cause the failure of the cell. Fig. I-5 and I-6 give insights of how an instability can lead to degradation of one or several cells in a stack environment [45]. For example, a flooding instability (Fig. I-5) can lead to liquid water plugs in the channels. This reduces the gas flow rate in the channels because the pressure drop is imposed. Less gas in the channels means less reactants and potential fuel starvation, which implies electrodes degradation. In addition, a lower gas flow rate in the channels reduces the water removal, strengthening cell flooding by liquid water.

In the following, the main degradation mechanisms are outlined and support the importance of water and heat management.

The Issue

Flooding instability

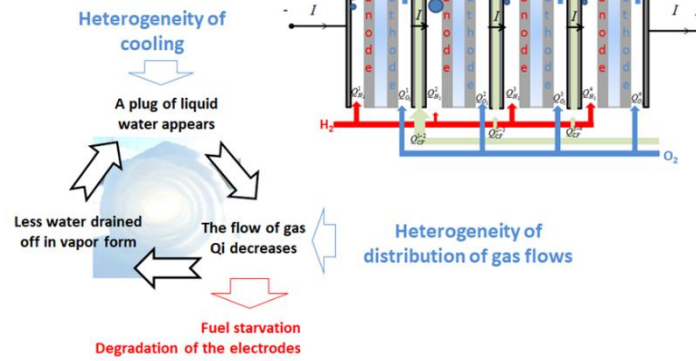


Figure I-5: Schematic of a snowball effect due to stack flooding

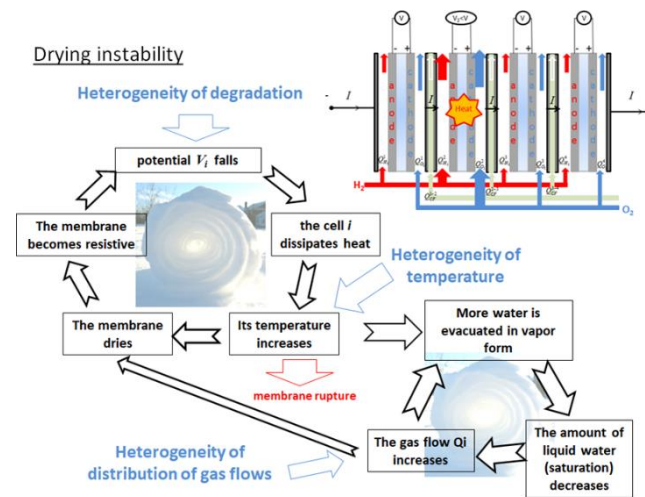


Figure I-6: Schematic of a snowball effect due to stack drying

### III – 1.1. Membrane

PFSA is mainly employed as electrolyte in PEMFC and is subject to degradations [36]. It is established that PFSA ageing is mainly due to chemical factors [46] even though some cofactors such as mechanical stress [47] can strengthen the degradation rate. Hydrogen peroxide  $H_2O_2$  can be formed at the cathode electrode of the cell. Together with iron ions coming from the cell materials, OH radicals can be formed and damage the PFSA chains. Two main mechanisms are involved: main chain unzipping and side-chain scission. The membrane degradations result in morphology and transport properties changes. Progressively, this can lead to pinholes and to an increase of gas crossover.

PFSA is a polymer able to adsorb and desorb solvent. The water adsorption causes swelling and the drying causes shrinkage, both leading to structural modifications. However, the membrane is highly constrained between GDLs and channels. Thus, the membrane is subject to stress that can damage its structure. Dry operations or humidity cycling are favorable to mechanical stress [48] and pinholes are more likely to appear. If the membrane is too permeable to gases, hydrogen and oxygen can achieve a direct reaction which is highly exothermic. In addition to reduce cell efficiency, the produced heat strengthens the damaging mechanisms linked to drying and pinhole appearance. The membrane is even more permeable and gas crossover increases: a destructive cycle leads to fast degradation [49]. Thus, to avoid any critical hydration regime, water management of the cell is crucial.

Conventional PFSA suffer from critical breakdown at high temperature because of their glass transition temperature starting at 80 °C. It has also be shown that after thermal cycling between 80 and -40 °C, membrane properties were highly affected [50]. In order to achieve large commercialization, heat management of the cell is thus of high importance.

### III – 1.2. Carbon support in the CL

Carbon is present in the catalyst layer in order to conduct electrons towards or from the electrochemical reaction sites. It has also the role of supporting the catalyst particle and to allow the gas diffusion through its pore to provide pathways for the reactant gases. The carbon corrosion leads to three consequences for the cell: the loss of electrochemical surface area due to metal nanoparticles detachment or agglomeration, the decrease of hydrophobicity affecting water management and losses in porosity increasing mass transport limitations [44]. By measuring carbon dioxide in exhaust gas of a working fuel cell, Macauley et al. [51] quantified the carbon corrosion during potential cycles. Carbon corrosion is observed during normal cycle potentials but start/stop induced corrosion is more prominent. CL thickness decreases during operation: carbon support compaction and thus porosity loss leads to increased mass transport limitations. Castanheira et al. [52] studied the degradation of Pt/C electrocatalysts as a function of the carbon support structure and of the aging protocol. Dissolution/redeposition and migration/aggregation/coalescence of Pt is observed but

the nature of the carbon support does not play a role for potentials between 0.6 and 1 V. For higher potentials, and thus for start/stop, corrosion differences are observed depending on the carbon support nature. Maranzana et al. [53] provided a numerical model for start/stop with experimental validation which is able to predict carbon corrosion.

The degradation of the carbon support is influenced by the amount of water in the cell. The management of water is therefore essential to slow down the aging of cells [48], [50].

### III – 1.3. Catalyst

Pt/C nanoparticles are degraded by four main mechanisms: (i) the carbon corrosion leads to particle detachment, (ii) particle migration and coalescence [54], (iii) Pt dissolution and redeposition (Ostwald ripening) and (iv) Pt redeposition in the PEM or ionomer [44]. Guilminot et al. [55] asserted that the alteration of the Pt/C materials is affected by environmental conditions such as humidity or temperature.

### III – 1.4. GDL

GDL degradations originates from dissolution in water, erosion by gas flow and corrosion, in a similar way to CL carbon support [42]. Ha et al. [56] experimentally showed the impact of dissolution in water and its consequences on the GDL properties such as hydrophobicity and structure, impacting the fuel cell performances. By coupling Pore Network Modeling and Performance Modeling, Pauchet et al. [57] investigated the link between the GDL degradations and the fuel cell performances. It is shown that as the hydrophilic pores fraction increases, the gas diffusion becomes less efficient. In addition, current heterogeneities exacerbate due to heterogenous liquid water distribution.

### III – 1.5. Ionomer in the electrode

During accelerate stress tests (AST), Yin et al. [58] highlighted that the CL microstructural change is due to ionomer migration, especially under high humidity conditions. Ionomer migrates and agglomerates, leading to crack generation within the

CL. From an experimental point of view, double layer capacitance and ionic resistance are correlated to the CL structure and so are indicators of its state. Gaumont et al. [59] developed a model that is applied to monitor the CL properties during AST.

## III – 2. Water and heat management

Water management of a PEMFC is of high importance. On the one hand, the membrane needs enough water to maintain its proton conductivity and thus to reduce as much as possible ohmic losses responsible of the linear region of the polarization curve. In order to ensure a sufficient water availability for the membrane, inlet gases are usually humidified. However, at the system scale, humidifiers are costly devices and the trend is to find strategies to get rid of them, as for the Toyota Mirai [60]. On the other hand, water can accumulate in the porous media (respectively in the channels) and hinder gas transport toward the catalyst layer (respectively disrupting the homogeneous distribution of gas flows between the different cells). This leads to an increase of mass transport losses and thus to a drastic performance loss at high current densities, lowering the maximum achievable current. Moreover, as exposed in the section III – 1. Degradations, the accumulation of water within the cell can lead to fuel starvation which contributes to carbon corrosion and to cell aging. On the opposite, if the membrane is too dry, mechanical stress is likely to result in irrevocable degradations such as pinholes.

### III – 2.1. Strategies for water management

In order to prevent cell flooding or drying, several strategies are usually implemented. The stoichiometry, which is the gas flow rate sent to the cell often expressed in proportion to gas consumption, has an important role in the water removal, especially for water in the channels. An increase in the gas flow rate leads to pressure loss increase, thus to a better droplet pullout and consequently to less concentration overpotential [61], [62], and therefore to a more homogeneous distribution of gas flows between cells [45]. Most studied flow field geometries are serpentine (simple or multiple), parallel or interdigitated channels, and mesh [63]. The geometry shows almost no influence on performances for low current density while it is crucial for the highest where mass transport limitation is a determining factor. High pressure drops

configurations exhibit better ability to remove liquid from the cell as well as a more homogeneous distribution of reactants in the cell. Serpentine and interdigitated channels increase water removal by allowing gas to pass under the lands and thus through the porous GDL, dragging liquid water with it. Parallel channels are more likely to suffer from preferential flow paths, favoring maldistribution of reactants. To increase the pressure drop, it is possible to reduce the hydraulic diameter of the channels, but a compromise must be found to avoid excessive consumption of the air compressor. There is an optimal pressure drop, which allows the good evacuation of the liquid water while controlling the consumption of the compressor.

For dry air operating conditions, Gaumont [64] proved that a counter-flow configuration exhibits higher and more homogeneous performances than co-flow. This is due to a better water circulation within the cell because water at the cathode outlet diffuses through the membrane to anode inlet, is transported with the hydrogen flow and then through the membrane from anode outlet to the dry cathode inlet. For air humidifier free systems, Toyota adopted this configuration to properly manage water in the cells [60]. The constraint is that a high recirculation rate of  $H_2$  must be implemented, which implies an expensive hydrogen recirculation pump.

Temperature has a high influence on water management. He et al. [62] studied water flooding of porous media in a cell using interdigitated flow fields by monitoring pressure losses. After reaching a steady-state, an increase in the plates temperature by  $10\text{ }^\circ\text{C}$  is achieved, resulting in a decrease of pressure losses, and thus indicating a discharge of the liquid water contained in the GDL. By applying temperature differences between the cell plates, Thomas et al. [65] highlighted that water is preferentially transported toward colder areas.

MPL is commonly added in the cell assembly. Even though its combined effects on the fuel cell are not fully understood, it is recognized that it improves cell performances and it is added to state-of-the-art GDLs. Thomas et al. [66] showed that the MPL has almost no impact on the water fluxes distribution of the cell. Owejan et al. [67] asserted that the MPL acts as a barrier, preventing the liquid water contained in the GDL to reach and flood the CL. They proposed that MPL provide in-plane diffusion paths for oxygen to overpass liquid blockage. For relatively low temperature ( $40^\circ\text{C}$ ) fuel cell,

Nagai et al. [68] visualized that an MPL with some special large pores is able to provide pathways for liquid water and thus to reduce CL flooding, small pores being taken by oxygen to reach active sites. By achieving X-Ray tomographic microscopy, Lamibrac et al. [69] investigated the role of the MPL in liquid water transport. They concluded that liquid water invades preferentially the cracks of the MPL, which requires high capillary pressure. Once these pores are filled, the macropores of the MPS are rapidly invaded and breakthrough is achieved.

### III – 2.2. Strategies for heat management

Stack cooling is of great importance to ensure reasonable working temperature in order to prevent any damage on the membrane. Different methods for stack cooling have been developed [70]:

- Edge cooling, which is an external cooling of the stack (for low power stacks)
- High air stoichiometry for open cathode cells
- Cooling with separated air flow by special channels carved into, or between, the bipolar plates (for stacks in the range of 100 W to 2 kW)
- Liquid cooling, which is the most employed for automotive application
- Phase change cooling

Since early heat transport models [71], the thermal resistance between the MEA and the plates is marked as one of the most critical parameters. For a given released heat power, it dictates the membrane temperature as well as the temperature gradient. By comparing two GDLs with different thermal conductivities with a simple heat transport model, Chuang et al. [72] highlighted that for a lower thermal conductivity, MEA temperature is higher and thermal gradient through the GDL is also higher. This influences the water transport by imposing a water saturation pressure field within the GDL that governs water vapor transport by diffusion.

### III – 2.3. Water and heat transport modeling

The modelling of transport phenomena in fuel cells has begun with the works of Springer [73] and Bernardi and Verbrugge [74]. These two models consider an assembly of a membrane, diffusion layers and catalyst layers. The temperature is

considered uniform and transport phenomena in one dimension in the through plane direction. The Bernardi and Verbrugge' model considers a fully hydrated membrane and uses the Stefan-Maxwell equations in the diffusion layers and the electrodes. Water flux due to pressure differences are considered and a cathodic pressure higher than the anodic one is assumed, balancing the electro-osmotic flux. Moreover, this model uses the transport of a charged liquid phase (water + protons) in an inert media. Thus, water is also transferred by a potential gradient.

The Springer model also uses the Stefan-Maxwell equations in the electrodes and takes into account the variation of water content of the membrane and hence of its properties as the protonic conductivity or diffusion coefficient of water [40]. The water flux in the membrane is modelled by a superposition of diffusion and electroosmotic drag, following the dilute solutions theory.

Then, Fuller at al. [75] use the concentrated solutions theory to model the water flux in the membrane. They also integrate thermal effects and add a second dimension in the direction of the channels.

Since the beginning of modelling, other models have been developed. For example, the Eikerling's model [76] considers the membrane as a porous media with a given water permeability. Hence, this media is crossed by a Darcy's flow in addition of the electro-osmotic drag. The membrane permeability depends on the pores size, the later depending on the water content: the more the membrane is hydrated, the more the pores are open and the higher the permeability is. The Schroeder paradox is explained by the pressure drop associated with the surface tension at the interface with the outside.

In the Colinart thesis [77], a membrane model composed of cylindrical surface charged pores is developed. The transfer of water and protons is studied and those fluxes influence each other. Water is thus moved by a pressure gradient and the electrical potential gradient.

One of the first models that describe the interaction between heat transport and two-phase water flow was published by Wang and Wang [78]. This model is three-dimensional and implemented in the CFD software Fluent. The main conclusions are

that water vapor diffusion flux is able to extract a flux comparable to water production. Up to 18% of produced heat is transferred by evaporation/condensation of water. Water vapor condenses under the lands and this plays a role in the GDL flooding. By running their 1D coupled model for heat and water transfer, Weber and Newman [79] properly described the heat-pipe effect. Due to the presence of a temperature field, and thus of a saturation pressure fields, water evaporates and condenses within the GDL, transporting water and heat.

Noting that a wide variety of models exist in the literature, Vetter and Schumacher [80] published an open implementation model to establish some modeling standards and to avoid starting from scratch. This model is one dimensional, non-isothermal and steady-state, and is easily editable for any purpose. Even though this model is easy to handle and fast computing, limitations exist, due to some neglected mechanisms.

Dynamic models are of high importance to study phenomenon such as startups, shutdowns and variation in the current demand, for automotive applications for instance. Goshtasbi et al. [81], [82] published transient models, aiming to reduce as much as possible the computation time in order to implement it for real-time control of fuel cells.

### III – 2.4. Parameters, sensitivity and estimation

In order to represent real systems, the fuel cell models must be experimentally validated. This validation requires the measurement of observable quantities that can be compared to model output data. A simple and widespread method to achieve that is to compare modelled and measured polarization curves [83], since it is an essential measurement representing fuel cell behavior. Alternatively, Weber and Hickner [84] aimed to validate a model for water-content profiles based on high-resolution imaging. Many parameters, especially in materials properties, were unknown, leading to quantitative discrepancies, even though trends were captured.

All fuel cell models are fed by parameters. Reduced models contain few parameters and most of them are not intrinsic: they contain several contributions like geometrical aspects for example. In this case, they are called effective. The advantage of these models is the speed of resolution which is essential for real-time control for instance.

The more complex models can contain dozens, even a hundred, of parameters, some of which may be intrinsic. They do not depend on the geometry or the materials used. However, these models are often expensive in terms of computing time.

The sensitivity of an output of the model with respect to a given parameter represents the influence that the variation of the parameter has on the variation of the model output. This tool allows to determine which parameter has the most influence on a given output, guiding experimenters on the parameters to be estimated with the most precision. Several comprehensive sensitivity analyses are available in the literature [85]–[87], highlighting the most important parameters of a model. In addition, if two parameters have a large sensitivity magnitude and similar effects on a given output, they cannot be separately identified and the corresponding system is ill-conditioned. In this case, parameters are said to be correlated. For instance, Goshtasbi et al. [86] notified a high collinearity between ionomer conductivity and electrical resistance on the high-frequency resistance of a fuel cell.

When some parameters of a model are unknown, estimations have to be conducted. Parameter estimation is a way to identify numerical values for a parameter involved in a model. The first way to achieve that is to perform in-situ experiments with a set of observable data, such as voltage or high-frequency resistance for instance. Then, by optimization methods, data fitting can provide estimations for the parameters of interest by reducing the difference between the observable data and the model output. The second way to achieve parameter estimation is to perform some ex-situ experiments. This has been done for diffusion coefficients of gases [88], water diffusion in the membrane [89], electroosmosis [90], capillary pressure [91] or thermal conductivity [92] in GDLs for example. This method is relevant only if the ex-situ estimated parameters can be properly integrated in a complete model and if the properties of the interfaces (interfacial electronic and thermal resistances) are known, which is barely the case.

### III – 3. Thesis objectives

Material and geometry testing in fuel cell is highly time-consuming and expensive. In addition, while laboratory-scale cells can benefit from special design for in-situ measurements such as pressure or temperature [65], industrial-scale fuel cell stacks

are difficult to instrument [93]. In order to overcome these difficulties, physical theory, modeling and simulation provide powerful tools to understand, analyze, predict and control the operation of fuel cell systems [94]. Among all phenomena, water and heat transfers are of high importance in fuel cells as they are involved in early failures, aging issues or efficiency loss. Thus, modeling of water and heat transfer mechanisms can participate in materials and design improvement, as well as in a better control of operating conditions in real time.

The main goal of this work is to provide a reduced-order model for coupled water and heat transfers in a fuel cell. This model must be simple enough to estimate its associated parameters, but complex enough to describe the physics of the transfers. All the involved parameters will be estimated, mainly using non-electrical observable data in order to remove coupling between the transfers and electrochemistry which would introduce many unknown parameters. Observable data are thus essentially quantities of water and temperatures. An original design of experiments is developed, allowing to accurately estimate the model parameters by in-situ experiments only. To match this objective, a new experimental set up was designed and realized from scratch. This model and the associated experiments can be used to characterize materials such as GDL or MEA but also to provide real-time information about the cell such as MEA temperature, amount of stored water

In the first instance, the estimation of crucial parameters for water transfer is achieved. The experimental set-up is extensively described as well as the design of experiments. A specific 1+1D model is developed for water transfer. Water balances are carried out on a zero-current fuel cell under highly controlled experimental conditions. The parameters estimation process is also described.

In the second instance, an innovative method is established to estimate the thermal resistance between the MEA and the bipolar plates. This method requires the application of temperature differences between the two plates of the fuel cell. Coupling between water transfer and temperature distribution is used to justify hypotheses about vapor flux.

Finally, a one-dimensional transient model is exposed, considering heat and water coupling. This model is compared to dynamic experiments, notably during triangle

shaped load cycles. Further works will improve this model by new parameters estimations such as MEA thermal capacitance or liquid water storage capacity of the cell.

# **Chapter II: In-situ estimation of water transport parameters**

<b>Introduction .....</b>	<b>52</b>
<b>I – Overview of water transport modelling.....</b>	<b>53</b>
I – 1. In the membrane.....	53
I – 2. In GDLs.....	57
I – 3. In the CLs.....	64
I – 4. In channels.....	65
<b>II – 1+1D model .....</b>	<b>66</b>
II – 1. Through-plane direction.....	67
II – 2. Along the channel .....	69
<b>III – Design of experiment .....</b>	<b>70</b>
III – 1. Experimental set-up.....	70
III – 2. Set-up design optimization: definition of the optimal exchange surface.....	78
III – 3. XP1: constant average concentration.....	81
III – 4. XP2: pressure variation .....	83
III – 5. XP3: condensation.....	86
<b>IV – Parameters estimation .....</b>	<b>86</b>
IV – 1. Method for parameters estimation validation .....	88
IV – 2. Estimations by XP1 .....	91
IV – 3. Estimation by XP2 .....	96
IV – 4. Comparison between XP1 and XP2.....	100
IV – 5. Liquid sorption influence.....	104
<b>V – Conclusions and outlooks.....</b>	<b>107</b>
<b>Appendix.....</b>	<b>110</b>

## Introduction

A fuel cell converts the chemical energy of the fuel, in this case hydrogen, into electrical energy. This conversion is accompanied by the production of water at the cathode which is proportional to the delivered current. Thus, stacks producing high electrical power generate large quantities of water in the cells.

The management of this water is essential for the systems since it can impact both the performances and the durability of the cell. Too much liquid water leads to feeding gas blockage into the porous layers of the assembly. On the opposite, a dry membrane increases losses, reduces efficiency and exacerbate the membrane ageing. In the case of embedded systems for mobility, the starting and stopping of stacks under freezing temperatures are very sensitive to the presence of liquid water. For all these reasons, the modelling of water transport in cells is essential for the control and the design of the systems and for the choice of the most suitable materials.

This chapter first presents a state of the art on the modeling of water transport in fuel cells, focusing on the mechanisms that will be considered in the rest of this manuscript. Then, a 1+1D lumped model of water transport in a cell is developed. It considers diffusion in the GDLs and in the membrane, with variations of boundary conditions along the channels. Finally, an original design of experiment is developed to allow the estimation of crucial water transport parameters. Two different methods are implemented and compared. Results for several materials are detailed and compared. The influence of liquid water sorption is investigated and discussed.

## I – Overview of water transport modelling

### I – 1. In the membrane

Weber and Newman [40] extensively described the fuel cell modeling history up to 2003. The modeling of the membrane is one of the main issue due to its crucial role in the fuel cell. While microscopic models aim to describe the structural interaction between water, membrane and protons, macroscopic models strive to represent species transport from a wider point of view. Macroscopic membrane models can be classified in two main categories: hydraulic and diffusive. Hydraulic models, originating from Bernardi and Verbrugge [74], consider the membrane system as two phases whereas diffusive models, of which one of the first is Springer's [73], treat the membrane as a single phase. Diffusive models are widely spread in the literature and show good agreement with experimental data. In that respect, this work focuses on this kind of models.

The dilute solution theory states that the relative molar flux density  $N$  of species  $i$  is proportional to the gradient of the electrochemical potential  $\bar{\mu}_i$  [95]:

$$N_i = -\frac{C_i D_i}{RT} \nabla \bar{\mu}_i \quad (\text{II-1})$$

Here,  $C_i$ ,  $D_i$ ,  $R$  and  $T$  are respectively the concentration and diffusion coefficient of species  $i$ , the ideal gas constant and the absolute temperature. By adding the solvent velocity  $v$  and expressing the electrochemical potential as  $\bar{\mu}_i = \mu^0 + z_i F \Phi + RT \ln a_i$ , this leads to the Nernst-Planck equation:

$$N_i = -D_i \nabla C_i - z_i u_i F C_i \nabla \Phi + C_i v \quad (\text{II-2})$$

With  $\mu^0$ ,  $z_i$ ,  $F$ ,  $\Phi$ ,  $u_i$  and  $a_i$  being the standard chemical potential, the species valence, the Faraday constant, the electrical potential, the mobility and the activity of species  $i$ .

While dilute solution theory considers only the interaction of each species with the solvent (in this case, the membrane), the concentrated solution theory takes into account all binary interactions between species. Even though the latter is more

rigorous, the former is enough accurate and seems to represent well enough the membrane system behavior.

### I – 1.1. Fick's diffusion

Water has a zero valence and by applying the dilute solution theory the adsorbed water ( $w$ ) in the membrane ( $M$ ), one can write:

$$N_w^{Diff} = -D_{w,M} \nabla C_w \quad (II-3)$$

The solvent velocity  $v$  being null. Thus, Eq. II-3 reduces to Fick's law of diffusion which has been historically developed for gas diffusion and developed in the part *In GDLs*.

The water concentration  $C_w$  within the membrane is defined as the number of water moles  $y_{H_2O}$  in a given volume of ionomer  $V_{io}$ . By assuming that the ionomer dimensions stay unchanged with water sorption:

$$C_w = \frac{y_{H_2O}}{V_{io}} = \frac{\lambda \rho_{dry}}{EW} \quad (II-4)$$

$\rho_{dry}$  is the density of the dry ionomer. The water content of the membrane  $\lambda$  is defined as the number of water molecule ( $n_{H_2O}$ ) per sulfonic site ( $n_{SO_3}$ ):

$$\lambda = \frac{n_{H_2O}}{n_{SO_3}} = \frac{\Delta m_{H_2O} \times EW}{m_{io} \times M_{H_2O}} \quad (II-5)$$

Here,  $\Delta m_{H_2O}$ ,  $m_{io}$ ,  $M_{H_2O}$  and  $EW$  are respectively the mass of adsorbed water, the mass of ionomer, the molar mass of water and the equivalent weight of the ionomer which is defined as the weight per sulfonic group.

The water sorption of polymer membranes has been extensively studied [36], [96]–[101]. In pioneering works, Zawodzinski et al. [96] used NMR to monitor water uptake of Nafion 117. Hinatsu et al. [101] compared water sorption for different types of membranes. A water sorption curve represents the water content of the ionomer as a function of the activity of the surrounding vapor. Two regimes are described along the vapor activity increase: (i) at low vapor activity, bound water links to sulfonic sites, is responsible of a rapid increase of water content up to 3-4 and contributes to a linear

increase all along the curve, (ii) for intermediate to high vapor activity, free water layers around sulfonic sites and increases the water content up to 14-16.

Eq. II-3, representing water diffusion through the membrane, is thus expressed using the water content:

$$N_w^{Diff} = -D_{w,M} \frac{\rho_{dry}}{EW} \nabla \lambda \quad (II-6)$$

The membrane being a complex material, with structural properties that vary with water sorption, the transport properties such as the diffusion coefficient  $D_{w,M}$  also depend on  $\lambda$ .

Springer et al. [73] determined the diffusion coefficient of water in Nafion 117 to be between  $1 \times 10^{-10} \text{ m}^2 \text{ s}^{-1}$  and  $3 \times 10^{-10} \text{ m}^2 \text{ s}^{-1}$ . This range is attributed to a so-called corrected diffusion coefficient, differing from the intradiffusion coefficient ranging from  $1 \times 10^{-10} \text{ m}^2 \text{ s}^{-1}$  up to  $6 \times 10^{-10} \text{ m}^2 \text{ s}^{-1}$ . This correction leads to the appearance of a peak around  $\lambda = 3$ . Zawodzinski et al. [96] used NMR to study sorption and diffusion of water in Nafion 117. They estimated the intradiffusion coefficient to be between  $1 \times 10^{-10} \text{ m}^2 \text{ s}^{-1}$  and  $8 \times 10^{-10} \text{ m}^2 \text{ s}^{-1}$ . This coefficient does not exhibit a peak. Performing *in-situ* water balance, Chadha et al. [102] studied water transfer within NRE 211. The final estimations of the diffusion coefficient of water in the membrane framed between  $1 \times 10^{-11} \text{ m}^2 \text{ s}^{-1}$  and  $4 \times 10^{-11} \text{ m}^2 \text{ s}^{-1}$ . Recently, Trinh et al. [103] estimated the diffusion coefficient in Nafion 117 and Nafion 211 using a special set-up that allows to measure water flux through the membrane as well as the sorption curve. For 70 °C experiments, the diffusion coefficient lays between  $2 \times 10^{-10} \text{ m}^2 \text{ s}^{-1}$  and  $5 \times 10^{-10} \text{ m}^2 \text{ s}^{-1}$  for N117 and between  $4 \times 10^{-11} \text{ m}^2 \text{ s}^{-1}$  and  $1 \times 10^{-10} \text{ m}^2 \text{ s}^{-1}$  for N211. One can note that those values are rather constant for water activity higher than 0.5. Finally, Caulk et al. [104] developed a method to measure water transport properties of a membrane. By properly discerning the membrane transport resistance, they estimated the diffusion coefficient in Nafion to range from  $1 \times 10^{-10} \text{ m}^2 \text{ s}^{-1}$  to  $9 \times 10^{-10} \text{ m}^2 \text{ s}^{-1}$  at 80 °C.

## I – 1.2. Electroosmotic drag

Even though water molecule has zero valence, it has been widely reported that some water movement is induced by protons transport across the membrane. This phenomenon is named electroosmosis drag (EOD). This mechanism being out of the Dilute Solution Theory frame [40], an EOD term is added to the water flux, employing the electroosmosis coefficient  $\xi$ :

$$N_w = -D_{w,M} \frac{\rho_{dry}}{EW} \nabla \lambda + \frac{\xi i}{F} \quad (\text{II-7})$$

Here,  $i$  represents the current density.

Some authors determined that this coefficient depends on temperature and water content. For example, Peng et al. [105] observed a decrease of the EOD coefficient with an increase in water content. Springer et al. [73] considered a linear increase of the EOD coefficient with membrane water content. Sellin et al. [90] concluded that it does not vary neither with the current density nor with the relative humidity and that it is only a function of temperature. According to Zawodzinski et al. [96], the EOD coefficient depends on the membrane nature and their thermal treatments. Kusoglu et al. [36] compiled results of numerous works and  $\xi$  seems to be around 1 for vapor equilibrated membrane and between 2.5 and 3 for liquid equilibrated membrane.

## I – 1.3. Sorption resistance

In their water transport model, Berg et al. [106] assumed that the actual water concentrations  $C_w$  at the membrane interfaces are different from the equilibrium values  $C_w^*$ , given by the sorption curve. The water flux is then linked to the concentration difference by a mass transfer coefficient  $\gamma$ :

$$\begin{aligned} N_w^a &= -\gamma(C_w^a - C_w^{a*}) \\ N_w^c &= \gamma(C_w^c - C_w^{c*}) \end{aligned} \quad (\text{II-8})$$

In a similar way, Goshtasbi et al. [81] modelled water transfer at the membrane interface without equilibrium between the membrane and to surrounding gas. The water flux at the interfaces is thus expressed considering the equilibrium water content,

the actual water content in the ionomer at the interface and a mass transfer coefficient  $k_i$ :

$$N_{a,c} = \pm \frac{\rho_{dry}}{EW} k_{a,c} (\lambda_{e,a,c} - \lambda_{a,c}) \quad (\text{II-9})$$

The water transfer coefficient  $\gamma$  is estimated to be  $\gamma = 5.7 \times 10^{-6} \text{ m s}^{-1}$ .

In his water modelling, Wu [107] considered the sorption resistance with the water content in a source term  $S_d = \gamma \frac{\rho_{dry}}{EW} (\lambda_e - \lambda)$  where  $\lambda_e$  is the water content at equilibrium and  $\gamma$  a mass transfer coefficient being in the range of  $0.1 - 100 \text{ s}^{-1}$ . This approach is also taken by Vetter and Schumacher [80] who considered source terms at the interfaces:

$$S_{a,d} = \pm \frac{k_{a,d}}{LV_m} (\lambda_e - \lambda) \quad (\text{II-10})$$

## I – 2. In GDLs

### I – 2.1. Water vapor transport laws

Historically, first Fick's law of diffusion is used to describe the motion of gas molecules within a binary mixture of components A and B. By analogy with heat conduction, A. Fick asserted that the diffusive mass flux of species A  $j_A$  ( $\text{kg}_A \text{ m}^{-2} \text{ s}^{-1}$ ) is proportional to its mass fraction  $\omega_A$  gradient in a given direction:

$$j_A = -\rho D_{AB} \nabla \omega_A \quad (\text{II-11})$$

The proportionality factor is the binary diffusion coefficient of pair A-B  $D_{AB}$  and  $\rho$  is the density of the mixture.  $j_A$  is defined with mass units. By dividing it by the molar mass of A  $M_A$ , one can link the molar flux density  $J_A^*$  ( $\text{mol}_A \text{ m}^{-2} \text{ s}^{-1}$ ) to the molar fraction gradient of A  $x_A$ :

$$J_A^* = -C_{tot} D_{AB} \nabla x_A \quad (\text{II-12})$$

With  $C_{tot}$  ( $\text{mol m}^{-3}$ ) being the total gas concentration. These fluxes are defined relatively to the mass (or molar) average velocity of the mixture. Thus, to obtain the absolute flux, the convective molar flux  $c_A v^*$  is added:

$$N_A = J_A^* + c_A v^* \quad (\text{II-13})$$

Here,  $c_A$  ( $\text{mol}_A \text{ m}^{-3}$ ) and  $v^*$  ( $\text{m s}^{-1}$ ) represent the partial concentration of A and the molar average velocity of the mixture. The latter is defined as the sum of all molar fluxes  $N_i$  divided by the total concentration:

$$v^* = \frac{\sum_i^N N_i}{C_{tot}} \quad (\text{II-14})$$

Finally, in the case of a binary mixture, the first Fick's law for the absolute molar flux of species A is expressed as:

$$N_A = -C_{tot} D_{AB} \nabla x_A + x_A (N_A + N_B) \quad (\text{II-15})$$

Molecular diffusion in multicomponent mixtures at low density is described by the Maxwell-Stefan equations:

$$\nabla x_i = - \sum_{\substack{j=1 \\ j \neq i}}^N \frac{x_j N_i - x_i N_j}{C_{tot} D_{ij}} \quad (\text{II-16})$$

Here,  $x_i$ ,  $N_i$  and  $D_{ij}$  represent respectively the molar fraction and the molar flux density of component i and the binary diffusion coefficient between components i and j.  $C_{tot}$  is the total gas phase concentration and is linked to the pressure and temperature by:

$$C_{tot} = \frac{P}{RT} \quad (\text{II-17})$$

In multicomponent mixtures, the molar flux is not necessarily directed towards the opposite of the molar fraction gradient as it is predicted by the first Fick's law. Three notable phenomena can occur: reverse diffusion, osmotic diffusion and diffusion barrier. The first one describes a flux against its own concentration gradient. The second one occurs even though the concentration gradient is null. The latter denotes no flux in the presence of a concentration gradient [108]. Those phenomena are well described by the Maxwell-Stefan equations. The drawback is the equations solving. For a N-species mixture, N-1 differential equations have to be solved and  $\frac{1}{2}N(N-1)$  binary diffusion coefficients are needed.

For binary mixture, it is shown that the first Fick's law and the Maxwell-Stefan equations are similar. Considering a mixture composed of species A and B:

$$\nabla x_A = -\frac{x_B N_A - x_A N_B}{C_{tot} D_{AB}} \quad (II-18)$$

The sum of the molar fractions is equal to 1 since the mixture only contains A and B:  $x_A + x_B = 1$ . This leads to the first Fick's law:

$$N_A = x_A(N_A + N_B) - C_{tot} D_{AB} \nabla x_A \quad (II-19)$$

For ternary mixture, it is possible to approximate the Maxwell-Stefan equations with Fick's law, following some assumptions. In a typical PEM fuel cell cathode, a 3-component mixture lays in the GDL: dioxygen ( $O_2$ ), dinitrogen ( $N_2$ ) and water vapor ( $w$ ). The molar fraction gradient of water vapor is described by the Maxwell-Stefan equation:

$$\nabla x_w = -\frac{x_{O_2} N_w - x_w N_{O_2}}{C_{tot} D_{w,O_2}} - \frac{x_{N_2} N_w - x_w N_{N_2}}{C_{tot} D_{w,N_2}} \quad (II-20)$$

Schwartz and Brow [109] demonstrated that, at 79 °C, the diffusion coefficient of water vapor in dioxygen  $D_{w,O_2}$  and in dinitrogen  $D_{w,N_2}$  were respectively  $0.352 \text{ cm}^2 \text{ s}^{-1}$  and  $0.359 \text{ cm}^2 \text{ s}^{-1}$ . At 55.6 °C they found values of  $0.318 \text{ cm}^2 \text{ s}^{-1}$  and  $0.303 \text{ cm}^2 \text{ s}^{-1}$ . Thus, it can be considered that the two diffusion coefficients are similar and assume a diffusion coefficient for water vapor in air:  $D_{w,air} = D_{w,O_2} \approx D_{w,N_2}$ . The Maxwell-Stefan equation is thus written as follows:

$$\nabla x_w = -\left( \frac{x_{O_2} N_w - x_w N_{O_2} + x_{N_2} N_w - x_w N_{N_2}}{C_{tot} D_{w,air}} \right) \quad (II-21)$$

The total molar fraction is equal to 1:  $x_{O_2} + x_{N_2} + x_w = 1$ . This leads to:

$$\nabla x_w = \frac{x_w(N_{O_2} + N_{N_2} + N_w) - N_w}{C_{tot} D_{w,air}} \quad (II-22)$$

The latter can be expressed as an approximated first Fick's law for a 3-component mixture:

$$N_w = x_w(N_{O_2} + N_{N_2} + N_w) - C_{tot}D_{w,air}\nabla x_w \quad (II-23)$$

One can assume that air constitutes a unique phase and write  $N_{air} = N_{O_2} + N_{N_2}$ .

## I – 2.2 Bulk diffusion coefficients

The Maxwell-Stefan equations contain binary diffusion coefficients  $D_{ij}$  which can lead to the appearance of  $D_{AB}$  and  $D_{BA}$  if the indexing is rigorously applied. Assuming a binary mixture of A and B, the relative mass flux densities are expressed as:

$$\begin{cases} j_A = -\rho D_{AB} \nabla \omega_A \\ j_B = -\rho D_{BA} \nabla \omega_B \end{cases} \quad (II-24)$$

The total mass fraction being equal to unity, the sum of the mass flux densities is:

$$j = j_A + j_B = \rho \nabla \omega_A (D_{BA} - D_{AB}) \quad (II-25)$$

The total relative mass flux density  $j$  is defined to be null. Thus, one can conclude that  $D_{AB} = D_{BA}$ .

Semi-empirical relations are exposed in the literature to determine the binary diffusion coefficient of two gas species. The first one [110] uses molar masses  $M_i$ , temperatures  $T_{ci}$  and pressures  $p_{ci}$  at the critical point of each species:

$$\frac{pD_{AB}}{(p_{cA}p_{cB})^{1/3}(T_{cA}T_{cB})^{5/12}(1/M_A + 1/M_B)^{1/2}} = a \left( \frac{T}{\sqrt{T_{cA}T_{cB}}} \right)^b \quad (II-26)$$

Here  $D_{AB}$  is given in  $\text{cm}^2 \text{s}^{-1}$ ,  $p$  is in atm and  $T$  in K.  $a$  and  $b$  are dimensionless constants that depend on the gas's nature (Appendix, Table II-4).

The second expression [111] contains molar masses and molar diffusion volume  $V_i$ :

$$D_{AB} = \frac{CT^{1.75}}{P} \frac{\sqrt{\frac{M_A + M_B}{M_A M_B}}}{(V_A^{1/3} + V_B^{1/3})^2} \quad (II-27)$$

Note that both expressions are symmetric with respect to A and B, representing the fact that the reciprocal diffusion coefficients are similar.

### I – 2.3. Effective diffusion coefficients

In a porous medium, species are not free to diffuse in all spatial directions in the same way. The microstructure of the medium influences this diffusive transport. To take these phenomena into account, an effective diffusion coefficient is used. It is the modification of the binary diffusion coefficient with the microstructural characteristics of the medium [112]:

$$D_{AB}^{eff} = \frac{\epsilon}{\tau} D_{AB} \quad (\text{II-28})$$

$\epsilon$  being the medium porosity and  $\tau$  the tortuosity. Relationships between tortuosity and porosity have been established for different materials to allow calculation without precise measurement of tortuosity. The function  $f(\epsilon)$ , depending only on the porosity, is then defined as the ratio of effective diffusion coefficient in the porous medium to the binary diffusion coefficient:

$$D_{AB}^{eff} = f(\epsilon) D_{AB} \quad (\text{II-29})$$

Many expressions for  $f(\epsilon)$  are found in literature, including the Bruggeman's, established for a sphere stack:

$$f(\epsilon) = \epsilon^{1.5} \quad (\text{II-30})$$

For a random stack of fibers, a percolation-type relation is preferred, considering a percolation threshold  $\epsilon_p$  [113]:

$$f(\epsilon) = \epsilon \left[ \frac{\epsilon - \epsilon_p}{1 - \epsilon_p} \right]^\alpha \quad (\text{II-31})$$

Here,  $\alpha$  is a constant to be determined. According to Tomadakis et al. [113], for perpendicular to fibers flux,  $\epsilon_p = 0.33$  and  $\alpha = 0.707$ . Pharoah et al. [112] estimated these constants to be  $\epsilon_p = 0.11$  and  $\alpha = 0.785$ .

By applying the percolation-type correlation to a carbon-fiber based GDL with an initial porosity of 0.84 and 0.77 once compressed [65], the effective diffusion coefficients are determined (Table II-1).

Table II-1: Effective diffusion coefficient calculation, based on two different porosities

Binary diffusion coefficients [110] ( $\times 10^{-5} \text{ m}^2 \text{ s}^{-1}$ )	Effective diffusion coefficients [113] ( $\times 10^{-5} \text{ m}^2 \text{ s}^{-1}$ )	Effective diffusion coefficients [112] ( $\times 10^{-5} \text{ m}^2 \text{ s}^{-1}$ )
$D_{w,O_2} = 3.772$	$D_{w,O_2}^{\text{eff}}(\epsilon = 0.84) = 2.613$ $D_{w,O_2}^{\text{eff}}(\epsilon = 0.77) = 2.157$	$D_{w,O_2}^{\text{eff}}(\epsilon = 0.84) = 2.712$ $D_{w,O_2}^{\text{eff}}(\epsilon = 0.77) = 2.297$
$D_{w,N_2} = 3.950$	$D_{w,N_2}^{\text{eff}}(\epsilon = 0.84) = 2.736$ $D_{w,N_2}^{\text{eff}}(\epsilon = 0.77) = 2.259$	$D_{w,N_2}^{\text{eff}}(\epsilon = 0.84) = 2.840$ $D_{w,N_2}^{\text{eff}}(\epsilon = 0.77) = 2.405$
$D_{w,\text{air}} = 3.910$	$D_{w,\text{air}}^{\text{eff}}(\epsilon = 0.84) = 2.708$ $D_{w,\text{air}}^{\text{eff}}(\epsilon = 0.77) = 2.236$	$D_{w,\text{air}}^{\text{eff}}(\epsilon = 0.84) = 2.811$ $D_{w,\text{air}}^{\text{eff}}(\epsilon = 0.77) = 2.381$

More recently, after an experimental study of GDLs used in fuel cells, Wang et al [114] note that Bruggeman's correlation with the exponent 1.5 does not describe the gas diffusivity in GDLs well enough. Indeed, this model was realized from isotropic porous media composed of spheres whereas GDLs are non-isotropic assemblies of cylindrical carbon fibers. Consequently, as also described by Zamel et al [88], the correlations used until now overestimate the effective diffusion coefficients.

## I – 2.4. Liquid water

For some working conditions, especially at high current density and thus at high water production rate, the GDL can be filled with liquid water due to condensation within it. Carrer [115] provided some regime maps of a fuel cell considering cell temperature, channels humidity and current to identify the liquid water transport regime. It can be observed that condensation within the GDL occurs at high current density and/or at high channels humidity. Literature provides many visualization of this phenomena, notably by X-Ray methods [68], [116]–[120] that allow to investigate the presence of liquid water in the GDL pores of working fuel cell.

GDL being a porous material, fluid interfaces are highly curved and capillary forces exist. By calculating typical adimensional numbers such as Reynolds, Capillary, Weber or Bond, Jiao et al. [121] showed that capillary forces are largely predominant compared to inertia or viscous effects. Capillary pressure is the pressure difference between the non-wetting and the wetting phases. The curvature of the non-wetting

phase creates an imbalance in forces and the capillary pressure appears. In the case of a hydrophobic GDL, water is the non-wetting phase and its pressure is higher than the gas phase [122]. Furthermore, carbon papers are complex porous media composed of a variety of pore diameters or shapes which are not all filled with liquid water. The saturation  $s$  is defined as the volume occupied by a given phase divided by the total void volume. This quantity is of high importance since it dictates the capillary pressure field  $P_c$  within the porous media:

$$P_c = \sigma \cos(\theta) \left(\frac{\epsilon}{K}\right)^{\frac{1}{2}} J(s) \quad (\text{II-32})$$

Here,  $\sigma$  ( $\text{N m}^{-1}$ ),  $\theta$  and  $K$  ( $\text{m}^2$ ) respectively represent the surface tension for liquid water / air, the contact angle between water and porous matrix and the intrinsic permeability of the porous media.  $J(s)$  is a function of saturation and is usually the Leverett function:

$$J(s) = \begin{cases} 1.417(1-s) - 2.120(1-s)^2 + 1.263(1-s)^3 & \text{if } \theta < 90^\circ \\ 1.417s - 2.120s^2 + 1.263s^3 & \text{if } \theta > 90^\circ \end{cases} \quad (\text{II-33})$$

Then, a generalized Darcy's law to multiphase flow is considered to determine the liquid water velocity  $v_w$  through the media [123]:

$$v_w = -\frac{k_{rw}}{\mu_w} K \nabla P_w \quad (\text{II-34})$$

Where  $k_{rw}$  and  $\mu_w$  are the relative permeability of the media for water and the dynamic viscosity of water. The relative permeability is often given as a function of saturation in the form of a power law [117]:

$$k_{rw} = s^\alpha \quad (\text{II-35})$$

It has to be noted that the Leverett function has been established for water transport in sand [124] whose morphology mismatches the carbon fibers based GDL. Other relations, such as a modified Leverett function [125], Van Genuchten or Brooks-Corey [91] attracted attention because of their better representation of fibers media. Zhou et al. [126], [127] published an extensive fuel cell model accounting for non-isothermal and two-phase flow effects. A special attention is paid to the modeling of the porous structure of the GDL and the CL. By performing ex-situ mercury intrusion porosimetry,

the Pore Size Distribution (PSD) is accurately represented and thus considered. Capillary pressure vs saturation relations are well representative of the porous media and the model matches experiments.

## I – 3. In the CLs

### I – 3.1. Knudsen diffusion

When the mean free path of the molecules is of the same order of magnitude than the mean pore size, Fick's diffusion does not apply anymore. In such a case, the porous matrix is the limiting part of the diffusion because the gas molecules collide with the walls of the matrix more often than with other molecules. This diffusion mechanism is called Knudsen diffusion and the Knudsen diffusion coefficient  $D_K$  is defined as follows:

$$D_K = \frac{d_p}{3} \sqrt{\frac{8RT}{2\pi M}} \quad (\text{II-36})$$

Here,  $d_p$  and  $M$  are respectively the mean pore diameter and the molar mass of the concerned species. Unlike the Fick's diffusion, Knudsen diffusion only depends on the temperature. In the same way as for the Fickian diffusion coefficient, the porosity and the tortuosity of the porous matrix can be considered to provide an effective Knudsen diffusion coefficient:

$$D_K^{eff} = \frac{\epsilon}{\tau} D_K \quad (\text{II-37})$$

### I – 3.2. Ionomer

The ionomer films in the CL have a thickness of about 10 nm [128]. The oxygen diffusion through the ionomer films has to be considered in modelling since they can cover the catalyst particles and thus hinder the access to catalytic sites [129]–[133]. This effect is ever more important for low-loading catalyst layers. Nevertheless, regarding water transport, the CL are treated as simple interfaces. Indeed, water pathways in the CL are complex, and do not reduce to the ionomer film thickness. The impact of the CL on water transfer can be included in sorption or interfacial effects. It

has to be noted that the membranes getting thinner, the CL contribution to water transfer is becoming more and more important.

## I – 4. In channels

*In-situ* visualizations of water in cells revealed that some working conditions (inlet humidity, stoichiometry, current, temperature) and employed materials (GDL and MEA) can lead to the appearance of liquid water in the channels [117], [120]. Coeuriot et al. [134] performed *ex-situ* experiments to demonstrate that pressure losses through the cell give good hints about the two-phase flow regime in the channels. The modelling of water in the channels can be considered as a full-fledged part but through-plane water transfer modelling only requires the setting of boundary conditions about water concentration in the channels. Depending on the working conditions and the geometry, the relative humidity can highly vary along the channels. Pressure losses also have an impact on the vapor transport and should be considered. In this sense, the development of a model that takes into account the along-the-channel variations seems more desirable.

An interface exists between the channels and the GDL and with it a mass transfer resistance that has to be estimated. A correlation between mass transfer coefficient  $k$  and Sherwood number  $Sh$  is used. It applies for laminar flow, with fully developed concentration profile in ducts:

$$Sh = k \frac{d_t}{D_w} = 3.66 \quad (\text{II-38})$$

where  $d_t$  is the channel hydraulic diameter. Diffusion coefficient of water vapor in hydrogen is  $D_{w,H_2} = 1.5 \times 10^{-4} \text{ m}^2 \text{ s}^{-1}$  and hydraulic diameter is  $d_t^a = 0.24 \text{ mm}$  for anode channels and  $d_t^c = 0.35 \text{ mm}$  for cathode channels. Finally, the mass transport resistance at the interface between channels and GDL is calculated as  $R_{\text{ch/GDL}} = \frac{1}{k}$ . This leads to  $R_{\text{ch/GDL}}^a = 0.44 \text{ s m}^{-1}$  and  $R_{\text{ch/GDL}}^c = 0.64 \text{ s m}^{-1}$ . For air as a gas carrier, the diffusion coefficient is approximately five times higher, leading to five times higher interfacial resistances. The diffusion resistance through the GDL is expressed as  $R_{\text{GDL}} = \frac{t_{\text{GDL}}}{D_w^{\text{eff}}}$ . Considering that  $D_{w,H_2}^{\text{eff}} = 1.5 \times 10^{-5} \text{ m}^2 \text{ s}^{-1}$ , the diffusion resistance for

water in hydrogen is  $R_{\text{GDL}} = 10 \text{ s m}^{-1}$ . It represents 22 times  $R_{\text{ch/GDL}}^a$  which implies that the interfacial resistances can be neglected.

## II – 1+1D model

The model developed herein aims to represent the steady-state water transfer within a cell with no current production and thus no water source. Consequently, no heat is produced by the cell. Nevertheless, the model is non-isothermal in order to represent the possibility to impose different temperatures to the plates. This reduced order model only contains two parameters to be estimated: the diffusion coefficient of water vapor in gaseous phase  $D_{\text{eff}}$  and the diffusion coefficient of water in sorbed form  $D_{\text{M}}$ . These effective coefficients depend on the materials and the geometry but are highly convenient for real-time control because the associated model is very simple and can be solved very quickly.

The considered assembly is composed of (i) two GDLs with homogeneous properties, with no distinction between the carbon paper and the MPL and (ii) a membrane with homogeneous properties sandwiched by catalyst layers considered as infinitely thin interfaces. Mass transfer resistances  $R_{\text{ch/GDL}}$  between channels and GDLs are neglected (or included in the effective gas diffusion parameter) since it shows to be negligible compared to diffusion resistance (see paragraph I – 4. In channels). Equilibrium is assumed for the water sorption at the MEA interfaces: the actual water content at the interface is given by the sorption curve which has been measured by gravimetric sorption experiment. Water sorption resistances are neglected (i) in order to reduce the number of parameters to be estimated and (ii) since literature is still unclear about sorption/desorption rates, spreading in a range from  $0.1 \text{ s}^{-1}$  to  $100 \text{ s}^{-1}$ , with still few experimental estimations [107]. Mass transfer resistances within the electrodes are also neglected, but this hypothesis is experimentally verified *a posteriori*.

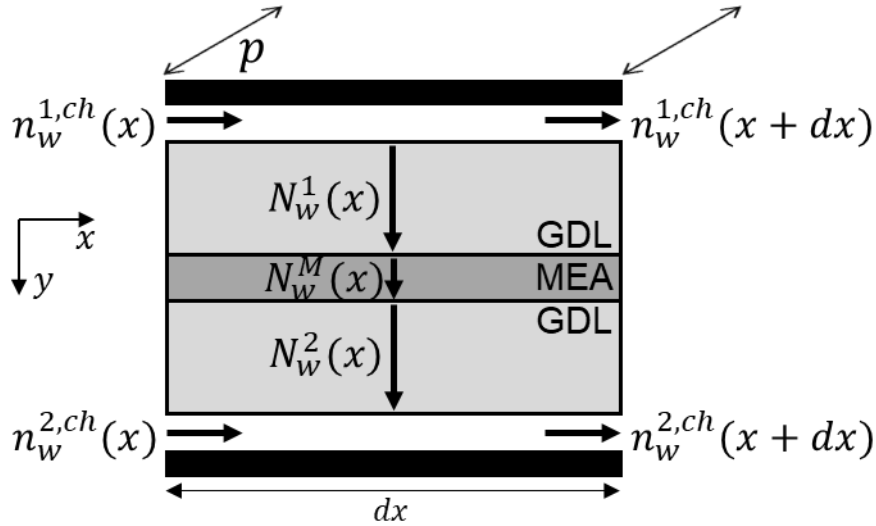


Figure II-1: Schematic of water transport 1+1D model

## II – 1. Through-plane direction

Water concentration differences  $\Delta C_w$  are applied between channels to trigger a water flux density  $N_w$  ( $\text{mol m}^{-2} \text{s}^{-1}$ ) through the assembly. Water vapor is carried by hydrogen or air, denoted with index  $g$ . Through plane flux density of the carrying gas  $N_g$  is always equal to zero because there is no gas consumption, same gas species are present in anode and cathode and driving force causing gas permeation through the membrane is negligible. Starting from side-1 channels, water vapor is transported through the GDL due to Fickian diffusion superimposed with convection:

$$N_w^1 = X_w^1(N_w^1 + N_g^1) - D_{w,g}^{eff,1} \nabla C_w^1 \quad (\text{II-39})$$

$X_w^1$  is the water vapor molar fraction that depends on the position.

The latter Eq. II-39 can be rewritten in the case of a zero dry gas flow ( $N_g^1 = 0$ ):

$$N_w^1 = -\frac{D_{w,g}^{eff,1}}{1 - X_w^1} \nabla C_w^1 \quad (\text{II-40})$$

Eq. II-40 exhibits an expression for the apparent diffusion coefficient  $\left(\frac{D_{w,g}^{eff,1}}{1 - X_w^1}\right)$  when the convection term is neglected. This expression depends on the water vapor molar fraction  $X_w^1$ . The higher the water molar fraction, the higher the difference between

apparent and effective Fickian diffusion coefficient. It is this apparent diffusion coefficient that should be taken into account when modeling the diffusion by a simple equivalent mass transfer resistance. By integrating Eq. II-40 with molar fraction of water in channels of side 1  $X_w^{1,ch}$  as a boundary condition, the exact solution for the molar fraction of water  $X_w^1$  is as follows:

$$X_w^1(y) = 1 - (1 - X_w^{1,ch}) \exp\left(\frac{N_w^1}{D_{w,g}^{eff,1} C_{tot}} y\right) \quad (\text{II-41})$$

Where  $C_{tot} = \frac{P}{RT}$ . At the interface between the GDL and the membrane, a sorption (or a desorption, depending on the gradient sign) of water vapor in the ionomer occurs. The sorption/desorption curve  $\lambda(X_w)$  which is required to link the water content  $\lambda_1$  to the vapor fraction  $X_w^1$  at the membrane interface was measured in-house using the IGAsorp sorption bench (from Hiden Isochema, Ltd). For the Gore membrane at 30°C:

$$\lambda(X_w) = 0.1186 + 13.245 \times \frac{X_w}{X_{sat}} - 21.678 \times \left(\frac{X_w}{X_{sat}}\right)^2 + 20.051 \times \left(\frac{X_w}{X_{sat}}\right)^3 \quad (\text{II-42})$$

With  $X_{sat}$  being the molar fraction of water vapor in saturated gas. Fick's law of diffusion superimposed on electroosmotic flow is used to model the transfer through the membrane in an operating fuel cell, similarly to Springer's model [73]. The water flux density  $N_w^M$  is written:

$$N_w^M = -\frac{\rho_{dry}}{EW} D_M^{eff} \frac{d\lambda_M}{dy} + \xi \frac{I}{F} \quad (\text{II-43})$$

where  $\rho_{dry}$  and  $EW$  being the density of dry ionomer and the equivalent weight, respectively.  $\xi$  is the electro-osmotic drag coefficient, which plays no role in this work because the current density  $I$  is always zero.  $D_M^{eff}$  is the effective diffusion coefficient of water in the membrane assumed to be uniform. In the following, it is assumed to be equal to the non-pressure dependent diffusion coefficient which is also called the effective sorbed phase diffusion coefficient. It is estimated as a function of the global average relative humidity ( $\overline{rh}$ ) of the cell.

Then, the water vapor fraction at the interface 2 ( $X_w^2$ ) is deduced by using the sorption law in the reverse mode ( $X_w$  deduced from  $\lambda_M$ ) and Fick's law of diffusion

superimposed with convection is again applied to calculate the water vapor fraction in the side-2 channels ( $X_w^{2,ch}$ ):

$$X_w^{2,ch} = 1 - (1 - X_w^2) \exp\left(\frac{N_w^2}{D_{w,g}^{eff,2} C_{tot}} t_{GDL}\right) \quad (II-44)$$

where  $t_{GDL}$  is the thickness of the compressed GDL. Since there is no water production (no current is produced) or consumption, the water flux density through the assembly is uniform and the following equality applies:

$$N_w^1 = N_w^M = N_w^2 \quad (II-45)$$

## II – 2. Along the channel

A 1+1D model aims to capture the variations of gas and vapor concentration along the channels and to solve the water transfer more accurately than an along-the-channel averaged 1D model.

$$\begin{aligned} \frac{dn_w^{1,ch}}{dx} &= -b \times N_w^1 \\ X_w^{1,ch}(x) &= \frac{n_w^{1,ch}(x)}{n_w^{1,ch}(x) + n_g^{1,ch}} \end{aligned} \quad (II-46)$$

where  $n_w^{1,ch}$  represents the along-the-channels water vapor flux ( $\text{mol s}^{-1}$ ) in the side-1 channels and  $b$  the exchanger width. An analogue expression for side-2 is:

$$\begin{aligned} \frac{dn_w^{2,ch}}{dx} &= b \times N_w^2 \\ X_w^{2,ch}(x) &= \frac{n_w^{2,ch}(x)}{n_w^{2,ch}(x) + n_g^{2,ch}} \end{aligned} \quad (II-47)$$

Eq. II-46 and II-47 are solved using MATLAB function *ode45*. The boundary conditions are given by the inlet water molar fractions  $X_w^{1,ch}(x = 0)$  and  $X_w^{2,ch}(x = 0)$ .

The total pressure variation is captured since it has shown influence on the final estimation. As developed in the following, the pressure losses  $\Delta P_{1,2}$  between the inlet

and outlet of the cell are measured. Assuming a linear profile for the pressure  $P_{1,2}$  along the channel:

$$P_{1,2}(x) = P_{out,1,2} + (L - x) \times \Delta P_{1,2} \quad (\text{II-48})$$

L is the length of the straight channels and  $P_{out,1,2}$  the imposed back pressure.

## III – Design of experiment

### III – 1. Experimental set-up

The objective of this set-up is to measure water fluxes through the cell in order to estimate transport parameters. A schematic of this bench is presented in Fig. II-2.

#### III – 1.1. Bench

The whole bench is centered around the fuel cell where the phenomena of interest occur. In order to control every parameter as accurately as possible, ancillary device are set up.

*Gas supply* – Starting from the set-up upstream, hydrogen used in these experiments originate from 200 bars pressure bottles with a high level of purity (less than 5 ppm of impurities). Air comes from a compressor, delivering a very low humidity gas whose dew point temperature has been measured around – 70 °C, representing 0.001% of water vapor within air.

Then, mass flowmeters accurately control the inlet gas flow. Two flowmeters for air and two for hydrogen from Brooks Instruments are used and have been calibrated by ML-800 (Drycal by Mesa Labs). Hydrogen flowmeters are ranged up to 90 slph and 30 slph whereas air flowmeters deliver flows up to 240 slph. Data given by the manufacturer exhibit an accuracy of  $\pm 0.9\%$  of set point for 20-100% of the full scale (FS) and  $\pm 0.18\%$  of the FS for <20% of the FS.

The dry gas flows in the membrane humidifiers whose features are developed in the devoted part *Humidifiers*. After the humidifier's outlet and before the cell inlet, electrovalves allow to send the flow to the cell or to by-pass it. Keller differential

pressure gauges are set up to measure the pressure losses through the cell. Their range is up to 1 bar.

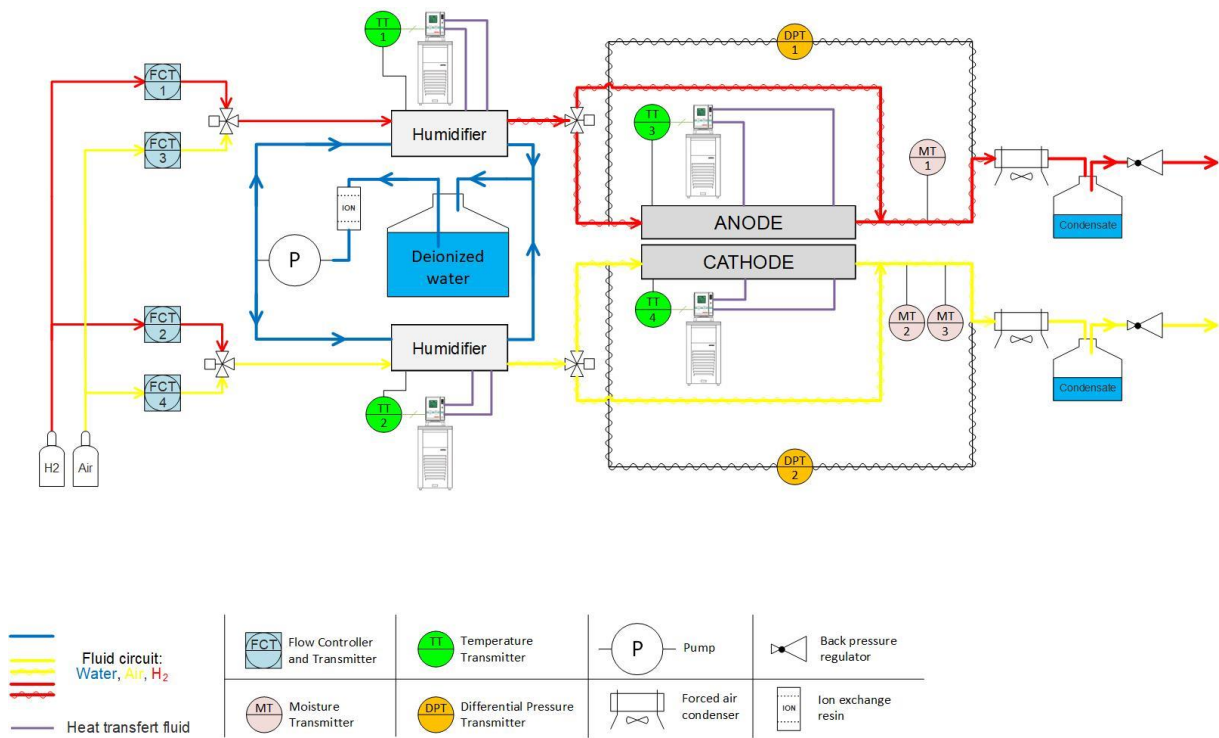


Figure II-2: Schematic of the experimental bench for water transport experiments

**Hygrometers** – After the cell, humidity sensors are used to measure water vapor fluxes. Two different types of sensors are employed. Vaisala HMT330 is a relative humidity sensor consisting in a polymer whose electric capacity depends on the relative humidity of the surrounding gas. This sensor thus gives the temperature and the relative humidity as outputs. The accuracy is  $\pm(1.5 + 0.015 \times \text{reading})\%$  rh. This sensor is placed at the outlet of the cathode side. Optidew (Michell Instruments) chilled mirror sensors are based on the temperature control of mirror on which water vapor condenses. An optical detector measures the thickness of the liquid film and the mirror temperature is tuned to 1) condense water if not already the case 2) maintain a constant film thickness by reaching equilibrium between condensation and evaporation. In this manner, the output data is the mirror temperature, assumed to be the dew point temperature of the gas. Both sensors display accuracy of  $\pm 0.15$  °C. One (Optidew Series 97430) is using a 4 wires Pt100 B class sensor and the other (Optidew Series 97551) a Pt1000 A class to measure the mirror temperature.

*Gas line ends* – By the end of the gas flow, a condenser is used to cool down the wet gas flow, a separator removes all the condensed liquid water and the dry gas passes through the back-pressure controller to impose the total pressure of the system. These are Brooks Instruments and are calibrated between 1 and 4 absolute bars. The gas finishes its paths by the gas exhaust.

*Overheating* – To prevent any condensation during the gas travel, all the pipes are overheated. This consists in heating cables producing 15 W per meter. The power supply of the cables is controlled by PID regulators based on the temperature measurement of thermocouples, located either inside gas flow where it is possible or close to the external surface of the pipes. Finally, all pipes are covered by insulating sleeve.

*Overheating drawbacks* – While overheating is absolutely mandatory, some drawbacks have been experienced. The first one is observed when heating cables are located too close to the humidifier and thus heat up the plates: oscillations are observed as well on 1-kHz resistance of the cell and on DP measurement, with the same characteristic time as PID regulation. Nevertheless, this effect has minor impact on final measurements. The second issue of overheating is its impact on the DP measurement by chilled mirrors sensors. To monitor this drawback, a temperature measurement has been inserted inside the sensor capsule to catch the gas temperature variation. The three humidity sensors have been assembled in series. Fig. II-3 represents, on the top, the humidifier temperature set at 40 °C, the Optidew and Vaisala sensors DP temperatures as a function of time. Below, the temperature of the gas measured inside the Optidew sensor is plotted as function of time. At  $t = 0$  s, overheating is tuned around 80°C and is then progressively lowered down to 45°C. When the gas is the hottest, the DP temperature given by the Optidew sensors (yellow and orange curves) is 0.8 to 1 °C higher than the real DP temperature, given by the humidifier temperature and confirmed by the Vaisala sensor. When gas is cooling down, the measurement is getting more and more accurate, reaching the Vaisala value. At  $t = 5200$  s, overheating is getting insufficient to prevent condensation and DP temperature suddenly drops out. This phenomenon is expected to originate from thermal exchange between the hot gas and the colder mirror, creating temperature heterogeneities and disturbing the measurement. It has been observed that hydrogen

had more impact than air on these temperature heterogeneities because of the higher thermal conductivity. This effect will explain some discrepancies between experiments and the model and will be denoted as the overheating effect.

One has to note that the shoulder exhibited at  $t = 600$  s is due to a sensor initialization cycle, evaporating the liquid film and thus sending it to next in series sensor. Moreover, this experiment succeeded a several hours of drying step to ensure no liquid water laid in the system.

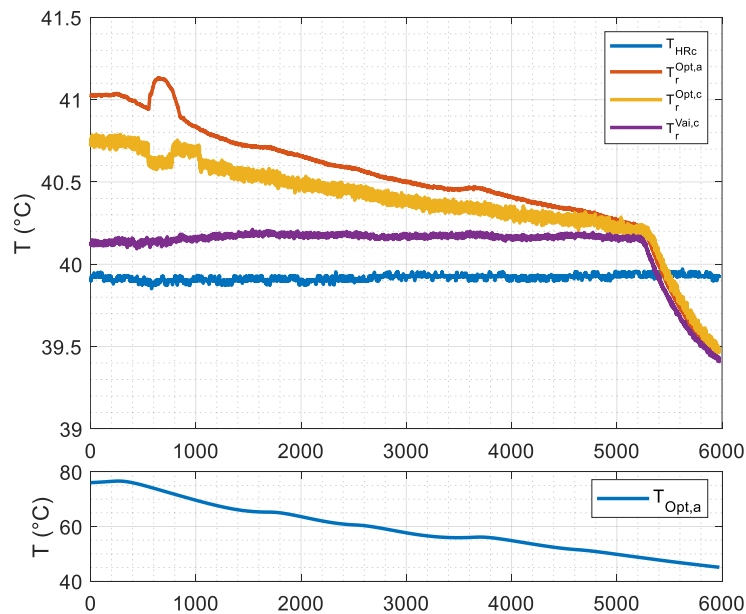


Figure II-3: Top: Humidifier temperature and DP temperature measurements versus time; Bottom: Gas temperature versus time

### III – 1.2. Humidifiers

*Advantages* – In order to humidify inlet gases, several options are available such as bubbler, commercial membrane humidifier or in-house membrane humidifiers. The choice fell on in-house membrane humidifiers due to several of their features. The size of the humidifier dictates its efficiency: the usage of a high exchange surface can guarantee a high level of humidification. The second advantage of membrane humidifier is its accuracy. While a bubbler requires the temperature control of a liquid water volume, the membrane humidifier is controlled by adjusting the plates temperature. The latter is quite easy by the usage of a heating fluid and a sufficient

flow rate. The typical accuracy of temperature control is  $0.1 - 0.15$  °C. Finally, membrane humidifier is well suited for gas switches. For future experiments, switches between different gases should be applied in order to study oxygen transfer for instance. The dynamic of such experiments is of high importance and a bubbler is not adapted because it creates gas mixing within the liquid volume.

*Materials* – Membrane humidifiers are composed of two plates carved with channels, sandwiching two GDLs, themselves sandwiching a PFSA membrane able to transport water. On one side, dry gas to humidify travels while on the other side, there are two possibilities: to use a highly wet gas or liquid water. In the goal to provide the best humidification performances as possible, liquid water is chosen. Fig. II-4 presents the humidifiers set-up. Liquid water and dry gas are in co-flow configuration. The heating fluid is split in two parallel circuits to regulate simultaneously both plates. It enters the humidifiers on the gas outlet side to assure that the end of gas path is always hotter than the inlet. Temperature measurements for regulation and for acquisition are both at the gas outlet and are achieved by Pt100 sensors. The humidifiers are assembled using Nafion 212 ( $50.8 \mu\text{m}$ ) and two Sigracet 28 and 36 AA GDL, which are hydrophilic without MPL. Gaskets are added to ensure no leakage of gas or water. The channels depths are  $0.7 \text{ mm}$  and  $0.3 \text{ mm}$  for water and gas respectively. The channels width is  $1.5 \text{ mm}$  and  $1 \text{ mm}$  for the land. The plates are made out of aluminum with a hard anodization to reduce corrosion. The tightening torque is controlled to be  $10 \text{ N m}$ .

The liquid water comes from a high-purity water tank and the circuit is split to feed in parallel both humidifiers. The pump delivers a water flow of  $50 \text{ ml min}^{-1}$  and excess water always comes back in the tank, ensuring enough water is provided to humidifiers.

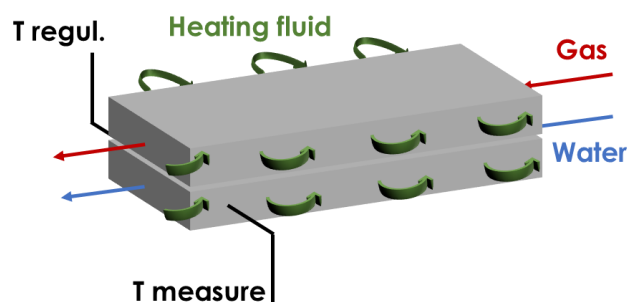


Figure II-4: Schematic of the membrane humidifier fluids configuration

*Optimizations* – Two optimizations about the humidifiers handling have been experienced (Fig. II-5):

- The heating fluid should pass through the plates from the gas outlet towards the gas inlet to ensure an increasing temperature in the gas flow direction (Fig. II-5b)). Otherwise, the gas saturates at high temperature at the inlet and cools down towards the outlet, creating undesirable water condensation within the channels (Fig. II-5a)).
- Both humidifiers should be fed by independent (or at least parallel) water circuits (Fig. II-5d)). When humidifiers are in series and when the hotter is before the colder, water feeding enters the colder humidifier being hotter than the plates and, as previously explained, the gas cools down towards the outlet and water may condense in the channels (Fig. II-5c)).

*Performances* – Some performances curves have been plotted to validate the humidifiers performances (Fig. II-6). These curves are realized with air, considering that hydrogen humidification is always better due to a higher diffusivity of water vapor in hydrogen than in air. In this set-up, three humidity sensors were put in series and four humidification temperatures are studied: 40, 50, 60 and 70 °C – corresponding to the temperature range of interest in this work. It can be observed that the DP temperature is a continuously decreasing function of the gas flow rate. Depending on the desired accuracy, one can find in these graphs the maximal flow rate to use for each humidification temperature. The less efficient point is reached for 70 °C at 100 slph where relative humidity is about 95%.

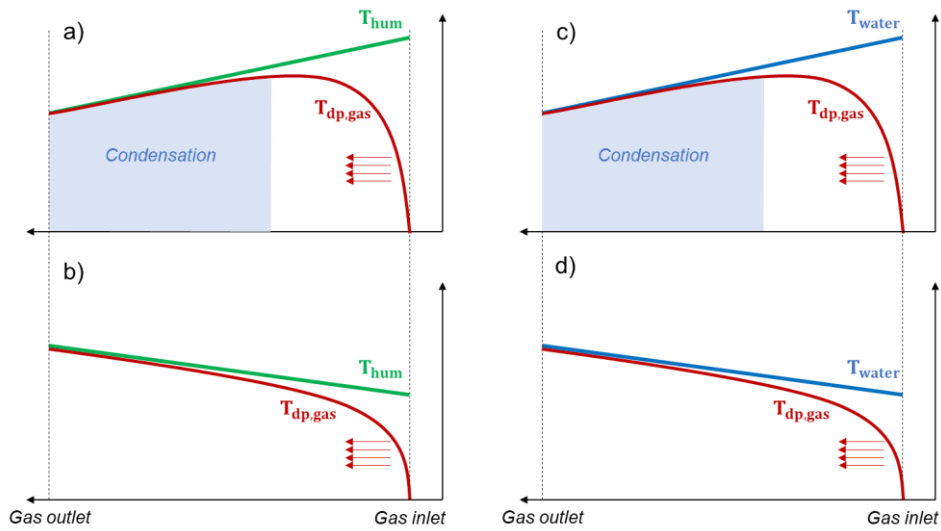


Figure II-5: Schematic of two phenomena creating condensation in humidifiers and associated mitigations. a) Heating fluids inlet close to gas inlet, b) Heating fluid inlet close to gas outlet, c) Water hotter than the plates, d) Water colder than the plates. Red arrows represent the gas flow direction.

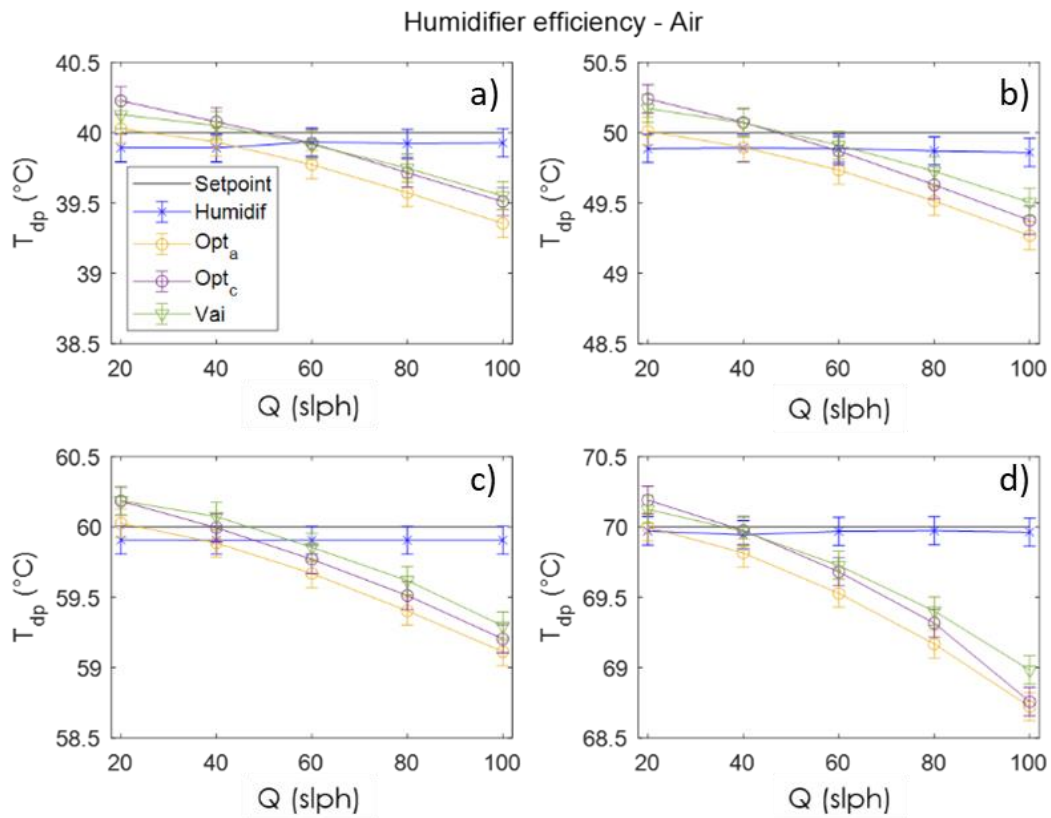


Figure II-6: Performances curves of a humidifier showing the measured dew point temperatures and the humidifier temperature as a function of air flow rate for a) 40 °C, b) 50 °C, c) 60 °C and d) 70 °C

### III – 1.3. Cell

*Plates* – The employed cell in the present work is a single cell of a total area of 25 cm<sup>2</sup>. Geometrical properties of the cell are given in Table II-2. The two plates are made out of brass with gold coating to ensure low electrical contact resistance and low corrosion. The temperature of each plate can be independently regulated in order to impose temperature differences between plates. In this sense, the contact surface between the plates is reduced to the active area only by adding height difference of 1.2 mm, as shown in Fig. II-7. This special feature divides the contact surface by 2.25 and thus guarantees a more homogeneous temperature field within plates. Each plate temperature is measured and regulated by two Pt100 probes inserted 50 mm deep.

In Fig. II-7, the gas inlet is located at the top where one inlet can be seen in the manifold. At the opposite, the manifold contains two holes: one is the gas outlet and the other one is a special gas inlet. This feature enables to dilute the wet outlet gas with a dry gas and evaporate potential liquid water in order to perform transient water balances.

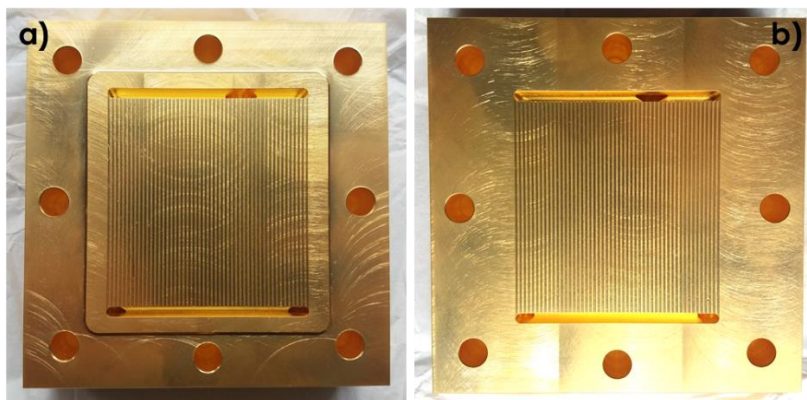


Figure II-7: a) anode and b) cathode plate. Anode plate has a height difference to decrease contact between plates

*Assemblies* – Different MEAs are employed in this work (Table II-2). The first one is provided by IRD and is based on a Gore M375.15 membrane, whose thickness is 15  $\mu\text{m}$ . Catalyst layers are loaded at 0.1 and 0.4 mg Pt/cm<sup>2</sup> for anode and cathode respectively. The second one is based on Nafion 117 (175  $\mu\text{m}$ -thick) and CLs are loaded at 0.4 mg Pt/cm<sup>2</sup> for anode and cathode. Finally, in order to investigate the role of the CL in the water transfer, Nafion XL is studied with and without CLs. In the case

of the MEA, the CLs are symmetrical with a loading of 0.4 mg Pt per cm<sup>2</sup>. The GDLs are standard Sigracet 22 BC, hydrophobic with MPL, with initial thickness of 235 µm. The assembly is completed with 150-µm-thick PTFE gaskets to ensure no leakage and a 23-µm-thick PEN subgasket, leading to a compressed thickness for the GDL of 173 µm, that is 26% of compression.

### III – 2. Set-up design optimization: definition of the optimal exchange surface

In order to obtain a good measurement, it is necessary that humidity equilibrium is not reached and that a humidity gradient remains between the two compartments up to the outlet. Otherwise, the effective surface area that participated in the exchange is unknown (e.g. if equilibrium is reached in the middle of the cell, only 50% of the surface area participates in the exchange). In order to respect this constraint when the entire 25 cm<sup>2</sup> surface area is used, very high flow rates must be used, for which the efficiency of the humidifiers falls. In that respect, it was chosen to reduce the exchange surface by using two PEN windows that sandwich the MEA and are therefore positioned between the electrodes and the GDL. On the other hand, the exchange surface must not be too small because a minimum flow rate exists to ensure a good humidity measurement (dry gas flow rates of 10-15 slph are required by humidity sensors to provide the best accuracy) and if the dew point temperature variation between the inlet and the outlet is too small, this implies a large uncertainty on the water flow rate through the MEA.

Table II-2: Geometrical cell properties and materials characteristics

	IRD Gore	Ion Power (N117)	Ion Power (NXL)	NXL
Membrane / thickness	M375.15 / 15 µm	Nafion 117 / 175 µm	Nafion XL / 29 µm	Nafion XL / 29 µm
Anode/cathode CL loadings (mg Pt/cm <sup>2</sup> )	0.1/0.4	0.4/0.4	0.4/0.4	∅
Exchange surface length	6 mm	25 mm	6 mm	6 mm
Anode channels	Width: 0.6 mm ; Depth: 0.15 mm ; Ribs: 0.4 mm			
Cathode channels	Width: 0.6 mm ; Depth: 0.25 mm ; Ribs: 0.4 mm			
Number of straight parallel channels	50			
Initial GDL thickness	215 µm			

The size of this window was optimized to maximize the sensitivities of our observable (the outlet dew point temperature) with respect to the model parameters (the diffusion coefficients of water vapor and adsorbed water). To perform the calculation of the optimal exchange surface area, water vapor diffusion coefficients are needed by the model. Thus, basis values for these coefficients are chosen after preliminary experiments:  $D_{w,air} = 5 \times 10^{-6} \text{ m}^2 \text{ s}^{-1}$ ,  $D_{w,H_2} = 25 \times 10^{-6} \text{ m}^2 \text{ s}^{-1}$  and  $D_{w,M} = 3 \times 10^{-10} \text{ m}^2 \text{ s}^{-1}$ .  $D_{w,H_2}$  is almost 5 times  $D_{w,air}$  according to the ratio of binary diffusion coefficients of water vapor in air and hydrogen. The reduced sensitivity  $S_{i,j}$  of an observable  $y_i$  data to a parameter  $\theta_j$  is defined as follows:

$$S_{i,j} = \frac{\partial y_i}{\partial x_j} \times \frac{x_j}{y_i} \quad (\text{II-49})$$

Here,  $S_{i,j}$  is dimensionless so that all sensitivities can be compared to each other. In this work, the observable data is unique and is the outlet dew point temperature and the two parameters are the diffusion coefficient in gas phase  $D_{w,g}$  and in the membrane  $D_{w,M}$ :

$$S_{D_{w,g}} = \frac{\partial T_{dp}^{out}}{\partial D_{w,g}} \times \frac{D_{w,g}}{T_{dp}^{out}} \quad (\text{II-50})$$

$$S_{D_{w,M}} = \frac{\partial T_{dp}^{out}}{\partial D_{w,M}} \times \frac{D_{w,M}}{T_{dp}^{out}}$$

Considering that this window should cover all the 50 channels (and thus being 50 mm large), its length has to be determined. According to the results presented in Fig. II-8, the optimal exchange surface that maximizes the sensitivity of our observable to the parameters to be estimated has a length of 6 mm for the Gore membrane and 25 mm for the Nafion® 117 one. This window is placed 1 cm downstream from the channels inlet to assure a thermal equilibrium between gas and channels (Fig. II-9 and Fig. II-10).

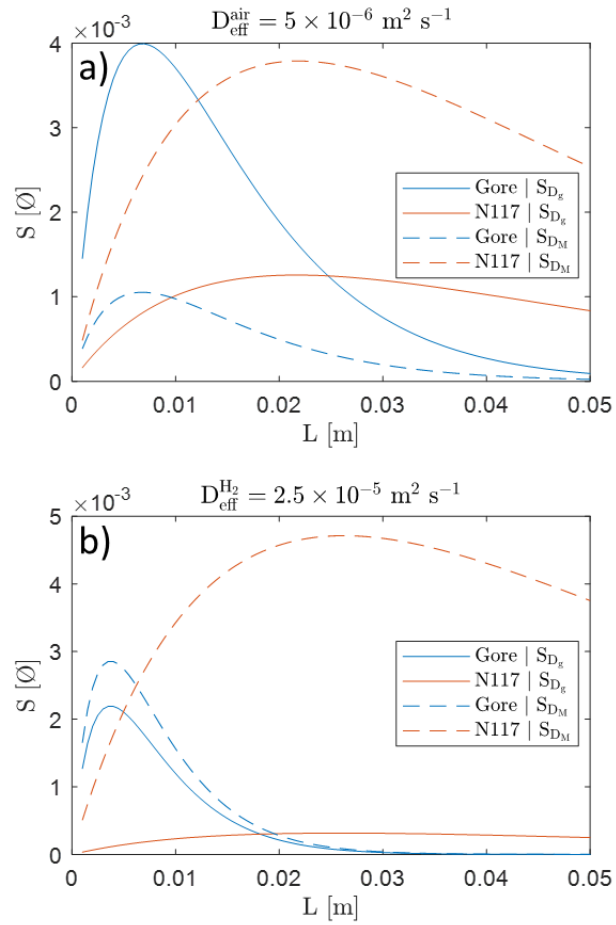


Figure II-8: Sensibility curves of the observable data with respect to two parameters of interest as a function of the exchange window length, for two MEAs, with  $D_M = 3 \times 10^{-10} \text{ m}^2 \text{ s}^{-1}$  a) With air -  $Q_{air} = 20 \text{ NL h}^{-1}$  b) With  $\text{H}_2$  -  $Q_{\text{H}_2} = 30 \text{ NL h}^{-1}$

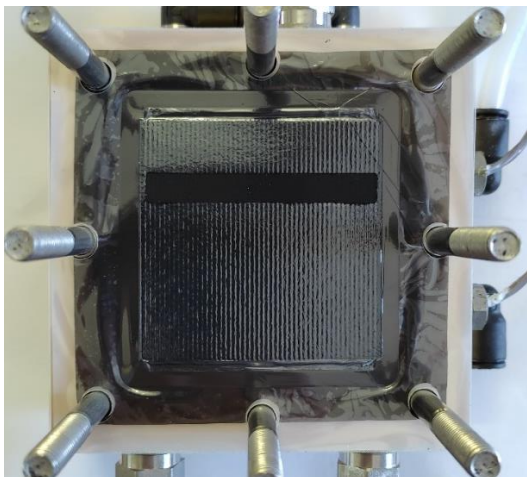


Figure II-9: View of an assembly with an exchange window of  $50 \times 6 \text{ mm}^2$ , at 10 mm after the inlet

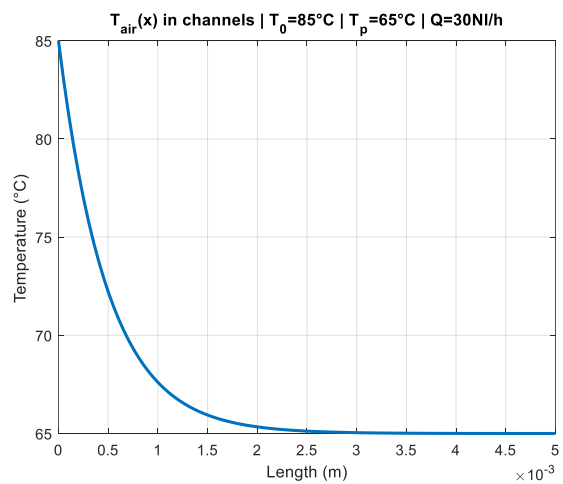


Figure II-10: Modelled temperature evolution of overheated air along the channel direction

### III – 3. XP1: constant average concentration

The design of experiment is planned to discriminate between the two parameters of interest which are the diffusion coefficient of sorbed water in the membrane  $D_M$  and the effective gas phase diffusion coefficient  $D_{eff}$  of water vapor in air or hydrogen. The first series of experiments, denoted as XP1, aims to measure concentration-difference driven through-plane water fluxes by keeping constant the average water concentration within the cell. This assumption allows to provide an estimation of the membrane diffusion coefficient  $D_M$  for a given average water concentration, considering that the membrane is in uniform conditions and that its transport properties are similar as long as the given average water concentration is constant.

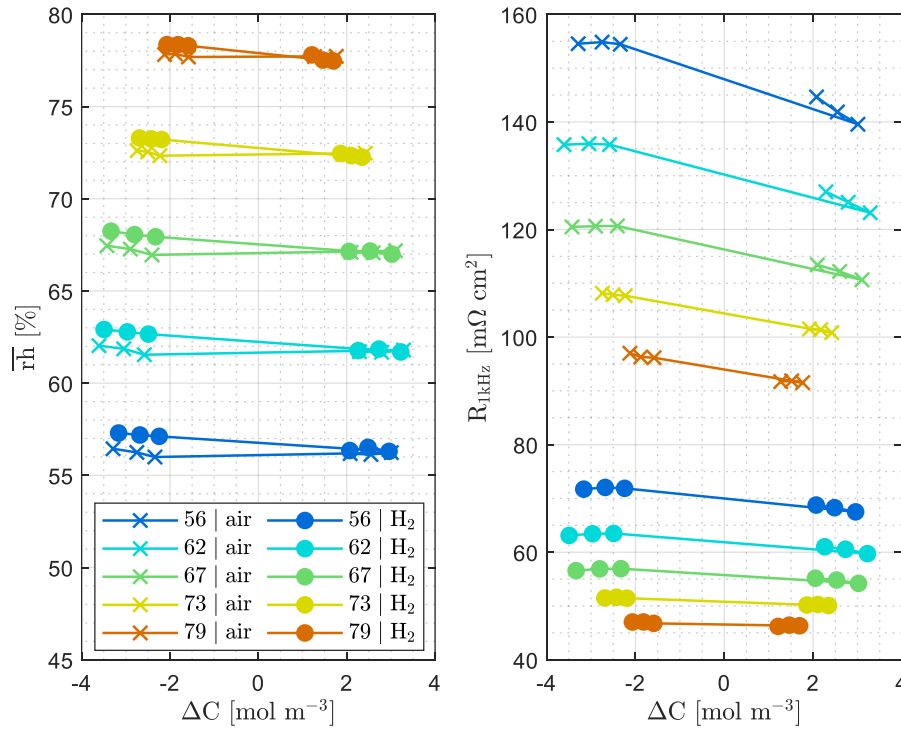


Figure II-11: Average relative humidity and 1-kHz resistance for XP1 – Gore MEA

In order to keep the average water concentration  $\bar{C}_w$  constant, humidifier temperatures  $T_{hum}$  are tuned one to the other:

$$\bar{C}_w = \frac{P_{sat}(T_{hum,a}) + P_{sat}(T_{hum,c})}{RT_p} \quad (\text{II-51})$$

With  $R$ ,  $T_p$  and  $P_{sat}$  being the universal gas constant, the plates temperature and the saturation pressure of water vapor respectively.

Fig. II-11 represents the average relative humidity of the cell  $\bar{r}h$  and the 1-kHz resistance  $R_{1kHz}$  for the Gore MEA as a function of the water concentration difference between channels  $\Delta C$ , calculated as  $\Delta C = \frac{1}{2}(C_{in}^a + C_{out}^a) - \frac{1}{2}(C_{in}^c + C_{out}^c)$ . The legend refers as each curve by the targeted  $\bar{r}h$  and the employed gas, crosses representing air/air configuration and dots  $H_2/H_2$ . This graph is presented in order to ensure that actual experimental conditions allow to satisfy the assumptions about the average water concentration. For each series,  $\bar{r}h$  is rather constant and close to the goal value, even though some small variations of less than 2% of  $\bar{r}h$  are observed. For hydrogen series,  $R_{1kHz}$  is rather constant, meaning that the hydration level of the membrane is similar for all points of a given series. For air series,  $R_{1kHz}$  is more or less two times higher than for hydrogen and variations are larger as well. This difference is explained by the fact that the resistance is measured at 1 kHz which is not enough to fully shunt the electrode.

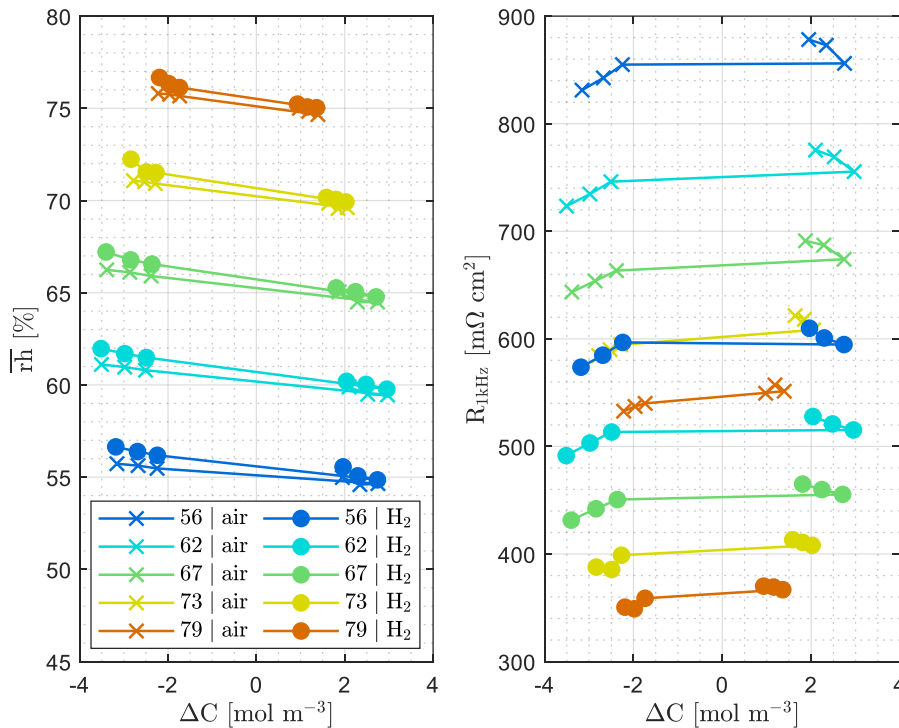


Figure II-12: Average relative humidity and 1-kHz resistance for XP1 – N117 MEA

Fig. II-12 represents  $\overline{rh}$  and  $R_{1\text{kHz}}$  for the N117 MEA, as a function of the water concentration difference. Here, small differences are observed on  $\overline{rh}$  between positive and negative  $\Delta C$ . Nevertheless,  $R_{1\text{kHz}}$  exhibits only slight variations within a given series, which allows to conclude that the membrane is in similar hydration state.

### III – 4. XP2: pressure variation

The second series of experiments about water transport, denoted as XP2, consists in total pressure variation of the system. The diffusion coefficient in the gas phase varies with the inverse of the pressure:

$$\frac{pD_{AB}}{(p_{cA}p_{cB})^{1/3}(T_{cA}T_{cB})^{5/12}(1/M_A + 1/M_B)^{1/2}} = a \left( \frac{T}{\sqrt{T_{cA}T_{cB}}} \right)^b \quad (\text{II-52})$$

Thus, by changing the total pressure of the cell, the gas phase diffusion mechanisms are impacted and can be captured. By maintaining all other experimental conditions constant, the pressure independent mechanisms are spared.

In XP2, pressure is varied from atmospheric up to 2 bars. This pressure is kept relatively low to prevent any unexpected leakage in the system that can spoil the water flux measurements. Consequently, the diffusion coefficient of gases is expected to be divided by 2.

The average relative humidities that are imposed in the following experiments are similar to the XP1 series, in order to be able to compare the results. The average relative humidities and associated 1-kHz resistances are presented in Fig. II-13, II-14, II-15 and II-16 for Gore MEA, N117 MEA, NXL MEA and NXL membrane respectively. On these graphs, one can observe that experimental conditions are well controlled, assuring a constant relative humidity for all points of a given series. The biggest discrepancies are for N117 MEA at high  $\overline{rh}$ . Nevertheless,  $R_{1\text{kHz}}$  varies by less than 10% so assumption of similar hydration state is considered as validated.

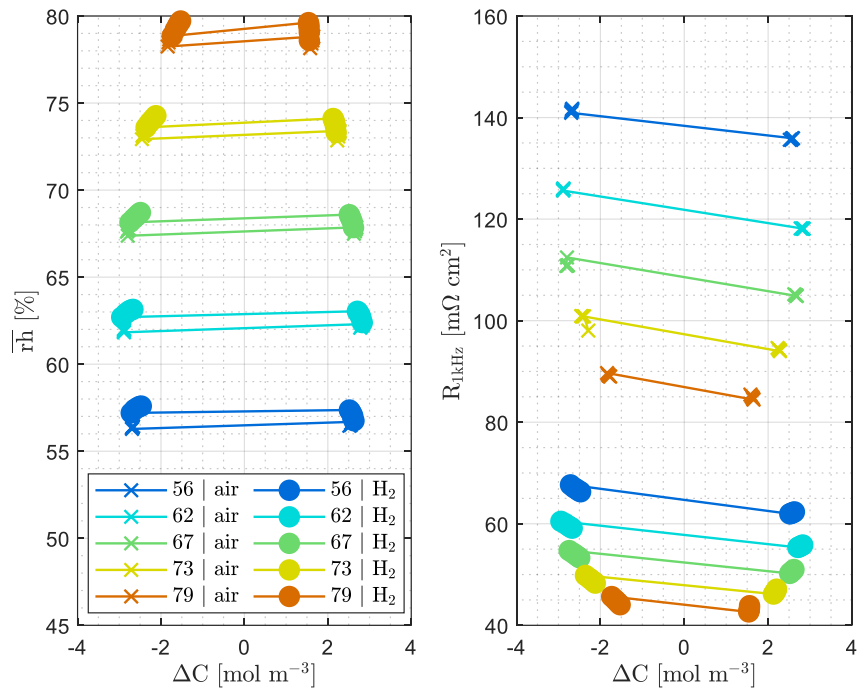


Figure II-13: Average relative humidity and 1-kHz resistance for XP2 – Gore MEA

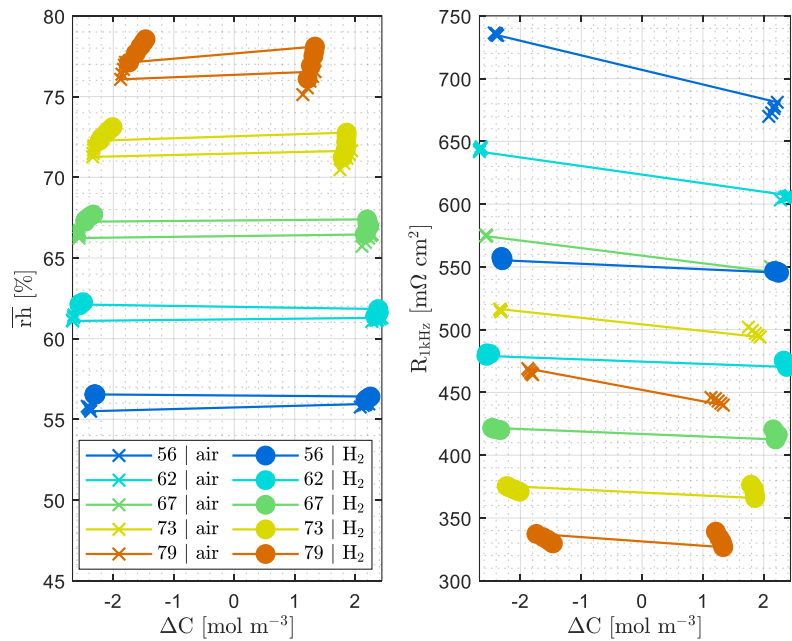


Figure II-14: Average relative humidity and 1-kHz resistance for XP2 – N117 MEA

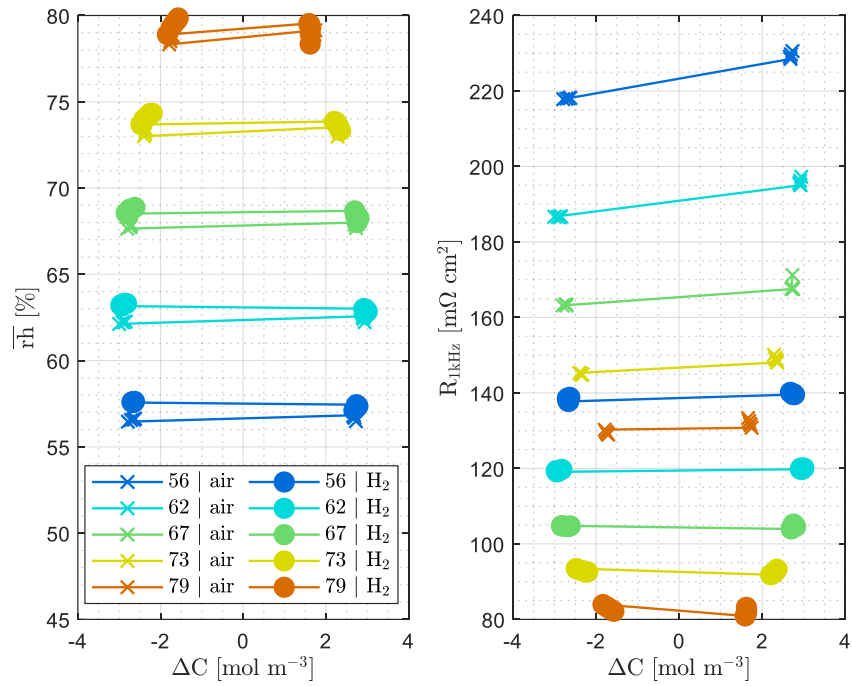


Figure II-15: Average relative humidity and 1-kHz resistance for XP2 – NXL MEA

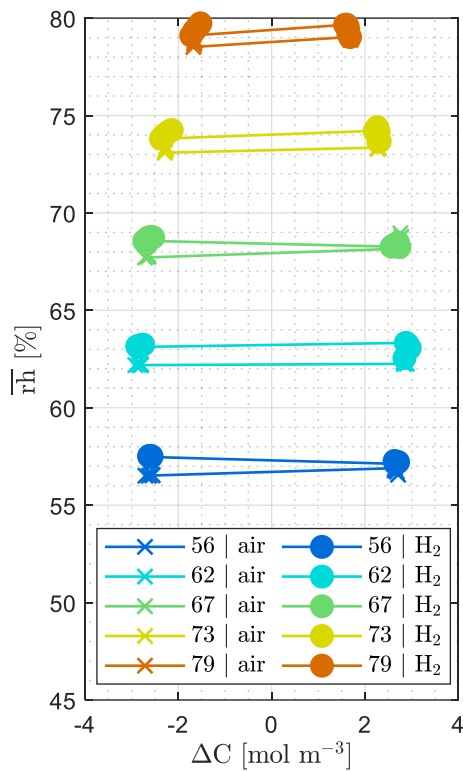


Figure II-16: Average relative humidity for XP2 – NXL membrane

### III – 5. XP3: condensation

This series of experiments aims to investigate the influence of liquid water on the transport properties of the membrane. The Schroeder's paradox describes an unexpected behavior of the membrane in the presence of liquid water. The chemical activity of liquid water and saturated vapor are both equal to 1. The water content of the membrane is a function of the surrounding activity of water and is thus expected to be similar for liquid water and saturated vapor. However, it has been shown experimentally [36] that the water content due to sorption with saturated vapor is between 12 and 14 whereas it is about 22 for liquid water sorption. The transport properties of the membrane are increasing functions of the water content and the diffusion coefficient in the membrane is thus expected to increase with liquid sorption.

In order to achieve in-situ liquid sorption of the membrane, a special set of experimental conditions is imposed to the cell (see Fig. II-17). A temperature difference  $\Delta T$  is applied between the two plates, thanks to the independent thermal regulations. The assembly being symmetric, the MEA is expected to be at the average temperature  $T_M = \frac{1}{2}(T_{hot} + T_{cold})$ . The hotter side is fed with a gas which is humidified at the dew point temperature  $T_{hum,hot}$ , comprised between  $T_{hot}$  and  $T_M$  in order to create condensation within the hotter half-cell. To prevent any undesirable condensation on the cold side, the gas of the latter is rather dry.

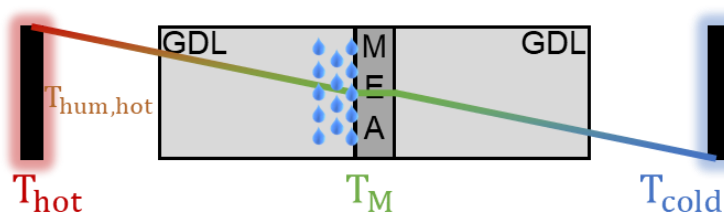


Figure II-17: Scheme of the assembly for XP3

### IV – Parameters estimation

Measuring the flux of water through the MEA as a function of the imposed concentration difference allows the estimation of an overall water transfer resistance

$R = \frac{\Delta C}{N_w}$ , but does not allow the separation of gaseous and adsorbed diffusion directly.

The model parameters (i.e. the effective gaseous and adsorbed diffusion coefficients  $D_{\text{eff}}$  and  $D_M$ ) are said to be correlated. There is an infinite number of  $D_{\text{eff}}$  and  $D_M$  pairs that minimize the difference between the model and the experiment. To decorrelate these parameters, two strategies have been implemented and compared:

*XP1* – As previously explained, these experiments are achieved using two different gas carriers (air and hydrogen) in order to decorrelate the gas phase diffusion from the diffusion in the membrane. This is done by assuming that the ratio of effective diffusion coefficients is equal to the ratio of the binary coefficients  $\left(\frac{D_{\text{eff}}^{\text{H}_2}}{D_{\text{eff}}^{\text{air}}} = 4.8\right)$ .

The estimation of the parameters is obtained by minimizing the deviation between experimental observable data (the outlet dew point temperature) and the modelled one, i.e. the following least squares sum:

$$LSS_{XP1} \left( D_{\text{eff}}^{\text{air}}(j), D_M(j) \right) = \sum_i \left[ \left( T_{\text{mod}}^{\text{air}}(i, j) - T_{\text{xp}}^{\text{air}}(i, j) \right)^2 + \left( T_{\text{mod}}^{\text{H}_2}(i, j) - T_{\text{xp}}^{\text{H}_2}(i, j) \right)^2 \right] \quad (\text{II-53})$$

In this expression,  $i = 1, \dots, n_{\text{points}}$  represents the index of a measurement point  $\Delta C_w^i$  within a given series defined by an average relative humidity  $\overline{\text{rh}}_j$ . Thus, one set of parameters is estimated for each average relative humidity  $\overline{\text{rh}}_j$ .  $T_{\text{mod}}^{\text{air}}$  is computed using  $(D_{\text{eff}}^{\text{air}}, D_M)$  whereas  $T_{\text{mod}}^{\text{H}_2}$  uses  $(\alpha \times D_{\text{eff}}^{\text{air}}, D_M)$  with  $\alpha = 4.8$ .

*XP2* – Experiments are performed for different total pressures. The effective gas phase diffusion coefficient is assumed to vary in a manner proportional to the inverse of the total pressure, like the binary coefficient  $\left( D_{\text{eff}} \sim \frac{1}{P} \right)$ . The effective diffusion coefficient in the adsorbed phase  $D_M$  is assumed not to depend on the total pressure. For a given  $\Delta C_w$ , and so a given  $\overline{\text{rh}}$ , the dew point temperature at the outlet of  $n^{\circ}2$  compartment is measured as a function of total pressure in the channels. As previously, several cell-average relative humidities  $\overline{\text{rh}}$  are imposed to explore membrane properties for different water content. The two parameters are decorrelated so that air data and hydrogen data can be processed separately. Of course it is also possible to treat all data together as in *XP1*. In the case of independent estimation, the following sum of least squares is minimized to determine the effective diffusion coefficients:

$$LSS_{XP2}^g (D_{eff}^g(j), D_M(j)) = \sum_i \left[ (T_{mod}^g(i, j) - T_{xp}^g(i, j))^2 \right] \quad (II-54)$$

Here,  $g$  represents air or hydrogen data.  $T_{mod}^g$  is computed using  $(D_{eff}^g/P_{1,2}, D_M)$ .

## IV – 1. Method for parameters estimation validation

A preliminary check is performed to ensure that the estimation method is consistent and well able to estimate the parameters of interest. This simulation of the experiments also quantifies the uncertainty associated with the estimated parameters as a function of the uncertainty of the measurements. The principle is the following: experimental results are simulated with the model using the experimental conditions for gas flow rates, pressure losses and humidifiers temperatures. The diffusion coefficients are chosen to be  $D_{w,air}^{eff} = 5 \times 10^{-6} \text{ m}^2 \text{ s}^{-1}$ ,  $D_{M,Gore}^{eff} = 3 \times 10^{-10} \text{ m}^2 \text{ s}^{-1}$  and  $D_{M,N117}^{eff} = 7 \times 10^{-10} \text{ m}^2 \text{ s}^{-1}$  for all average relative humidities. The calculated dew point temperatures at the compartment n°2 outlet  $T_{dp}^{2,out}$  are then noised by adding normally distributed random values with a standard deviation corresponding to the measurement uncertainty (i.e. 0.1°C) and average value of zero. A random noise scaled to 1% standard deviation is also added to the gas flow rates. These data are used as observables to estimate the two effective diffusion parameters  $D_{w,air}^{eff}$  and  $D_M^{eff}$ . By repeating the numerical experiment a large number of times (Monte Carlo's method), one can deduce the uncertainty on the estimated parameters. A hundred simulations of XP1 are performed to depict a statistically representative view of the estimation uncertainty – see Fig. II-18.

In these subgraphs of Fig. II-18, the error bars are constructed using the standard deviations of the hundred estimations for each parameter. First, it is observed that the inversion method is accurate: all estimations are well centered around values chosen for simulations. The uncertainty of the estimated parameter varies with the average relative humidity: a given shift on the dew point temperature leads to more water flux variation at high humidity due to the non-linearity of the saturation pressure and sorption curve. For gas phase coefficients  $D_{w,g}^{eff}$  obtained with Gore MEA (Fig. II-18a and II-18b) the standard deviation is between 4.5 and 8.8% of the reference value. For the diffusion coefficient in the membrane (Fig. II-18c), the lowest uncertainty

represents 4.4% of the reference whereas the highest is 15.4% at high relative humidity. Concerning N117 MEA, the standard deviation of  $D_{w,g}^{eff}$  (Fig. II-18d and II-18e) is between 13 and 21% of the reference value. Finally, for the membrane coefficient (Fig. II-18f), it lays between 3.9 and 8.5% of the reference. N117 being thicker than the Gore membrane, the sensitivity to the membrane coefficient is higher since sorbed water transfer resistance is more significant. This is at the expense of the gaseous phase sensitivity whose uncertainty is consequently higher. Note that these uncertainties on the estimated parameters are the consequence of an uncertainty of 0.1°C on the dew point temperature measured at the outlet of compartment n°2 and of 1% uncertainty on the dry gas flow rates. The uncertainty of 0.1°C corresponds to the specification of the sensor but it is probably a little underestimated because it was qualitatively observed that it depends on the gas overheating.

Rather than absolute uncertainty, standard deviations of the relative uncertainties are applied for all subsequent experimental estimations. Since realistic reference values has been chosen for this estimation, it is considered that uncertainties are representative of the estimation accuracy, or at least an accurate order of magnitude. This assumes that there is no model bias.

The results presented hereafter arise from the best experimental protocol that have been performed. Here, experimental conditions are accurately controlled and no outlier point is observed. In addition, each parameter estimation of XP1 (respectively XP2) originates from 6 (respectively 5) experimental measurements, which are all consistent.

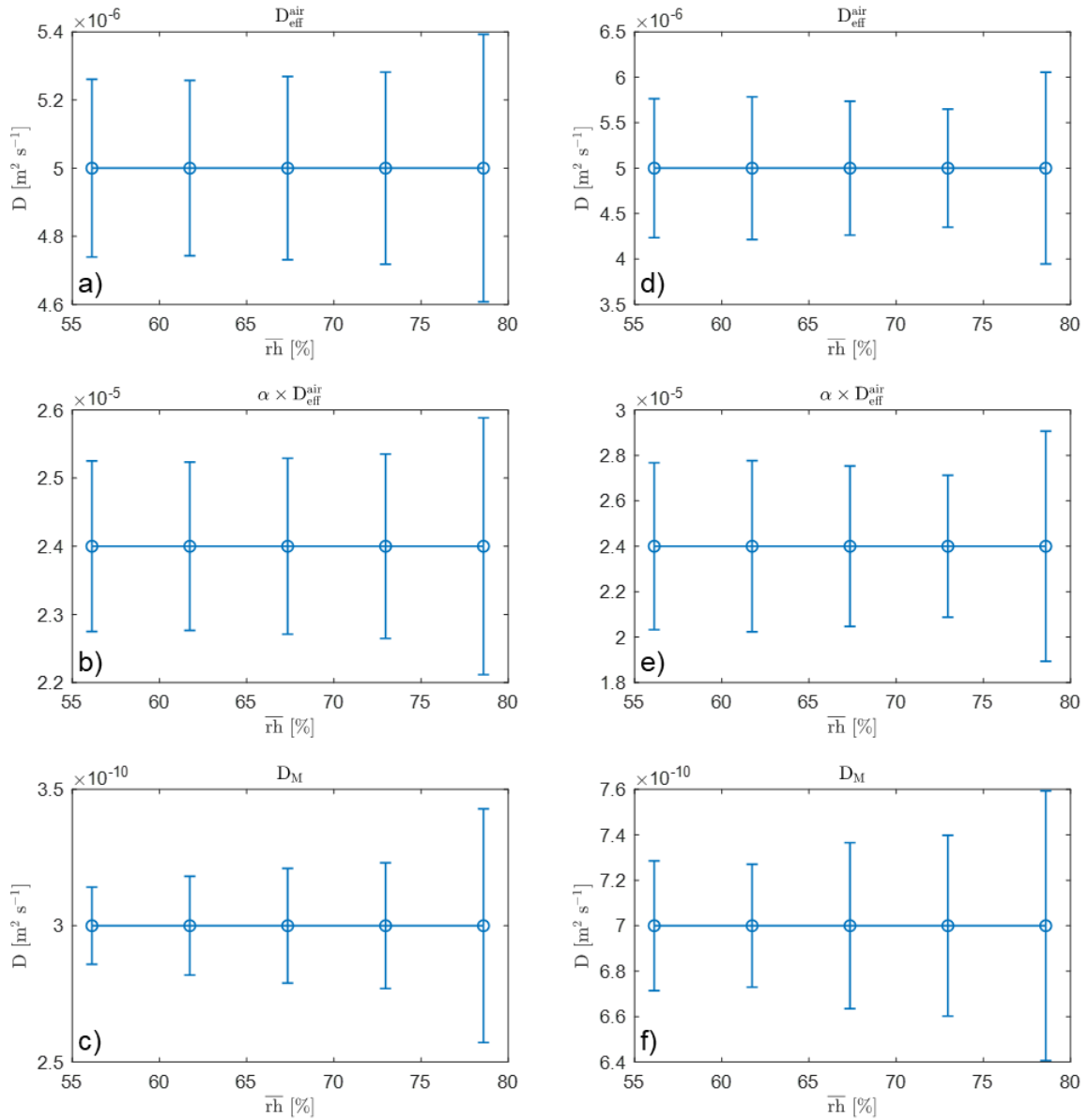


Figure II-18: Estimated parameters with noised simulated data for Gore MEA - a) to c) - and N117 MEA - d) to f). We can note the better precision of estimation of gas diffusion parameters with the gore membrane and the variation of the precision with the relative humidity

## IV – 2. Estimations by XP1

### IV – 2.1. Gore MEA

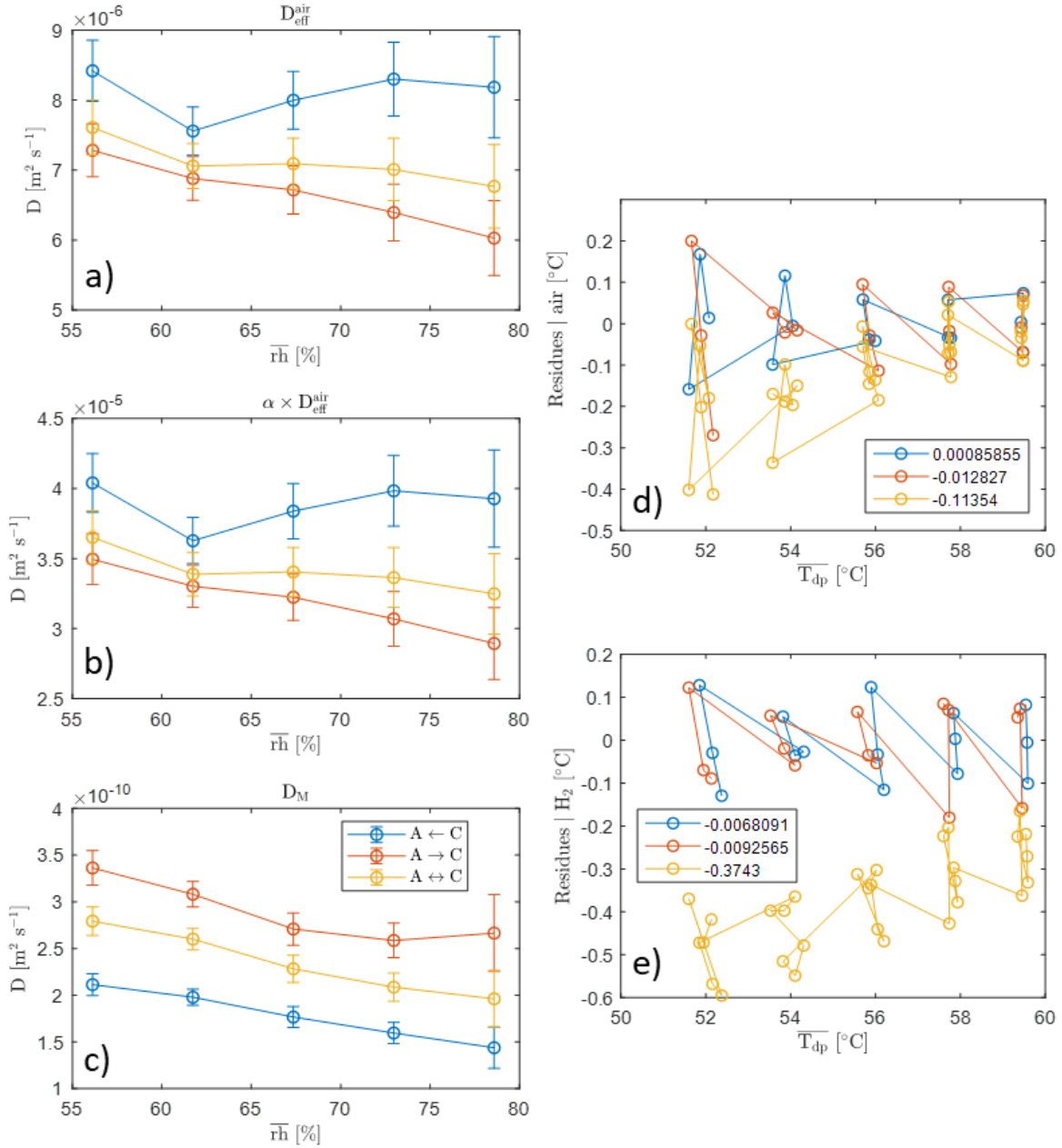


Figure II-19: Estimated parameters (a), (b) and (c)) and associated residues (d) and (e)) – XP1 and Gore MEA. The uncertainty bars correspond to a standard deviation error of 0.1°C on the dew point temperatures and of 1% on the flow rates

Fig. II-19 represents the estimation of the diffusion coefficients by XP1 for the MEA based on Gore membrane and the associated residues. In Fig. II-19a, the effective diffusion coefficient of water vapor in air  $D_{eff}^{air}$  is plotted as a function of  $\bar{r}h$ . In Fig. II-

19b,  $\alpha \times D_{\text{eff}}^{\text{air}}$  is plotted, representing the effective diffusion coefficient of water vapor in hydrogen, according to the assumptions made. The diffusion coefficient of water in the membrane  $D_M$  is represented in Fig. II-19c. All these estimations are based on the observable data supplied by the Optidew sensor placed at the cathode outlet. Each graph is composed of three curves, representing three different estimations. As the legend refers, blue dots are related to water fluxes from the anode towards the cathode (so-called “negative” fluxes, triggered by “negative”  $\Delta C$  and denoted as  $A \leftarrow C$ ). Orange dots are related to positive fluxes ( $A \rightarrow C$ ) and yellow dots ( $A \leftrightarrow C$ ) are based on all data processed together.

The accuracy of a parameter estimation has to be evaluated with respect to the estimation residues, being the difference between the model and the experimental outputs. Fig. II-19d and II-19e show residues for air and hydrogen experiments respectively. The color code is the same for all graphs and the legend refers as the residues average for each series.  $A \leftarrow C$  and  $A \rightarrow C$  series exhibit residues with a maximum of 0.2 °C between experiments and model, with an average very close to zero.  $A \leftrightarrow C$  estimation is associated with residues whose average is lower than zero:  $-0.11$  °C and  $-0.37$  °C for air and hydrogen respectively. Moreover, one can notify that the residues magnitude decreases with increasing  $\overline{T_{\text{dp}}}$ , especially for hydrogen experiments. As defined here, negative residues imply that the measured outlet DP is higher than the modelled. This can be due to the overheating of gases which is achieved to prevent any water condensation in the pipes. As it is demonstrated in paragraph III – 1.1. Bench, this overheating has an effect on the dew point temperature measurement by artificially increasing the sensor’s mirror temperature. Consequently, the experimental dew point is higher than the actual one, thus leading to negative residues. This effect is more likely to occur with hydrogen, due to its higher thermal conductivity, and for low dew point temperatures, where the difference between the gas temperature and the dew point is high.

The effective diffusion coefficient of water vapor in air is estimated to lay in the range between  $6 \times 10^{-6} \text{ m}^2 \text{ s}^{-1}$  and  $8.5 \times 10^{-6} \text{ m}^2 \text{ s}^{-1}$ . The associated diffusion coefficient in hydrogen is between  $2.9 \times 10^{-5} \text{ m}^2 \text{ s}^{-1}$  and  $4 \times 10^{-5} \text{ m}^2 \text{ s}^{-1}$ . Theses estimations contain several contributions:

- Porosity and tortuosity of the GDL, which depend on the nature of the material (woven or non-woven), its PTFE loading, its initial porosity and the compression level;
- 2D effects: gas diffusion paths are longer towards the CL regions under the land and the apparent diffusion coefficient appears to be lower;
- Diffusion through MPL and CL where the pores are smaller;
- The mass transfer resistance of laminar flow in channels and Darcy flow in the plane of the GDL.

These results are not intrinsic to the materials but depend on the flow fields geometry, the clamping, on the gas flow rate, etc... The values are of the same order of magnitude as those estimated in the literature but the comparison is not easy because it depends on the diffusion length used to calculate the coefficient. Here we have chosen the thickness of the compressed GDL while the transfer being in reality in 2 dimensions, the equivalent effective length is certainly greater because of the diffusion under the ribs of the channels.

The diffusion coefficient of water in sorbed phase is estimated between  $1.5 \times 10^{-10} \text{ m}^2 \text{ s}^{-1}$  and  $3.3 \times 10^{-10} \text{ m}^2 \text{ s}^{-1}$ . The coefficient slightly decreases with increasing  $\bar{r}_h$ , whereas an increase should be expected due to a higher hydration level of the membrane. Nevertheless, the estimated effective diffusion coefficient takes into account other phenomena as for example the sorption/desorption resistance that has the effect of reducing the water content gradient across the membrane. Indeed, if the water flux is greater at high humidities, the discontinuity at the interface between the gas and the ionomer due to the sorption/desorption resistance should be greater, resulting in a lower water gradient through the membrane and thus a lower water flux than expected. As this interfacial resistance is not modeled, this effect results here in a lower effective diffusion coefficient.

As it can be observed on Fig. II-19, parameters estimation intervals do not overlap for all points, even by considering uncertainty. To achieve that, uncertainty should be higher, around 10%. It means that the uncertainty is probably underestimated and

others error sources exist. For instance, the overheating effect creates higher deviations than the considered 0.1 °C, but does not occur in a similar way for all points.

### IV – 2.2. N117 MEA

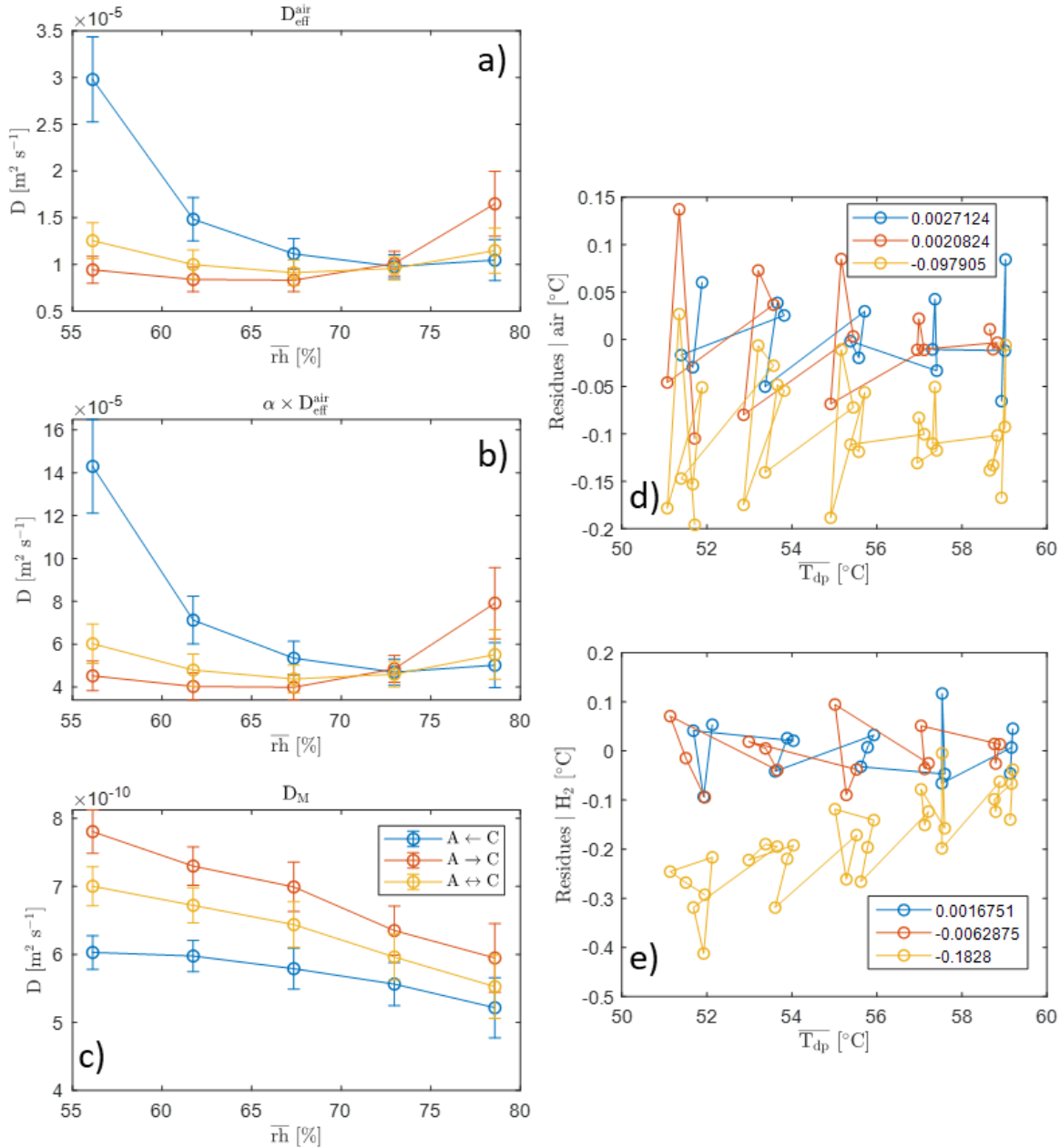


Figure II-20: Estimated parameters (a), b) and c)) and associated residues (d) and e)) – XP1 – N117 MEA. The uncertainty bars correspond to a standard deviation error of 0.1°C on the dew point temperatures and of 1% on the flow rate

The diffusion coefficients estimations and the associated residues for the N117 MEA are presented in Fig. II-20. The observable data used for these estimations is still the Optidew at the cathode outlet. As for Gore MEA, A ← C and A → C series ended with

low magnitude (0.15 °C) and decorrelated residues with an average of zero. A ↔ C series exhibits correlated residues with an average of −0.1 °C and −0.18 °C for air and hydrogen respectively. For hydrogen, the residues magnitude decreases with  $\overline{T_{dp}}$ , as for Gore MEA.

The estimation of gas diffusion coefficients for the lowest  $\overline{r_h}$  leads to a value which is far from the others. Here, the sensitivity to this parameter is low, leading to a high deviation. For higher  $\overline{r_h}$ , the estimations are consistent and only vary a few. Discarding the first point, the effective diffusion coefficient of water vapor in air lays between  $1 \times 10^{-5} \text{ m}^2 \text{ s}^{-1}$  and  $1.5 \times 10^{-5} \text{ m}^2 \text{ s}^{-1}$  and the associated values for hydrogen are between  $4.8 \times 10^{-5} \text{ m}^2 \text{ s}^{-1}$  and  $7.2 \times 10^{-5} \text{ m}^2 \text{ s}^{-1}$ . These values are 2/3 higher than the estimated ones with the Gore MEA. This can be due to:

- A low sensitivity to gas phase diffusion with the N117 MEA because the gas phase resistance is very small compared to the sorbed phase mass transfer resistance.
- The influence of electrodes since the two MEAs have different ones;

The diffusion coefficient in the membrane is between  $5 \times 10^{-10} \text{ m}^2 \text{ s}^{-1}$  and  $8 \times 10^{-10} \text{ m}^2 \text{ s}^{-1}$ , depending on the data employed for the estimation. These values are globally higher than for the Gore MEA. This may originate from the structure of the membrane (the Gore one is reinforced with ePTFE whereas N117 is only made out of PFSA) or from the sorption resistance that is relatively more important for a thinner MEA. Nevertheless, the Gore membrane is 11 times thinner than N117 and the total transport resistance is thus lower (6 times lower). The same slight decrease of the coefficient with average  $\overline{r_h}$  is observed.

## IV – 3. Estimation by XP2

### IV – 3.1. Gore MEA

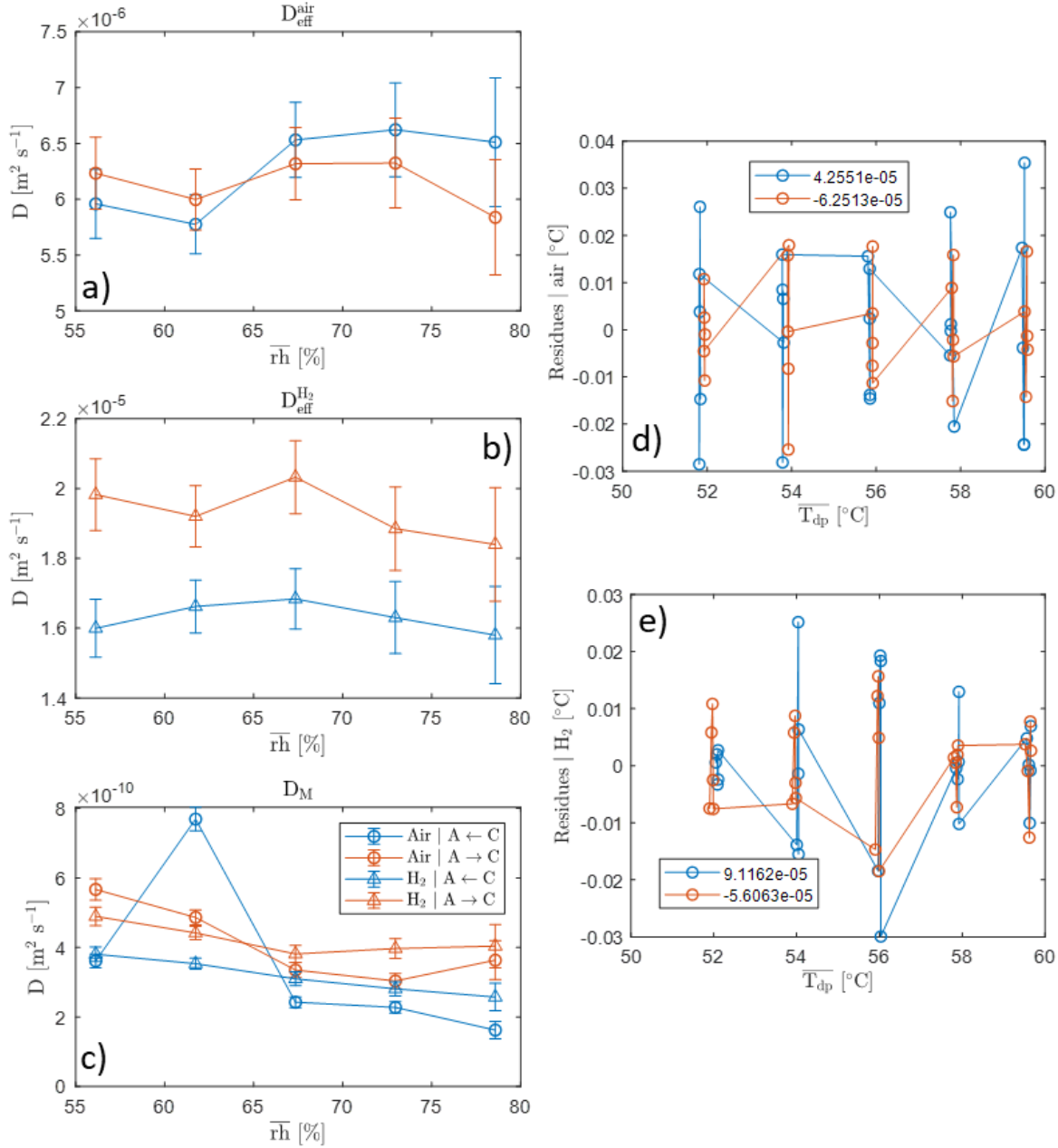


Figure II-21: Estimated parameters (a), (b) and (c)) and associated residues (d) and (e)) – XP2 – MEA Gore. The uncertainty bars correspond to a standard deviation error of 0.1°C on the dew point temperatures and of 1% on the flow rate

Fig. II-21 exhibits estimated parameters and residues for the Gore MEA based on XP2. In Fig. II-21a, the estimated  $D_{eff}^{air}$  are represented as a function of the average relative humidity of the cell for the negative (blue) and positive (orange) water fluxes. In Fig. II-

21b, estimations of  $D_{\text{eff}}^{\text{H}_2}$  are plotted and in Fig. II-21c, the diffusion coefficient of water in the membrane  $D_M$  is represented, for air and hydrogen as well as for positive and negative fluxes. One can observe that  $D_{\text{eff}}^{\text{air}}$  lays in a narrow range between  $5.8 \times 10^{-6} \text{ m}^2 \text{ s}^{-1}$  and  $6.6 \times 10^{-6} \text{ m}^2 \text{ s}^{-1}$ . Only small variations are observed and both estimations are consistent. For hydrogen coefficient  $D_{\text{eff}}^{\text{H}_2}$ , the values are little more spread out between  $1.6 \times 10^{-5} \text{ m}^2 \text{ s}^{-1}$  and  $2 \times 10^{-5} \text{ m}^2 \text{ s}^{-1}$ . Nevertheless, each estimation has small variations with the relative humidity. The diffusion coefficient in the membrane  $D_M$  varies between  $1.6 \times 10^{-10} \text{ m}^2 \text{ s}^{-1}$  and  $7.7 \times 10^{-10} \text{ m}^2 \text{ s}^{-1}$ , depending on  $\overline{\text{rh}}$  and on the estimation. One has to note that, the Gore membrane being very thin, the sensitivity to  $D_M$  compared to  $D_{\text{eff}}^{\text{air}}$  can be low, especially when pressure is raised.

The estimation residues are presented in Fig. II-21d and II-21e for both gases.  $A \leftrightarrow C$  data is discarded because of the non-zero centered mean of the residues.  $A \leftarrow C$  (blue) and  $A \rightarrow C$  (orange) exhibit low magnitude and decorrelated residues with average around zero, which is a sign of an accurate estimation.

#### IV – 3.2. N117 MEA

The estimated parameters and residues for the MEA based on N117 are presented in Fig. II-22. Here, estimation with air experiment only contains the negative fluxes because positive fluxes experiment was not successful. In Fig. II-22a, the diffusion coefficient of water vapor in air is presented and varies between  $3.5 \times 10^{-6} \text{ m}^2 \text{ s}^{-1}$  and  $10 \times 10^{-6} \text{ m}^2 \text{ s}^{-1}$ . One can note that the values for the highest  $\overline{\text{rh}}$  undergo a smaller deviation and are comprised between  $4.8 \times 10^{-6} \text{ m}^2 \text{ s}^{-1}$  and  $6.8 \times 10^{-6} \text{ m}^2 \text{ s}^{-1}$ . This can be explained by the sensitivity to this parameter: when the membrane is thick as N117, the main transport resistance occurs in the membrane. Thus, the gas phase resistance is small, or even neglectable. It is all the more the case for hydrogen experiment, presented in Fig. II-22b where  $D_{\text{eff}}^{\text{H}_2}$  is plotted. The estimated values spread between  $1.2 \times 10^{-5} \text{ m}^2 \text{ s}^{-1}$  and  $2.3 \times 10^{-5} \text{ m}^2 \text{ s}^{-1}$ . The associated diffusion coefficients in the membrane  $D_M$  are presented in Fig. II-22c. The values for the parameters are comprised between  $0.6 \times 10^{-9} \text{ m}^2 \text{ s}^{-1}$  and  $1.3 \times 10^{-9} \text{ m}^2 \text{ s}^{-1}$ .

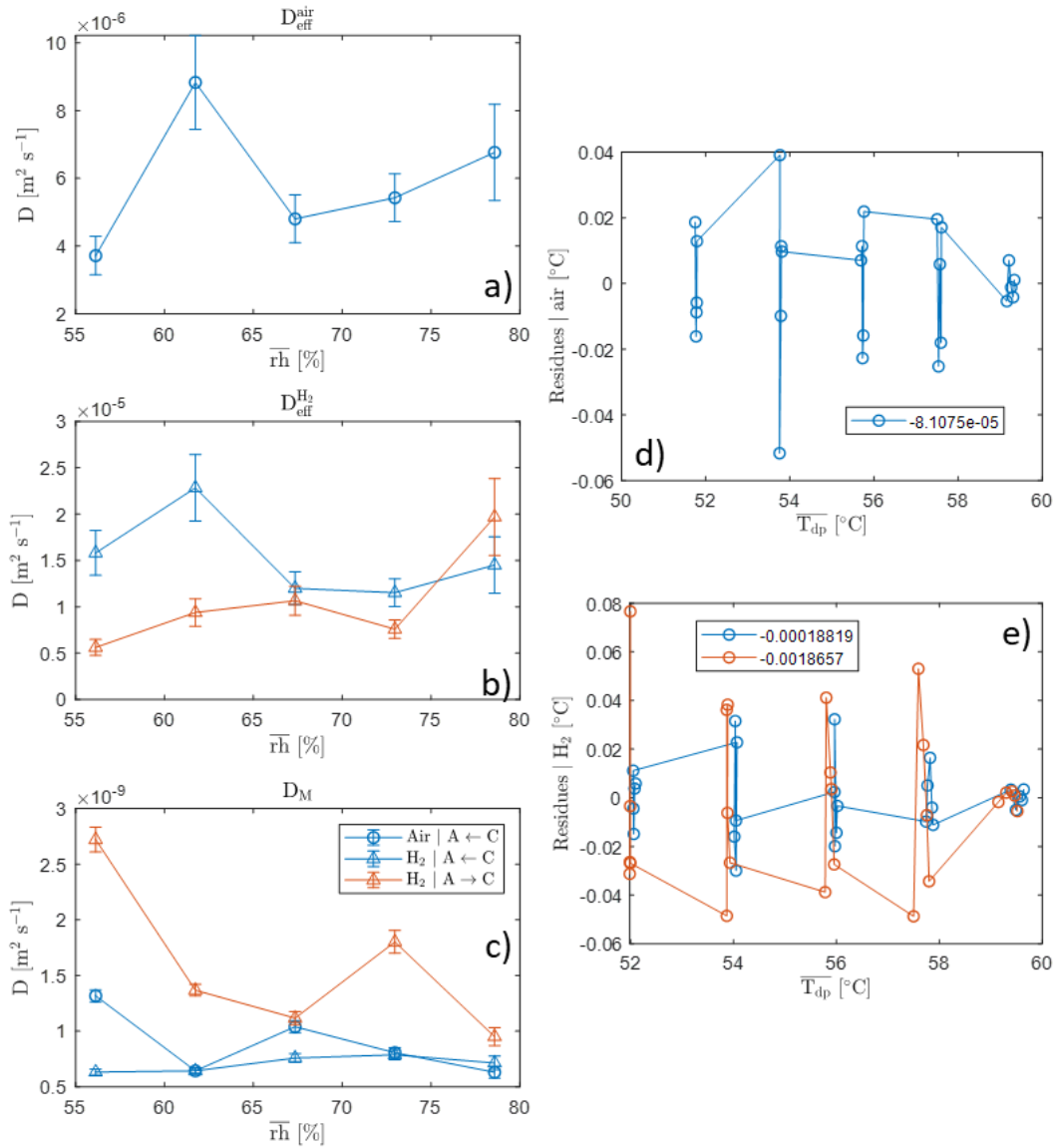


Figure II-22: Estimated parameters (a), b) and c)) and associated residues (d) and e)) – XP2 – N117 MEA. The uncertainty bars correspond to a standard deviation error of 0.1°C on the dew point temperatures and of 1% on the flow rate

### IV – 3.3. NXL membrane and MEA

The last material that has been studied by XP2 is the membrane NXL with and without CLs. Fig. II-23 presents the estimated parameters and residues for both materials, solid lines being attributed to the MEA and dash line representing the stand-alone membrane. Fig. II-23a represents the estimated diffusion coefficients of water vapor in air  $D_{eff}^{air}$ . The values spread between  $5 \times 10^{-6} m^2 s^{-1}$  and  $6.8 \times 10^{-6} m^2 s^{-1}$  for both materials.  $D_{eff}^{H_2}$  (Fig. II-23b) exhibits values from  $1.5 \times 10^{-5} m^2 s^{-1}$  up to  $2.2 \times 10^{-5} m^2 s^{-1}$ . The diffusion coefficient in the membrane is presented in Fig. II-23c for

both materials. One has to note that the MEA and the stand-alone membrane are treated in the same way during data processing, considering the same thickness and homogeneous properties. The estimated values all lay between  $2.9 \times 10^{-10} \text{ m}^2 \text{ s}^{-1}$  and  $6.2 \times 10^{-10} \text{ m}^2 \text{ s}^{-1}$  with no obvious distinction between the membrane and the MEA. The same decrease with  $\overline{rh}$  is observed. The associated residues are presented in Fig. II-23d, II-23e, II-23f and II-23g and all show small magnitude and a zero-average. This comparison implies that the presence of electrodes has no influence on the parameters of this water transfer model and strengthens the assumption that the electrodes do not create resistance to water transfer.

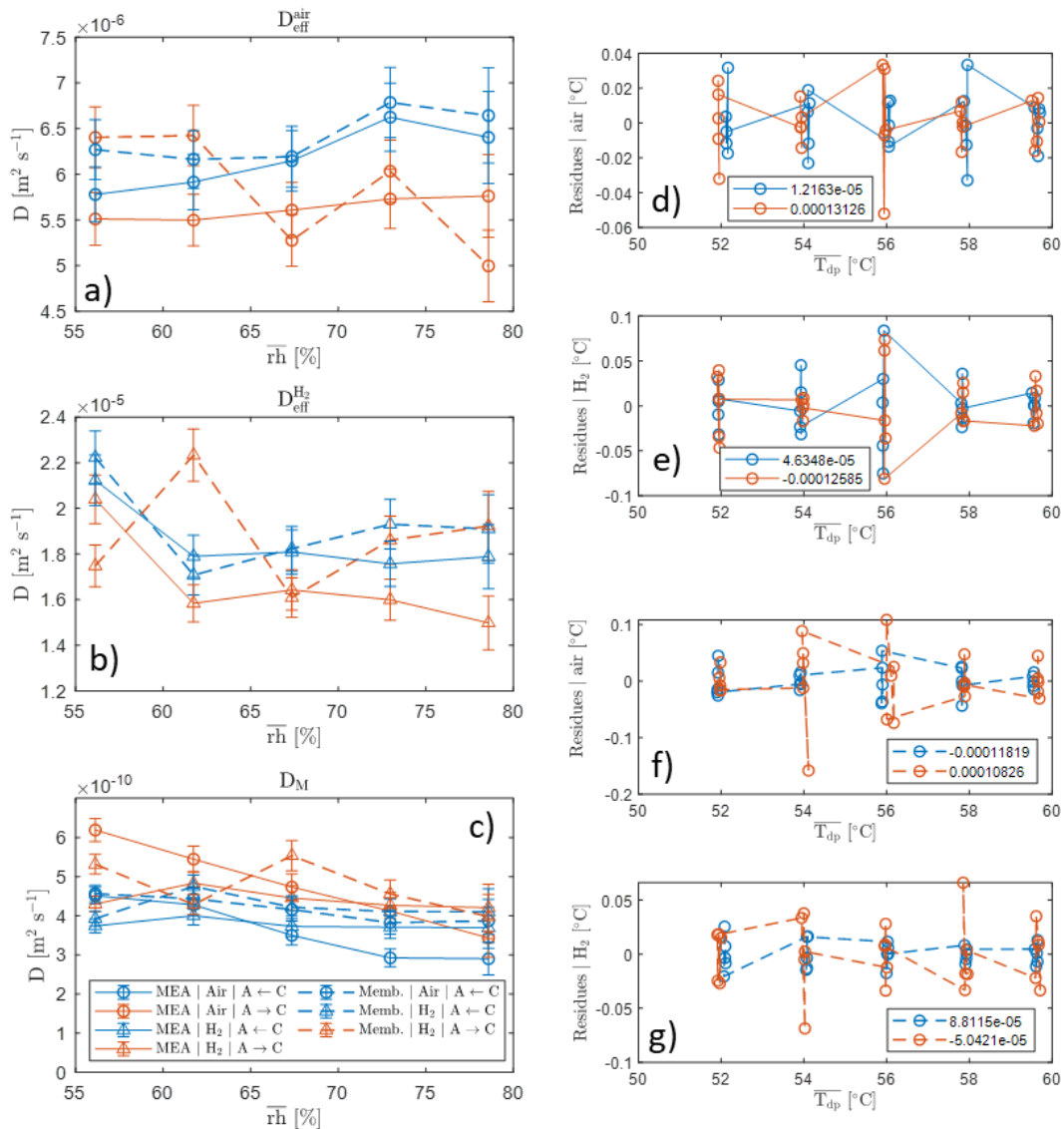


Figure II-23: Estimated parameters (a), (b) and (c)) and associated residues (d) to g)) – XP2 – NXL: Membrane vs MEA. The uncertainty bars correspond to a standard deviation error of 0.1°C on the dew point temperatures and of 1% on the flow rate

### IV – 3.4. Comparison between all materials

By comparing all experiments of XP2, it is observed that the diffusion coefficient of water in air  $D_{\text{eff}}^{\text{air}}$  is comprised in the same interval between  $5 \times 10^{-6} \text{ m}^2 \text{ s}^{-1}$  and  $7 \times 10^{-6} \text{ m}^2 \text{ s}^{-1}$ , if one only considers the most sensitive experiments (with Gore and NXL membranes). The same experiments lead to an estimation of diffusion coefficient of water in hydrogen between  $1.4 \times 10^{-5} \text{ m}^2 \text{ s}^{-1}$  and  $2.2 \times 10^{-5} \text{ m}^2 \text{ s}^{-1}$ . Concerning the membrane, the Gore and the NXL MEAs exhibit similar diffusion coefficients which are lower than for the N117. One reason for this difference is the different natures of those membranes: NXL and Gore are reinforced with PTFE whereas N117 is not. PTFE has poor water transport properties and this leads to lower diffusive capability of reinforced membranes. Nevertheless, N117 being highly thicker than the others, the total transport resistance that it creates is higher and is thus detrimental for back diffusion of water. Another explanation to this difference can be the interfacial resistances  $R_i$ . By assuming that these are similar for all materials, their relative contribution to thinner membranes is higher and thus reduce the apparent diffusion coefficient  $D_M^{\text{ap}}$ :

$$R_{\text{tot}} = \frac{t_M}{D_M^{\text{ap}}} = \frac{t_M}{D_M} + 2 \times R_i$$

$$\Rightarrow D_M^{\text{ap}} = \frac{1}{\frac{1}{D_M} + 2 \frac{R_i}{t_M}} \quad (\text{II-55})$$

Here, it can be concluded that when the membrane thickness  $t_M$  increases, the apparent diffusion coefficient tends to the one of the membrane.

### IV – 4. Comparison between XP1 and XP2

Fig. II-24 gathers the estimated parameters for the three employed MEAs. Regarding Gore MEA, XP1 and XP2 lead to slightly different estimations for  $D_{\text{w,air}}^{\text{eff}}$  (Fig. II-24a): the values are comprised between  $6 \times 10^{-6} \text{ m}^2 \text{ s}^{-1}$  and  $9 \times 10^{-6} \text{ m}^2 \text{ s}^{-1}$ . XP1 assumes that the ratio between  $D_{\text{w,H}_2}^{\text{eff}}$  and  $D_{\text{w,air}}^{\text{eff}}$  is equal to 4.8. Consequently, one can observe that the estimation of  $D_{\text{w,H}_2}^{\text{eff}}$  (Fig. II-24b) is much higher by XP1 than by XP2. The latter allows an independent estimation of both gaseous coefficients and leads to a ratio in the order of 3 instead of 4.8. To explain this fact that the ratio of effective diffusion

coefficients is lower than the ratio of binary diffusion coefficients ( $3 < 4.8$ ), some hypotheses are formulated:

- In a porous medium, the diffusion of hydrogen is further slowed down compared with the diffusion of heavier molecules because of the Kramers-Kistemaker effect [135]: the microscopic velocity of hydrogen molecules being faster, they interact more with the wall and are slowed down more. This effect should not be confused with the "single component" Knudsen diffusion which does not depend on the pressure and is therefore included here in the diffusion coefficient in the sorbed phase  $D_M^{\text{eff}}$
- Darcy flow in the GDL plane due to the pressure drop along the channels results in a transfer resistance (decrease in transfer resistance compared to pure diffusion) that is not proportional to pressure, or not inversely proportional to the binary diffusion coefficient, or that depends on the viscosity of the carrier gas.

XP2 with N117 and NXL end up to the same conclusion, even though N117 experiments exhibit a higher deviation in the results because of the lower sensitivity to the gas phase diffusion.

Concerning the diffusion coefficient of water in the sorbed phase (Fig. II-24c), the general trend is that N117 has a higher diffusion coefficient than Gore and NXL membranes. This can originate from the different natures of those membranes (Gore and NXL are reinforced with ePTFE whereas N117 is only made out of PFSA) or from the interfacial sorption/desorption resistance and Knudsen resistance which have higher relative impact for a thin membrane. (Knudsen diffusion is included here not in the effective diffusion coefficient in the gas phase but in the adsorbed phase because it does not depend on the pressure). Nevertheless, Gore and NXL membranes are thinner than N117 and the actual transport resistance is still lower (6 times lower).

Estimated values are consistent with the compiled experimental data by Vetter and Schumacher [136], even though present values lay in the higher part of the range. The references cited above [73], [96], [103], [104] present values between  $10^{-10} \text{ m}^2 \text{ s}^{-1}$  and  $9 \times 10^{-10} \text{ m}^2 \text{ s}^{-1}$  for N117, which is perfectly consistent with the values estimated here for this kind of membranes. For reinforced type membranes (NR211), literature [102], [103] provides values between  $10^{-11} \text{ m}^2 \text{ s}^{-1}$  and  $10^{-10} \text{ m}^2 \text{ s}^{-1}$ . Here, diffusion

coefficients of Gore MEA are slightly higher, between  $10^{-10} \text{ m}^2 \text{ s}^{-1}$  and  $4 \times 10^{-10} \text{ m}^2 \text{ s}^{-1}$ . This difference can originate from the consideration of the gas diffusion mechanism.

The same slight decrease of  $D_M^{\text{eff}}$  with increasing  $\bar{r}_h$  is observed on all estimations, being due to the effectiveness of this parameter in the model, but at first order, the effective diffusion coefficients can be considered as independent of the averaged humidity, as long as liquid water is not present. Finally, the fact that we estimate an effective diffusion coefficient in the sorbed phase of the same order of magnitude whatever the thickness of the membrane and the presence or not of an electrode tends to confirm that the sorption/desorption resistance is not predominant.

Fig. II-25a to II-25c represents the comparison between estimated coefficients for the Gore membrane by XP1, depending on the value of  $\alpha$ . The theoretical value is  $\alpha = 4.8$  whereas XP2 estimations lead to  $\alpha = 3$ . Considering the latter, estimated gaseous coefficients are lower and membrane diffusion coefficients are. This modification induces values for the parameters that are consistent with XP2, as presented in Fig. II-25d to II-25f.

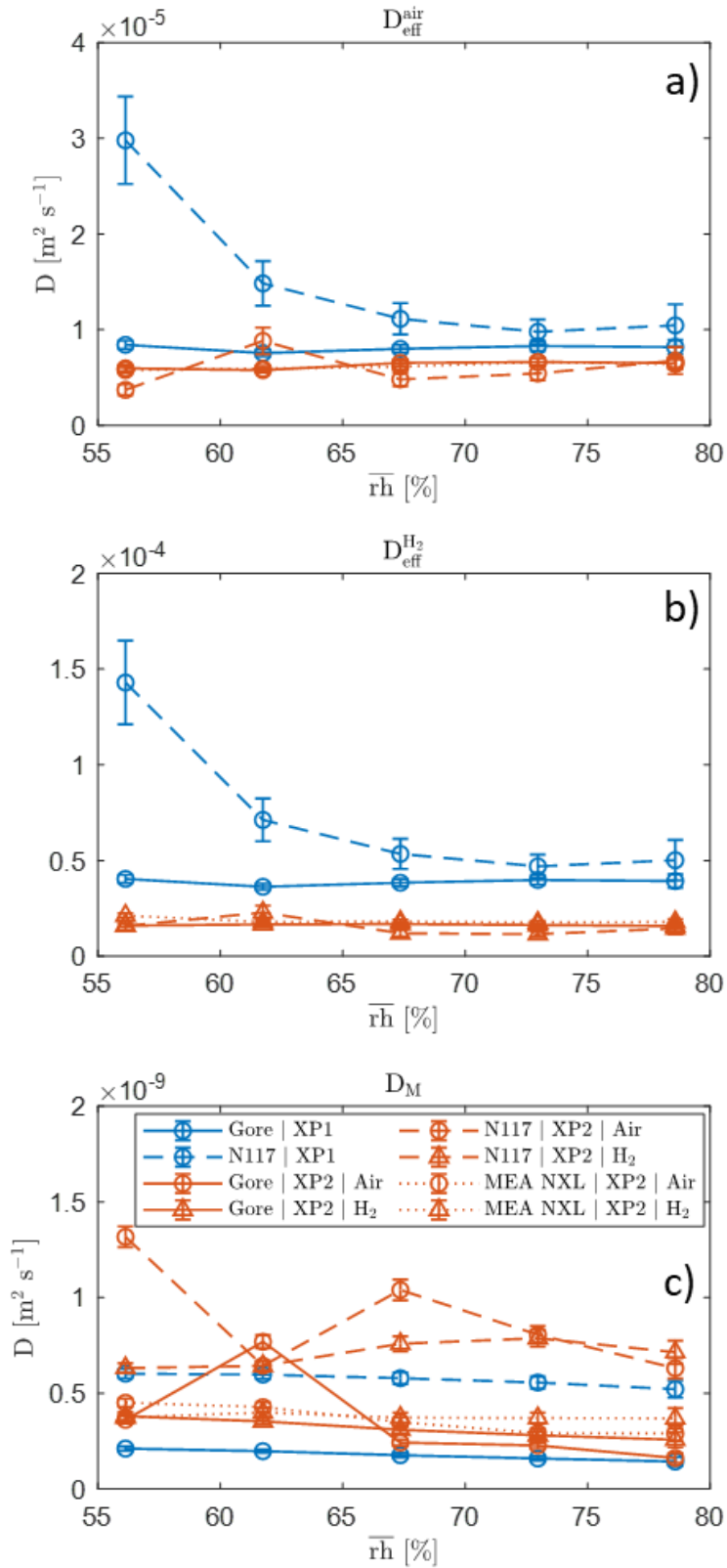


Figure II-24: Estimated parameters for all employed MEAs – only estimation based on negative fluxes are presented.

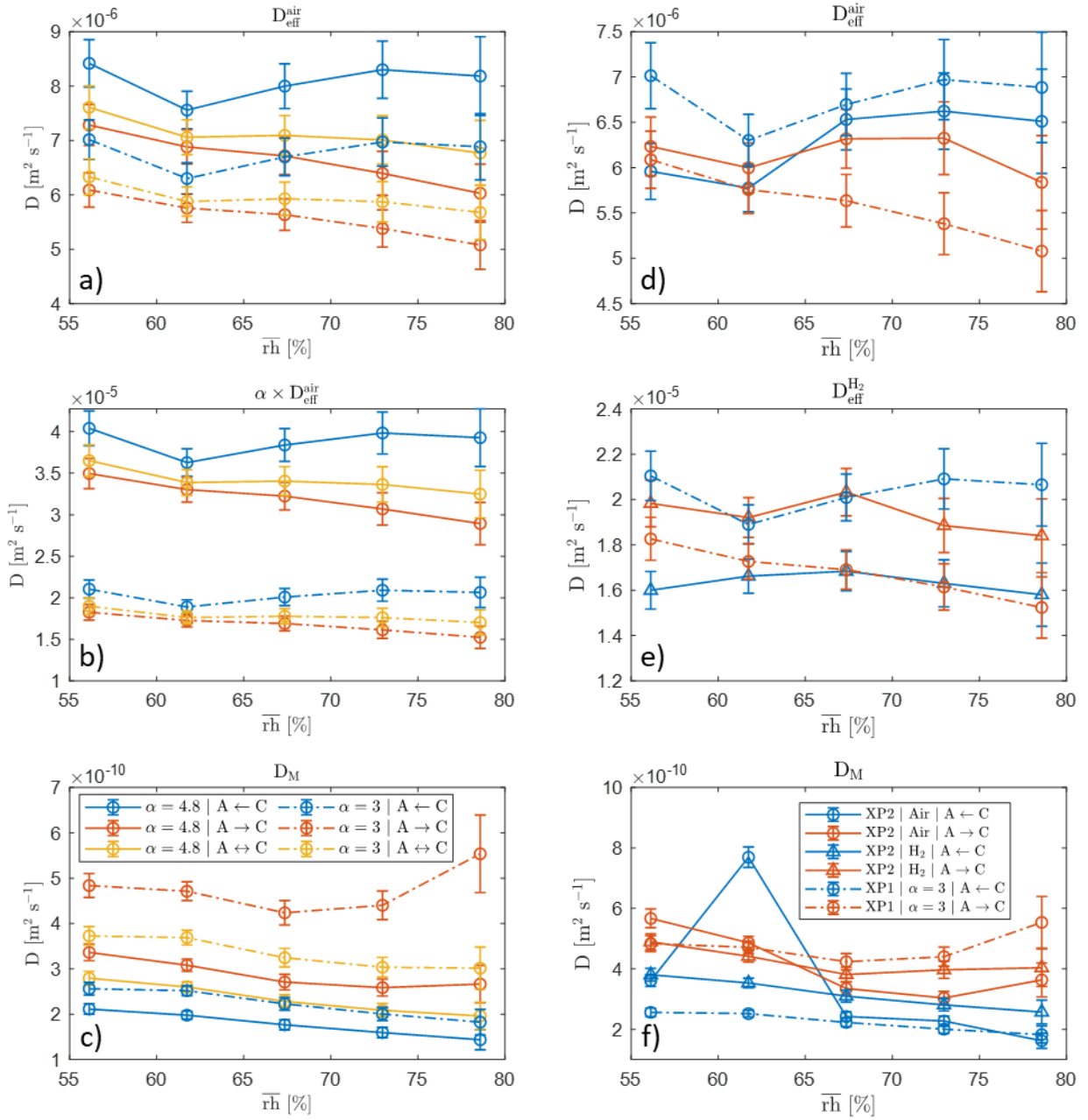


Figure II-25: Estimated parameters for Gore MEA by XP1 depending on the alpha value (a), (b), c)) and comparison between XP2 and XP1 with  $\alpha = 3$  (d), (e), f))

## IV – 5. Liquid sorption influence

The condensation experiments have been conducted with the N117 MEA in order to have the best sensitivity to the membrane transport. For the same reason, hydrogen

is employed to reduce the gas diffusion resistance. Experimental conditions for XP3 are reported in Table II-3.

Table II-3: Experimental conditions for XP3

$T_{pl}^a$	70 °C
$T_{pl}^c$	60 °C
$T_{hum,a}$	[60.1 ; 64.1 ; 66.1 ; 68 ; 68.6 ; 69] °C
$T_{hum,c}$	45 °C

For each  $T_{hum,a}$ , the associated through-plane water flux is measured on each side of the cell even though anode measurements are expected to be noisy due to water condensation. Fig. II-26 represents the water flux density as a function of the imposed  $\Delta C$  between the channels and three measurements are exposed (one for the anode and two for the cathode) since three sensors were available. The water fluxes are averaged during the last 1200 s of three hours constant working steps in order to reach (pseudo) steady-state and capture stochastic phenomena. Here, only  $T_{hum,a}$  varies and it thus responsible for  $\Delta C$  variations. The total transfer resistance is plotted in the inserted graph, being  $R_{tot} = \frac{\Delta C}{N_w}$ . This data splits into two groups of three points for low and high  $\Delta C$ . The transfer resistance is high for the three points at the lowest  $\Delta C$ : it lays between  $250 \text{ s m}^{-1}$  and  $340 \text{ s m}^{-1}$ . This variation is due to the increase in the total average relative humidity generated by the increase of  $T_{hum,a}$ . When the latter reaches  $68 \text{ °C}$  (the fourth point of the graph), a strong shift appears in the water flux as well as in the total transfer resistance. For the three highest  $\Delta C$ , the water flux is out of the trend suggested by the first three points. The associated transfer resistance decreases down to  $150 \text{ s m}^{-1}$  and does not vary with  $\Delta C$  (and thus with average humidity). This shift is attributed to a change in the membrane sorption, switching from vapor equilibrium to liquid equilibrium. This leads to a higher water content gradient through the membrane, possibly a higher average water content, and finally to higher water flux through the MEA. We propose here two models to take into account the Schroeder's paradox:

- 1- In a first step the effective diffusion coefficient in the adsorbed phase  $D_M^{eff}$  is estimated as before, without changing the sorption curve. The effective gas

diffusion coefficient of water vapor in hydrogen is assumed to be known:  $D_{w,H_2}^{\text{eff}} = 2 \times 10^{-5} \text{ m}^2 \text{ s}^{-1}$ . The estimated  $D_M^{\text{eff}}$  coefficient is plotted on Fig. II-27 in blue. We notice an increase of 38% of the effective diffusion coefficient to take into account the effect of the Schroeder paradox.

- 2- In a second step, the sorption curve is modified, changing only the water content for 100% RH: it is increased from 14 to 18. The estimated effective diffusion coefficient  $D_M^{\text{eff}}$  is plotted on Fig. II-27 in orange. It can be seen that the estimated values are similar to the values without condensation of liquid water. The effects of the Schroeder's paradox can therefore be modelled simply, without changing the effective diffusion coefficient in the adsorbed phase but considering a discontinuity in the sorption curve at  $rh = 100\%$ .

It has to be noted that for a saturated hot compartment, water content at the membrane interface is imposed and the gas phase diffusion in this side has no impact on the estimation.

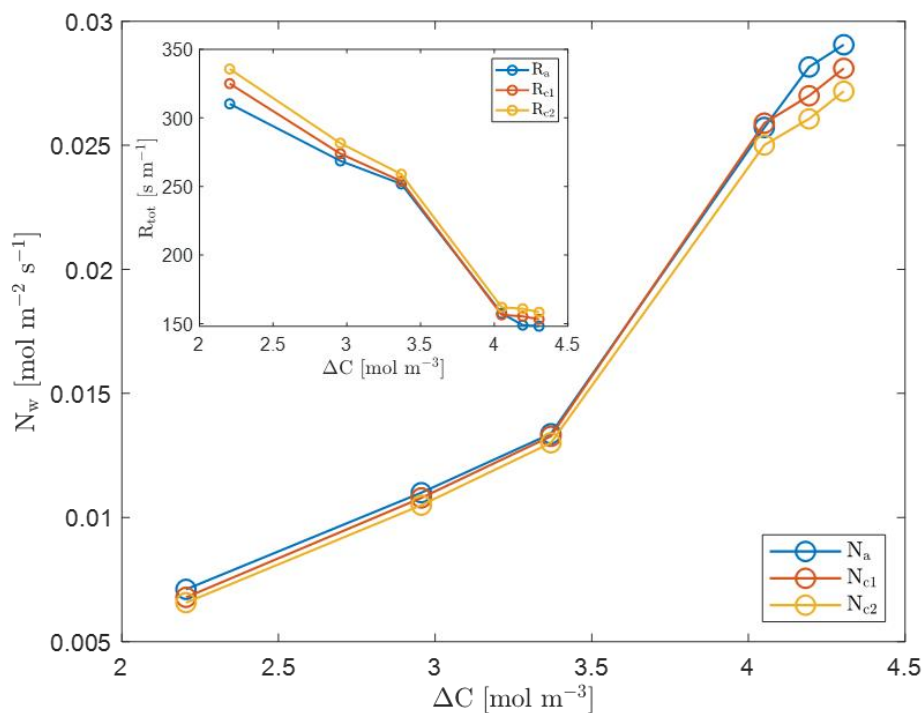


Figure II-26: Through-plane water flux density as a function of channels concentration difference and associated total transfer resistance

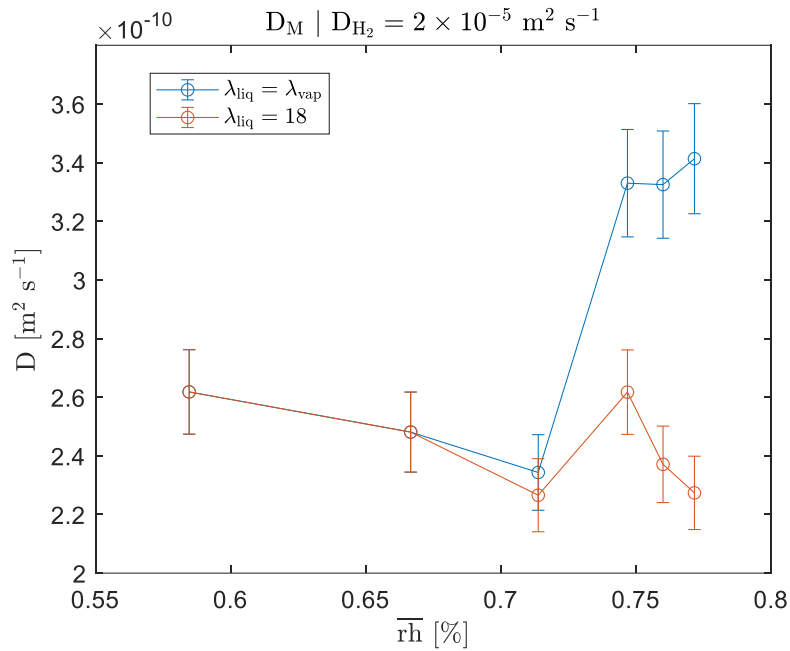


Figure II-27: Estimated effective diffusion coefficients through N117 membrane. In blue, the sorption curve used is the one measured for a vapor equilibrated membrane (the Schroeder paradox effect is taken into account by a higher effective diffusion coefficient). In red, the sorption curve is modified: the water content is fixed at 18 if the relative humidity is 100% - water content for lower  $rh < 100\%$  stay unchanged (the effect of the Schroeder paradox is considered by the modification of the sorption curve only)

## V – Conclusions and outlooks

In this chapter, a fundamental study of water transport in a fuel cell is conducted. The final goal being the development of a coupled model for heat and water transport, some parameters are to be estimated. In this way, a reduced order model is built to represent water transfer within a cell. This model only contains two parameters: the effective diffusion coefficient of water vapor in air or hydrogen, and the diffusion coefficient of adsorbed water in the MEA.

In order to properly estimate those parameters, special experiments are set up. The home built experimental bench allows an accurate control of experimental conditions such as inlet relative humidity, thanks to the usage of oversized membrane humidifiers. Humidity sensors, or dew point temperature sensors, make the calculation of through-plane water fluxes possible. By adjusting the exchange surface in the cell, a maximum sensitivity on observable data with regards to the parameters is reached. Then, two types of experiments are designed to estimate the parameters of interest. The

simulation of noised data and a hundred model inversions allow to provide the statistical uncertainty on the parameter estimations.

The first type of experiments (XP1) aims to decorrelate the two parameters by changing the gas species: water vapor diffusivity changes depending on the carrier gas. The reduced model contains two additional assumptions for these experiments:

- The diffusion coefficient in the MEA only depends on the average relative humidity of the cell and is thus independent of water concentration gradients or surrounding gas species,
- The ratio between the effective diffusion coefficients of water vapor in hydrogen and air is equal to the binary one, being 4.8.

Two MEAs are employed, inducing two different behaviors regarding the parameter sensitivity. Even though some differences are observed depending on the materials but also on the data set chosen for the estimation, the gas phase diffusion coefficients exhibit some consistent intervals.

The second type of experiments (XP2) provides the opportunity to decorrelate parameters by pressure variations. The gaseous diffusion coefficient varies inversely to the total pressure and the diffusion through the membrane is assumed pressure independent and only depends on the average relative humidity of the cell. Consequently, pressure variation provides the opportunity to discriminate between both contributions to the water transfer. The estimations are consistent with XP1 if one considers the most sensitive experiments: gas phase coefficient estimations with N117 show large deviation compared to those with Gore membrane. In addition, XP2 allows to evaluate the ration between gas phase diffusion coefficients: it is estimated to be on the order of 3 instead of 4.8. Taking this into account for XP1 shows large impact on gas phase diffusion coefficient estimations.

Gore and NXL membranes exhibit lower values for the diffusion coefficient than N117. This can originate from the PTFE reinforcement of Gore and NXL that weakens the transport properties of the membranes. The reinforced membranes are thinner than N117 and thus interfacial resistances can also have a higher relative impact on the total transport properties and lower the apparent diffusion coefficient. Finally, the

ionomer nature can have an impact, depending on the concentration of active sites (EW)

The last experiment aims to investigate the influence of liquid water sorption on the membrane transport properties. N117 is chosen to increase the sensitivity of the water flux to the membrane diffusion. By applying temperature difference between the plates and accurately control the inlet relative humidity of gases, water condensation is achieved within one electrode, leading to liquid water sorption of the membrane. An increase of the through-plane water flux is measured in such a case and is related to an increase of the diffusion coefficient, which is quantified with the developed model.

All the above-mentioned error bars are based on an absolute uncertainty of  $\pm 0.1$  °C on the dew point temperatures and 1% deviation on the gas flow rates. These deviations are the typical errors of the employed devices. Nevertheless, estimations revealed some discrepancies between each other, depending on the water flux direction for instance. Thus, uncertainty is probably underestimated and some non-considered error sources exist. As an example, the error measurement created by overheating is not considered as it depends on the gas species, the overheating temperature, the gas flow rate and the dew point temperature. Other errors can originate from the pressure losses measurement for instance.

## Appendix

Table II-4: Values of constant terms for the calculation of bulk diffusion coefficients in eq. II-26

[110]	Non-polar gas pairs (excluding He and H <sub>2</sub> )	Pair of H <sub>2</sub> O and non-polar gas
a	$2.745 \times 10^{-4}$	$3.640 \times 10^{-4}$
b	1.823	2.334

Table II-5: Data for the calculation of bulk diffusion coefficients in eq. II-26

Species	Molar mass (g/mol)	Molar diffusion volume (cm <sup>3</sup> ) [137]	Critical point pressure (atm)	Critical point temperature (K)
O <sub>2</sub>	32	16.3	49.77	154.4
N <sub>2</sub>	28	18.5	33.56	126
H <sub>2</sub> O	18	13.1	218.3	647.15
Air	29	19.7	37.2	132.5

Table II-6: Calculated bulk diffusion coefficients of water vapor in dioxygen, dinitrogen and air

T (K)	D <sub>w,i</sub> [111] (eq. II-27) ( $\times 10^{-5} \text{ m}^2\text{s}^{-1}$ )			D <sub>w,i</sub> [110] (eq. II-26) ( $\times 10^{-5} \text{ m}^2\text{s}^{-1}$ )		
	O <sub>2</sub>	N <sub>2</sub>	Air	O <sub>2</sub>	N <sub>2</sub>	Air
273	2.21	2.21	2.15	2.04	2.14	2.12
278	2.33	2.28	2.22	2.13	2.23	2.21
283	2.40	2.36	2.29	2.22	2.33	2.30
288	2.48	2.43	2.36	2.31	2.42	2.40
293	2.55	2.50	2.43	2.41	2.52	2.50
298	2.63	2.58	2.51	2.51	2.63	2.60
303	2.71	2.66	2.58	2.61	2.73	2.70
308	2.79	2.73	2.66	2.71	2.84	2.81
313	2.87	2.81	2.73	2.81	2.94	2.91
318	2.95	2.89	2.81	2.92	3.06	3.02
323	3.03	2.97	2.89	3.03	3.17	3.14
328	3.11	3.05	2.96	3.14	3.28	3.25
333	3.19	3.13	3.04	3.25	3.40	3.37
338	3.28	3.22	3.12	3.36	3.52	3.49
343	3.36	3.30	3.21	3.48	3.65	3.61
348	3.45	3.38	3.29	3.60	3.77	3.73
353	3.54	3.47	3.37	3.72	3.90	3.86

Table II-7: Experimental conditions and measurement for XP1 protocol with two CCMs

CCM	$\Delta C_w$ (mol m <sup>-3</sup> )		$\bar{r}h$ (%)		$n_w$ ( $\times 10^{-6}$ mol s <sup>-1</sup> cm <sup>-2</sup> )		$R_{1kHz}$ (m $\Omega$ cm <sup>2</sup> )		$rh_1^{in}$ (%)		$rh_2^{in}$ (%)		$rh_1^{out}$ (%)		$rh_2^{out}$ (%)	
	Air	H <sub>2</sub>	Air	H <sub>2</sub>	Air	H <sub>2</sub>	Air	H <sub>2</sub>	Air	H <sub>2</sub>	Air	H <sub>2</sub>	Air	H <sub>2</sub>	Air	H <sub>2</sub>
	Gore	-2.34	-2.24	55.99	57.12	-2.47	-4.15	154.45	71.87	36.55	37.33	76.55	77.17	50.46	52.97	62.62
-2.75		-2.68	56.24	57.19	-3.13	-5.13	154.84	72.04	32.99	33.64	80.35	80.49	49.88	51.94	63.96	64.42
-3.29		-3.16	56.44	57.30	-3.44	-6.34	154.54	71.72	29.17	29.82	83.81	84.19	48.12	50.62	66.77	66.59
-2.58		-2.49	61.54	62.66	-2.68	-5.03	135.78	63.49	40.38	41.18	83.70	84.51	55.24	57.73	69.16	69.44
-3.05		-2.97	61.86	62.78	-3.50	-6.21	135.95	63.44	36.53	37.21	87.89	88.20	54.45	56.63	70.98	71.29
-3.61		-3.49	62.03	62.91	-3.96	-7.56	135.77	63.12	32.44	33.06	91.74	92.12	52.66	55.18	73.72	73.70
-2.41		-2.33	66.96	67.94	-2.64	-4.84	120.66	56.94	47.71	48.45	87.61	88.34	60.91	63.12	74.15	74.38
-2.90		-2.80	67.27	68.06	-3.34	-6.10	120.62	56.90	43.68	44.41	91.97	92.14	60.05	62.09	76.15	76.18
-3.43		-3.34	67.45	68.24	-3.96	-7.46	120.48	56.57	39.43	40.10	95.97	96.37	58.72	60.86	78.36	78.57
-2.23		-2.19	72.33	73.21	-2.52	-4.86	107.69	51.45	54.86	55.60	91.59	92.37	66.72	68.40	78.95	79.50
-2.51		-2.42	72.55	73.24	-2.93	-5.48	107.87	51.62	52.72	53.54	94.05	94.26	66.19	67.91	80.22	80.28
-2.75		-2.69	72.61	73.30	-3.22	-6.12	108.16	51.49	50.64	51.26	95.98	96.37	65.69	67.35	81.01	81.31
N117	-1.58	-1.59	77.69	78.30	-1.85	-3.49	96.16	46.77	66.09	66.76	91.82	92.34	73.63	74.58	82.34	82.97
	-1.88	-1.82	77.86	78.36	-2.09	-4.16	96.30	47.03	63.96	64.73	94.21	94.35	72.86	74.13	83.70	83.69
	-2.12	-2.07	77.82	78.36	-2.44	-4.84	97.01	47.02	61.81	62.51	96.02	96.40	72.20	73.56	84.44	84.52
	-2.25	-2.24	55.47	56.19	-0.93	-1.06	854.94	596.68	37.14	36.93	76.76	76.99	50.71	51.89	60.54	61.42
	-2.68	-2.69	55.62	56.39	-1.13	-1.31	842.59	584.80	33.48	33.28	80.34	80.55	49.91	51.02	62.23	63.14
	-3.16	-3.18	55.73	56.64	-1.37	-1.65	831.23	573.65	29.66	29.52	84.06	84.49	48.65	49.87	64.30	65.46
	-2.51	-2.49	60.80	61.49	-1.12	-1.33	746.10	513.39	41.05	40.76	84.11	84.28	55.07	56.35	66.99	67.69
	-2.98	-2.98	60.97	61.70	-1.38	-1.67	734.60	503.17	37.09	36.82	87.96	88.16	54.16	55.37	68.91	69.64
	-3.51	-3.52	61.11	61.97	-1.66	-2.05	723.45	491.45	32.96	32.71	92.00	92.32	52.77	54.12	71.26	72.21
	-2.38	-2.36	65.91	66.56	-1.12	-1.37	663.45	450.61	48.43	47.98	88.05	88.23	59.92	61.23	72.01	72.52
	-2.87	-2.84	66.11	66.78	-1.42	-1.76	653.78	442.06	44.35	43.95	92.07	92.30	59.07	60.43	73.82	74.29
	-3.39	-3.40	66.24	67.21	-1.73	-2.20	643.54	431.46	40.00	39.64	96.26	97.01	57.91	59.47	76.05	76.69
-2.29	-2.27	70.92	71.51	-1.14	-1.42	594.44	398.85	55.64	55.08	92.07	92.28	64.51	65.76	77.06	77.43	
-2.53	-2.49	71.02	71.55	-1.29	-1.67	589.94	385.59	53.62	53.06	94.18	94.51	64.12	65.52	77.94	78.02	
-2.78	-2.84	71.08	72.24	-1.44	-1.95	584.43	387.84	51.40	50.88	96.33	97.78	63.64	65.19	78.87	79.36	
-1.74	-1.74	75.67	76.13	-0.88	-1.11	540.03	358.81	67.03	66.20	92.08	92.26	69.63	70.62	80.52	80.83	
-1.96	-1.98	75.76	76.34	-1.02	-1.30	537.13	349.08	64.18	65.00	94.21	94.52	69.32	70.45	81.25	81.71	
-2.22	-2.19	75.81	76.67	-1.16	-1.51	532.75	350.58	62.77	62.41	96.30	96.85	68.82	70.46	82.11	82.43	

Table II-8: Experimental conditions and measurements for XP2 protocol with two CCMs

CCM	$\Delta C_w$ (mol m <sup>-3</sup> )		$\bar{r}h$ (%)		$n_w$ ( $\times 10^{-6}$ mol s <sup>-1</sup> cm <sup>-2</sup> )		$R_{1kHz}$ (m $\Omega$ cm <sup>2</sup> )		$rh_1^{in}$ (%)		$rh_2^{in}$ (%)		$rh_1^{out}$ (%)		$rh_2^{out}$ (%)	
	Air	H <sub>2</sub>	Air	H <sub>2</sub>	Air	H <sub>2</sub>	Air	H <sub>2</sub>	Air	H <sub>2</sub>	Air	H <sub>2</sub>	Air	H <sub>2</sub>	Air	H <sub>2</sub>
	Gore	-2.70	-2.71	56.28	57.20	-2.55	-5.39	140.93	67.67	33.00	33.88	80.19	80.50	51.17	53.25	63.25
-2.69		-2.63	56.34	57.40	-2.30	-4.72	141.15	67.14	33.02	33.92	80.19	80.62	50.23	52.16	63.20	63.79
-2.68		-2.57	56.38	57.50	-2.04	-4.18	141.36	66.79	33.05	33.94	80.15	80.63	50.25	52.88	63.10	63.12
-2.68		-2.52	56.40	57.57	-1.85	-3.74	141.59	66.50	33.07	33.97	80.15	80.65	50.19	53.43	63.02	62.60
-2.67		-2.47	56.43	57.59	-1.70	-3.39	141.74	66.23	33.09	33.99	80.13	80.61	50.22	53.85	62.95	62.13
-2.89		-2.94	61.83	62.70	-3.06	-6.07	125.61	60.48	36.60	37.26	87.89	88.07	55.59	56.35	69.10	70.76
-2.89		-2.84	61.89	62.91	-2.73	-5.29	125.79	60.04	36.62	37.39	87.91	88.11	55.46	57.43	69.10	69.79
-2.89		-2.77	61.96	63.05	-2.40	-4.67	125.84	59.63	36.65	37.45	87.88	88.18	55.50	58.23	69.02	69.08
-2.88		-2.72	61.96	63.11	-2.14	-4.18	125.95	59.33	36.67	37.46	87.82	88.21	55.40	58.81	69.07	68.49
-2.88		-2.67	62.03	63.15	-1.98	-3.78	126.03	59.13	36.70	37.49	87.88	88.22	55.40	59.25	68.97	67.99
-2.80		-2.74	67.38	68.15	-2.93	-5.87	112.45	54.72	43.76	44.55	91.94	92.02	60.79	62.34	74.98	75.54
-2.82		-2.65	67.61	68.36	-2.57	-5.12	110.78	54.24	43.74	44.61	92.03	92.17	60.82	63.35	75.21	74.66
-2.79	-2.59	67.68	68.51	-2.29	-4.51	110.82	53.84	43.77	44.68	92.10	92.22	60.99	64.10	75.01	74.00	
-2.78	-2.53	67.73	68.63	-2.07	-4.03	110.89	53.53	43.79	44.75	92.10	92.30	61.08	64.69	74.86	73.49	
-2.77	-2.49	67.77	68.71	-1.90	-3.63	110.93	53.29	43.81	44.76	92.14	92.35	61.13	65.18	74.79	73.13	
-2.46	-2.36	72.93	73.60	-2.59	-5.22	100.92	49.84	52.86	53.74	94.25	94.38	66.81	68.65	79.91	79.80	
-2.44	-2.27	73.12	73.88	-2.30	-4.51	100.82	49.31	52.90	53.82	94.33	94.49	67.01	69.66	79.89	79.14	
-2.42	-2.21	73.19	74.05	-2.02	-3.95	100.85	48.90	52.95	53.87	94.25	94.51	67.13	70.39	79.75	78.62	
-2.39	-2.16	73.21	74.17	-1.84	-3.52	100.86	48.59	53.00	53.92	94.20	94.52	67.31	70.90	79.48	78.17	
-2.29	-2.12	73.91	74.28	-1.71	-3.17	98.05	48.31	53.93	53.95	94.41	94.55	68.82	71.35	79.39	77.84	
-1.84	-1.73	78.25	78.86	-1.94	-3.91	89.69	45.67	64.26	65.01	94.17	94.41	73.30	75.15	83.65	83.32	
-1.82	-1.66	78.48	79.21	-1.72	-3.35	89.38	45.11	64.28	65.10	94.26	94.47	73.62	76.10	83.65	82.94	
-1.80	-1.60	78.65	79.45	-1.51	-2.94	89.20	44.66	64.30	65.14	94.30	94.53	73.87	76.81	83.67	82.61	
-1.79	-1.56	78.77	79.60	-1.36	-2.62	89.08	44.32	64.32	65.18	94.33	94.56	74.06	77.31	83.67	82.34	
-1.77	-1.53	78.84	79.71	-1.25	-2.34	88.99	44.05	64.36	65.25	94.31	94.54	74.24	77.66	83.68	82.13	
-2.37	-2.30	55.50	56.54	-0.77	-0.87	734.49	555.31	32.73	32.76	79.48	79.43	52.94	55.47	58.78	59.72	
-2.39	-2.29	55.62	56.33	-0.73	-0.85	734.68	556.36	32.73	32.76	79.50	79.40	52.83	55.37	59.09	59.60	
-2.41	-2.31	55.69	56.33	-0.71	-0.85	735.13	556.96	32.73	32.75	79.53	79.45	52.68	55.09	59.36	59.74	
-2.40	-2.31	55.76	56.34	-0.66	-0.84	735.94	557.69	32.71	32.75	79.50	79.44	52.82	55.04	59.33	59.70	
-2.43	-2.31	55.81	56.35	-0.65	-0.83	736.38	557.96	32.69	32.76	79.52	79.45	52.48	54.98	59.77	59.72	
-2.67	-2.56	61.10	62.12	-0.95	-1.16	641.83	479.10	36.39	36.43	87.39	87.43	57.55	60.34	65.49	65.88	
-2.67	-2.56	61.16	62.13	-0.89	-1.13	643.16	479.49	36.36	36.43	87.35	87.43	57.45	60.20	65.59	65.84	
-2.66	-2.55	61.31	62.07	-0.86	-1.11	643.94	481.19	36.44	36.44	87.45	87.37	57.65	60.00	65.52	65.70	
-2.65	-2.55	61.39	62.17	-0.84	-1.10	644.50	480.81	36.44	36.48	87.48	87.51	57.75	60.08	65.50	65.75	
-2.65	-2.50	61.47	62.26	-0.82	-0.99	645.73	480.73	36.48	36.49	87.54	87.52	57.71	60.65	65.61	65.29	
-2.57	-2.47	66.23	67.25	-1.05	-1.26	574.44	421.80	43.45	43.52	91.40	91.42	62.36	64.97	70.64	71.32	
-2.56	-2.46	66.40	67.35	-0.99	-1.22	575.06	421.51	43.49	43.57	91.42	91.44	62.41	64.99	70.84	71.37	
-2.57	-2.44	66.51	67.41	-0.92	-1.18	575.43	421.13	43.45	43.49	91.39	91.41	62.44	65.19	71.06	71.27	
-2.56	-2.38	66.64	67.58	-0.88	-1.05	575.15	420.49	43								

# **Chapter III: Estimation of thermal resistance between plates and MEA**

<b>Introduction .....</b>	<b>113</b>
<b>I – Heat sources .....</b>	<b>113</b>
I – 1. Reversible losses .....	115
I – 2. Activation losses .....	115
I – 3. Joule effect.....	116
I – 4. Concentration losses .....	117
I – 5. Conclusions about heat sources.....	117
<b>II – Overview of heat transfer mechanisms and modelling.....</b>	<b>118</b>
II – 1. Conduction in GDLs.....	118
II – 2. Thermal contact resistances.....	119
II – 3. Conduction in the membrane.....	120
II – 4. Coupling between heat and water .....	121
<b>III – Estimation of the thermal resistance between MEA and plates .....</b>	<b>122</b>
III – 1. Principle .....	122
III – 2. Materials .....	126
III – 3. Results .....	127
III – 4. Comparison with literature .....	134
<b>IV – Conclusions and outlooks.....</b>	<b>135</b>

## Introduction

A standard PEM fuel cell in typical working conditions can exhibit an efficiency up to 60% [138]. Thus, a cell can produce about the same amount of electrical power in heat. The produced heat has to be evacuated from the cell by a cooling system [70] which usually consists of a cooling fluid inserted into the bipolar plates. The management of this heat is essential. An MEA temperature which is too high can lead to an increase of degradation rates [139] of the membrane and thus to a decrease of durability and performances. Also, temperature homogeneity over the entire active surface area is an important issue [140]. Temperature heterogeneities cause hot spots that are deleterious for the materials and cold spots where liquid water can accumulate, thus decreasing performances [141].

The thermal conductivity of the GDL is one of the main parameters for heat management in an assembly since heat is removed by conduction from the MEA towards the plates [142]. The GDL being a porous media made out of carbon fibers, its thermal conductivity depends on many factors (morphology and porosity for instance) and is highly anisotropic [112]. Therefore, effective thermal conductivity is commonly employed in heat transfer modeling. It contains the effect of the GDL morphology, the compression and the liquid saturation. In addition, this conductivity is defined as one-dimensional and thus incorporates the 2-D effects since the contact between the GDLs and the plates is not made on the entire surface. Finally, as it is the case in this work, contact resistances between GDL and plates are usually integrated in the effective thermal conductivity. Hence, the estimated values are only valid for the employed materials and geometry

## I – Heat sources

Power conversion by fuel cell suffers from several losses, as described in Chapter I. These reversible or irreversible losses decrease the efficiency of the cell and create heat. For typical working conditions where the electrical efficiency is 50%, the same amount of heat power than electric power is produced and has to be evacuated from the cell or stack. Since the cell temperature needs to be controlled to prevent any damage on the materials, such as the membrane, heat management is of high

importance. Moreover, its close link with water management make it crucial for the global durability of the cells and the systems.

The total energy that dihydrogen  $H_2$  can produce at 298 K is related to the standard enthalpy of reaction  $\Delta_r H$ , depending on whether the water is produced in liquid or gaseous form:



If all this energy could contribute to the production of electricity, a theoretical voltage  $E^{TH}$  could be defined as:

$$E^{TH} = \frac{\Delta_r H_{298K}}{2F} \quad (\text{III-1})$$

This voltage would then be  $E_l^{TH} = 1.48 \text{ V}$  in the case of a liquid water production and  $E_g^{TH} = 1.25 \text{ V}$  in the case of vapor. Nevertheless, due to multiple losses during the operation of the cell, the actual voltage  $U$  is always lower than  $E^{TH}$ . Consequently, the total heat production of the cell  $Q_{heat}$  is obtained by subtracting the electrical power  $I \times U$  to the chemical power  $I \times E^{TH}$  [24]:

$$Q_{heat} = I \times (E^{TH} - U) \quad (\text{III-2})$$

An analog way to compute this is to directly consider the standard enthalpy of reaction. This value is more commonly employed as a Lower Heating Value (or Higher Heating Value) in the case of water produced in vapor form (or liquid form, respectively) and expressed in  $\text{J kg}^{-1}$ . This leads to the following expression for  $Q_{heat}$ :

$$\begin{aligned} Q_{heat,g} &= I \left( \frac{LHV \times M_{H_2}}{2F} - U \right) \\ Q_{heat,l} &= I \left( \frac{HHV \times M_{H_2}}{2F} - U \right) \end{aligned} \quad (\text{III-3})$$

Here,  $M_{H_2}$  represents the molar mass of hydrogen. These calculations provide the total heat power which is produced within the cell (or the stack) without considering any location. However, this global amount of heat originates from different losses

throughout the cell and the location of each heat source is different. In order to achieve accurate modelling of heat (and related transport mechanisms), the distinction between all contributions can be necessary. The next description is organized following the main regions of a polarization curve: reversible, activation, ohmic and concentration losses. Finally, some coupled water and heat transfers are described.

## I – 1. Reversible losses

The difference between the theoretical voltage  $E_{th}$  and the reversible voltage  $E^0$  lays in the difference between the hydrogen enthalpy and Gibbs energy. Only the latter can be converted into electricity and the remaining part is dissipated as heat. This contribution is expressed with the entropy variation  $\Delta S_{rev}^{tot}$  [41]:

$$q_{th} = \Delta G^{tot}(T, P) - \Delta H^{tot}(T, P) = -T\Delta S_{rev}^{tot}(T, P) \quad (III-4)$$

Here,  $q$  is a molar energy ( $J \text{ mol}^{-1}$ ). The associated heat power  $Q_{th}$  is:

$$Q_{th} = \frac{I}{2F} q_{th} \quad (III-5)$$

This heat source is attributed to the electrodes but the rigorous distribution between both is difficult to establish.

## I – 2. Activation losses

Irreversibilities due to the reactions create losses denoted as activation losses. Each electrode (superscript  $i$ ) contributes to these losses which dominate the polarization curve at low current densities.

$$q_{act}^i = -T\Delta S_{irr}^i(T, P) \quad (III-6)$$

The associated overpotential  $\eta_{act}^i = -q_{act}^i/2F$  is described by electrochemical models (see Chapter I) and allow to expressed the activation related heat release:

$$Q_{act}^i = \eta_{act}^i \times I \quad (III-7)$$

These heat sources are located in the electrodes.

## I – 3. Joule effect

### I – 3.1. Protonic resistance

The non-ideal proton conductivity  $\sigma$  of the membrane leads to Joule effect in the passage of protons. The proton conductivity highly depends on the water content of the membrane and the temperature. Many correlations are suggested in the literature [36]. Consequently, a water content profile  $\lambda(z)$  in the thickness of the membrane leads to a proton conductivity profile  $\sigma(\lambda(z))$  and the protonic resistivity of the membrane  $r_M$  ( $\Omega$  m) is expressed as the inverse of the conductivity:

$$r_M(z) = \frac{1}{\sigma(\lambda(z), T)} \quad (\text{III-8})$$

Therefore, the volumetric heat source  $Q_M'''$  ( $\text{W m}^{-3}$ ) is expressed as Joule effect and is non-uniformly distributed within the membrane thickness:

$$Q_M'''(z) = r_M(z) \times i^2 \quad (\text{III-9})$$

Dickinson and Smith [143] gathered values for the water content dependent protonic conductivity of Nafion membranes. At 80 °C, the highest protonic conductivity reaches values around  $25 \text{ S m}^{-1}$  and tends to  $0 \text{ S m}^{-1}$  for low water content. Considering an intermediate value, a 50- $\mu\text{m}$  thick membrane creates a protonic resistance of  $R_{H^+} = 40 \text{ m}\Omega \text{ cm}^2$ .

### I – 3.2. Electronic resistance

The effective electronic conductivity of GDLs depends on several parameters such as the fibers structures, the compression, the initial porosity or the PTFE content for example. Through-plane electronic conductivity values found in the literature [144], [145] spread within large range from  $300 \text{ S m}^{-1}$  to  $1400 \text{ S m}^{-1}$  for experimental measurements and even up to  $3 \times 10^4 \text{ S m}^{-1}$  for Bruggeman correlation. These variations are attributed to calculation methods and compression level during experiments. The electrical resistance created by a  $200 \times 10^{-6} \text{ m}$  thick GDL with an electronic conductivity of  $300 \text{ S m}^{-1}$  is  $R_e^{\text{GDL}} = 6.7 \text{ m}\Omega \text{ cm}^2$ , which is one order of magnitude lower than  $R_{H^+}$ .

Contact resistances exist between each layers of the cell and add to the total electronic resistance. The contact resistance between the CLs and the GDLs is often neglected since both layers are porous materials, leading to a negligible contact resistance. The main contact resistance is between the GDLs and the bipolar plates and is lower than  $10 \text{ m}\Omega \text{ cm}^2$  [146]. This resistance depends on the GDL properties such as porosity, structure, compression but also on the plates (surface, roughness) [147]. To decrease the contact resistance, an increase in the clamping pressure is desirable, but is at the expense of the GDL gas diffusivity. Some surface treatments or coatings are also to decrease the contact resistance between GDL and bipolar plates [148].

### I – 4. Concentration losses

The concentration losses become the dominant part in the polarization curve for high currents. After the linear part due to ohmic losses, the voltage drops more rapidly with the current until reaching a limit current for which the voltage drops to zero. The concentration overvoltage is denoted  $\eta_{conc}$  and the associated heat production  $Q_{conc}$  can be attributed to the electrodes.

$$Q_{conc} = \eta_{conc} \times I \quad \text{(III-10)}$$

### I – 5. Conclusions about heat sources

Ramousse et al. [41] provide a quantitative comparison between activation losses, reversible losses associated with water desorption and Joule effect, which are the three main heat sources of a fuel cell. It is observed that activations losses dominate for all current densities up to  $1 \text{ A cm}^{-2}$ . Joule effect is negligible for small currents and strongly increases with it. Reversible losses are higher than Joule effect for small currents. This model neglects water condensation or vaporization in the cell and concentration losses are not considered.

As it has been shown previously, heat production from Joule effect is dominated by the protonic resistance in the membrane. Considering also that the activation losses are localized in the electrodes, the total heat produced in the cell is assumed to be located within the MEA. In order to develop a reduced order model that considers a uniform and isothermal MEA, it is reasonable to compute this total heat production by the

measurement of the cell voltage, without distinction between sources, and to locate this production within the MEA.

## II – Overview of heat transfer mechanisms and modelling

### II – 1. Conduction in GDLs

The effective thermal conductivity of the GDL is of high importance to properly model heat transfer between the MEA and the bipolar plates. Experimental values in the literature [65], [149]–[151] spread in a large range, depending on the measurement conditions such as *in* or *ex-situ*, compression or water saturation of the GDL for example. The wide variety of materials (MPL or not, carbon fibers configuration, binder, porosity, fibers and pores diameters, ...) extends the range of value even further.

Burheim et al. [92] measured thermal conductivity of GDL as a function of compaction pressure and liquid water saturation. For dry GDL, the thermal conductivity is comprised between 0.27 and 0.4 W K<sup>-1</sup> m<sup>-1</sup>, depending on the compaction level. 26% saturated GDL exhibit higher thermal conductivities due to the presence of liquid water within the pores: from 0.45 to 0.57 W K<sup>-1</sup> m<sup>-1</sup>. Chowdhury et al. [152] investigated the impact of a non-homogeneous compression of the GDL on the thermal conductivity and end up to values between 0.5 and 2 W K<sup>-1</sup> m<sup>-1</sup>. Karimi et al. [149] measured effective thermal conductivities of GDL with varying PTFE loading and end up to values between 0.25 and 0.7 W K<sup>-1</sup> m<sup>-1</sup>. Thomas et al. [65] inserted platinum wires between CLs and GDLs to measure the MEA temperature. By coupling this with heat flux measurement, the effective thermal conductivity of the GDL was estimated to be 0.25 W K<sup>-1</sup> m<sup>-1</sup>. Bock et al. [153] extensively studied the influence of the MPL on the GDL effective thermal conductivity. Depending on the compaction, Toray papers (straight random fibers) exhibit effective thermal conductivity between 0.2 and 0.7 W K<sup>-1</sup> m<sup>-1</sup> while the Freudenberg (felt-like fibers) one is comprised between 0.11 and 0.16 W K<sup>-1</sup> m<sup>-1</sup>. Ramousse et al. [154] adopted both analytical and experimental approach to determine effective thermal conductivity and concluded that experimental estimations are still the most efficient way given the numerous parameters and the

anisotropy of the materials. Experimental measurements led to effective thermal conductivity between 0.2 and 1.36 W K<sup>-1</sup> m<sup>-1</sup> considering experimental deviation.

Conduction being the dominating heat transfer mechanism, the heat flux density  $\phi_{GDL}$  from the MEA towards bipolar plates is modelled following Fourier's law:

$$\phi_{GDL} = -\kappa_{eff}\nabla T \quad (III-11)$$

When no heat source is considered within the GDL (in the case of no water condensation or vaporization for instance), the temperature profile through the GDL is linear and a conduction thermal resistance  $R_{th}^{GDL}$  is usually defined:

$$R_{th}^{GDL} = \frac{t_{GDL}}{\kappa_{eff}} \quad (III-12)$$

With  $t_{GDL}$  being the thickness of the GDL. The effective thermal conductivity contains several contributions:

- 2D effects: heat pathways are longer from the electrodes to the plates for areas under the channels;
- Structure: heat is transferred by the carbon fibers and the conduction path is consequently longer than the thickness of the GDL, depending on the GDL structure;
- Liquid saturation: liquid water having a higher thermal conductivity than air, a saturated GDL has a higher effective thermal conductivity;
- Contact resistances: depending on the measurement procedure, contact resistance between GDL and bipolar plate can be included into the conduction thermal resistance and the resulting effective thermal conduction contains this contribution.

## II – 2. Thermal contact resistances

In the same way as electronic contact resistances, thermal contact resistances exist between layers of the cell. It is globally assumed that the thermal contact resistance between two porous media is negligible due to the same structure of both layers (ref)

and that the main thermal contact resistance in a fuel cell is between the GDL and the bipolar plates. This originates from two causes:

- The contact is between a porous material and a flat surface;
- The contact only occurs with the lands of the plate, reducing the total contact surface.

The measurement of such a resistance is a challenging task because it has to be discriminated from the conductive resistance within the GDL. Both contributions highly depend on the compression of the GDL: the contact resistance is expected to decrease with compression as well as bulk resistance due to a decrease of the porosity.

Karimi et al. [149] estimated the contact resistance between a GDL and a flat surface to be between 1 and  $4 \times 10^{-4} \text{ m}^2 \text{ K W}^{-1}$ , depending on the compression load. By using bipolar plates with realistic channels, Chowdhury et al. [152] measured the thermal contact resistance and end up to the same interval. As a comparison, a 200  $\mu\text{m}$  thick GDL with a thermal conductivity of  $\kappa = 0.5 \text{ W K}^{-1} \text{ m}^{-1}$  creates a conduction resistance of  $R_{\text{th}}^{\text{GDL}} = 4 \times 10^{-4} \text{ m}^2 \text{ K W}^{-1}$  which as the same order of magnitude than the contact resistance.

## II – 3. Conduction in the membrane

Burheim et al. [92] measured thermal conductivity of Nafion as a function of water content and compression. The measured conductivities are between 0.185 and 0.254  $\text{W K}^{-1} \text{ m}^{-1}$ . On their side, Khandelwal and Mench [155] observed that thermal conductivity of Nafion is a slight decreasing function of temperature – between  $0.16 \pm 0.03 \text{ W K}^{-1} \text{ m}^{-1}$  at room temperature and  $0.13 \pm 0.02 \text{ W K}^{-1} \text{ m}^{-1}$  at 65 °C for dry Nafion – and an increasing function of relative humidity – up to 0.3  $\text{W K}^{-1} \text{ m}^{-1}$  at 65 °C and 100% rh.

Thomas et al. [65] measured the temperature at the membrane interface with platinum wires and observed that a current density of  $i = 1.5 \text{ A cm}^{-2}$  causes negligible temperature difference within a 30- $\mu\text{m}$ -thick membrane. On the modeling side, Wang et al. [156] published a complete model where it can be seen that, for  $i = 2.2 \text{ A cm}^{-2}$  at  $U = 0.35 \text{ V}$ , the temperature difference between the 18- $\mu\text{m}$ -thick membrane interfaces

is less than 1 °C. Weber and Newman [79] showed, by modelling, that a 50- $\mu\text{m}$ -thick membrane could experience a temperature difference up to 3 °C between its interfaces at a 0.2 V cell voltage.

Membranes being increasingly thin, the thermal resistance tends to decrease as well as temperature differences within it. One way to simplify modelling and to reduce model order is to consider that the membrane and the electrodes (MEA) have a uniform temperature and thus to neglect thermal effects.

## II – 4. Coupling between heat and water

### II – 4.1. Heat-pipe effect

While the first reduced order models of water transfer were isothermal [73], [74], more complete models have considered the coupling between water and heat transfer. Among them, the model of Wang and Wang [78] is one of the first to describe the importance of heat transfer upon water transfer: the temperature field within the cell has a major impact on the vapor phase diffusion of water. Weber and Newman [79] highlighted the existence of the so-called heat-pipe effect, referring to a coupled transfer of heat and water due to the temperature field: water evaporates close to the CLs, diffuses through the GDL and condenses towards the gas channels. This water transfer is associated to heat transfer since evaporation/condensation is endo/exothermic. This phenomenon appears especially when gases in channels are saturated. In this case, partial pressure of water vapor is equal to the saturation pressure  $P_{\text{sat}}(T)$  within the whole GDL and the only driving force for vapor flux is the temperature gradient [157]. Fick's law is written for saturated water vapor:

$$N_w = -\frac{D_w}{R} \nabla \left( \frac{P_{\text{sat}}(T)}{T} \right) \quad (\text{III-13})$$

This relation highlights that even for saturated gases, when a temperature field exists, a water vapor flux is triggered from hot towards cold regions. This has been experimentally validated [65], [157]–[159].

This phenomenon highly depends on the temperature field through the GDL.

## II – 4.2. Evaporation/condensation

When the partial pressure of water vapor reaches the saturation pressure, water condenses. This condensation is associated with a heat release, being equal to the latent heat  $L_v = 41.6 \text{ kJ mol}^{-1}$ . On the opposite, when partial pressure is lower than the equilibrium pressure, being the saturation pressure, liquid water evaporates and heat is adsorbed. Knowing the molar flux of water that condenses or evaporates  $n_{c-e}$  leads to the expression of the released or adsorbed heat:

$$Q_{c-e} = \pm n_{c-e} L_v \quad (\text{III-14})$$

## II – 4.3. Sorption/desorption

At the ionomer interfaces, water is adsorbed (or desorbed) from vapor phase (or liquid phase) which creates heat source (or sink). The associated enthalpy variation  $\Delta H_{\text{sorp}}$  is close to the latent heat of water  $L_v = 41.6 \text{ kJ mol}^{-1}$  but some experimental measurements exhibit values, depending on the temperature, between 45 and 52  $\text{kJ mol}^{-1}$  [41].

# III – Estimation of the thermal resistance between MEA and plates

## III – 1. Principle

The thermal resistance between the MEA and a plate can be estimated considering that heat is mainly transported by conduction through the GDL [65]. Heat flux  $\phi_{\text{GDL}}$ , thermal resistance  $R_{\text{th}}$ , MEA temperature  $T_M$  and plates temperatures  $T_{\text{pl}}^{a,c}$  are linked by the following expression:

$$R_{\text{th}} = \frac{|T_M - T_{\text{pl}}^{a,c}|}{\phi_{\text{GDL}}} \quad (\text{III-15})$$

In order to estimate  $R_{\text{th}}$ , one need to measure the heat flux through the GDL and the temperature difference between MEA and plates.

In a fuel cell, the total produced heat flux is given by subtracting the output electric power to the chemical power provided to the cell:

$$\phi_{tot} = i \times S_{MEA} \left( LHV \frac{M_{H_2}}{2F} - U \right) \quad (III-16)$$

With  $i$ ,  $S_{MEA}$ ,  $LHV$ ,  $M_{H_2}$ ,  $F$  and  $U$  being respectively the current density ( $A\ cm^{-2}$ ), the surface area of the MEA ( $cm^2$ ), the hydrogen Low Heating Value ( $J\ kg^{-1}$ ), the molar mass of hydrogen ( $kg\ mol^{-1}$ ), the Faraday constant ( $96485\ C\ mol^{-1}$ ) and the output voltage (V).

Under usual working conditions,  $\phi_{tot}$  is split into two contributions  $\phi_{GDLa}$  and  $\phi_{GDLc}$  and is evacuated toward both plates with different ratios depending on plates temperatures, thermal resistances of GDL, localization of the heat sources, flow fields design or contact resistances for instance.

Heat flux through the GDL  $\phi_{GDL}$  has to be well known to give an accurate estimation of the thermal resistance. Thus, the cell has to be operated in order to cancel one of the two contributions  $\phi_{GDL}^a$  or  $\phi_{GDL}^c$ , to assure that the total flux  $\phi_{tot}$  is exclusively evacuated through one GDL. One way to achieve this is to find operating conditions leading to temperature difference of zero between anode or cathode plates and MEA:

$$T_M - T_{pl}^{a,c} = 0 \Rightarrow \phi_{GDL}^{a,c} = 0 \quad (III-17)$$

Hence, the cell is operated by imposing a temperature difference between the two plates, the hot side being the zero-flux side and the cold one the total-flux side. To verify Eq. III-17,  $T_M$  is increased by increasing the current density, until it equals the temperature of the hot plate (Fig. III-1).

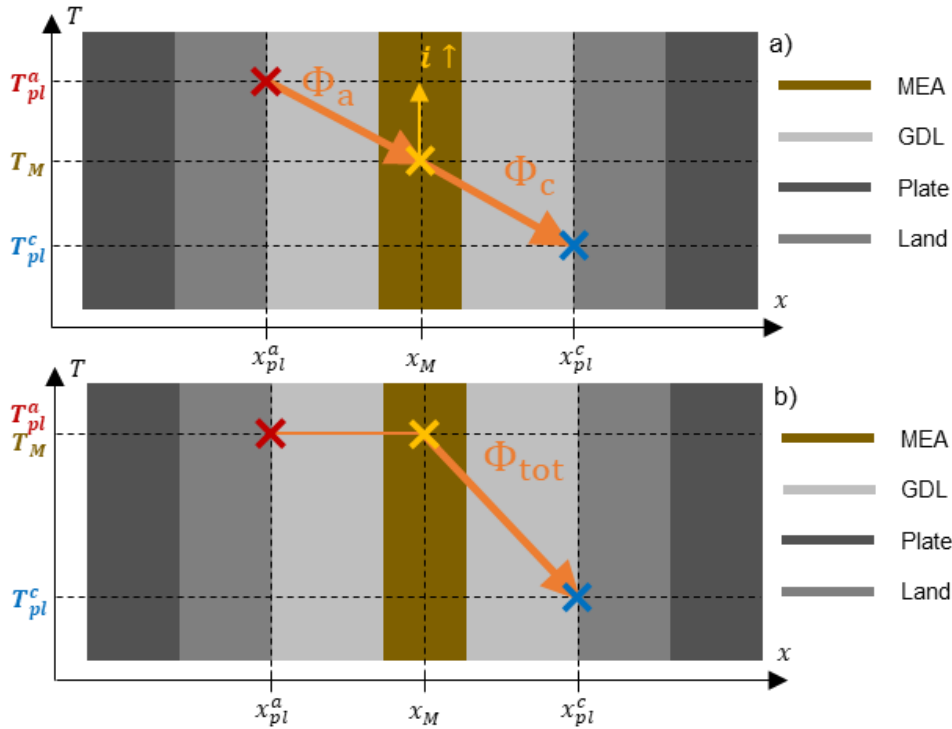


Figure III-1: Measurement principle of the thermal resistance on a simplified cell schematic in “hot anode/cold cathode” configuration. a)  $T_{pl}^a > T_M > T_{pl}^c$ .  $T_M$  is increased by increasing current until b)  $T_{pl}^a = T_M > T_{pl}^c$ . The total flux  $\phi_{tot}$  is evacuated through cathode GDL

From an experimental point of view, the difficulty is to determine when the MEA is at the same temperature as the hot plate, and even more so without temperature sensor near the MEA or heat flux sensors. The solution is based on the link between water vapor flux and temperature gradient, causing a gradient of saturation vapor pressure within the GDL. The diffusive vapor flux density through the GDL  $N_w$  is expressed with the Fick’s law and ideal gas law.

$$N_w(x) = -D_{GDL}^{eff} \nabla C_w(x) = -\frac{D_{GDL}^{eff}}{R} \nabla \left( \frac{P_w(x)}{T(x)} \right) \quad (III-18)$$

Where  $D_{GDL}^{eff}$  ( $m^2 s^{-1}$ ) is the effective diffusion coefficient of water vapor in the GDL, considering porosity and saturation of the porous structure,  $C_w$  ( $mol m^{-3}$ ) the concentration of vapor,  $R$  the universal gas constant,  $T$  (K) the temperature and  $P_w$  (Pa) the vapor partial pressure.

By assuming that the GDL pores contain liquid water, which is the case for most of the working conditions in a fuel cell [160] and moreover when inlet gases are fully

humidified, the partial pressure of water vapor is equal the saturation pressure  $P_{sat}(T)$  and the vapor concentration profile only depends on the temperature profile.

$$N_w(x) = -\frac{D_{GDL}^{eff}}{R} \nabla \left( \frac{P_{sat}(T(x))}{T(x)} \right) \quad (III-19)$$

Therefore, when the measurement of the water flux crossing the GDL is zero, one can consider that the GDL is isothermal and so the MEA is at the same temperature than the plate.

$$N_w(x) = 0 \Rightarrow \nabla \left( \frac{P_{sat}(T(x))}{T(x)} \right) = 0 \Rightarrow T(x) = T_{pl}^{a,c} \quad (III-20)$$

Where  $x_{pl}$  denotes the GDL/plate interface coordinate. The last implication is valid since  $P_{sat}(T(x))/T(x)$  is a monotonic function of  $x$  for a linear profile of temperature.

Then, the thermal resistance  $R_{th}$  can be calculated by using the plates temperatures  $T_{pl}^a$  and  $T_{pl}^c$ , the voltage of the cell  $U$  and the current density  $i$  for which the water vapor flux through the hot GDL is null.

$$R_{th} = \frac{T_{pl}^{hot} - T_{pl}^{cold}}{\phi_{tot}} \quad (III-21)$$

An effective one-dimensional thermal conductivity can also be defined by using a 1D expression:

$$\kappa^{eff} = \frac{t_{GDL}}{R_{th}S} \quad (III-22)$$

Where  $e_{GDL}$  (m) is the thickness of the compressed GDL. In this work,  $t_{GDL}$  is equal to the total thickness of the gaskets used in the assembly, i.e.  $t_{GDL} = 173 \mu\text{m}$ .

Two configurations can be used to estimate the thermal resistance. The first one is the “hot anode/cold cathode” configuration, as presented in Fig. III-1. Here, a higher temperature is imposed on the anode plate than on the cathode plate and water balance of the anode is computed. The current density is increased until reaching the target point of no water flux through anode GDL, meaning that  $T_{pl}^a = T_M$ . The second configuration is the opposite one: “cold anode/hot cathode”. Here, the thermal gradient

is inverted and the cathode water balance is computed in order to catch the current density value cancelling water flux through cathode GDL and giving  $T_{pl}^C = T_M$ .

### III – 2. Materials

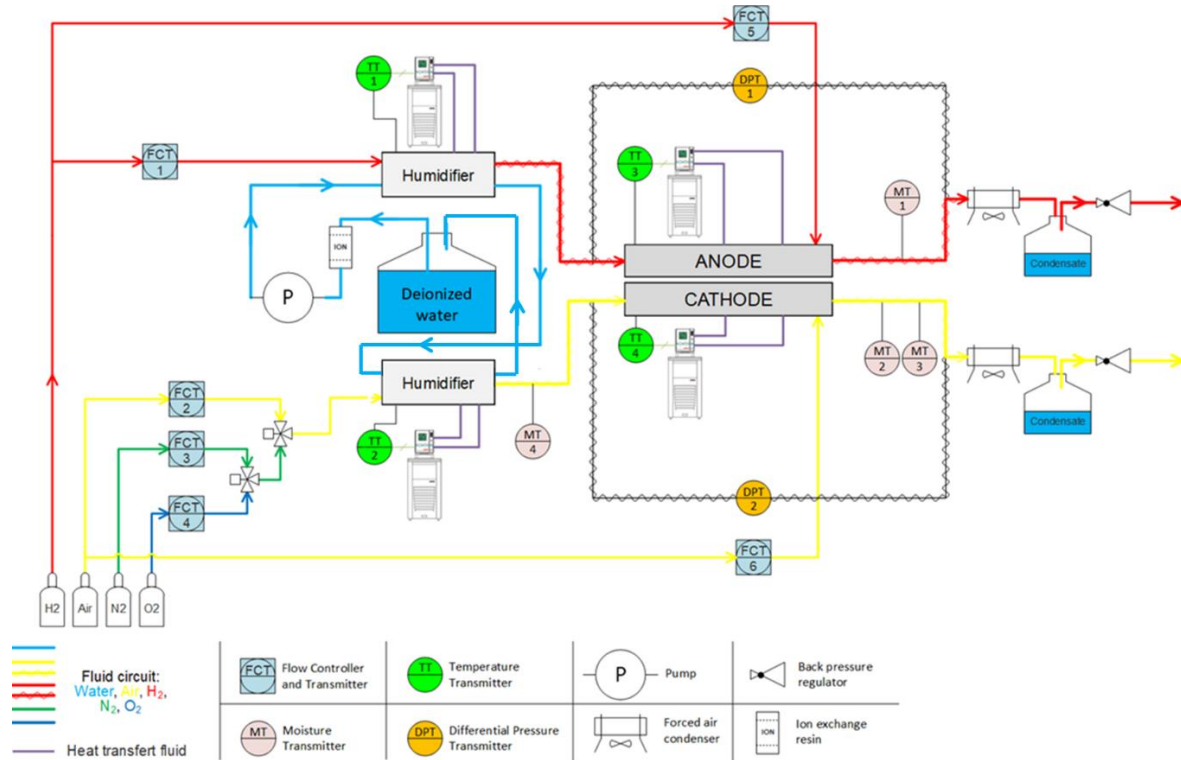


Figure III-2: Schematic of the experimental bench

The experimental bench (Fig. III-2) for the present experiments is similar to the bench presented in Chapter II. Here, the main difference is that gas lines are added toward the cell outlets. Indeed, the cell plates (Fig. III-3) benefit from a special feature which is a special gas inlet close to classical gas outlet of the manifold. This feature allows (i) to dilute an eventual excessively wet gas with the addition of dry gas in order to prevent any measurement issue and (ii) to evaporate liquid water droplet that exit the channels and lay in the manifold. The latter improves the removal of water from the cell and consequently improves water fluxes calculation.

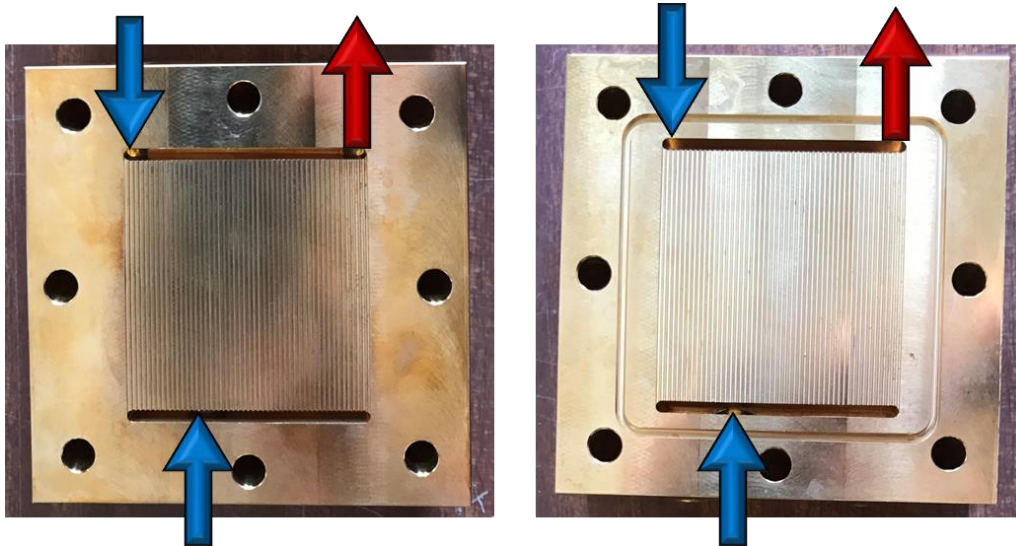


Figure III-3: Cell plates. Blue (and red) arrows represents the gas inlets (and outlets, respectively)

The MEA employed for these experiments has been purchased to Johnson Matthey. It is based on a three-layer membrane with a thickness of  $30\ \mu\text{m}$  on which have been applied two catalyst layers with a platinum loading of  $0.1\ \text{mg cm}^{-2}$  for the anode and  $0.4\ \text{mg cm}^{-2}$  for the cathode.

The GDLs are 28 BC Sigracet with an initial thickness of  $235\ \mu\text{m}$ , with a microporous layer on one side. The substrate is treated with 5% of PTFE. The total thickness of the gaskets and subgaskets is  $173\ \mu\text{m}$  and the tightening torque is controlled to be  $5\ \text{N m}$ .

### III – 3. Results

The design of experiments allows two configurations:

- The anode plate is the hot side while the cathode is the cold side. Here, the water flux through the anode GDL  $N_a$  has to be cancelled by an appropriate increase of the MEA temperature  $T_M$ . The whole water production is thus removed on the cathode side.
- The cathode plate is the hot side while the anode is the cold side. In this configuration, the water flux through the cathode GDL  $N_c$  must be null.

### III – 3.1. Hot anode / cold cathode (“ha/cc”)

For this configuration, the initial average temperature is set at  $T_{av} = 70\text{ °C}$  with a temperature difference  $\Delta T = 5\text{ °C}$ . Fig. III-4 represents the target configuration and the water balance:

$$N_a + \frac{i}{2F} = N_c \quad (III-23)$$

The required working point is spotted when the anode water flux  $N_a = 0$ . The water balance also suggests that it occurs when  $N_c = \frac{i}{2F}$ .

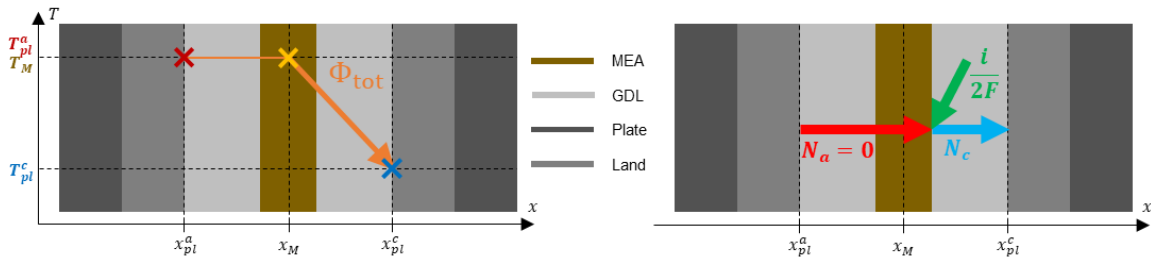


Figure III-4: Schematic of temperature field and water fluxes for the configuration hot anode / cold cathode.  $N_a$  is accounted positive towards the MEA and  $N_c$  is positive towards the channels.

Fig. III-5, III-6 and III-7 respectively represent the water fluxes, the voltage and the plates temperatures as a function of the current. Herein, the values are average on at least 1200 seconds of steady working conditions. Three experiments have been performed and are superimposed on each graph. Experiment number 2 (#2) was limited to low currents and is only presented to validate the data in this interval. The difference between experiment #1 and #3 is the dry gas addition. #1 benefited from a dilution gas flow rate of twice the inlet value, which is twice higher than for #3. Consequently, the influence of liquid water is reduced for #1 since the liquid water is better removed from the cell.

One can observe on Fig. III-5 that the targeted points are not reached for any current:  $N_a$  is strictly positive in this current interval and  $N_c$  is always higher than  $\frac{i}{2F}$ . The exception is for  $N_c^{\#3}$ : it crosses the water production flux for  $I = 45\text{ A}$ . Nevertheless, this is not consistent with the water flux  $N_c^{\#1}$ . This is attributed to experimental discrepancy due to the presence of liquid water at the outlet of the cell. Experiment #1 is less

sensitive to this thanks to a higher drying gas flow rate and leads to  $N_c^{\#3} > \frac{i}{2F}$ . Therefore, it is concluded that this configuration is not successful.

Thomas et al. [66] observed similar water balance in a fuel cell while applying a lower temperature at the cathode than at the anode. This repartition can be due to a weak back diffusion of water through the MEA combined to a strong electro-osmotic drag mechanism: this promotes water at the cathode. Additionally, the concentration gradient due to the temperature field is favorable to water transport towards the cathode channels.

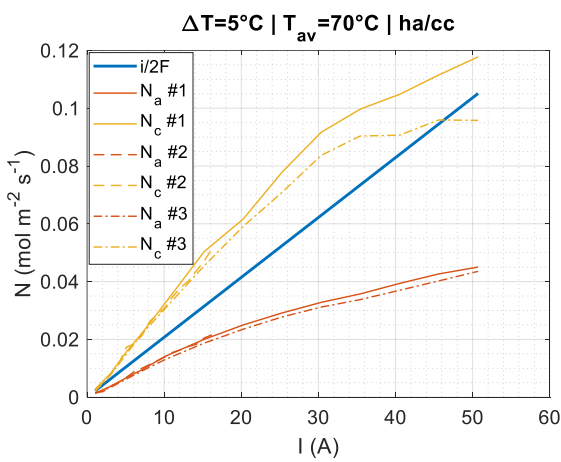


Figure III-5: Water fluxes for three ha/cc experiments

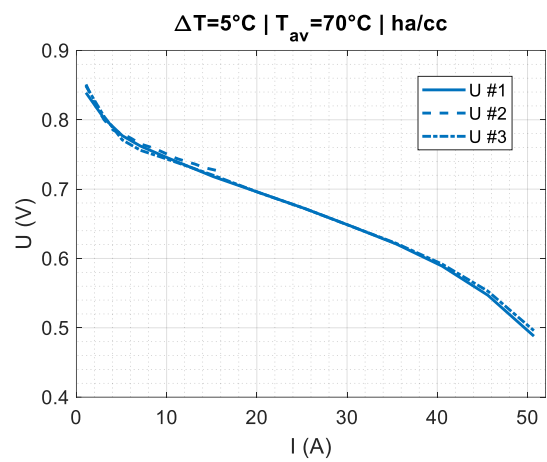


Figure III-6: Polarization curve for three ha/cc experiments

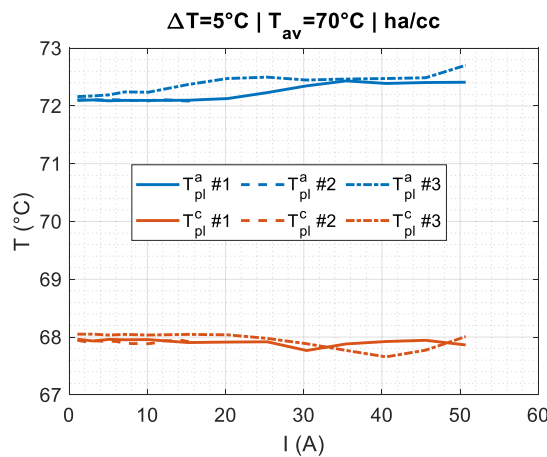


Figure III-7: Plates temperatures for three ha/cc experiments

### III – 3.2. Hot cathode / cold anode (“hc/ca”)

This second configuration showed to be more favorable to the estimation of the effective thermal conductivity of the GDL since the targeted points are actually reached. Fig. III-8 represents the targeted working conditions: the MEA is heated-up until it reaches the same temperature as the cathode plate, leading to the cancelling of the water flux through the cathode GDL  $N_c$ .

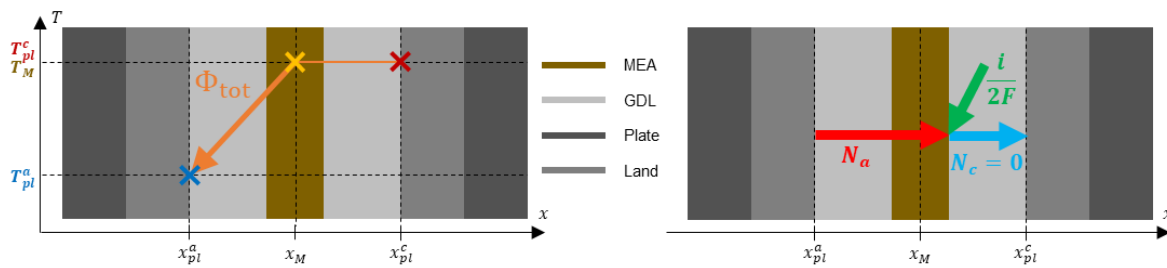


Figure III-8: Schematic of temperature field and water fluxes for the configuration hot cathode / cold anode

The initial average temperature is set at  $T_{av} = 65 \text{ }^\circ\text{C}$  in these experiments and two temperature differences are imposed:  $\Delta T = 2 \text{ }^\circ\text{C}$  and  $\Delta T = 5 \text{ }^\circ\text{C}$ . In both cases, two experiments are superimposed and the difference is the dry gas addition flow rate: it is twice higher for #2 than for #1. The presented data is averaged during at least 1200 seconds of steady working conditions.

#### III – 3.2.a) $\Delta T = 5 \text{ }^\circ\text{C}$

Fig. III-9, III-10 and III-11 respectively represent the water fluxes (the fluxes are plotted being multiplied by  $-1$ ), the voltage and the plates temperatures for the “hc/ca” experiments with  $\Delta T = 5 \text{ }^\circ\text{C}$ . In Fig. III-9, the water flux  $N_a^{\#1}$  has been discarded. A too low dry gas addition led to measurement issues due to the presence of liquid water (in an analogous way as  $N_c^{\#3}$  of Fig. III-5). In this configuration,  $N_a$  is observed to be negative in the whole current range while  $N_c$  is negative for the low currents and positive for current higher than 22 – 25 A. Similar water balances have been observed with equivalent temperature differences [66].

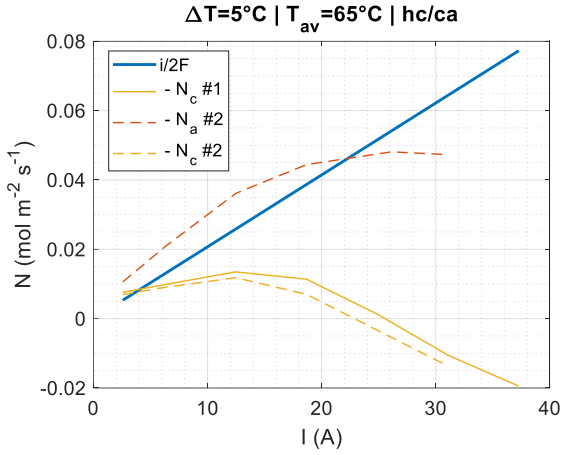


Figure III-9: Water fluxes for two “hc/ca” experiments at  $\Delta T = 5 \text{ }^\circ\text{C}$ .  $N_a^{\#1}$  is discarded due to measurement issue

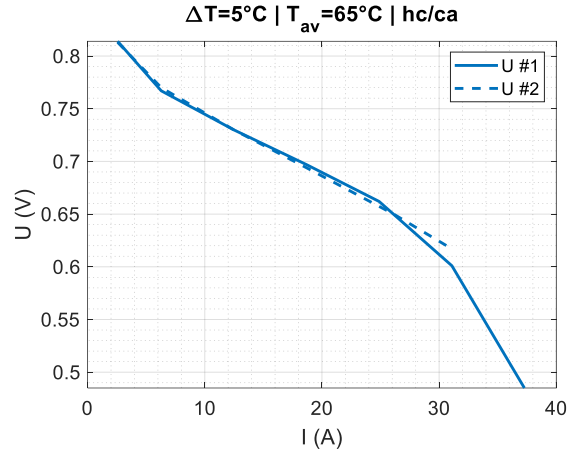


Figure III-10: Polarization curve for two “hc/ca” experiments at  $\Delta T = 5 \text{ }^\circ\text{C}$

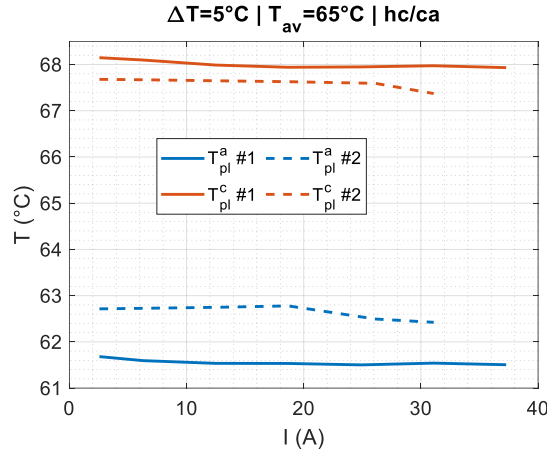


Figure III-11: Plates temperature for two hc/ca experiments at  $\Delta T = 5 \text{ }^\circ\text{C}$

The targeted working conditions appear when the cathode water flux  $N_c$  is null, as well as when  $-N_a = \frac{i}{2F}$ , according to the water balance of Eq. III-23. Fig. III-9 exhibits three currents where these conditions are met. Table III-1 provides experimental data that are useful for the calculation of the effective thermal conductivity of the GDL. Blue data are the experimental measurement while orange derive from calculation. The targeted currents  $I_{\text{target}}$  are first identified. Then, the associated voltage  $U$  is read in Fig. III-10. These two values together allow to compute the total heat flux  $\phi_{\text{tot}}$  that is produced by the cell according to Eq. III-16. Then, the measurements of the plate temperatures  $T_{\text{pl}}^a$  and  $T_{\text{pl}}^c$  are used to calculate the thermal resistance between the MEA and the plates  $R_{\text{th}}$  (Eq. III-15), assuming that the whole heat flux is removed by the cold side of the cell. It has to be notified that the effective temperature difference is not  $5 \text{ }^\circ\text{C}$  as expected

but only 4 °C because of the plates temperature regulation. Finally, the effective thermal conductivity  $\kappa_{\text{eff}}$  is estimated with Eq. III-12, considering a compressed thickness of the GDL  $t_{\text{GDL}} = 173 \times 10^{-6}$  m and a total surface  $S = 25$  cm<sup>2</sup>.

The final values for  $\kappa_{\text{eff}}$  present a good reproducibility between the two presented experiments as well as within a same experiment.  $N_c^{\#2} = 0$  and  $N_a^{\#2} = \frac{i}{2F}$  give very close results on the thermal conductivity, suggesting that both criteria are insightful regarding the temperature repartition in the assembly. Even though the operating conditions were different for experiment #1, if no issue due to liquid water occurs, the final result is only slightly different from #2. Based on these three experiments, the average effective thermal conductivity of the GDL is  $\kappa_{\text{eff}}^{\Delta 5} = 0.177$  W K<sup>-1</sup>m<sup>-1</sup>.

Table III-1: Data for estimation of effective thermal conductivity of the GDL by hc/ca and D5 experiments. Blue rows are experimental data and orange rows are calculated

Target	$N_c^{\#1} = 0$	$N_c^{\#2} = 0$	$N_a^{\#2} = \frac{i}{2F}$
$I_{\text{target}}$ (A)	$I_c^{\#1} = 25.5$	$I_c^{\#2} = 22.9$	$I_a^{\#2} = 22.3$
$U$ (V)	$U_c^{\#1} = 0.656$	$U_c^{\#2} = 0.669$	$U_a^{\#2} = 0.673$
$T_{\text{pa}}$ (°C)	$T_{\text{pa,c}}^{\#1} = 61.5$	$T_{\text{pa,c}}^{\#2} = 62.6$	$T_{\text{pa,a}}^{\#2} = 62.6$
$T_{\text{pc}}$ (°C)	$T_{\text{pc,c}}^{\#1} = 67.9$	$T_{\text{pc,c}}^{\#2} = 67.6$	$T_{\text{pc,a}}^{\#2} = 67.6$
$\Phi_{\text{tot}}$ (W)	$\Phi_c^{\#1} = 15.25$	$\Phi_c^{\#2} = 13.40$	$\Phi_a^{\#2} = 12.96$
$R_{\text{th}}$ (K W <sup>-1</sup> )	$R_c^{\#1} = 0.42$	$R_c^{\#2} = 0.37$	$R_a^{\#2} = 0.38$
$\kappa_{\text{eff}}$ (W K <sup>-1</sup> m <sup>-1</sup> )	$\kappa_c^{\#1} = 0.16$	$\kappa_c^{\#2} = 0.19$	$\kappa_a^{\#2} = 0.18$

### III – 3.2.b) $\Delta T = 2$ °C

Fig. III-12, III-13 and III-14 respectively illustrate the water fluxes, the polarization curve and the plates temperatures for the experiment in “hc/ca” configuration with a temperature difference between the plates of  $\Delta T = 2$  °C. The same behavior as previously is observed. First,  $N_a^{\#1}$  is here again discarded due to the same liquid water issue that impacts the flux measurement. Then, the water fluxes balance is highly similar as the previous experiment except that the targeted currents are smaller. Indeed, the temperature difference between the plates being smaller, the heat production needed to increase the MEA temperature up to the hot plate temperature is lower. The same data processing is performed for this experiment and results are

provided in Table III-2. Estimated values of  $\kappa_{\text{eff}}$  are similar for the three measurements, the average being  $\kappa_{\text{eff}}^{\Delta 2} = 0.163 \text{ W K}^{-1} \text{ m}^{-1}$ .

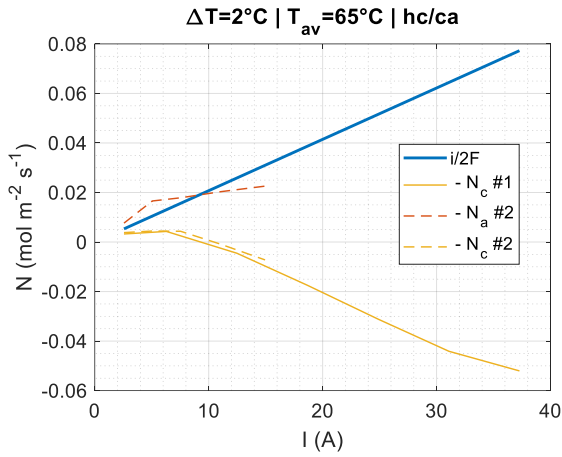


Figure III-12: Water fluxes for two hc/ca experiments at  $\Delta T = 2 \text{ }^\circ\text{C}$ .  $N_a \#1$  is discarded due to measurement issue

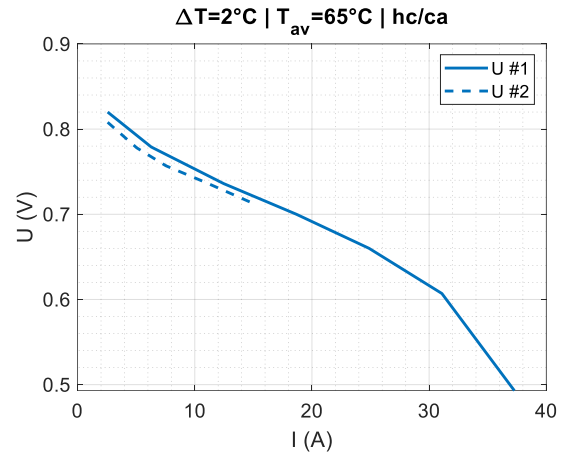


Figure III-13: Polarization curve for two hc/ca experiments at  $\Delta T = 2 \text{ }^\circ\text{C}$

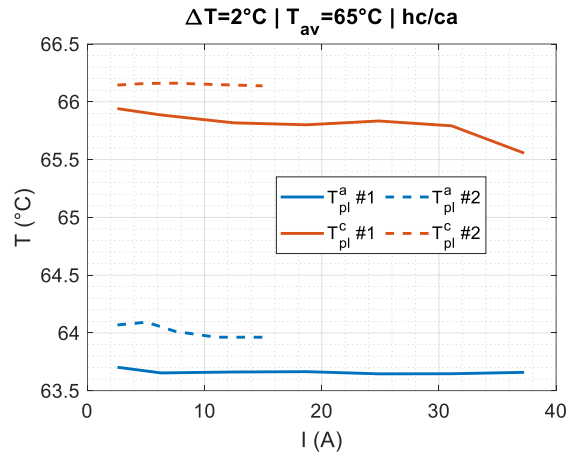


Figure III-14: Plates temperature for two hc/ca experiments at  $\Delta T = 2 \text{ }^\circ\text{C}$

Table III-2: Data for estimation of effective thermal conductivity of the GDL by hc/ca and D2 experiments. Blue rows are experimental data and orange rows are calculated

Target	$N_c^{\#1} = 0$	$N_c^{\#2} = 0$	$N_a^{\#2} = \frac{i}{2F}$
$I_{\text{target}} \text{ (A)}$	$I_c^{\#1} = 9.3$	$I_c^{\#2} = 10.5$	$I_a^{\#2} = 9.2$
$U \text{ (V)}$	$U_c^{\#1} = 0.758$	$U_c^{\#2} = 0.740$	$U_a^{\#2} = 0.747$
$T_{\text{pa}} \text{ (}^\circ\text{C)}$	$T_{\text{pa,c}}^{\#1} = 63.7$	$T_{\text{pa,c}}^{\#2} = 64.0$	$T_{\text{pa,a}}^{\#2} = 64.0$
$T_{\text{pc}} \text{ (}^\circ\text{C)}$	$T_{\text{pc,c}}^{\#1} = 65.8$	$T_{\text{pc,c}}^{\#2} = 66.1$	$T_{\text{pc,a}}^{\#2} = 65.9$
$\Phi_{\text{tot}} \text{ (W)}$	$\phi_c^{\#1} = 4.61$	$\phi_c^{\#2} = 5.40$	$\phi_a^{\#2} = 4.67$
$R_{\text{th}} \text{ (K W}^{-1}\text{)}$	$R_c^{\#1} = 0.47$	$R_c^{\#2} = 0.40$	$R_a^{\#2} = 0.40$
$\kappa_{\text{eff}} \text{ (W K}^{-1} \text{ m}^{-1}\text{)}$	$\kappa_c^{\#1} = 0.15$	$\kappa_c^{\#2} = 0.17$	$\kappa_a^{\#2} = 0.17$

These estimates are consistent with previous estimates in the 5-degree difference case. The slight difference may come from the consideration of the convective-diffusion term which is larger in the higher current case. The amount of water in the GDL may also influence the final estimate.

### III – 4. Comparison with literature

Table III-3: Data from literature about effective thermal conductivity of GDLs

Ref.	Effective thermal conductivity ( $\text{W K}^{-1} \text{m}^{-1}$ )	Thermal resistance contributions	Material	Method
<b>Present work</b>	$\kappa_{\text{eff}} = 0.15 - 0.19$	Conduction + contacts	Sigracet 28BC	<i>In-situ</i>
[149]	$\kappa_{\text{eff}} = 0.25 - 0.7$	Conduction	SpectraCarb	<i>Ex-situ</i>
[154]	$\kappa_{\text{eff}} = 0.26 - 0.34$	Conduction + contacts	Sigracet	<i>Ex-situ</i>
[155]	$\kappa_{\text{eff}} = 0.22 - 0.48$	Conduction	Sigracet	<i>Ex-situ</i>
[65]	$\kappa_{\text{eff}} = 0.25$	Conduction + contacts	Sigracet	<i>In-situ</i>
[92]	$\kappa_{\text{eff}} = 0.27$	Conduction	SolviCore	<i>Ex-situ</i>

The estimated values for  $\kappa_{\text{eff}}$  lay in the interval between  $0.15 \text{ W K}^{-1} \text{m}^{-1}$  and  $0.19 \text{ W K}^{-1} \text{m}^{-1}$ . These values contain the two-dimensional effect, the contact resistances influence and are valid for the employed materials with the same compression level. This explains why the herein reported values are lower than the literature data. Table III-3 sums up some data from the literature concerning the estimation of thermal conductivity of GDLs. The details about the considered thermal resistances is provided as well as the employed materials and the *ex-situ* or *in-situ* method.

Karimi et al. [149] estimated thermal resistance of GDLs with different PTFE loading as well as contact resistances at several compression levels. The authors concluded that both resistances were decreasing functions of the compression load. The calculated effective thermal conductivities (which do not contain the contribution of contact resistance) are comprised between  $0.25 \text{ W K}^{-1} \text{m}^{-1}$  and  $0.7 \text{ W K}^{-1} \text{m}^{-1}$ . Khandelwal and Mench [155] reported values between  $0.22 \text{ W K}^{-1} \text{m}^{-1}$  and  $0.48 \text{ W K}^{-1} \text{m}^{-1}$  depending on the PTFE loading. *Ex-situ* estimations are performed with standard apparatus consisting of a cylinder whose ends are temperature-controlled and in the middle of which the samples are inserted. The effective conductivity is thus purely one-dimensional. *In-situ* estimations consider the effects of

the lands and channels and thus two-dimensional effects are incorporated in the estimated value. These experiments lead to lower values, even more when the contact resistances are integrated in the final estimation.

## IV – Conclusions and outlooks

Heat sources in a cell are multiple and unavoidable because of the losses during the operation of the cell. They are located at different places in the assembly according to their nature and are of the same order of magnitude than the produced electrical power. The management and removal of such heat power is crucial for the cell performances and durability.

Heat conduction being identified as the main transfer mechanism through the GDL, the estimation of the thermal conductivity is of high importance for the heat transfer modeling of a fuel cell. In this work, an original design of experiment is set up in order to estimate the effective thermal conductivity of the GDL. This relies on the link between heat and water transfer, one of the expressions of which is the heat-pipe effect. This mechanism enables vapor transport even in saturated vapor, due to a temperature field that causes saturation pressure gradients. A temperature difference between the plates is applied and current is incrementally raised. This leads to an increasing heat production that gradually increases the MEA temperature. Once the latter reaches the hotter plate temperature, the temperature field within the related GDL is uniform. The cell being fed by saturated gases, the saturation pressure field is uniform as well and the water flux through the GDL is null. This measurable data is used as a condition to determine when the total heat flux produced by the cell is removed by the colder side. In this case, the temperature difference between the MEA and the cold plate is known as well as the total heat flux. Thus, the thermal resistance is calculated as well as the effective thermal conductivity.

The estimated values show good agreement with the literature data. The present estimations contain several contributions: heat conduction, contact resistances and two-dimensional effects. Even though these values are only usable with a given set-up, the effective thermal conductivity is very convenient since it can be

implemented in a lumped model that eliminates the need for a more complex model where two-dimensional effects and interfaces should be modelled.

Some further work is still to achieve in order to completely develop the method and benefit from all its advantages:

- i. The insertion of platinum wires close to the MEA should allow to measure the temperature at the interface CL/GDL and thus validate the method. Flux meters could also be employed.
- ii. The implementation of the convective part of the water flux could give more accurate results, even more at high current when the consumed gas flow rates are important and impact vapor diffusion.
- iii. Materials with different morphologies and thicknesses could be assembled and characterized to decorrelate the contact resistance contribution from the conduction.
- iv. The influence of the channels/land geometry can also be investigated in order to study the impact of the two-dimensional effects.
- v. Liquid water exhibits a thermal conductivity of  $0.6 \text{ W K}^{-1}\text{m}^{-1}$  and showed to influence the effective thermal conductivity of the GDL. Estimations in different conditions about water content of the cell could inform about this influence.

# **Chapter IV: Experimental and modelling study of heat and water transport during load cycling**

<b>Introduction .....</b>	<b>138</b>
<b>I – 1D transient model for coupled heat and water transport .....</b>	<b>139</b>
I – 1. Heat transport .....	139
I – 2. Water transport .....	140
I – 3. Liquid water saturation.....	142
<b>II – Dynamic regime experiments .....</b>	<b>143</b>
II – 1. Materials .....	143
II – 2. Design of experiment .....	144
II – 3. Processing method .....	150
II – 4. Transient experiments – Results .....	154
II – 5. Pseudo-steady state experiments – Results .....	165
<b>III – Comparison between model and pseudo-steady state experiments .....</b>	<b>172</b>
III – 1. Parametrization.....	172
III – 2. Heat transfer .....	175
III – 3. Water storage .....	177
<b>IV – Conclusions and outlooks.....</b>	<b>179</b>
<b>Appendix .....</b>	<b>183</b>

## Introduction

In the field of hydrogen mobility, fuel cells go through lots of cycling during acceleration, deceleration, startups and shutdowns of vehicles [139]. Even though sharp power demand is smoothed by the batteries and supercapacitors [161], it is necessary that the fuel cell stack increases its power regime in order to ensure the power supply after the discharge time of the capacitors [162].

Water and heat management is even more important during transient regime [163]. Dry conditions can lead to severe degradations due to hot spots for example [164]. Flooding conditions could hinder diffusion of reactant gases, cause fuel starvation and voltage instabilities [165]. In both cases, durability and performances are affected. Efficient models are needed in order to properly control fuel cell systems during such regimes [82], prevent the cell from degrading working conditions.

This Chapter is dedicated to a preliminary study of water storage in transient regimes in a fuel cell. A one-dimensional model for coupled transfers of heat and water is developed. It assumes that some liquid water can be stored within the cathode GDL. Then, specific experiments are set up, aiming to simultaneously measure the cell voltage, the 1-kHz resistance and the water balance during triangle load cycles. Results during transient regime are exposed, as well as pseudo-steady state. Finally, the model is parametrized in order to provide a rough comparison with experiments. The ultimate goal of this work is to estimate parameters to feed a lumped model for heat and water transfer in transient regime.

## I – 1D transient model for coupled heat and water transport

A transient model is developed in order to represent coupled heat and water transfer during load cycling. Assumption, transfer laws and associated parameters are described in the following. Such a model can be used together with experimental data to estimate parameters of heat and water transport. All symbols are listed in Appendix.

### I – 1. Heat transport

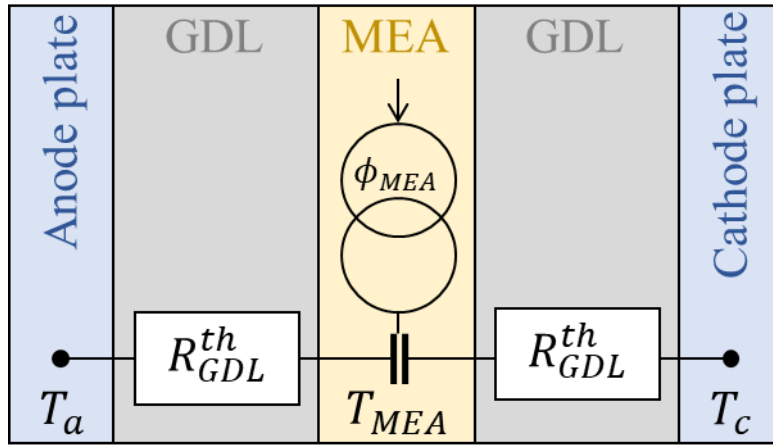


Figure IV-1: Diagram of heat transfer model

Fig. IV-1 is a diagram of the modelled heat transfer in the cell. The plate temperatures  $T_c$  and  $T_a$  are imposed as they are accurately regulated by the thermalization water circuit that flows within it. Due to the low thickness of the membrane (15  $\mu\text{m}$ ), the generated heat is assumed to be uniformly produced in the volume of the MEA and is denoted as  $\phi_{MEA}$  (see Chapter III). This heat flux contains two contributions: the electrochemical losses and phase change heat of water contained in the cell, which is attributed to MEA.

$$\phi_{MEA} = i \left( \frac{LHV_{H_2}}{2F} - U \right) + \frac{V_c \rho_{H_2O,l}}{M_{H_2O}} L_v \frac{dS_c}{dt} \quad (\text{IV-1})$$

Heat fluxes through the GDL  $\phi_{GDL}^{a,c}$  are assumed purely conductive as conduction is identified as the main heat transport mechanism within it [166]. Thermal resistances

$R_{GDL}^{th}$  are thus defined and depend on the thickness of the compressed GDL  $t_{GDL}$  and its effective thermal conductivity  $\kappa_{GDL}^{eff}$ , which incorporates the contact resistance contributions, as developed in Chapter III.

$$\phi_{GDL}^{a,c} = \frac{T_{a,c} - T_{MEA}}{R_{GDL}^{th}} \quad (IV-2)$$

In transient regime, the thermal capacity of the MEA  $K_{MEA}^{th}$  is considered and the MEA temperature  $T_{MEA}$  evolves due to the sum of three fluxes:

$$K_{MEA}^{th} \frac{dT_{MEA}}{dt} = \phi_{MEA} + \frac{T_a - T_{MEA}}{R_{GDL}^{th}} + \frac{T_c - T_{MEA}}{R_{GDL}^{th}} \quad (IV-3)$$

The characteristic time for the MEA to reach its steady state value depends on  $K_{MEA}^{th}$ . For very thin membranes, the thermal capacity is low and the characteristic time may be negligible. Eq. IV-3 is associated with the initial condition  $T_{MEA}(t = 0) = \frac{T_a + T_c}{2}$ .

## I – 2. Water transport

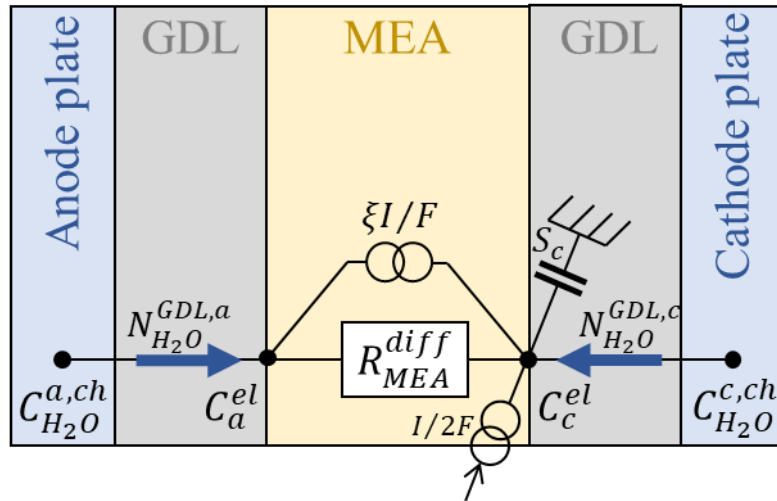


Figure IV-2: Diagram of the modelled water transfer in the cell

### I – 2.1 In the GDLs

For water transport, the boundary conditions are the water concentration in the channels  $C_{H_2O}^{a,c,ch}$ . The water vapor flux  $N_{H_2O}^{GDL,a,c}$  between the channels and the MEA

interfaces, where the water vapor concentration  $C_{a,c}^{el}$  is defined, is modelled by Fickian diffusion superimposed with convection due to gas fluxes:

$$N_{H_2O}^{GDL,a} = \frac{C_{H_2O}^{GDL,a}}{C_{tot}^a} (N_{H_2O}^{GDL,a} + N_{H_2}^{GDL,a}) - D_{H_2O}^{GDL,a} \frac{dC_{H_2O}^{GDL,a}}{dy}$$

$$N_{H_2O}^{GDL,c} = \frac{C_{H_2O}^{GDL,c}}{C_{tot}^c} (N_{H_2O}^{GDL,c} + N_{O_2}^{GDL,c}) - D_{H_2O}^{GDL,c} \frac{dC_{H_2O}^{GDL,c}}{dy}$$
(IV-4)

Where  $C_{tot}^{a,c} = P_{a,c}/RT_{a,c}$  represents the total concentration. The cell capacity regarding vapor storage is neglected and diffusion is assumed to be in steady state. Hydrogen molar flux density  $N_{H_2}^{GDL,a}$  is linked to the current density by the Faraday's law:

$$N_{H_2}^{GDL,a} = \frac{i}{2F}$$
(IV-5)

In a similar way, the oxygen molar flux density  $N_{O_2}^{GDL,c}$  is expressed as:

$$N_{O_2}^{GDL,c} = \frac{i}{4F}$$
(IV-6)

Eq. IV-4 are analytically solved to express  $C_{a,c}^{el}$  as a function of boundary conditions  $C_{H_2O}^{a,c,ch}$ .

$$C_a^{el} = \left( C_{H_2O}^{a,ch} - C_{tot}^a \frac{N_{H_2O}^{GDL,a}}{N_{H_2O}^{GDL,a} + N_{H_2}^{GDL,a}} \right) \exp \left( \frac{N_{H_2O}^{GDL,a} + N_{H_2}^{GDL,a}}{C_{tot}^a D_{H_2O}^{GDL,a}} t_{GDL} \right)$$

$$+ C_{tot}^a \frac{N_{H_2O}^{GDL,a}}{N_{H_2O}^{GDL,a} + N_{H_2}^{GDL,a}}$$
(IV-7)

$$C_c^{el} = \left( C_{H_2O}^{c,ch} - C_{tot}^c \frac{N_{H_2O}^{GDL,c}}{N_{H_2O}^{GDL,c} + N_{O_2}^{GDL,c}} \right) \exp \left( \frac{N_{H_2O}^{GDL,c} + N_{O_2}^{GDL,c}}{C_{tot}^c D_{H_2O}^{GDL,c}} t_{GDL} \right)$$

$$+ C_{tot}^c \frac{N_{H_2O}^{GDL,c}}{N_{H_2O}^{GDL,c} + N_{O_2}^{GDL,c}}$$
(IV-8)

Note that water fluxes are accounted positive from the channels towards the MEA.

## I – 2.2. In the MEA

The water content at the interfaces of the MEA  $\lambda_a$  and  $\lambda_c$  are given by the sorption curve:

$$\begin{aligned}\lambda_a &= \lambda \left( \frac{C_a^{el}}{C_{sat}^{MEA}} \right) \\ \lambda_c &= \lambda \left( \frac{C_c^{el}}{C_{sat}^{MEA}} \right)\end{aligned}\quad (IV-9)$$

Where  $C_{sat}^{MEA} = P_{sat}(T_{MEA})/RT_{MEA}$  is the saturation concentration at the MEA interface. It assumes that there is no sorption resistance and that the equilibrium is instantly established. Water flux through the MEA  $N_{H_2O}^{MEA}$  is the sum of two contributions: diffusion and electroosmotic drag. The diffusion mechanism is characterized by a diffusion resistance  $R_{MEA}^{diff} = \frac{t_{MEA}}{D_M}$ , if one considers that the diffusion coefficient does not depend on the water content.

$$N_{H_2O}^{MEA} = \frac{\rho_{dry}}{EW} \frac{\lambda_a - \lambda_c}{R_{MEA}^{diff}} + \frac{\xi i}{F} \quad (IV-10)$$

## I – 3. Liquid water saturation

Liquid water is assumed to be stored in the cathode compartment, as described by the capacity in Fig. IV-2. This liquid water is modelled by the saturation  $S_c$  of the considered wettable volume  $V_c$ . The latter represents the available volume for the liquid water filling and is expressed as a length which is a fraction of the GDL thickness. The maximum saturation  $S_{lim}$  is also introduced. Once the saturation  $S_c$  reaches the cut-off value  $S_{lim}$ , it is assumed that liquid water exits the cathode compartment due to capillary forces. The time derivative of the saturation  $S_c$  is expressed as the sum of three fluxes: diffusion in the cathode GDL, in the MEA and the water production.

$$V_c \frac{\rho_{H_2O,l}}{M_{H_2O}} \frac{dS_c}{dt} = N_{H_2O}^{GDL,c} + N_{H_2O}^{MEA} + \frac{i}{2F} - \chi_1 \exp\left(\frac{S_c - S_{lim}}{\chi_2}\right) \quad (IV-11)$$

The exponential term is added in the water balance in order to smoothly limit the water saturation under  $S_{lim}$ . The two additional parameters  $\chi_1$  and  $\chi_2$  are only of numerical



The load is a KIKUSUI PLZ334WL and two function generators RSDG 830 from RS PRO are employed to superimpose the ramp current profile to a sinusoidal oscillation.

## II – 2. Design of experiment

### II – 2.1 Current profiles

Load cycles are imposed to the cell to investigate water management. Triangle shaped current profiles can be representative of some automotive working conditions, especially during acceleration and slowdown. Water and heat management is of high importance during these transition phases because heterogeneities can appear such as hot spots or flooded areas and thus lower performances or even degrade materials.

The current profiles are defined by four parameters:

- Minimum current  $I_{\min}$ ,
- Maximum current  $I_{\max}$ ,
- Sweeping velocity  $v$ , defined in  $A s^{-1}$ , that dictates the duration of one period,
- Number of periods  $N_p$ .

In order to investigate hydration level of the cell, a 1-kHz sinusoidal oscillation is superimposed to the triangle current profiles. Combined with cell voltage measurement, this oscillation allows the computation of the 1-kHz resistance that gives hints on the hydration of the membrane and of the electrodes. This oscillation is characterized by two parameters which are the frequency  $f$ , set at 1 kHz, and the absolute current amplitude  $\Delta I$ . The data acquisition rate is set at 100 kHz, leading to 100 points per period. Due to the current oscillations, the effective minimum current is  $I_{\min} - \Delta I$  and the effective maximum current is  $I_{\max} + \Delta I$ .

The current amplitude is usually set as a percentage of the imposed but for technical considerations, the current amplitude is set at a constant absolute value in the following experiments and an optimal has to be found. Amplitude should high enough to lead to a significant voltage oscillation and thus to a high signal to noise ratio. On the other hand, amplitude should be low enough to keep the current in a narrow range so that classical Electrochemical Impedance Spectroscopy linearity assumptions are verified.

Several values for the current amplitude have been experimented:  $\Delta I = 1$  A, which represents 10% of the lowest current of the profiles, and 2% of the highest, and  $\Delta I = 2$  A. As presented in Fig. IV-4, the employed load was not able to provide  $\Delta I = 2$  A at the required frequency and a triangle shaped current profile with insufficient amplitude was obtained. This experiment showed that  $\Delta I = 1$  A is close to the maximum amplitude that the load could provide at the frequency, and this value is kept for the following experiments.

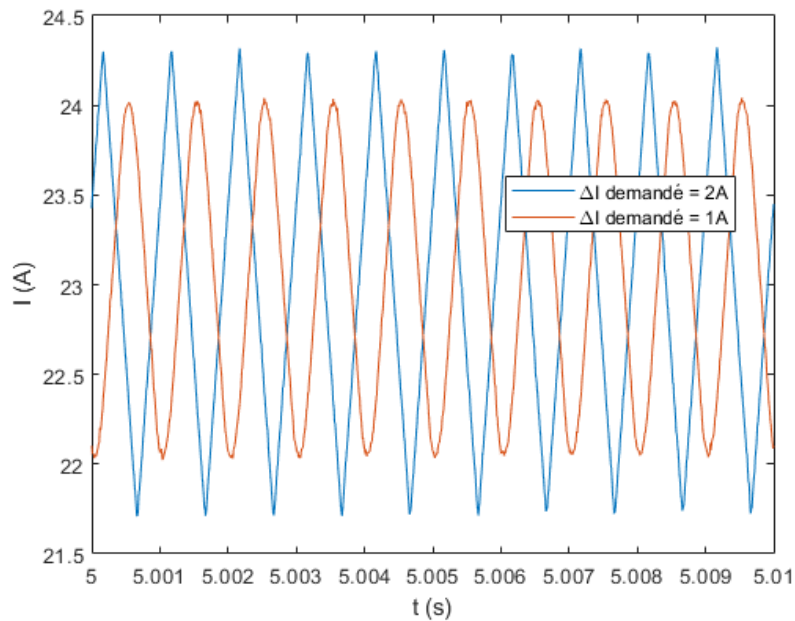


Figure IV-4: Current oscillations for a required amplitude of 1 A (orange) and 2 A (blue)

## II – 2.2. Procedure

Three preliminary steps precede the cycling:

- At least three hours of continuous gas flow at a dew point temperature of 40 °C through the cell maintained at 65 °C. This step properly removes all the liquid water present in the pores of the GDLs and the channels and ensures a reproducible starting point for all measurements.
- At least two hours for the temperature setting of the humidifiers, to ensure a homogeneous temperature field within it and thus an accurate and constant inlet relative humidity. The inlet relative humidity is set to be slightly less than 100%

to prevent water condensation in the pipes before the cell inlet while guaranteeing uniform water conditions along the channels.

- Measurement of the inlet gases dew point temperature by a cell by-pass. The measure is used for the whole following experiment since the temperature of the humidifiers and the gas flow rates setpoint are kept constant.

## II – 2.3. Feeding gases and stoichiometry

One of the main targets of this Chapter is to study water storage in the cell during a dynamic current regime. Some constraints have to be considered about gas feeding and stoichiometry:

- Sensitivity to stored water flux:

A sufficient sensitivity to the stored water flux  $N_{st}$  is needed. Fig. IV-5 represents a diagram of all water vapor and gas fluxes in the cell. At the inlets, gases ( $n_{H_2}^{a,in}$ ,  $n_{air}^{c,in}$ ) and water vapor ( $n_w^{a,in}$ ,  $n_w^{c,in}$ ) enter the channels. Through-plane water vapor fluxes densities  $N_a$  and  $N_c$  (assumed uniform along the channels), that are accounted as positive towards the channels, reach or leave the channels and two water balances are considered:

$$\begin{aligned} N_a \times S &= n_w^{a,out} - n_w^{a,in} \\ N_c \times S &= n_w^{c,out} - n_w^{c,in} \end{aligned} \quad (IV-12)$$

$n_w^{a,out}$  and  $n_w^{c,out}$  being the water fluxes that exit the cell at anode and cathode sides and  $S$  the total active area.

The third water balance is written at the cathode compartment, assuming that the flux through the MEA  $N_M$  is always equal to the flux through the anode GDL  $N_a$ :

$$N_{st} = \frac{i}{2F} - N_a - N_c \quad (IV-13)$$

Eq. IV-13 shows that the accuracy on  $N_{st}$  is highly related to the accuracy on  $N_a$  and  $N_c$ . These through-plane fluxes are calculated with Eq. IV-12 using inlet and outlet water vapor fluxes. In order to have the best sensitivity,  $N_a$  and  $N_c$  should be of the

same order of magnitude than the inlet water flux. The inlet dew point temperature being set to 65 °C (rh = 100%), one way to adapt the inlet water flux is to vary the gas stoichiometry.

For small currents ( $i < 0.4 \text{ A cm}^{-2}$ ), Thomas et al. [65] showed that water production is removed equally on both sides of the cell. Consequently, as a first approach, assuming steady state and no water storage, one can write:

$$\begin{aligned} N_a &= 0.5 \frac{i}{2F} \\ N_c &= 0.5 \frac{i}{2F} \end{aligned} \quad (\text{IV-14})$$

For higher currents, an additional contribution  $\phi$  should be considered leading to  $N_a = 0.5 \frac{i}{2F} \pm \phi$  and  $N_c = 0.5 \frac{i}{2F} \pm \phi$ . Nevertheless, this order of magnitude approach limits to Eq. IV-14.

In an objective to have a sufficient sensitivity to  $N_a$  and since it is obtained by the difference between cell inlet and outlet water fluxes, it is desirable that  $0.1 \times N_w^{a,in} < N_a < N_w^{a,in}$ . To meet this condition, anode stoichiometry  $\Lambda_a$  should be as follows:

$$\begin{aligned} 0.1\Lambda_a \frac{i}{2F} \frac{P_{sat}(65)}{P - P_{sat}(65)} < 0.5 \frac{i}{2F} < \Lambda_a \frac{i}{2F} \frac{P_{sat}(65)}{P - P_{sat}(65)} \\ 1.57 < \Lambda_a < 15.7 \end{aligned} \quad (\text{IV-15})$$

For the cathode stoichiometry  $\Lambda_c$ , an analog calculation is carried out if one considers a molar fraction of oxygen  $x_{O_2}$  in nitrogen:

$$\begin{aligned} 0.1 \times N_w^{c,in} < N_c < N_w^{c,in} \\ 0.1\Lambda_c \frac{1}{x_{O_2}} \frac{i}{4F} \frac{P_{sat}(65)}{P - P_{sat}(65)} < 0.5 \frac{i}{2F} < \Lambda_c \frac{1}{x_{O_2}} \frac{i}{4F} \frac{P_{sat}(65)}{P - P_{sat}(65)} \end{aligned}$$

For air, and thus for  $x_{O_2} = 0.21$ :

$$0.66 < \Lambda_c < 6.6 \quad (\text{IV-16})$$

Here, it is understood that to aim  $N_a \sim N_w^{c,in}$ , the stoichiometry at the cathode must be as low as 0.66 which is not sufficient to properly feed the cell. One way to increase the lowest boundary for  $\Lambda_c$  is to increase the molar fraction of oxygen in the feeding gas. For synthetic air with  $x_{O_2} = 0.5$ :

$$1.57 < \Lambda_c < 15.7 \quad (IV-17)$$

For pure oxygen with  $x_{O_2} = 1$ :

$$3.14 < \Lambda_c < 31.4 \quad (IV-18)$$

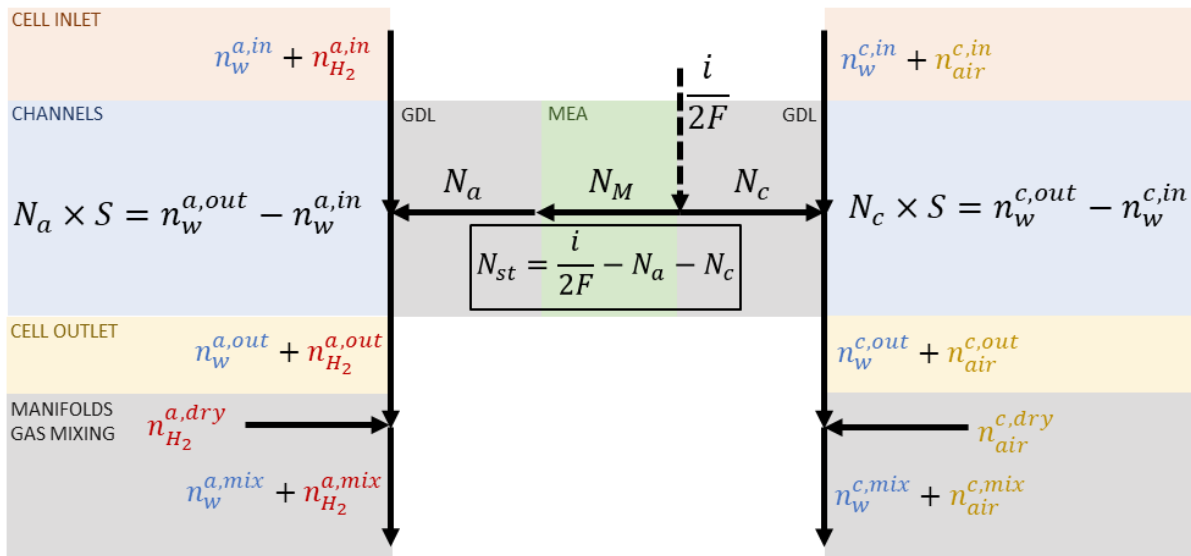


Figure IV-5: Diagram of water and gas fluxes in the cell

- Humidifiers efficiency:

The membrane humidifiers are efficient in a given range of gas flow rate, as described in Chapter II. In order to feed the cell with saturated gases, the humidifier temperature is set to 65 °C. At this temperature, it has been observed that the humidifier efficiency decreases for flow rates higher than 60 slph. Thus, it is necessary to contain the inlet gas flow rate below this value.

The active area of the cell is 25 cm<sup>2</sup> and a current density up to 2 A cm<sup>-2</sup> is delivered, leading to a total current of 50 A. Table IV-1 shows the needed gas flow rates for such a cell current and stoichiometries set to 1.5 for hydrogen and to 2 for oxygen. The gas flow rate of air  $Q_{air}$  is higher than the limit for the humidifiers to be fully efficient at 65 °C.

Consequently, it is preferable to use  $O_2$  and  $N_2$  mixture (synthetic air) with  $x_{O_2} = 0.5$  or pure oxygen to feed the cell with saturated gases. Hydrogen flow rate needed for  $I = 50$  A and  $\Lambda_a = 1.5$  is 31 slph which is the maximum flow rate available with the employed gas flow meter. This confirms that current has to be limited to 50 A during the experiments.

Table IV-1: Inlet gas flow rates of different feeding gas for the maximum cell current

	Hydrogen $Q_{H_2} (\Lambda_a = 1.5)$	Air $Q_{air} (\Lambda_c = 2)$	Synthetic air $Q_{0.5} (\Lambda_c = 2)$	Pure $O_2$ $Q_{O_2} (\Lambda_c = 2)$
$I = 50$ A	31 slph	99.5 slph	41.8 slph	20.9 slph

- Voltage:

Even though pure oxygen seems to be the best candidate for the water balance, it has been observed during preliminary experiments that the cell voltage at  $2 \text{ A cm}^{-2}$  was about  $0.6 \text{ V}$  with this feeding gas. In order to investigate the dynamic water management in a wider range of voltage, it is chosen to use synthetic air with  $x_{O_2} = 0.5$  so that mass transfer limitations appear in the polarization curve.

## II – 2.4. Experimental conditions

Table IV-2: Experimental conditions for load cycling experiments

Oxygen molar fraction $x_{O_2}$	0.5
Maximum current $I_{max}$	50 A
Minimum current $I_{min}$	10 A
Sweeping velocity $v$	$0.6 ; 1 ; 1.4 ; 2 \text{ A s}^{-1}$
Oxygen stoichiometry $\Lambda_c$ at $I_{max}$	1.5
Oxygen stoichiometry $\Lambda_c$ at $I_{min}$	7.5
Hydrogen stoichiometry $\Lambda_a$ at $I_{max}$	1.5
Hydrogen stoichiometry $\Lambda_a$ at $I_{min}$	7.5
Cathode dry gas addition (proportion of inlet gas flow rate)	1.5
Anode dry gas addition (proportion of inlet gas flow rate)	1.5
Inlet relative humidity	> 98%

Experimental conditions for the following experiments are presented in Table IV-2. It has to be noted that the gas flow rate remains constant for the whole experiment. Thus, in order to provide enough feeding gas at the maximum current, the absolute gas flow rate is determined relatively to the stoichiometry and the maximum current. Consequently, when current is lower, the effective stoichiometry is higher than the presented one.

## II – 3. Processing method

During standard experiments, such as developed in Chapter II and III, about twenty measurements (current, voltage, temperatures, relative humidities, ...) are recorded at a frequency of 1 Hz. In the present experiment, data is acquired at a frequency of 100 kHz, representing 100 points per period of current oscillation, which is necessary to the proper conduct of the resistance calculation. Consequently, the amount of acquired data is limited to the bare essentials: time, current, voltage, Vaisala sensors temperatures and relative humidities.

### II – 3.1. 1-kHz resistance

The calculation of the 1-kHz resistance originates from the current and voltage measurements. The total current  $I(t)$  is decomposed into two contributions: the triangular profile part  $I_{tri}(t)$  and the oscillation part  $I_{sin}(t)$ . The total voltage  $U(t)$  decomposes into an average part  $U_{av}(t)$  and oscillations  $U_{sin}(t)$ :

$$\begin{aligned} I(t) &= I_{tri}(t) + I_{sin}(t) \\ U(t) &= U_{av}(t) + U_{sin}(t) \end{aligned} \tag{IV-19}$$

The first step of the data processing is to extract the oscillating parts from the total signals. Fig. IV-6a represents a typical current profile  $I(t)$  applied to the cell. Being given the number of periods, minimums and maximums of current are located and piecewise linear fit is performed between those values. Fig. IV-6c represents ten periods of current oscillations  $I_{sin}(t)$ , confirming its sinusoidal shape, and current linear fit  $I_{tri}(t)$ .

The voltage response  $U(t)$  to the current profile is not exactly triangular due to the non-linearity between current and voltage along the polarization curve. Consequently, a linear fit between extremums is not applicable for the voltage. A moving average is applied on the voltage in order to extract  $U_{av}(t)$  (Fig. IV-7a). This average is performed on 20 000 points, representing 0.2 second of data. Fig. IV-7b represents ten periods of voltage oscillations  $U_{sin}(t)$  with the moving average  $U_{av}(t)$ .

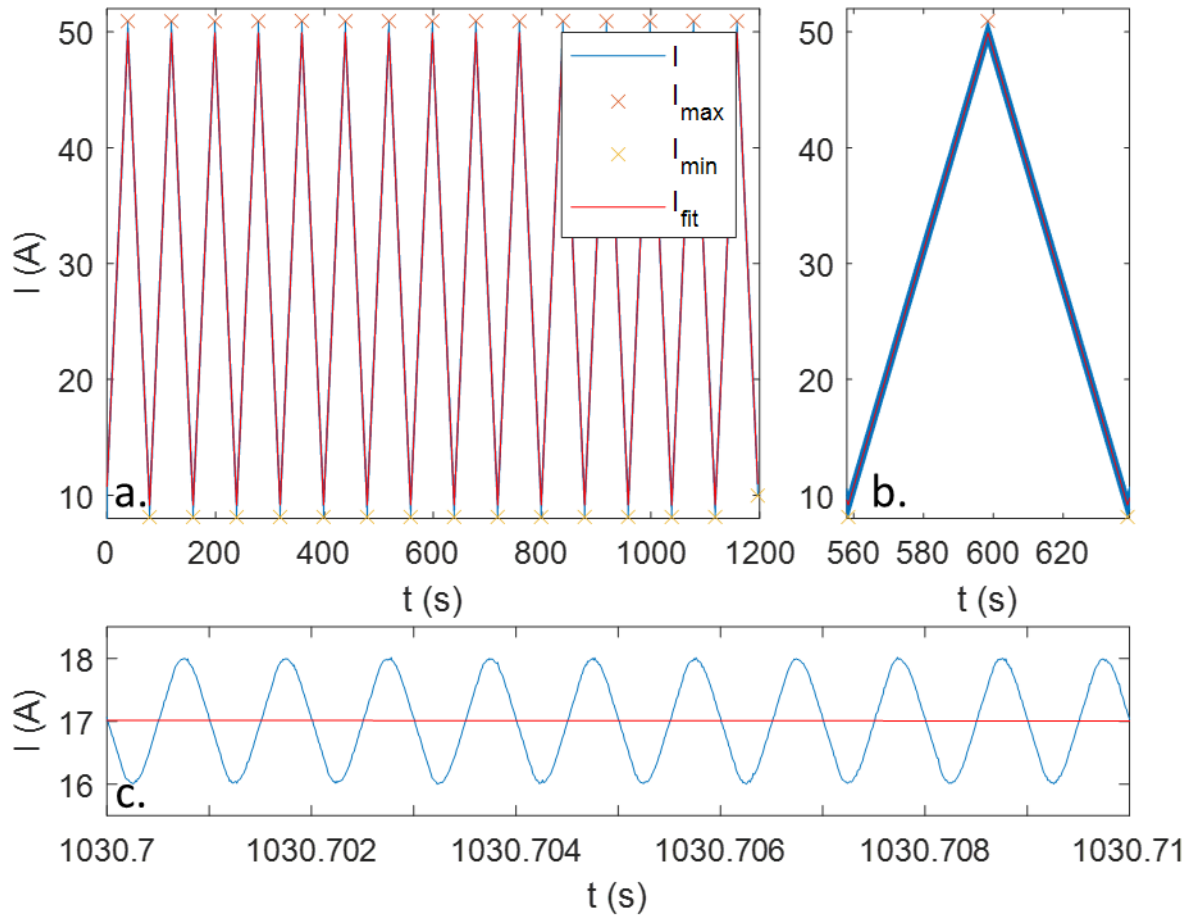


Figure IV-6: a. Current profile between 10 A and 50 A with current extremums and piecewise linear fit. b. Zoom in one period. c. Oscillations and fit during 0.01 s

The oscillating part of the signals are extracted by subtracting  $I_{tri}(t)$  from  $I(t)$  and  $U_{av}(t)$  from  $U(t)$ . The total time interval of 1200 seconds is sliced into 0.1 second intervals  $\delta t_k$  and sinusoidal fits of  $I_{sin}(t)$  and  $U_{sin}(t)$  are performed as:

$$\begin{aligned} I_{sin}(t) &= A_I^k \sin(\omega t + C_I^k) \\ U_{sin}(t) &= A_U^k \sin(\omega t + C_U^k) \end{aligned} \quad (IV-20)$$

$$t \in \delta t_k$$

Here,  $A_I^k$  and  $A_U^k$  are the oscillations amplitudes of current and voltage respectively,  $\omega = 2\pi \times f$  is the angular frequency, known and thus provided to the optimization function and  $C_I^k$  and  $C_U^k$  are the phase shifts. For each time interval  $\delta t_k$ , the 1-kHz resistance  $R_{1kHz}^k$  is computed by dividing the voltage amplitude  $A_U^k$  by the current amplitude  $A_I^k$ :

$$R_{1kHz}^k = \frac{A_U^k}{A_I^k} \quad (IV-21)$$

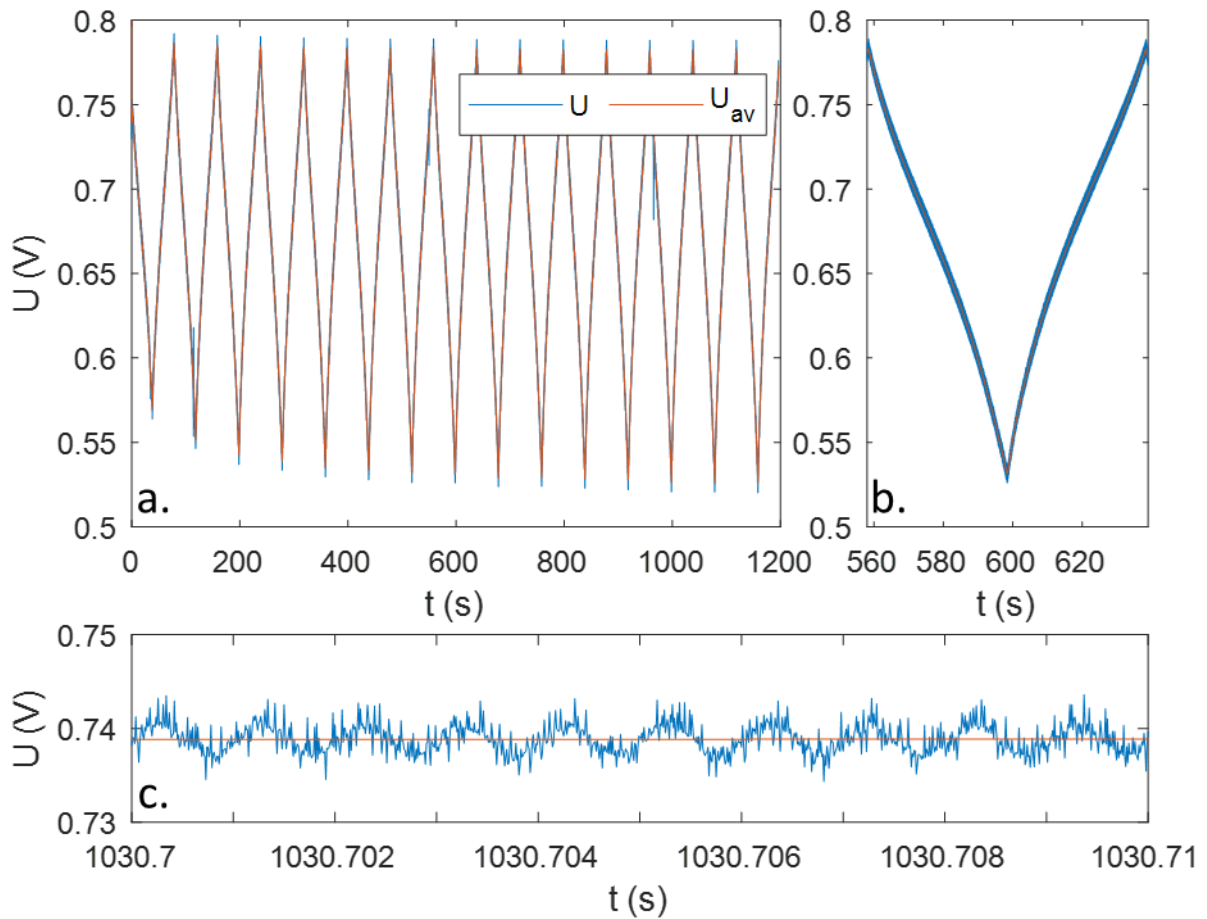


Figure IV-7: a. Voltage profile associated to Fig. IV-6 with moving average. b. Zoom on one period. c. Oscillations and average during 0.01 s

## II – 3.2. Water balance

Water management is of high importance during dynamic current regime in order to avoid cell flooding or drying and consequently to benefit from the best performances. Water balance in real-time is performed during the load cycling experiments. The aim is to investigate water storage within the cell and how it influences the performances.

Fig. IV-5 represents all water fluxes within the cell. As it has been previously exposed, the stored water flux  $N_{st}$  is computed by performing the difference between inlet and outlet water fluxes  $n_w^{a,c,in}$  and  $n_w^{a,c,out}$ .

$$n_w^{a,in} = n_{H_2}^{a,in} \times \frac{P_{sat}(T_{dp}^{a,in})}{P_a^{in} - P_{sat}(T_{dp}^{a,in})}$$

$$n_w^{c,in} = n_{air}^{c,in} \times \frac{P_{sat}(T_{dp}^{c,in})}{P_c^{in} - P_{sat}(T_{dp}^{c,in})}$$
(IV-22)

Here,  $P_a^{in}$  and  $P_c^{in}$  respectively represent the total pressure at the anode and cathode inlets.  $T_{dp}^{a,in}$  and  $T_{dp}^{c,in}$  are the inlet dew point temperatures of the gas mixture at the anode and cathode (measured is by by-passing the cell and sending the inlet gas straight into the outlet humidity sensors, see section II – 2.2. Procedure). At the outlet, the water fluxes are:

$$n_w^{a,out} = \left( n_{H_2}^{a,in} - \frac{I}{2F} + n_{H_2}^{a,dry} \right) \times \frac{P_{sat}(T_{dp}^{a,out})}{P_a^{out} - P_{sat}(T_{dp}^{a,out})}$$

$$n_w^{c,out} = \left( n_{air}^{c,in} - \frac{I}{4F} + n_{air}^{c,dry} \right) \times \frac{P_{sat}(T_{dp}^{c,out})}{P_c^{out} - P_{sat}(T_{dp}^{c,out})}$$
(IV-23)

In Eq. IV-23, the first term of the right hand contains three contributions: the inlet gas flow rate  $n_g^{a,c,in}$ , the gas flux consumed by the electrochemical reaction ( $\frac{I}{2F}$  for the anode,  $\frac{I}{4F}$  for the cathode) and the addition of dry gas  $n_g^{a,c,dry}$  to evaporate the potential liquid water in the channel end. It is assumed that the latter does not carry any water vapor with it.

The stored water flux  $n_{st}(t) = S \times N_{st}(t)$ , given by Eq. IV-13, is integrated to determine the amount of water stored in the cell, denoted as  $\tilde{n}_{st}$  (mol), as a function of time:

$$\tilde{n}_{st}(t) = \int_{\tau=0}^{\tau=t} n_{st}(\tau) d\tau \quad (IV-24)$$

This assumes that the cell does not contain any liquid water at the beginning of the experiment and that the sorbed water in the membrane is negligible. Practically, this integral is simplified into a cumulative sum (*cumsum* function of MATLAB) of the stored water flux multiplied by the constant time step of data acquisition  $\Delta\tau$ :

$$\tilde{n}_{st}(t) = \Delta\tau \times \sum_{\tau=0}^{\tau=t} n_{st}(\tau) \quad (IV-25)$$

The above presented model assumes that water is stored within the cathode GDL. The stored water  $\tilde{n}_{st}(t)$  is converted into the GDL saturation  $S_c$ , assuming that all water is in liquid form:

$$S_c(t) = \frac{\tilde{n}_{st}(t) \times M_w}{\rho_{w,liq} V_c} \quad (IV-26)$$

With  $V_c = \epsilon V_{GDL}$ .  $M_w$  is the molar mass of water,  $\rho_{w,liq}$  is the density of liquid water,  $\epsilon$  is the porosity of the compressed GDL and  $V_{GDL}$  is the total volume of compressed GDL.

## II – 4. Transient experiments – Results

### II – 4.1. Voltage and 1-kHz resistance

#### II – 4.1.a) Time data

Fig. IV-8 represents the time data for the cell voltage during the experiments with four sweeping velocities: 0.6, 1, 1.4 and 2 A s<sup>-1</sup>. The four experiments are performed for the same time range of 1200 seconds and the number of periods is thus different for the four experiments, respectively 9, 15, 21 and 30. It can be seen that both the minimum and maximum voltages ( $U_{min}(t)$  and  $U_{max}(t)$ ) decrease with time. After 9 periods at the

lowest velocity, pseudo steady-state is not reached since  $U_{\min}(t)$  and  $U_{\max}(t)$  are not stable. For the highest velocity, pseudo steady-state is reached after 10-15 periods.

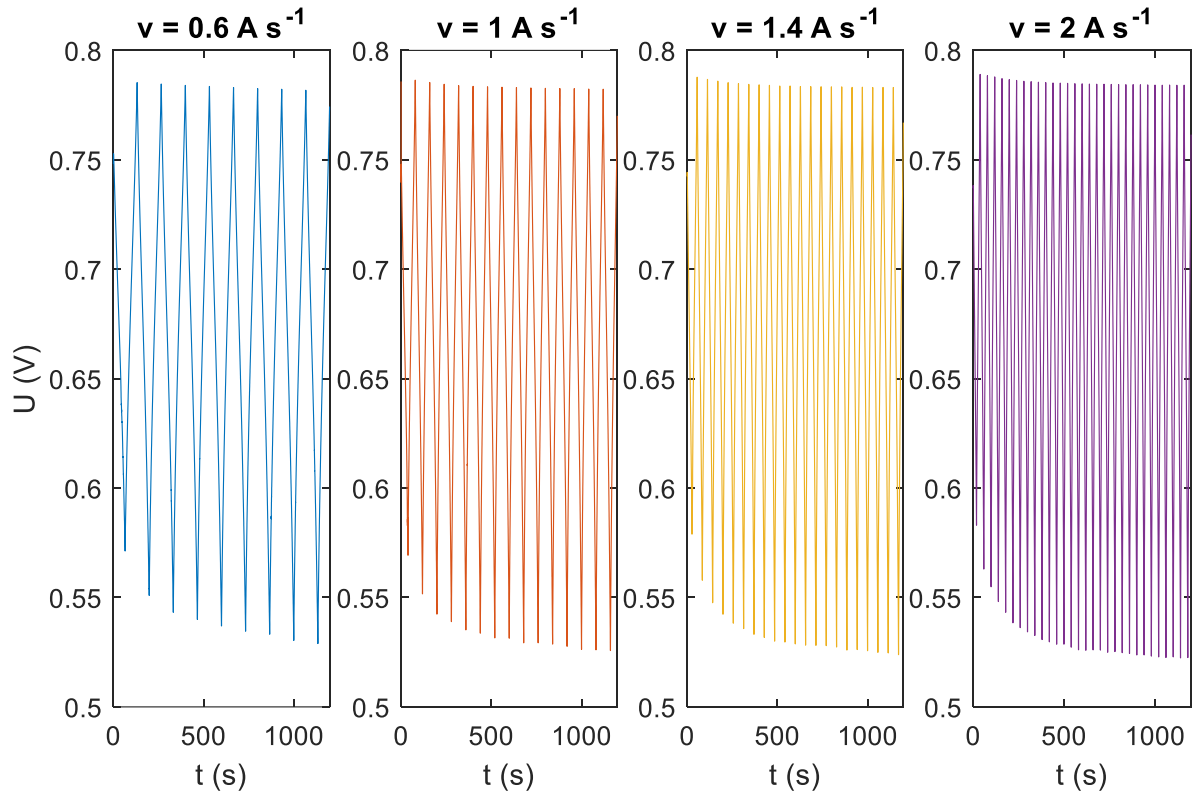


Figure IV-8: Cell voltage vs time for 4 sweeping velocities

## II – 4.1.b) Polarization curves and hysteresis

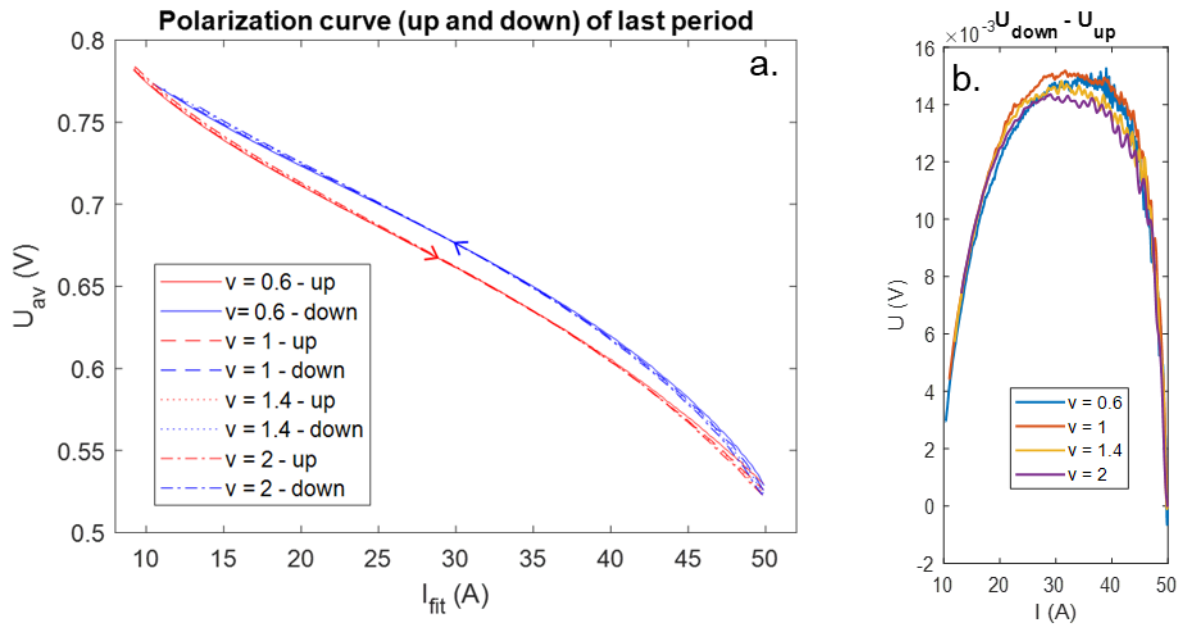


Figure IV-9: a. Polarization curves of last period for each sweeping velocity  $v$ . b. Voltage difference between decreasing and increasing current ramps

The polarization curves of the last period of each experiment are presented in Fig. IV-9a. For each sweeping velocity  $v$ , the polarization curves are nearly the same and a hysteresis appears between the increasing and decreasing current curves. Fig. IV-9b represents the voltage difference between the increasing and decreasing current ramps for each sweeping velocity. The maximum difference is reached around 30 A ( $1.2 \text{ A cm}^{-2}$ ), with a value between 14 mV and 15 mV. This difference has no obvious dependence on the sweeping velocity. It has to be noted that the experiment with  $v = 0.6 \text{ A s}^{-1}$  only contains 9 periods. Temporal data suggests that the pseudo-steady-state, and thus minimum voltage, are not exactly reached by the end of the experiment.

Polarization curves suggest that overvoltages are higher during the increasing current ramp than for the decreasing one. Fig. IV-10 represents  $R_{1\text{kHz}}$  (which is a contribution to overvoltages) as a function of current for increasing and decreasing ramp, for each velocity. The values are averaged on the last five periods of the experiments. This graph shows that  $R_{1\text{kHz}}$  globally decreases with increasing sweeping velocity, between a maximum of  $1.65 \text{ m}\Omega$  ( $41.25 \text{ m}\Omega \text{ cm}^2$ ) and a minimum of  $1.54 \text{ m}\Omega$  ( $38.5 \text{ m}\Omega \text{ cm}^2$ ). Leaving aside the shift on the values, each  $R_{1\text{kHz}}$  behaves similarly with the current: starting from  $I = 10 \text{ A}$  ( $0.4 \text{ A cm}^{-2}$ ), the resistance slightly increases up to  $I =$

20 A ( $0.8 \text{ A cm}^{-2}$ ) and then continuously decreases for the remaining up ramp. A similar symmetric behavior is observed for the downhill ramp but the resistance is higher in the current interval between 30 A and 50 A ( $1.2 \text{ A cm}^{-2}$  and  $2 \text{ A cm}^{-2}$ ). For the lower current values, the resistance during decreasing ramps is lower than for the increasing ones.

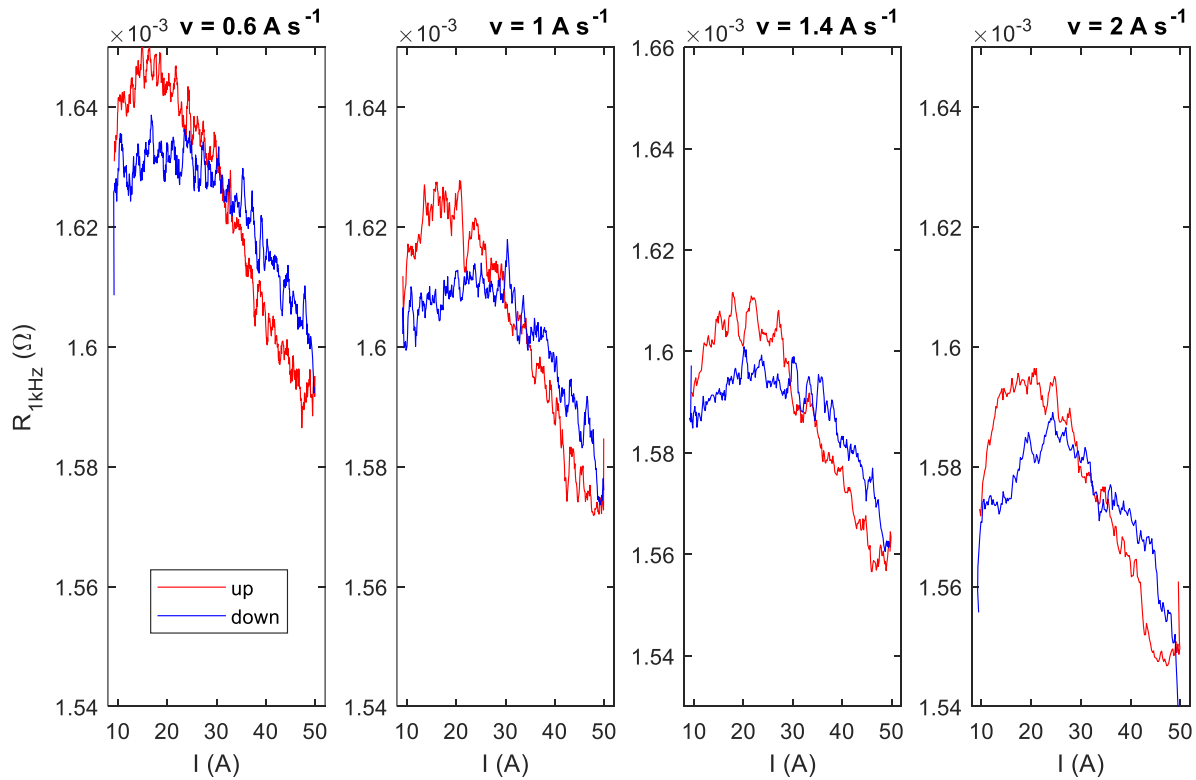


Figure IV-10: 1-kHz resistance versus current for each sweeping velocity. Curves are averaged on the last 5 periods

As suggested by the time data of Fig. IV-8, the pseudo-steady state is not reached for all the sweeping velocities. This could explain the shift in  $R_{1\text{kHz}}$  of Fig. IV-10. In the Appendix, 1-kHz resistance for all periods and for the four studied sweeping velocities are represented. For a given velocity, all periods are similar and no significant evolution of  $R_{1\text{kHz}}$  is observed. In addition, one can notice a difference of  $R_{1\text{kHz}}$  for the four velocities from the first period. Consequently, one can conclude that the shift in  $R_{1\text{kHz}}$  of Fig. IV-10 is due to the sweeping velocity and not to the duration of transient regime.

For each velocity, Fig. IV-10 shows that  $R_{1\text{kHz}}$  is equal for increasing and decreasing current at  $I = 30 \text{ A}$ . Consequently, the hysteresis between both polarization curves does not originate from this contribution to overvoltage. This is confirmed by Fig. IV-11

which presents the polarization curves corrected by ( $R_{1\text{kHz}} \times I$ ) of last period for each sweeping velocity. At  $I = 50$  A, voltage decreases with increasing velocity whereas  $R_{1\text{kHz}}$  decreases. These voltage differences do not originate from  $R_{1\text{kHz}}$  either. It has to be noted that the charge transfer resistance contributes to  $R_{1\text{kHz}}$  and varies with the inverse of the current.

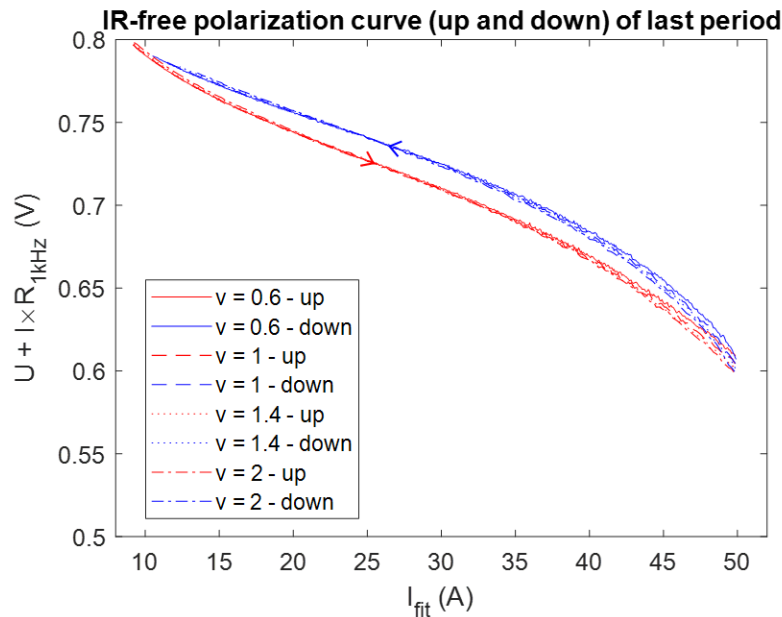


Figure IV-11: Polarization curve corrected by the overvoltage due to the 1 kHz resistance for the last period and for each sweeping velocity  $v$

#### II – 4.1.c) Temperature influence

The MEA temperature has an effect on  $R_{1\text{kHz}}$  and its influence has to be discussed. During triangle shaped current profile, MEA temperature is expected to follow the same variations: at high current, a large amount of heat is produced in the cathode CL and in the membrane, increasing the MEA temperature.

A specific experiment is conducted to investigate the effect of temperature and relative humidity on the 1-kHz resistance. Hioki 3560 AC m $\Omega$  HiTESTER is connected to the cell to measure the resistance. The cell is fed with air and hydrogen and current is kept at 0 A so that the MEA temperature is equal to the plate temperature. Fig. IV-12 represents  $R_{1\text{kHz}}$  as a function of the plate temperature. The inlet dew point temperature follows the increase of plate temperature so that inlet relative humidity is very close to 1 for all points. In this case, the membrane is fully humidified for all points

and the resistance is observed to decrease with increasing temperature. In standard assemblies of PEMFC, a temperature difference between plates and MEA up to 10 °C [65] can be observed at high current density, depending on cell efficiency and assembly materials. According to Fig. IV-12, a 5 °C temperature variation of a fully humidified MEA leads to a  $R_{1kHz}$  variation from 1.68 mΩ down to 1.61 mΩ.

By assuming that the MEA is fully humidified during the whole triangle experiment ( $rh = 1$ ),  $R_{1kHz}$  only varies with the MEA temperature  $T_M$ . Fig. IV-12 allows to fit  $T_M$  as a function of  $R_{1kHz}$  for  $T_M \in [65 ; 70]$  °C. The chosen expression is:

$$T_M = 60.67 + \exp(21.39 - 11.87 \times R_{1kHz}) \quad (IV-27)$$

Where  $T_M$  and  $R_{1kHz}$  are respectively expressed in °C and mΩ. By using this relation, it is possible to estimate the MEA temperature during the triangle experiments. Fig. IV-13 represents the estimated  $T_M$  as a function of time for the four considered sweeping velocities. For the lowest velocity ( $v = 0.6 \text{ A s}^{-1}$ ),  $T_M$  varies between 67 °C and 73 °C during the last period, respectively at  $I = 10 \text{ A}$  and  $I = 50 \text{ A}$ . This temperature variation is realistic and similar values can be found in the literature. However, for the highest sweeping velocity ( $v = 2 \text{ A s}^{-1}$ ),  $T_M$  exhibits higher values and stronger variations of about 10 °C for the last periods. Moreover, the maximum values, reached at  $I = 50 \text{ A}$ , are close to 83 °C, which is 18 °C higher than the plate temperature. It should be noted that these temperature values are outside the range used for the fit of Eq. IV-27 and therefore the order of magnitude should be considered more than the exact value.

At a current density of  $i = 2 \text{ A cm}^{-2}$  and a voltage of  $U = 0.52 \text{ V}$ , the total heat flux produced by the cell is  $\phi_{MEA} = i \left( \frac{LHV_{H_2}}{2F} - U \right) = 1.47 \text{ W cm}^{-2}$ . Assuming that this flux is equally evacuated by both GDLs, the expected temperature difference between the MEA and the plates is  $\Delta T = \frac{\phi_{MEA}}{2} \frac{t_{GDL}}{\kappa_{GDL}^{eff}} = 6.4 \text{ °C}$ . This difference is 3 times lower than the one estimated with the calibration of  $T_M(R_{1kHz})$ . Thus, it suggests that not only the temperature has an impact on  $R_{1kHz}$  but relative humidity should play a role as well.

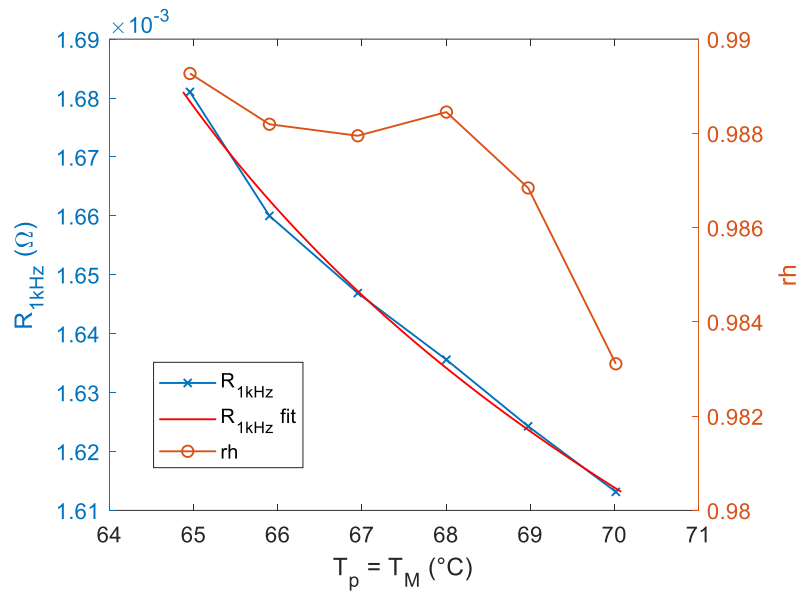


Figure IV-12: 1-kHz resistance versus cell plates temperature with no current for constant inlet relative humidity

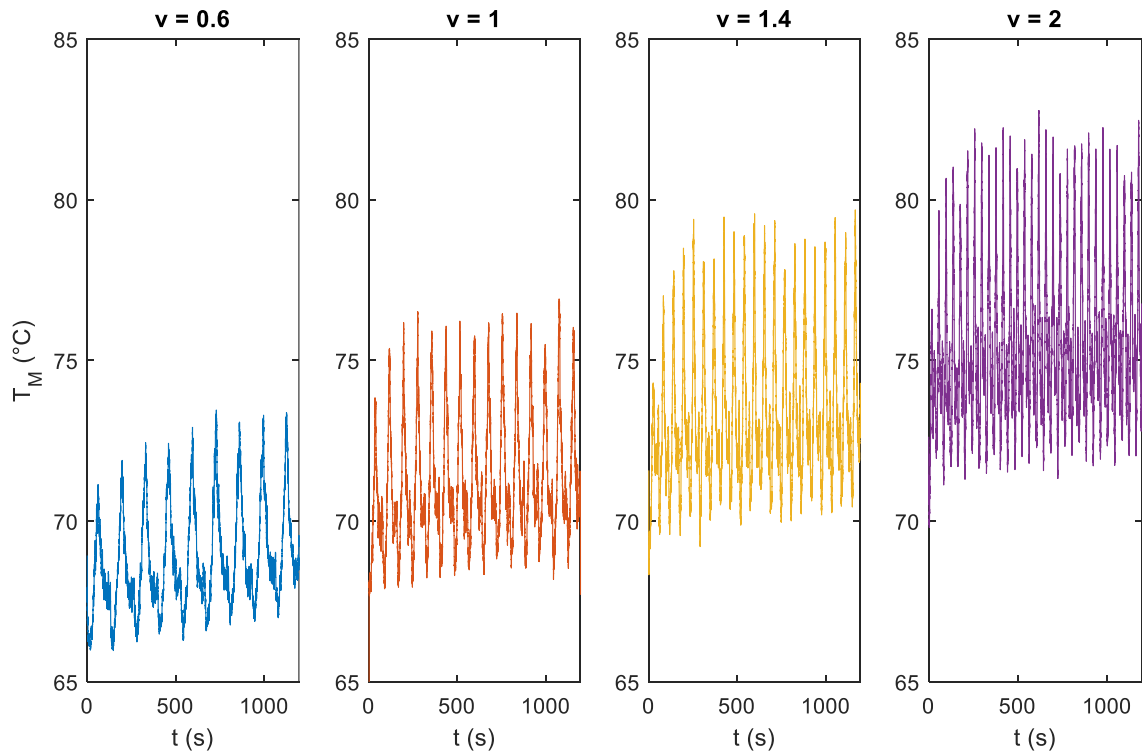


Figure IV-13: Estimated MEA temperature based on the variation of the 1-kHz resistance with temperature for a fully humidified membrane. The cell plates are regulated at 65 °C

## II – 4.2. Water balance

The cell water balance is computed using the outlet dew point temperatures as presented by Eq. IV-23. These experimental values are represented in Fig. IV-14 for

the four sweeping velocities. One can observe that this data exhibits several plateaus with time.  $T_{dp}^c$  highly increases during the first 60 seconds and then stabilizes at 57 °C with small spikes. After 900 to 1000 seconds, another plateau at 60 °C is reached. The same trend is observed for the four sweeping velocities. A similar behavior is noticed for  $T_{dp}^a$  except that only one plateau is reached after 300 seconds at 56 °C with higher spikes. The spikes are caused by the appearance of water droplets in the channels that are removed towards the manifold and dried by the gas addition. The frequency of the fluctuations increases with increasing sweeping velocity.

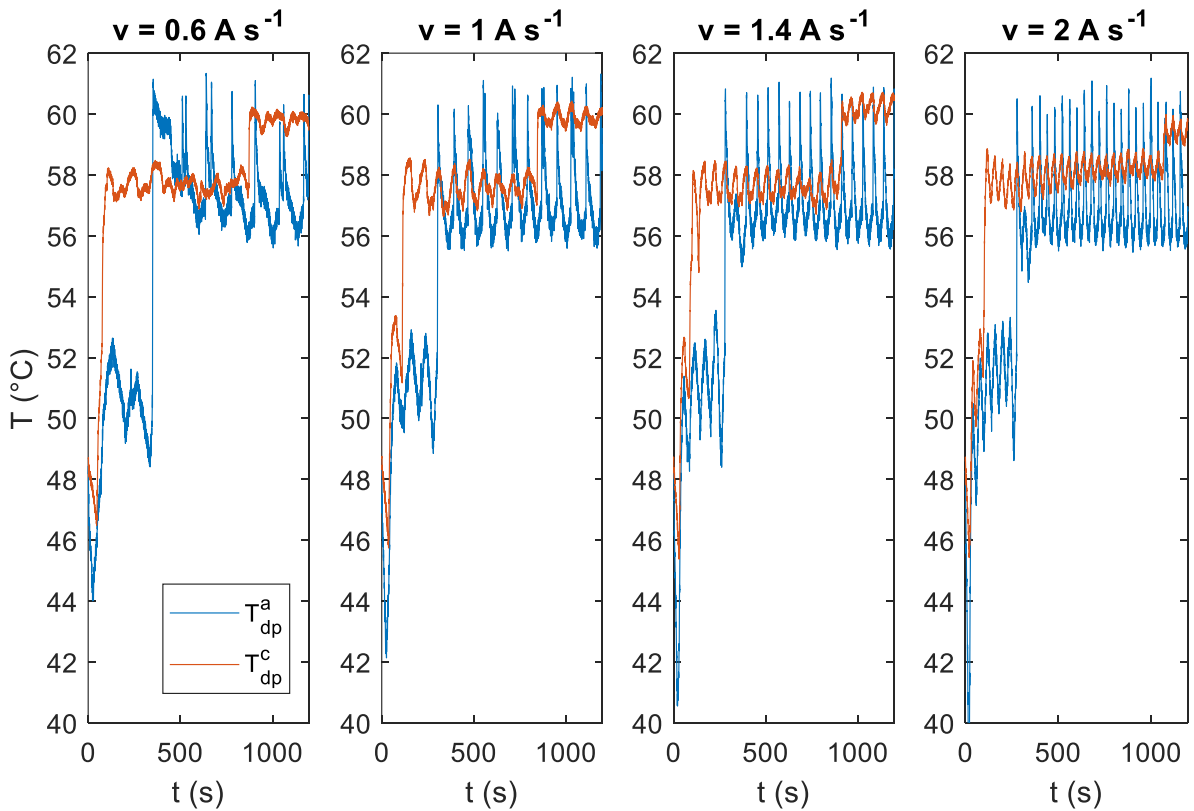


Figure IV-14: Outlet dew point temperatures with time for the four velocities

Fig. IV-15 represents the stored water flux in the cell  $n_{st}$  with time, calculated with Eq.IV-12, IV-13, IV-22 and IV-23 for the four studied sweeping velocities. The dash lines represent the production of water  $\frac{I}{2F}$  at the maximum current of 50 A. For all velocities,  $n_{st}$  alternates between positive and negative values, depicting storage and discharge phases respectively. At the beginning of each experiment, the cell is free of liquid water due to the drying step. Consequently, the first periods mainly lead to

positive values of  $n_{st}$  and thus water storage in the cell. This is even more obvious for the highest velocity ( $v = 2 \text{ A s}^{-1}$ ) where the periods are shorter.

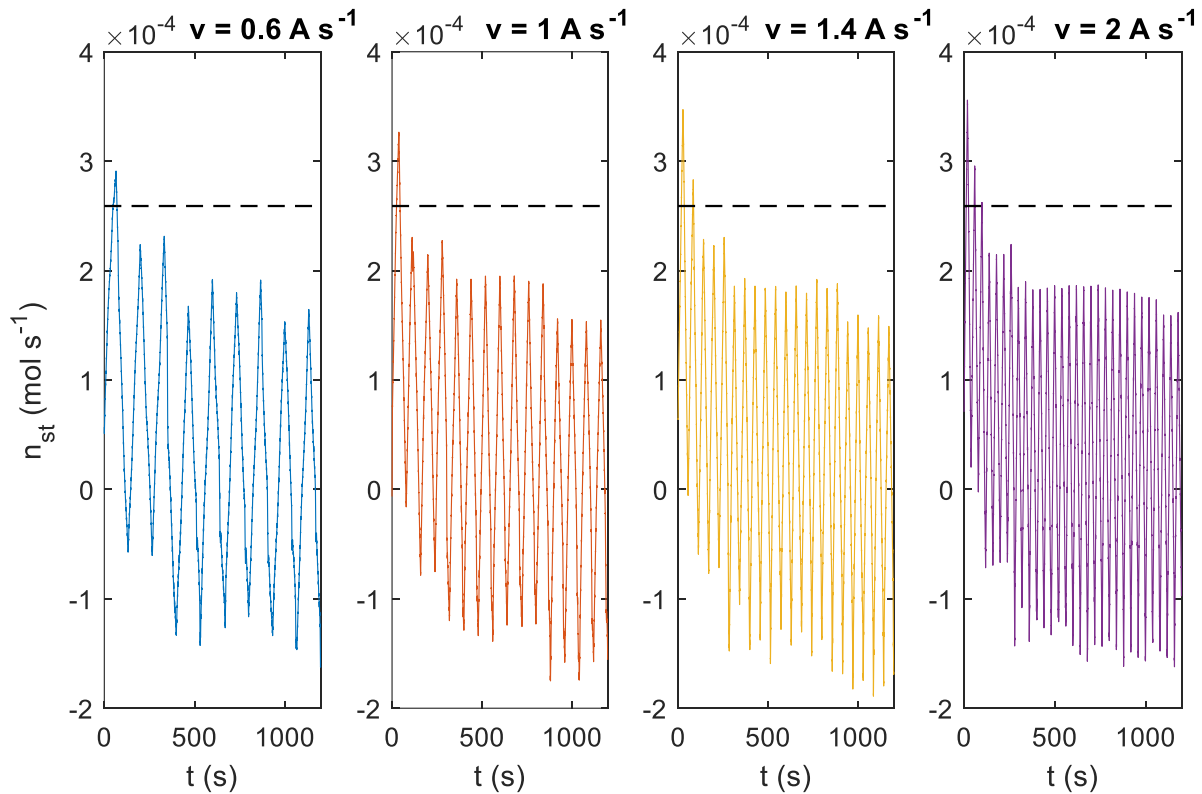


Figure IV-15: Stored water flux vs time for four sweeping velocities. The dash lines represent the water production  $\frac{I}{2F}$  at the maximum current (50 A).

The cell being fed with saturated gases, the consequence of a stored water flux is the presence of liquid water inside the cell, the amount of water vapor in the cell being negligible. The water saturation of the cell, based on the pore volume of the cathode GDL, as expressed by Eq. IV-26, is represented in Fig. IV-16 as a function of time and for the four sweeping velocities. One can notify that the saturation values exceed unity, which is not expected for the saturation of a porous media. This suggests that the volume of liquid water that is stored in the cell is higher than the considered pore volume. Indeed, some liquid water can lay in the channels for instance, increasing the volume available for water storage. The total volume of the cell  $V_{cell}$  (Table IV-3) that can be filled by liquid water is composed of:

- some pores of the two compressed GDLs,
- the channels of anode and cathode plates,

- between the gap between the GDL and the gasket (0.5 mm at the periphery of the GDL).

It is assumed here that no liquid water is stored in the manifolds of the cell. This assumption is strengthened by the dew point temperature observation:  $T_{dp}^a$  and  $T_{dp}^c$  are always below the cell temperature of 65 °C, suggesting that liquid water is never in equilibrium at the cell temperature.

Table IV-3: Total cell volume available for liquid water

Volume	Value
2 GDLs, compressed at $t_{GDL} = 173 \mu\text{m}$ with a porosity of $\epsilon = 0.5$	$2 \times (52 \times 10^{-3})^2 \times 173 \times 10^{-6} \times 0.5$ $= 4.68 \times 10^{-7} \text{ m}^3$
50 parallel cathode channels	$50 \times (50 \times 10^{-3}) \times (0.25 \times 10^{-3}) \times (0.6 \times 10^{-3})$ $= 3.75 \times 10^{-7} \text{ m}^3$
50 parallel anode channels	$50 \times (50 \times 10^{-3}) \times (0.15 \times 10^{-3}) \times (0.6 \times 10^{-3})$ $= 2.25 \times 10^{-7} \text{ m}^3$
2 gaps between GDL and gasket	$2 \times \left( (52 + 2 \times 0.5) \times 10^{-3} \right)^2 - (52 \times 10^{-3})^2$ $\times 150 \times 10^{-6} = 3.15 \times 10^{-8} \text{ m}^3$
<b>Total volume</b>	<b><math>V_{cell} = 1.1 \times 10^{-6} \text{ m}^3</math></b>

Consequently, a saturation based on  $V_{cell}$  is defined and should always be lower than unity:

$$S^*(t) = \frac{\tilde{n}_{st}(t) \times M_w}{\rho_{w,liq} V_{cell}} \quad (\text{IV-28})$$

Fig. IV-17 represents  $S^*$  as a function of time for the four sweeping velocities,  $\tilde{n}_{st}(t)$  being the cumulative sum of the stored water flux,  $S^*(t)$  increases and the maximum value is around 0.9. Similarly to Fig. IV-16, all the four curves reach the same maximum value, even though all experiments are not in pseudo steady-state at the end of the time interval. Nevertheless, one can conclude that the volume of stored water in the cell is independent of the sweeping velocity. The main difference between the four curves of Fig. IV-16 and IV-17 is the amplitude of the saturation oscillations. When the sweeping velocity is low ( $v = 0.6 \text{ A s}^{-1}$ ),  $n_{st}$  alternates between long phases of storage and discharge, leading to a large amplitude in the associated saturation: during the last

period, the maximum and the minimum differ by 0.46 in Fig. IV-16. For a higher velocity ( $v = 2 \text{ A s}^{-1}$ ),  $n_{st}$  changes from positive to negative faster and oscillations of saturation are smaller: 0.1 between the last maximum and minimum.

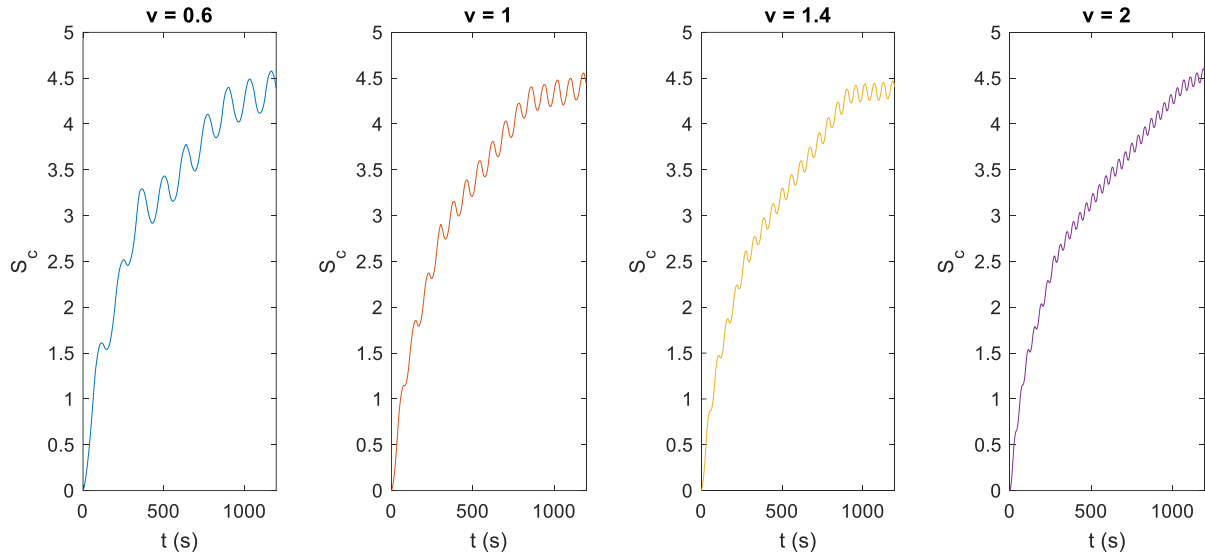


Figure IV-16: Liquid water saturation based on the pores volume of a compressed GDL with a porosity of 0.5

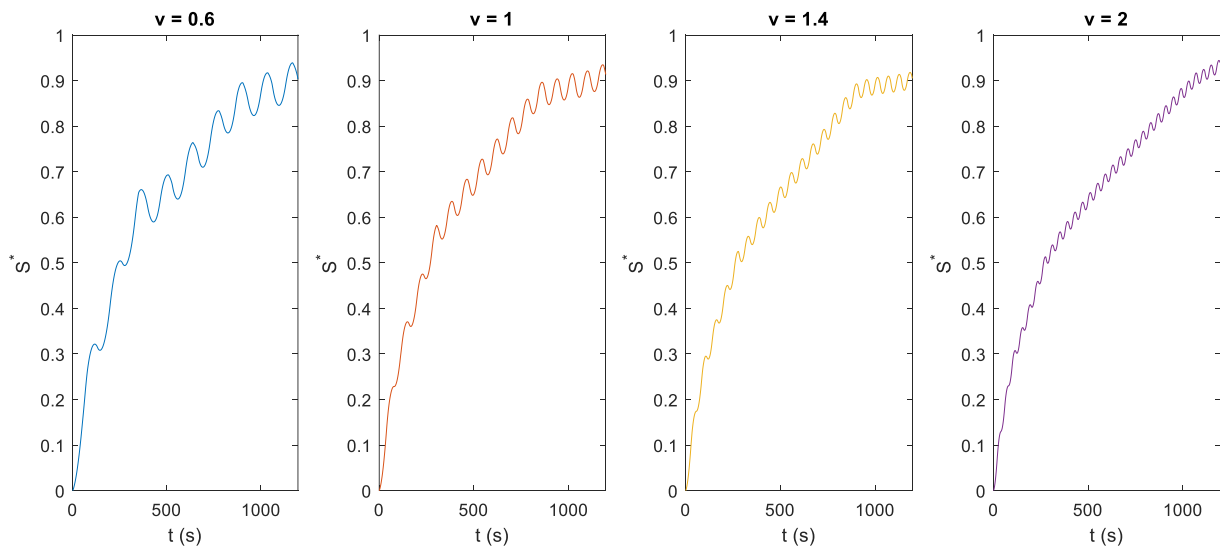


Figure IV-17: Liquid water saturation based on the total available volume in the cell

Fig. IV-18 illustrates the time evolution of some values of interest for a sweeping velocity of  $1 \text{ A s}^{-1}$ . After the very first periods, the stored water flux is synchronized with the current profile:  $n_{st}^{ad} = \frac{n_{st}(t)}{I_{max}/2F}$  reaches its maximum value at the same time as the current does, as well as for the minimum values.  $R_{1kHz}$  is in counter-phase with the

current: the minimum value is reached at the maximum current. Finally, the water saturation of the cell seems out of step with the others values. The maximum saturation is observed during the downhill current ramps and the minimum value during the uphill current ramp. This phase shift is due to the fact that the saturation is calculated as the integral of the stored flux: it increases as long as the flux is positive, reaching its maximum when  $n_{st}^{ad}$  turns negative.

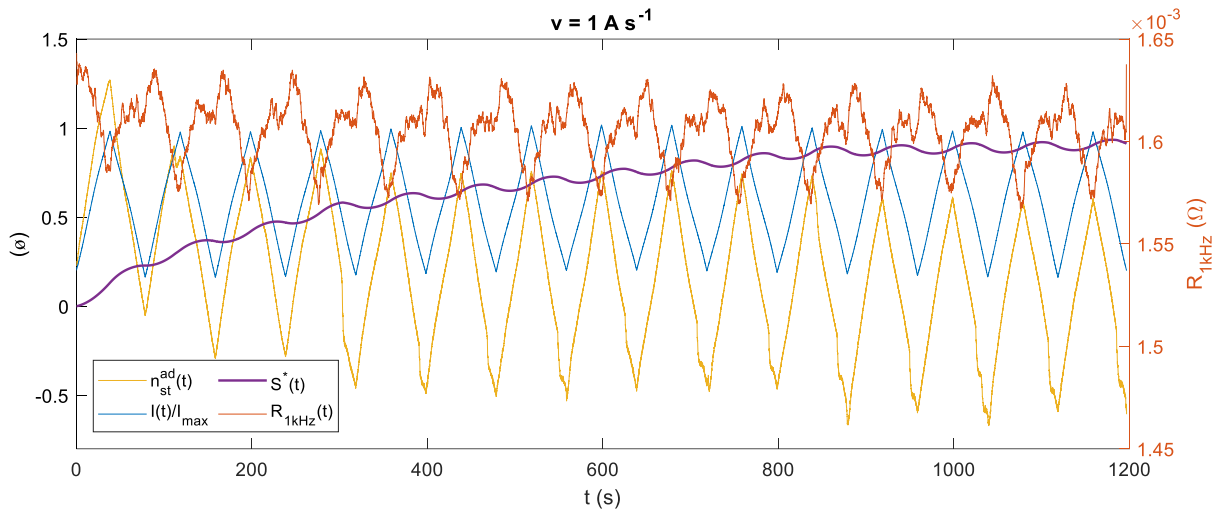


Figure IV-18: Time evolution of adimensional stored water flux  $n_{st}^{ad}$ , adimensional current  $I/I_{max}$ , 1-kHz resistance  $R_{1kHz}$  and saturation  $S^*$  for  $v = 1 \text{ A s}^{-1}$

## II – 5. Pseudo-steady state experiments – Results

Previous results showed that the pseudo-steady state was not reached after the 1200 seconds of the experiments. A pseudo-steady state is a regime where all the quantities are similar for all periods, oscillating around a constant average value. In order to reach a pseudo-steady state, experiments must be conducted during a sufficient time interval. Nevertheless, the acquisition rate of data leads to massive data files size. Consequently, in order to study established pseudo steady-state regime of the cell, another procedure is set up. For one hour, triangle load cycles are imposed to the cell, but with a reduced acquisition rate to lighten data files. After one hour, similar acquisition as previously described is performed so that the 1-kHz frequency can be computed. The sweeping velocity is  $v = 2 \text{ A s}^{-1}$ . Thus, the first hour of continuous load cycling contains 90 periods.

## II – 5.1. Transient regime

Fig. IV-19 represents the cell voltage during the first 90 periods of the pseudo steady-state experiment. The minimum voltage highly decreases during the first 15 periods and then continuously stabilizes. Even though the same working conditions (gas flow rate, inlet rh, gas composition) as for the transient experiments were used here, the minimum voltage is observed to be lower. This can originate from the ageing of the MEA after the high number of cycles that have been imposed. Inappropriate starts-up and shuts-down can also be responsible for such an ageing, because of fuel starvation for example.

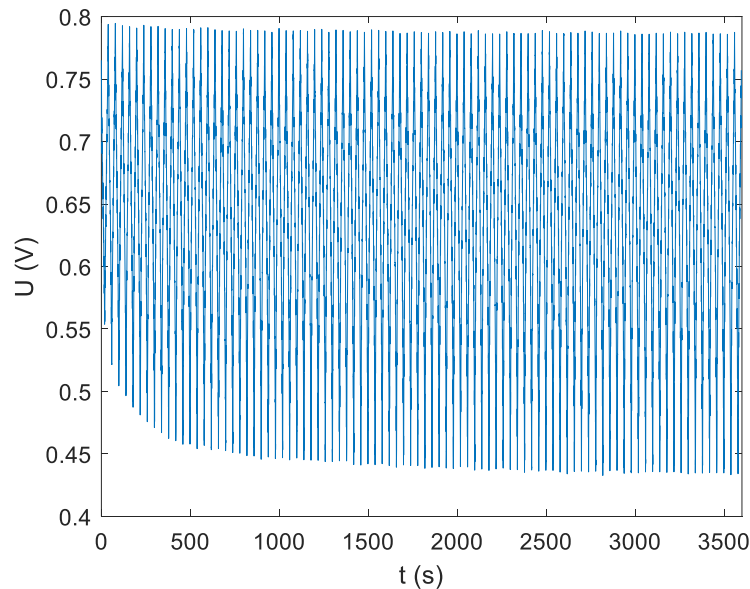


Figure IV-19: Cell voltage during transient regime with  $v = 2 \text{ A s}^{-1}$

Water storage during transient regime is also monitored. Fig. IV-20 presents the stored water flux  $n_{st}$  during the transient regime which precedes the pseudo-steady state. On this graph, two curves are represented: the raw data for  $n_{st}$  and the corrected data, being  $n_{st} - \delta_{st}$ . This correction is assumed to be an offset originating from the measurement errors (dew point temperatures and gas flow rates especially). It is calculated as the average of  $n_{st}$  during the last third (1200 s) of the experiment:

$$\delta_{st} = \frac{1}{N/3} \sum_{t=2N/3}^{t=N} n_{st}(t) \quad (\text{IV-29})$$

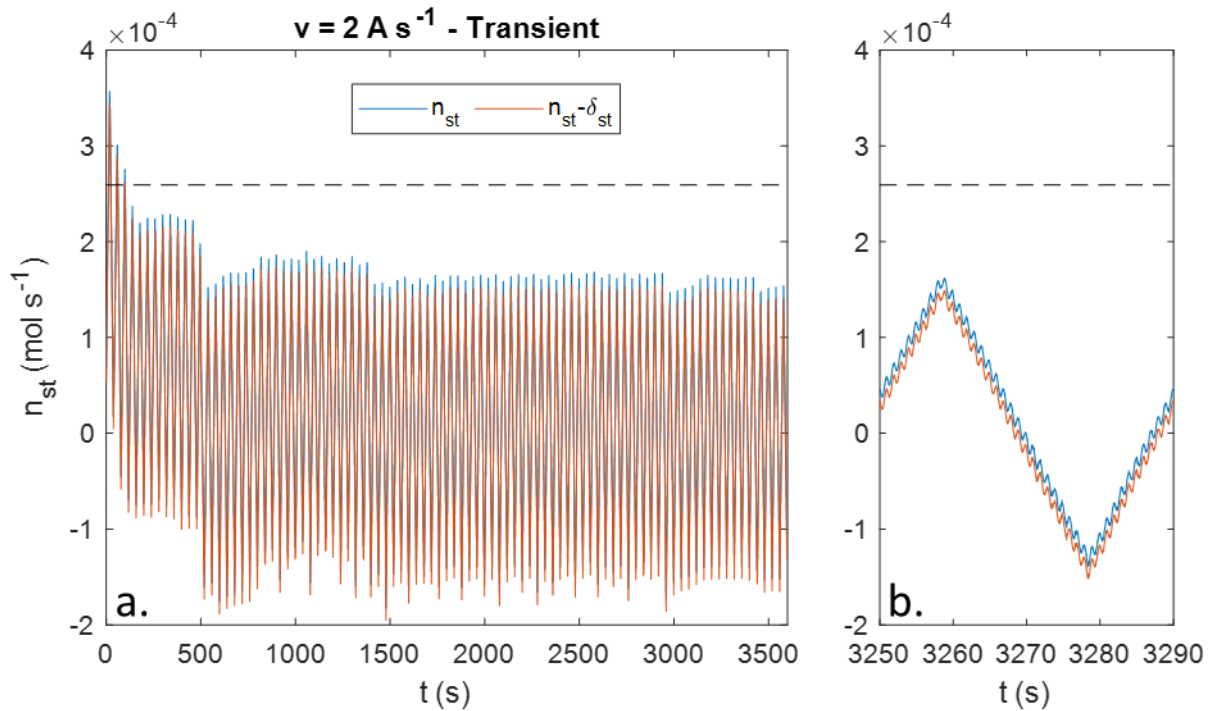


Figure IV-20: a. Stored water flux during the transient regime before pseudo-steady state ( $\delta_{st} = 1.28 \times 10^{-5} \text{ mol s}^{-1}$ ) b. Zoom on one period. The black dash line represents the water flux production of 50 A

The offset correction proposed here represents less than 10% of the maximum value of  $n_{st}$ . This slight difference leads to a significant effect on the saturation value  $S_c$ . Indeed, Fig. IV-21 represents the calculated saturation, based on the pore volume of a unique GDL. After a sharp increase during the first 500 seconds, the blue curve, based on the raw value of  $n_{st}$ , exhibits a linear variation with time. This trend originates from the integration of the residual offset, leading to high values of  $S_c$  and continuous increase, even after one hour. The orange curve, calculated with the corrected stored water flux shows the same sharp increase during the first 500 seconds, a low variation until 1500 seconds and then stabilizes. This plateau suggests that the pseudo-steady state is reached after 1500 seconds, which is also noticeable on the voltage curve.  $S_c$  stabilizes around 4.3, which is similar to the values observed during the transient experiments. The amplitude of 0.12 for the fluctuations is also similar.

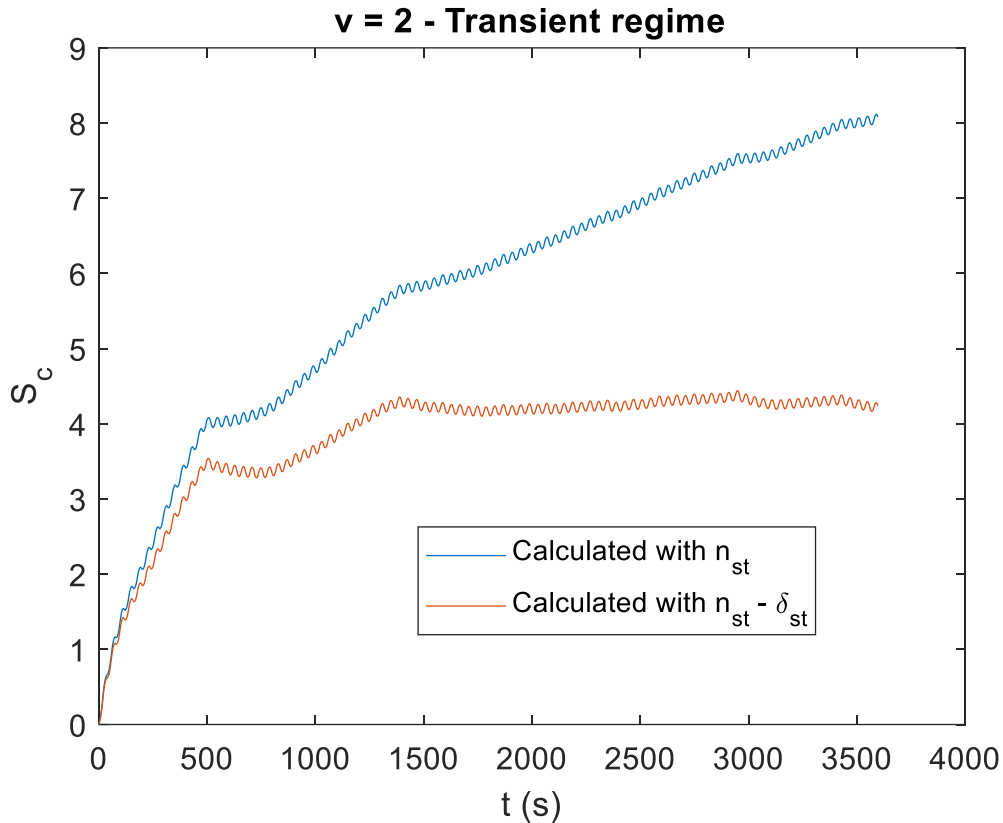


Figure IV-21: Saturation based on 1 GDL pore volume during transient regime before pseudo-steady state

## II – 5.2. Voltage and 1-kHz resistance in pseudo-steady state

The cell voltage during the last 15 periods of the pseudo-steady state experiment is presented in Fig. IV-22. It varies between 0.78 V and 0.44 V. One can notify that these two limits are constant for all periods, meaning that the cell voltage reached a pseudo-steady state. The polarization curves for the last 5 periods are presented in Fig. IV-23. This graph exhibits a hysteresis between the increasing and decreasing current, voltage being higher during the downhill current ramp. The five curves perfectly superimpose, meaning that the pseudo-steady state is reached.

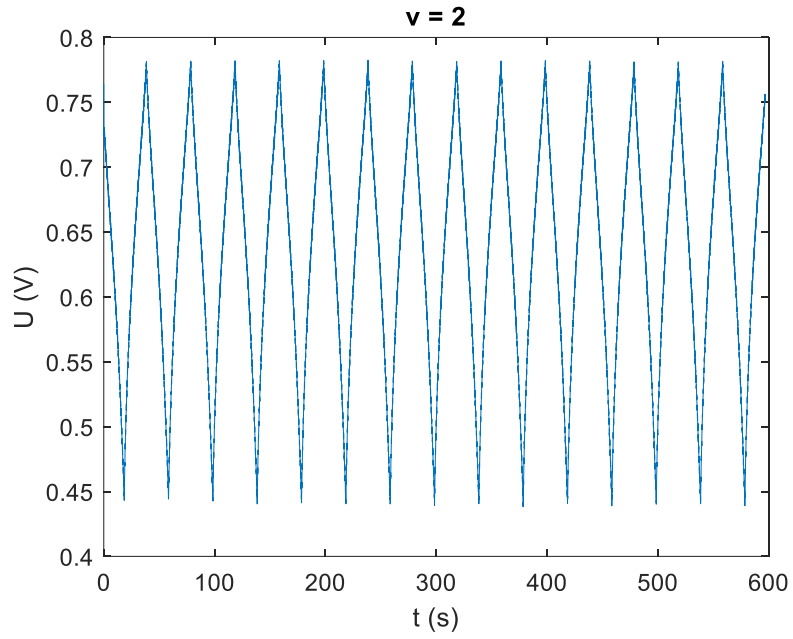


Figure IV-22: Cell voltage during 15 periods in pseudo steady-state at a sweeping velocity of  $v = 2 \text{ A s}^{-1}$

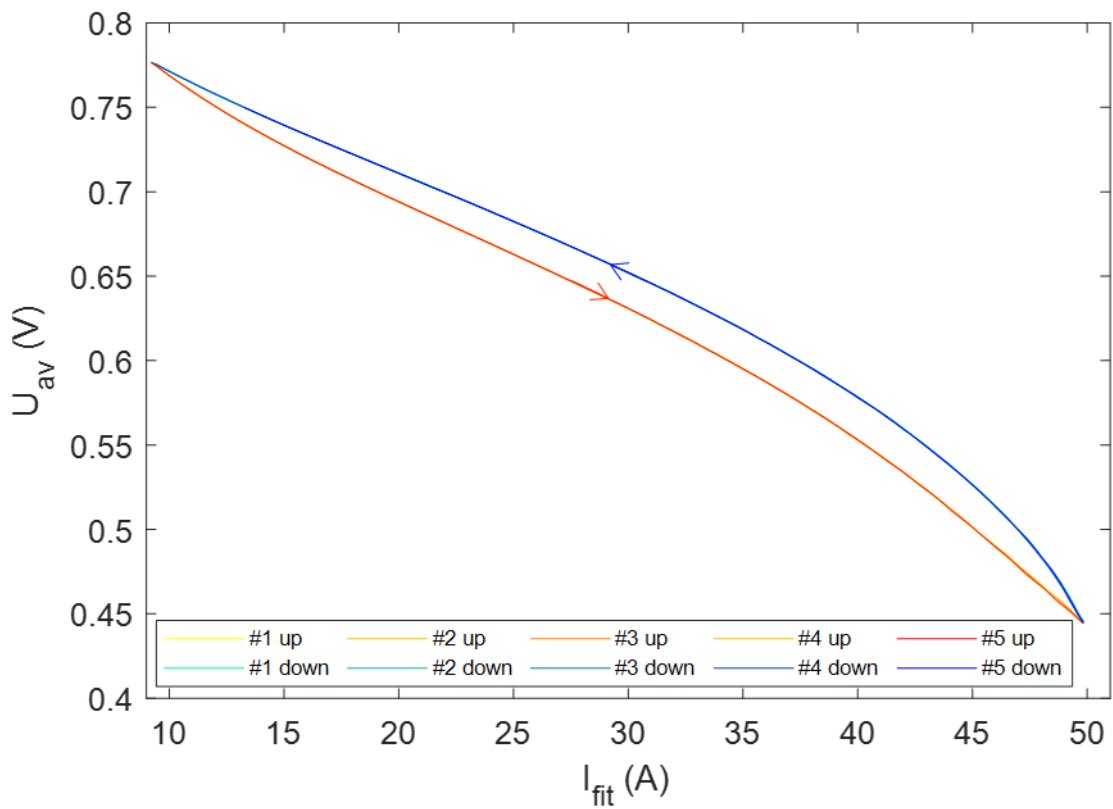


Figure IV-23: Polarization curve of last 5 periods of pseudo-steady state experiment

Fig. IV-24 represents the 1-kHz resistance average during the last 5 periods of the pseudo-steady state experiment. For current between 10 A and 25 A,  $R_{1\text{kHz}}$  increases with current and values are similar for downhill and uphill current ramp. The maximum resistance is reached between  $I = 20\text{ A}$  and  $I = 25\text{ A}$ . After this maximum,  $R_{1\text{kHz}}$  decreases with increasing current and a difference is observed between uphill and downhill ramp: the resistance is higher when current decreases. The variation is quite linear for the blue curve while a minimum resistance is observed at  $I = 43\text{ A}$  for the red curve. This difference suggests that the ionomer is more humidified during the uphill current ramp. In addition, the slight increase of the resistance after  $I = 43\text{ A}$  suggests that the ionomer becomes dryer for the highest currents, right before the downhill ramp.

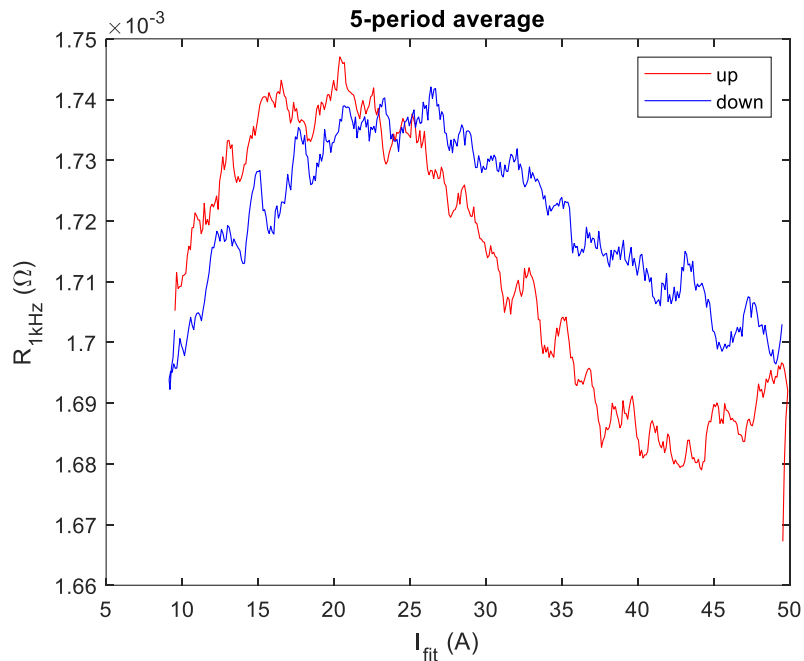


Figure IV-24: 1-kHz resistance average on the 5 last periods of the pseudo-steady state experiment

### II – 5.3. Water balance in pseudo-steady state

As it was explained in section II – 5.1. Transient regime, the pseudo-steady state being reached, the stored water flux should be centered to 0, alternating from storage phases to discharge phases, balancing each other. Fig. IV-25 represents  $n_{\text{st}}$  corrected of its average  $\delta_{\text{st}}$ .

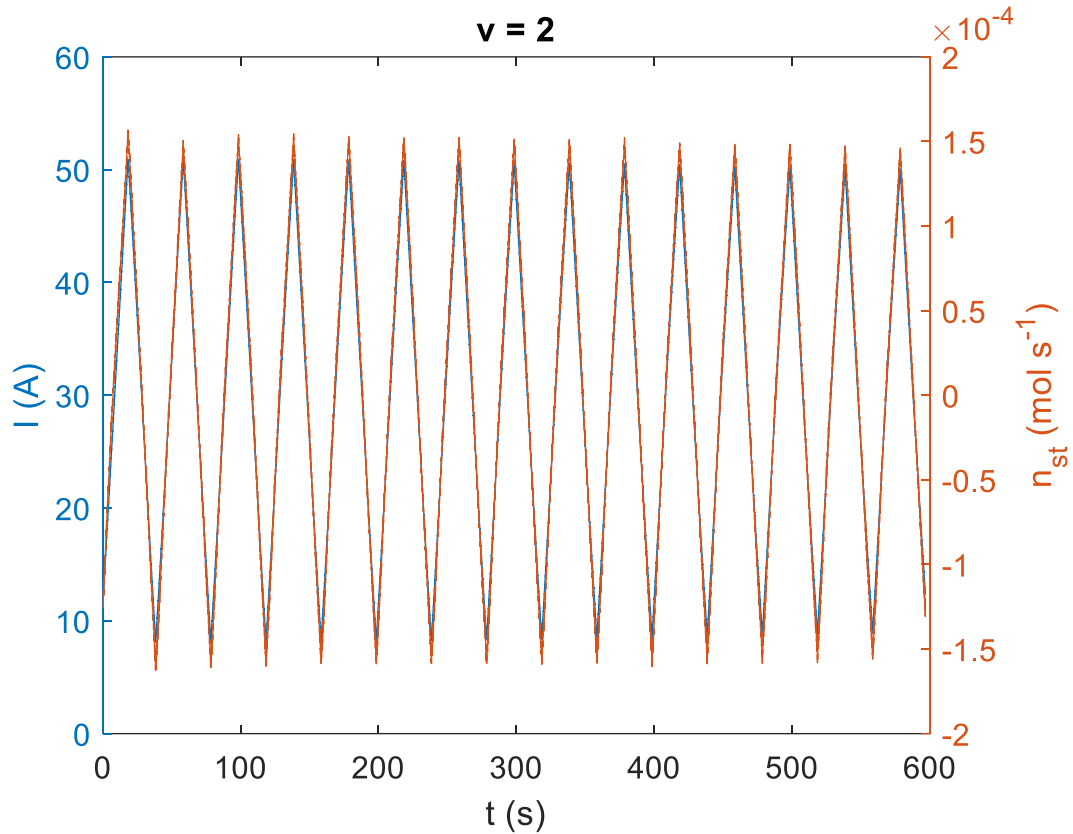


Figure IV-25: Corrected stored water flux during pseudo-steady state ( $\delta_{st} = 1.33 \times 10^{-5} \text{ mol s}^{-1}$ )

The resulting saturation is presented in Fig. IV-26. This value is calculated so that at  $t = 0$  the cell has already reached its pseudo-steady state average value. Consequently, only the oscillating part of the water content of the cell is extracted here and the saturation can be split with two contributions: the constant average value  $S_c^\infty$  and the oscillating part  $\Delta S_c(t)$ .

$$S_c(t) = S_c^\infty + \Delta S_c(t) \quad (\text{IV-30})$$

The amplitude of  $\Delta S_c(t)$  is 0.12, as previously described by other experiments. The maximum saturation appears at the beginning of the downhill current ramp while the minimum is reached during the increasing ramp.

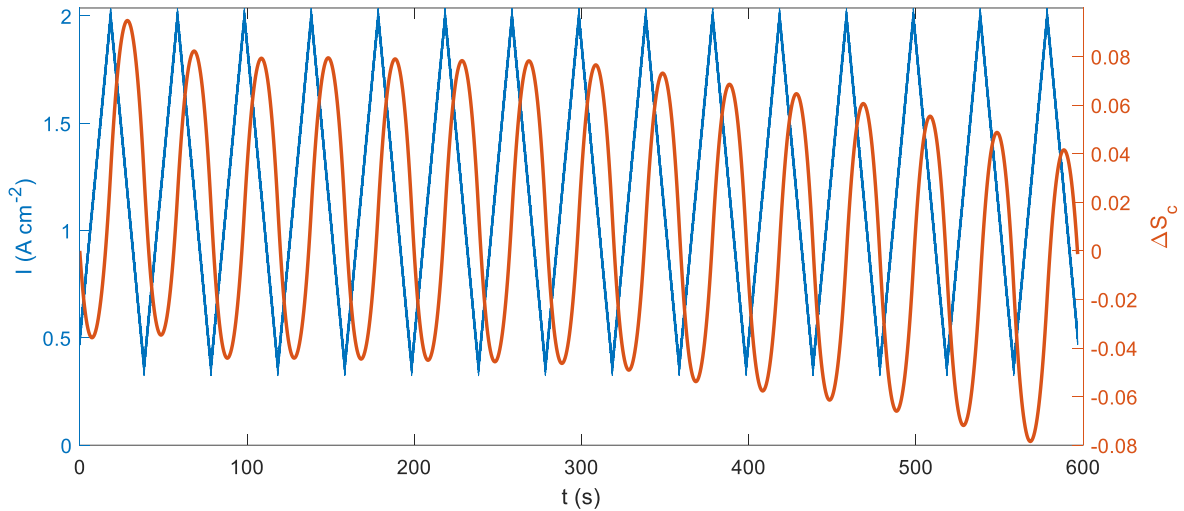


Figure IV-26: Saturation calculated based on the pore volume of 1 GDL during pseudo-steady state superimposed with current profile

### III – Comparison between model and pseudo-steady state experiments

The development of a model in parallel with experiments should lead to the estimation of crucial parameters for water transport modeling. The wettable volume  $V_c$  and the limiting saturation  $S_{lim}$  appear to have a major influence on the water storage and have to be estimated. Here, only a preliminary work is exposed, roughly comparing experiments and modeling and giving insights on the improvements to achieve.

#### III – 1. Parametrization

The above developed model contains parameters that influence water transport and storage in the cell:

$$p = [\kappa_{GDL}, V_c, D_c^{eff}, D_a^{eff}, D_M, \xi, S_{lim}, \chi_1, \chi_2] \quad (IV-31)$$

Some of these parameters have been estimated with previous experiments, as developed in previous chapters. Consequently, some parameters are kept constant during the model study:

$$\left\{ \begin{array}{l} \kappa_{GDL} = 0.2 \text{ W m}^{-1} \text{ K}^{-1} \\ D_c^{eff} = 6.5 \times 10^{-6} \text{ m}^2 \text{ s}^{-1} \\ D_a^{eff} = 2 \times 10^{-5} \text{ m}^2 \text{ s}^{-1} \\ D_M = 3 \times 10^{-10} \text{ m}^2 \text{ s}^{-1} \end{array} \right. \quad (\text{IV-32})$$

### III – 1.1. Electro-osmotic drag

The electro-osmotic drag (EOD) has been studied by Peng et al. [105] for reinforced Nafion membranes, similar as the employed Gore membrane. The authors showed that, for a current density range from 20 to 100 mA cm<sup>-2</sup>,  $\xi$  is a decreasing function of the water content, starting from  $\xi = 0.9$  for  $\lambda = 2$  down to  $\xi = 0.1$  for  $\lambda > 8$ . Sellin et al. [90] studied the EOD as a function of the current density and concluded that  $\xi$  is independent of the current. For pure Nafion membranes, the authors showed that  $\xi$  is independent of the relative humidity but is an increasing function of the temperature. Nafion XL exhibit a variation of the EOD coefficient with the relative humidity at 60 °C: from  $\xi = 0.7$  at rh = 0.5 down to  $\xi = 0.4$  at rh = 0.95.

In the present experiments, the feeding gas are humidified close to saturation, suggesting that the membrane is well humidified. For this reason, and regarding literature data, EOD coefficient is fixed at  $\xi = 0.4$  for the whole current range, regardless of the water content of the membrane.

### III – 1.2. Polarization curve

The voltage hysteresis is considered in the model. Both curves of Fig. IV-23 are fitted with an expression similar as the one proposed by Weber and Newman [40]:

$$U = \beta_1 + \beta_2 \times \ln(I) + \beta_3 \times I + \beta_4 \times \ln\left(1 - \frac{I}{I_{lim}}\right) \quad (\text{IV-33})$$

The estimated parameters for increasing and decreasing current ramps are listed in Table IV-4 and the curves are plotted in Fig. IV-27. It has to be notified that  $\beta_3$  represents the ohmic part of the overvoltage and is thus strictly negative. The limiting current  $I_{lim}$  is lower for  $U_{down}$  than for  $U_{up}$ , as well as the OCV  $\beta_1$ . Nevertheless, this parametrization does not intend to model the link between voltage and current, but only

to numerically implement the measured polarization curves, considering the hysteresis.

Table IV-4: Fitting parameters for the voltage hysteresis

	$\beta_1$ (V)	$\beta_2$ (V)	$\beta_3$ (V A <sup>-1</sup> )	$\beta_4$ (V)	$I_{lim}$ (A)
$U_{up}$	0.9185	-0.054	0	0.1531	60.3
$U_{down}$	0.8803	-0.034	-0.0011	0.0997	54.4

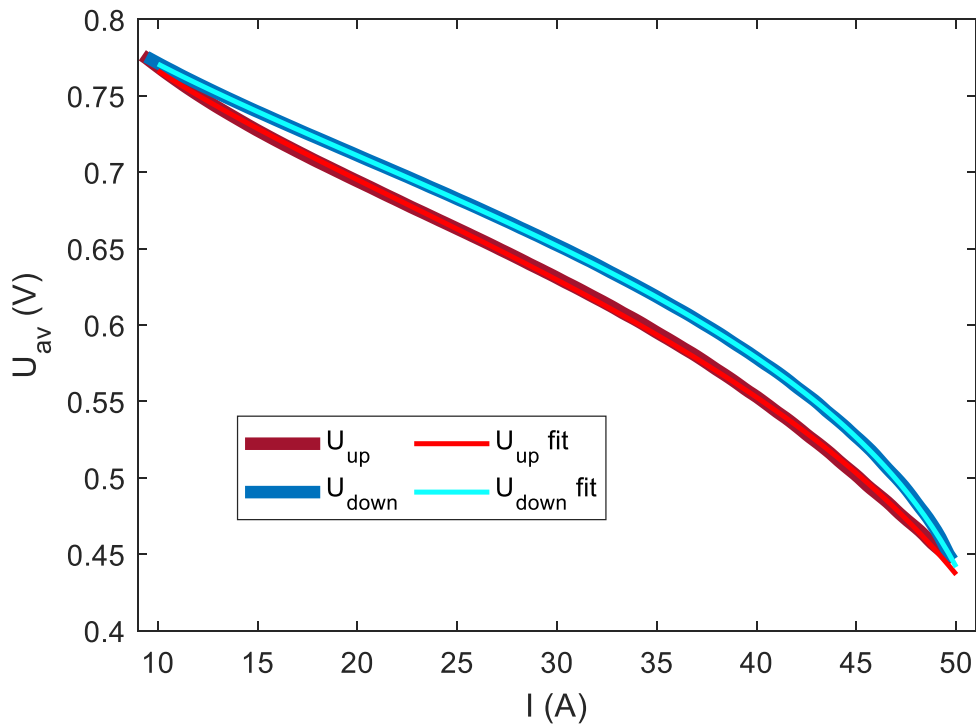


Figure IV-27: Fit for voltage hysteresis based on expression of [40]. Fitted parameters are given in Table IV-4..

### III – 1.3. Wettable volume and limiting saturation

The wettable volume of the cathode compartment  $V_c$  is composed, according to the model assumptions, of the hydrophilic GDL pores. Indeed, only a fraction of the available porosity  $\epsilon$  is effectively favorable to be filled with liquid water: some pores are hydrophobic due to the presence of PTFE as a binder of the carbon fibers. Following the model development,  $V_c$  is expressed as a volume per square meter of MEA, thus as a wettable thickness in meter.

$$V_c = \epsilon_{GDL} \times (1 - \epsilon_{PTFE}) \times t_{GDL} \quad (IV-34)$$

All the hydrophilic pores may not all be filled, even if the amount of liquid water is sufficient to. The limiting saturation  $S_{lim}$  is the maximum value that  $S_c$  should reach. This value is influenced by the morphology of the porous layers. García-Salaberri et al. [167] observed that the breakthrough pressure in a GDL corresponds to an average saturation between 0.12 and 0.52. Thus, the limiting saturation is set at 0.2 in this work. Once this threshold is reached, liquid water is assumed to flow in liquid form due to capillary pressure out of the GDL, toward the channels.

### III – 2. Heat transfer

Heat transfer and consequently temperature distribution within the cell is highly dependent on the cell efficiency and thus on the cell voltage. Fig. IV-28 represents the current profile, defined with the same sweeping velocity, maximum and minimum current as the previous experiments. The cell voltage is modelled as previously developed, considering the polarization hysteresis.

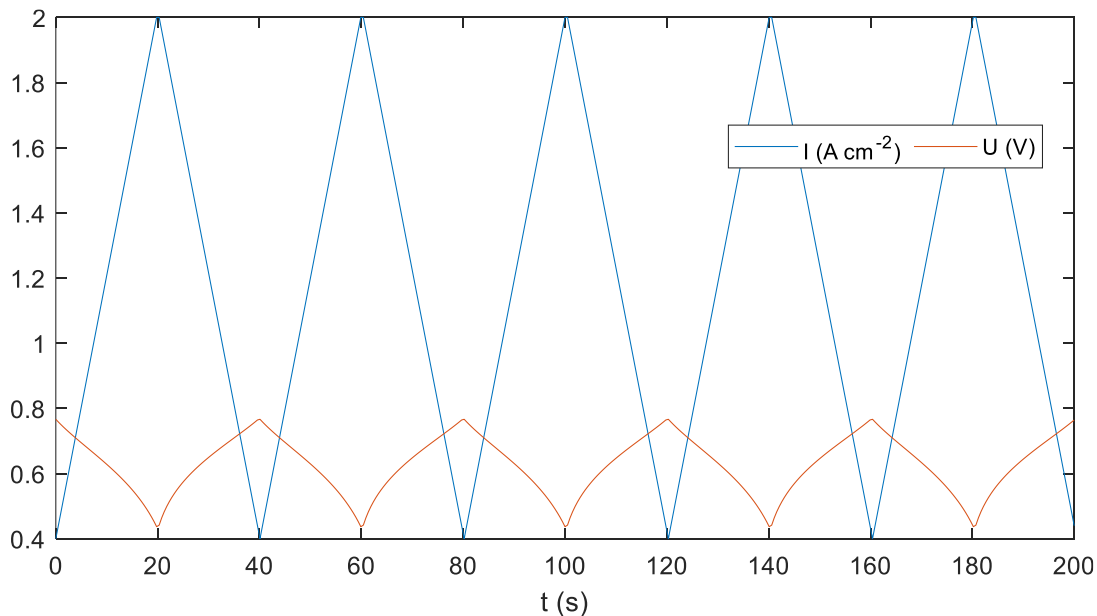


Figure IV-28: Current profile and fitted voltage considering the polarization hysteresis

The modelled MEA temperature is presented in Fig. IV-29 for three different values for  $\kappa_{GDL}$ , the reference being  $\kappa_{GDL} = 0.2 \text{ W m}^{-1}\text{K}^{-1}$ . The first observation is that there is no significant phase shift between the current profile and the MEA temperature: the thermal capacity of the MEA ( $K_{MEA}^{th} = 121.2 \text{ J m}^{-2}\text{K}^{-1}$ ) is too low to create a time shift between maximum current and maximum temperature. Then, one can observe the

influence of a 10% variation of  $\kappa_{GDL}$  on  $T_{MEA}$ . The highest thermal conductivity leads to the lowest MEA temperature of 71 °C, which is 6 °C higher than the plates temperatures. The lowest  $\kappa_{GDL}$  lead to an MEA temperature of 73 °C and  $T_{MEA} = 72$  °C with the reference value of  $\kappa_{GDL} = 0.2 \text{ W m}^{-1}\text{K}^{-1}$ . The last observation is the slope discontinuities, mainly for the highest temperature. This variation is due to the phase change of water represented in Fig. IV-30, along with the total heat flux produced by the cell with time. When the water saturation is null, a discontinuity in the associated phase change heat flux appears and slightly influences the MEA temperature.

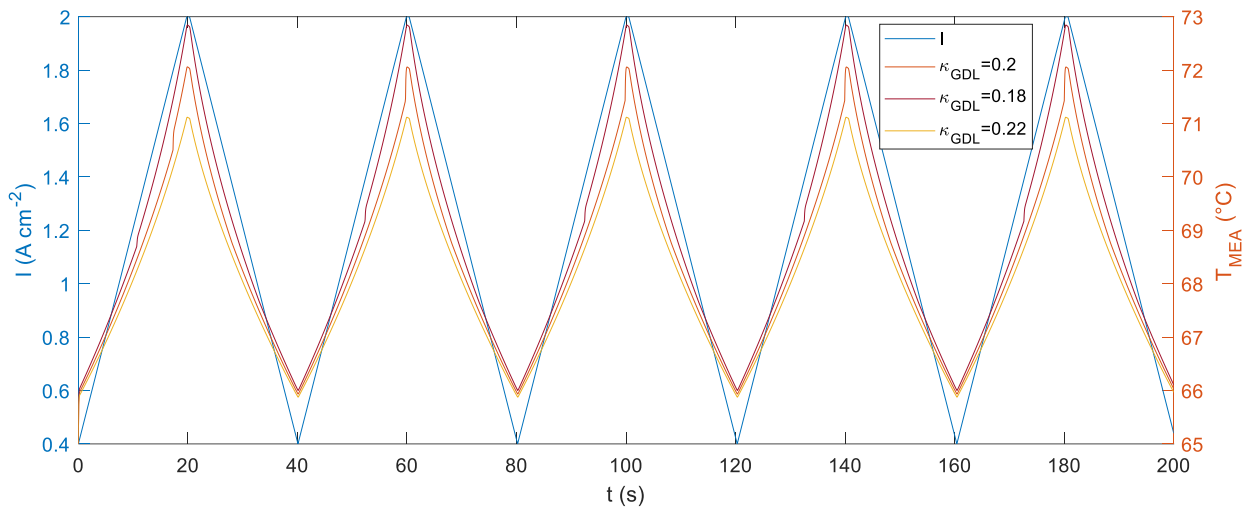


Figure IV-29: MEA temperature with time, for three different values for the GDL thermal conductivity (expressed in  $\text{W m}^{-1} \text{K}^{-1}$ )

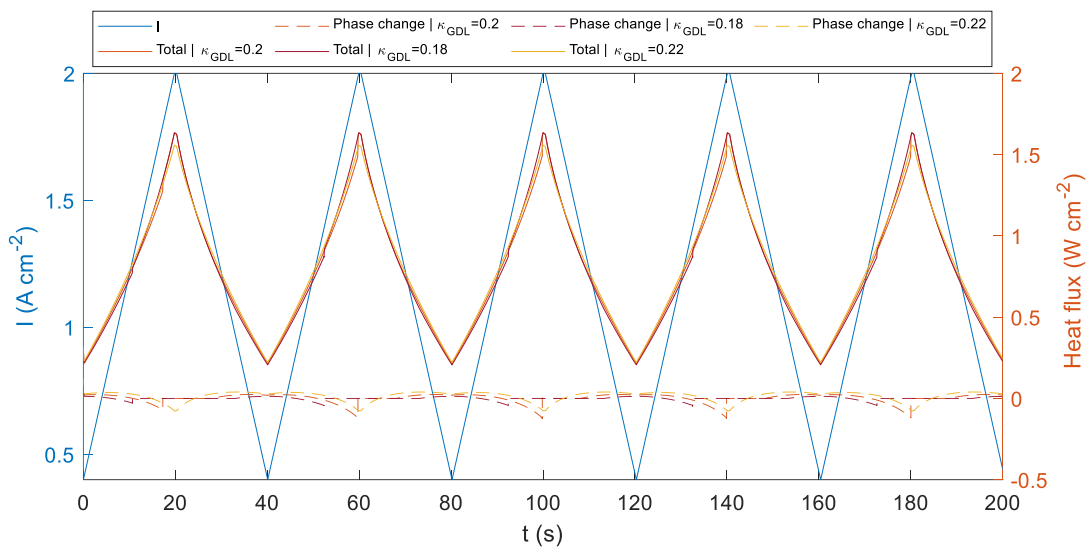


Figure IV-30: Heat fluxes with time for three values of  $\kappa_{GDL}$

### III – 3. Water storage

According to the assumptions of the model, water only lays in the cathode GDL. At  $t = 0$ , the water saturation  $S_c(t = 0)$  is fixed at 0. Fig. IV-31 superimposes the current profile with the cathode saturation, for two different values of  $V_c$ . For the present set of parameters, it is seen that the saturation never hits the limiting value and decreases down to 0 during each period. The amplitude of the saturation oscillations highly depends on  $V_c$ . If the compressed GDL has a porosity of  $\epsilon = 0.5$  and considering that all pores can be filled with liquid water (full line orange curve), the maximum saturation is  $S_c = 0.03$ . Dividing the wettable volume by five leads to a five times higher amplitude on the saturation (dash orange curve). It is seen in this figure that the maximum saturation is reached during the increasing current ramp and the minimum during the decreasing current ramps. It suggests that the water discharge is controlled by thermal effects: when the MEA temperature increases, the heat-pipe effect dominates and a large amount of water vapor is exhaust through the GDL.

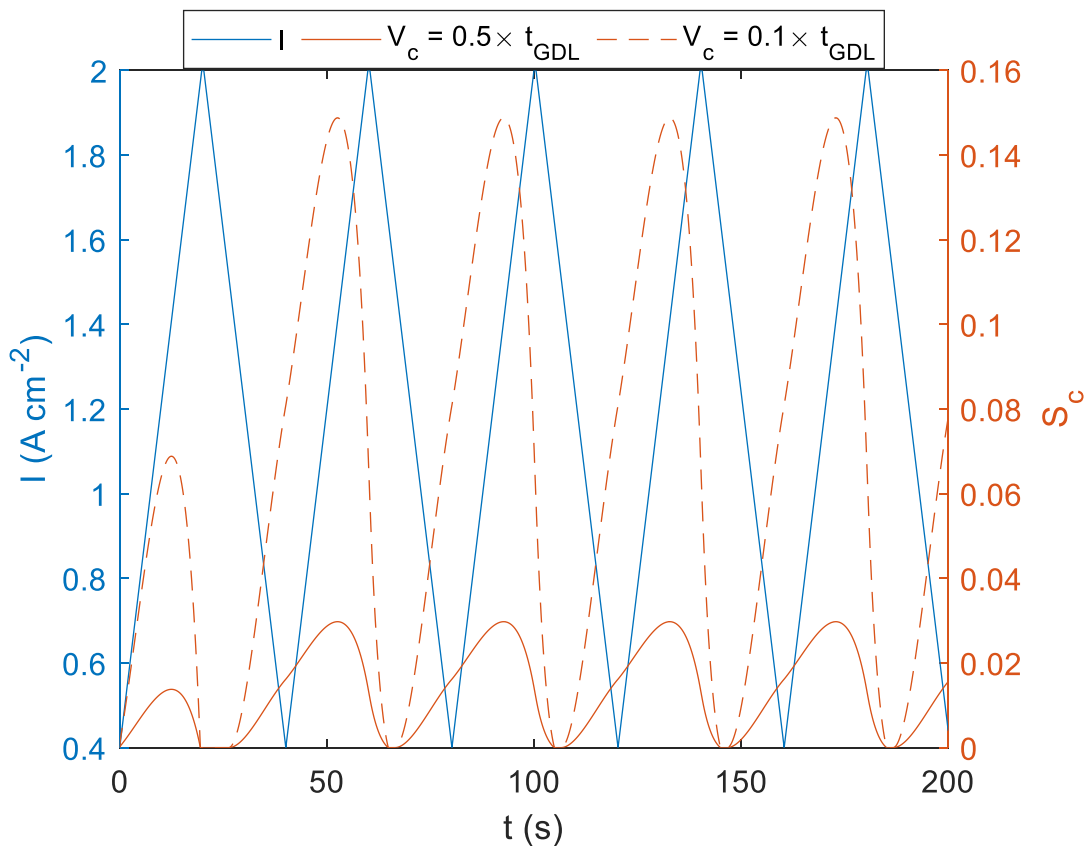


Figure IV-31: Cathode saturation with time along with current profile. Saturation is computed with two different values of wettable cathode volume

Fig. IV-32 represents the experimental saturation superimposed with the two previously exposed modelled profiles. It is observed that the experimental data oscillated around zero while the modelled profiles are strictly positive. It comes from the fact that experimental data is assumed to be in pseudo-steady state with a starting point at  $S_c = 0$ . The main difference between those curves is the time shift. Indeed, the experimental saturation is at the maximum while the modelled is at its minimum. Both experimental and modelled data seem to be in counter-phase. Since water storage is probably controlled by thermal effect, the time shift can be influenced by the thermal capacity of the assembly. Fig. IV-33 represents the modelled water saturation with a reference value for the thermal capacity of the MEA and by multiplying this value by 10. It is observed that this capacity definitely has an effect on the time shift of the maximum saturation. Nevertheless, this effect is too low to explain the phase shift between experimental and modelled data.

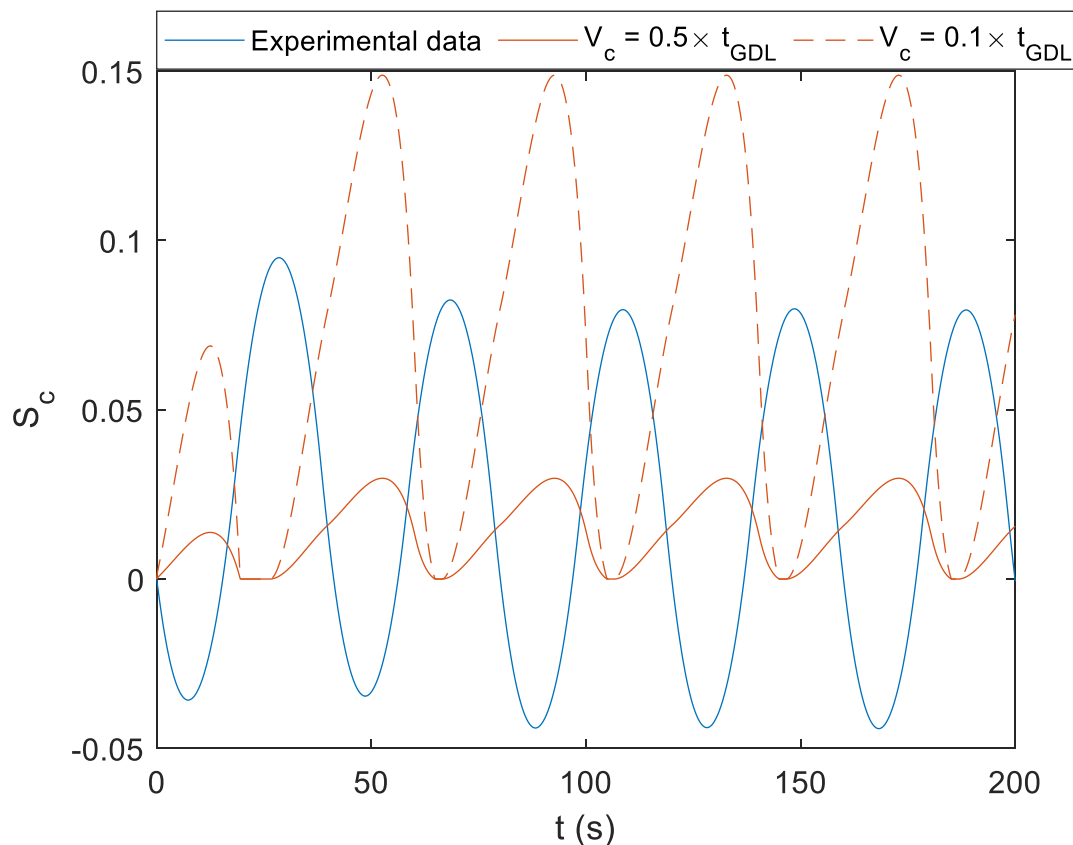


Figure IV-32: Cathode saturation with time. Experimental data is superimposed with two modelled profiles

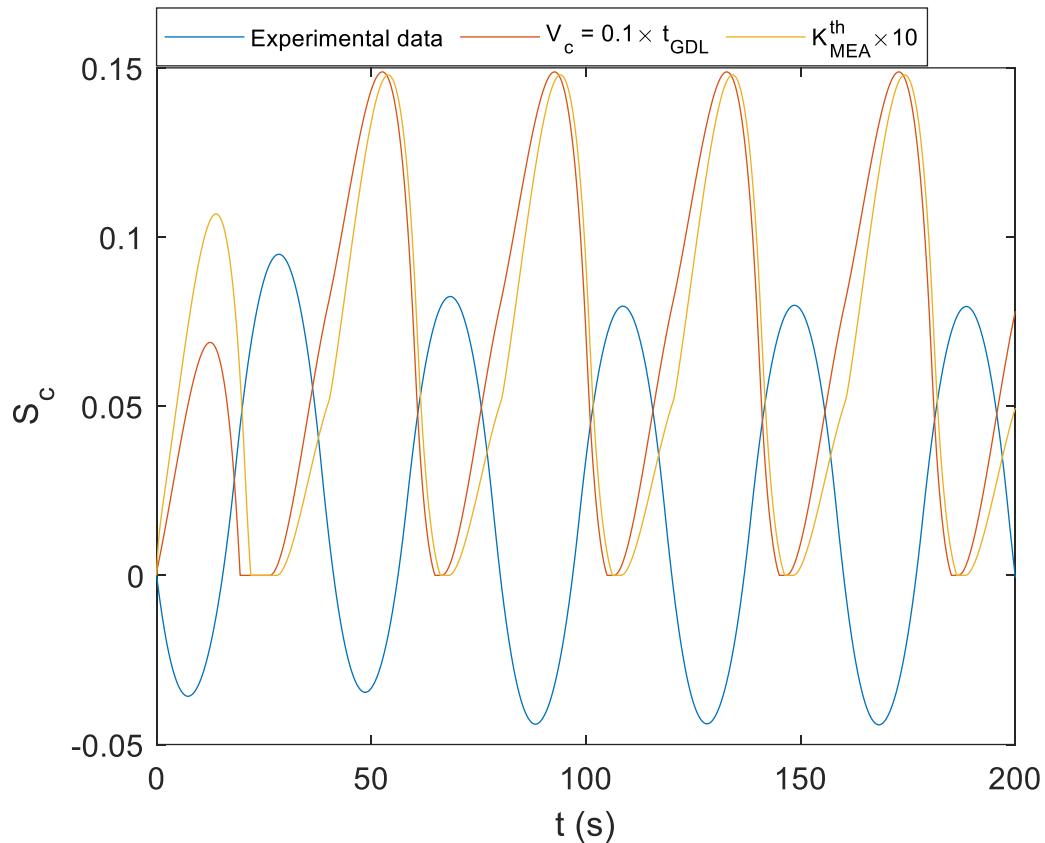


Figure IV-33: Cathode saturation with time. Thermal capacity of the MEA is varied to investigate time shift

The model presented as it is needs to be further improved. The assumptions need to be refined and made more realistic. Deeper investigations must be conducted to understand precisely where the water is stored in the cell.

## IV – Conclusions and outlooks

In this Chapter, preliminary work is presented about the dynamic regime of a fuel cell. First, a one-dimensional model has been developed, aiming to represent coupling between heat and water transfer in a transient regime. The charge transfer is not modelled since it is assumed that the cell voltage is known and this value is sufficient to determine the total heat flux produced by the cell. The coupling between heat and water is mainly achieved by the modeling of the water saturation of the cathode compartment.

A complete experimental protocol has been set up in order to study water transfer during load cycling. Triangle shaped current profiles have been chosen since

it can be representative of automotive environment. During these experiments, the voltage and the 1-kHz resistance are measured simultaneously with water balance. The transient regime as well as the pseudo-steady state were investigated. Experiments led to several conclusions and observations.

- i. For all the periods of these experiments, the voltage presents a hysteresis: an increasing current lead to a lower voltage (and thus to lower performances) than a decreasing current. It is concluded that the 1-kHz resistance is not responsible for such a difference.
- ii. The 1-kHz resistance varies with the current and different profiles are observed depending on the current variation. This resistance contains several contributions such as (i) protonic resistance of the membrane, (ii) of the electrodes, (iii) charge transfer resistances and (iv) electronic resistance of all components. The protonic resistance is highly dependent on the water content of the ionomer but also on the temperature. It is showed that the effects of temperature alone cannot lead to such variations. Variations of water content and charge transfer with current should play a role together with the temperature.
- iii. The amount of water stored in the cell exceeds the volume of the GDL pores without surpassing the total volume available of the cell (pores, channels, manifolds). Liquid is thus stored in the channels and the manifolds of the cell.
- iv. The total amount of liquid water which is stored during the triangle experiments does not depend on the sweeping velocity. It is observed that, even though oscillations amplitude differs from each velocity, the saturation plateau is fixed at a constant value.
- v. The saturation data is highly sensitive to any offset in the water fluxes measurements. Even though efforts have been focused on accuracy, the remaining uncertainty could lead to linear drift of the saturation. This has to be corrected by using the pseudo-steady state data, assuming that the saturation should oscillate around a constant value.
- vi. Experimental data showed that the saturation reaches its maximum value during the decreasing current ramp, and its minimum during the increasing ramp. In contrast, the model suggests that the saturation hits its maximum during the increasing ramp and its minimum during the decreasing ramp. From the model results, it seems that water storage is dominated by thermal effects: when the MEA

temperature is maximum, water saturation drops, suggesting that water is massively discharged from the cell. This may be due to the heat-pipe effect. It is shown that the thermal capacity of the MEA is not responsible for the time shift between experimental and modelled saturation.

More work is needed to go further in the exploration of heat and water management during dynamic regimes.

- i. The wettable volume of the GDL is still an unknown value and some *in-situ* experiments should be able to estimate it. The correlation between  $S_{lim}$  and  $V_c$  must be investigated.
- ii. The measurement of pressure losses in the channels could allow to make the distinction between water stored in the channels and somewhere else.
- iii. The measurement of high frequency resistance could inform about the hydration level of the membrane only, without considering the electrodes [168].
- iv. Experimental improvements are still possible. The application of a fixed stoichiometry for all current values could lead to a lower uncertainty. An estimation of the travel time of gases in the pipes would add a time shift in the water balance and improve the time synchronization of all data. The time shift can be investigated with the implementation of several sweeping velocities during the pseudo-steady state.
- v. Several oxygen concentrations must be employed to investigate the influence of gas mixture on the polarization hysteresis.
- vi. Since liquid water is stored in the whole GDL, the model should consider the temperature field within it. The thermal capacity of the saturated GDL could be at the origin of the phase shift between experimental and modelled saturation.
- vii. Saturation effects are not all considered in the model. When the liquid saturation increases, the gas diffusion is hindered [169] and the effective diffusion coefficient should decrease. On the contrary, when the saturation increases, the membrane could be, at least partially, liquid-equilibrated and the diffusion coefficient should increase [170], if the water is assumed to be in the electrode.
- viii. The model assumes that saturation is evacuated in liquid form once it reaches the limiting value. When it is below, the only discharge mechanisms are the diffusion in

vapor form through the GDL or sorbed form through the membrane. Nevertheless, capillary flow of liquid water may exist for lower saturation values.

- ix. Membrane water sorption is known to be a mechanism with a long characteristic time [171] while the present model assumes instantaneous equilibrium at the MEA interface. The addition a of sorption time could lead to a time shift of water transfer through de membrane.

## Appendix

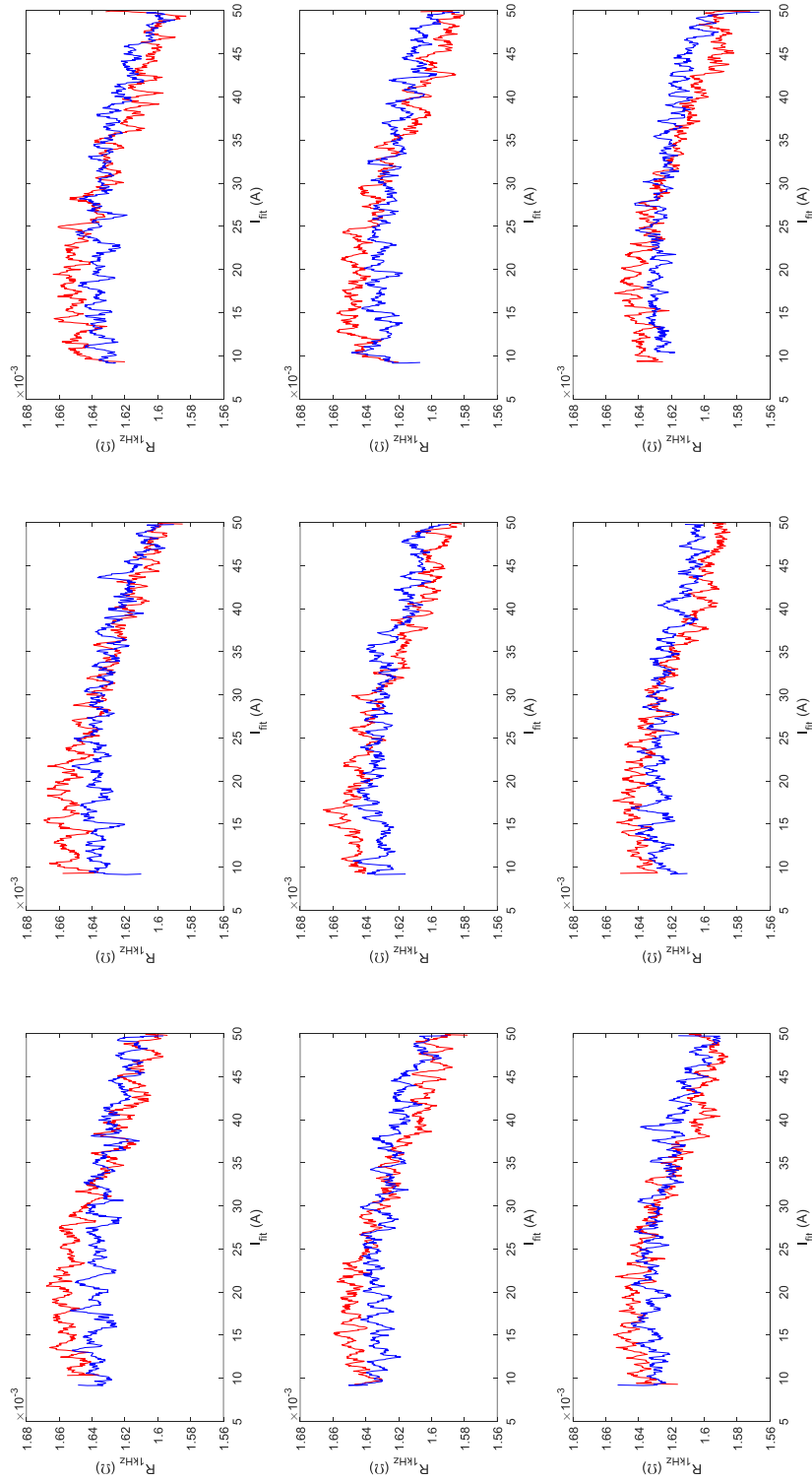


Figure IV-34: 1-kHz resistance for all periods of pseudo-steady state experiments ( $v = 0.6 \text{ A s}^{-1}$ )

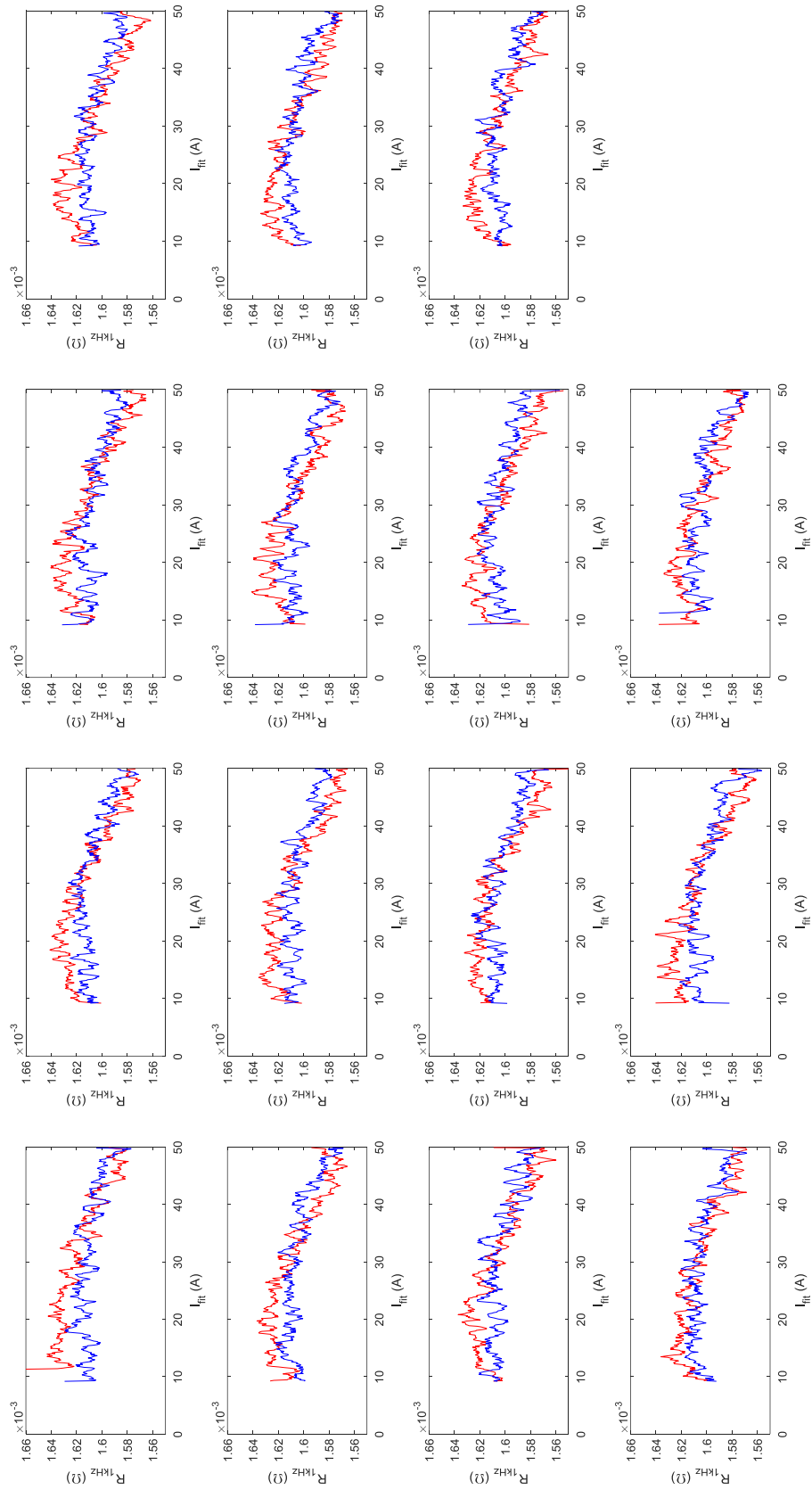


Figure IV-35: 1-kHz resistance for all periods of pseudo-steady state experiments ( $v = 1 \text{ A s}^{-1}$ )

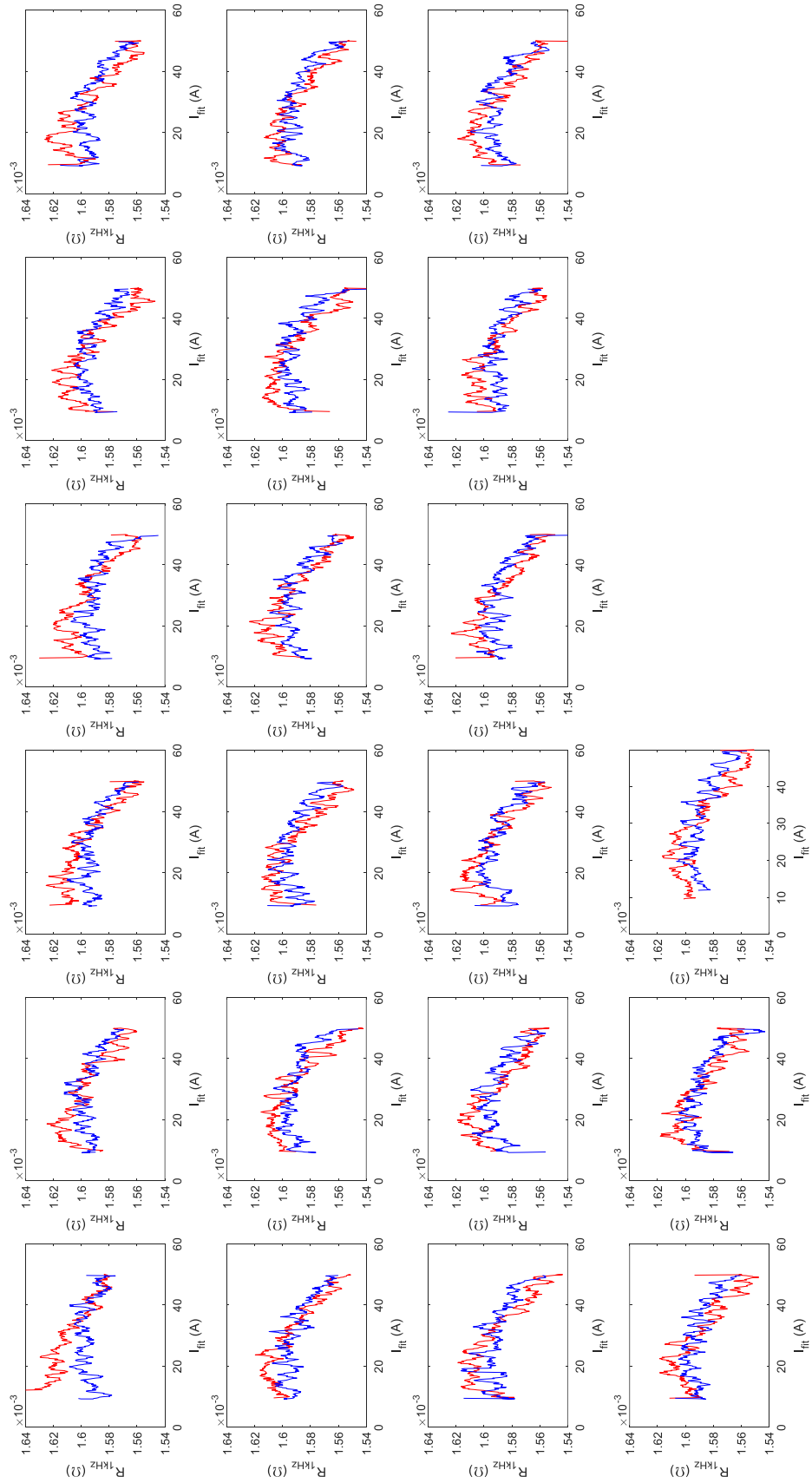


Figure IV-36: 1-kHz resistance for all periods of pseudo-steady state experiments ( $v = 1.4 \text{ A s}^{-1}$ )

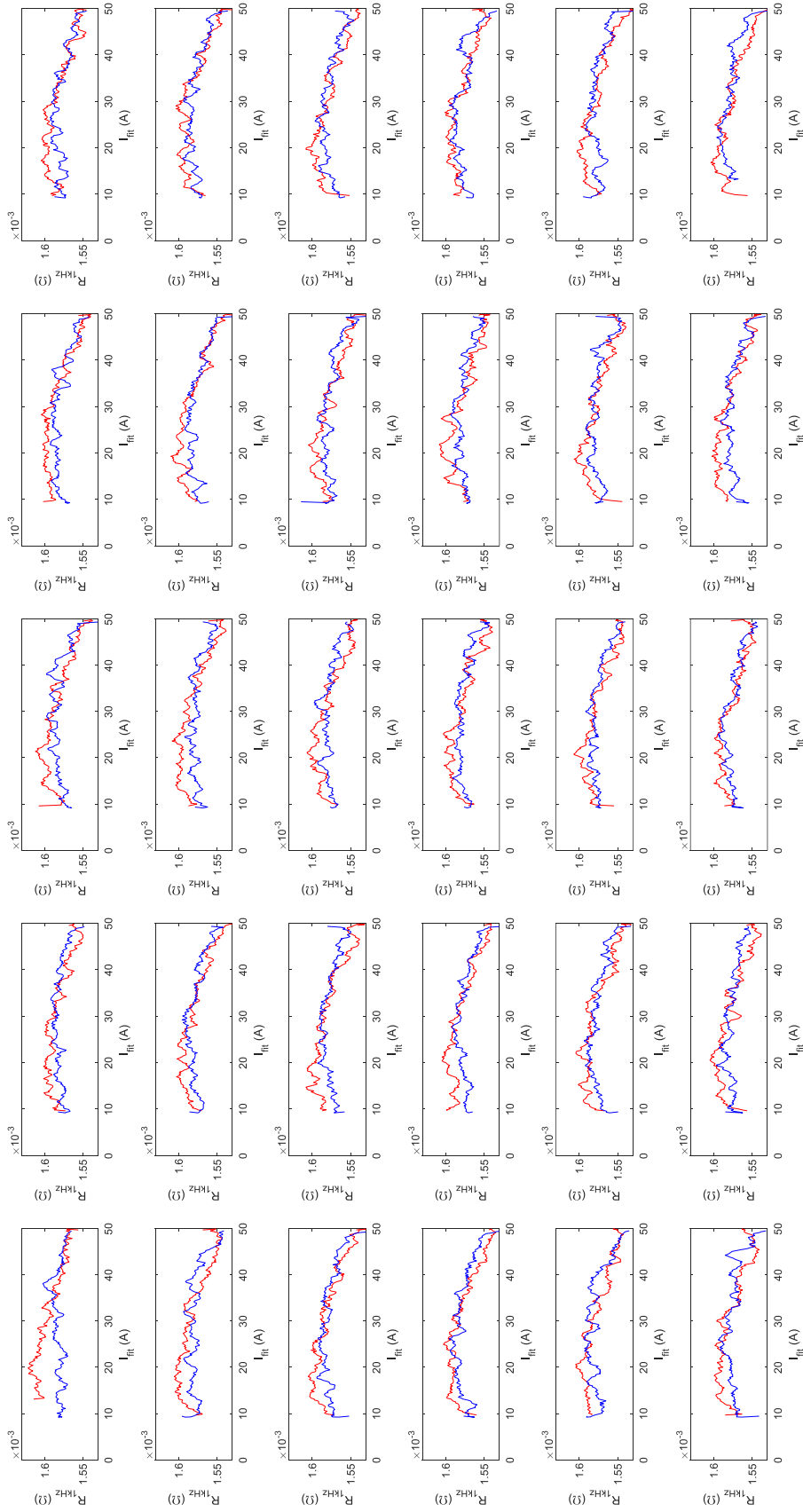


Figure IV-37: 1-kHz resistance for all periods of pseudo-steady state experiments ( $v = 2 \text{ A s}^{-1}$ )

Table IV-5: List of symbols

$C_{H_2O}^{a,ch}, C_{H_2O}^{c,ch}$	Water vapor concentration in anode and cathode channels [mol m <sup>-3</sup> ]
$C_a^{el}, C_c^{el}$	Water vapor concentration at the anode and cathode interface of the MEA [mol m <sup>-3</sup> ]
$C_{H_2O}^{GDL,a}, C_{H_2O}^{GDL,c}$	Water vapor concentration in anode and cathode GDL [mol m <sup>-3</sup> ]
$C_{tot}^a, C_{tot}^c$	Total concentration in anode and cathode compartment [mol m <sup>-3</sup> ]
$C_{sat}^{MEA}$	Saturation concentration of water vapor at the MEA interfaces [mol m <sup>-3</sup> ]
$D_{H_2O}^{GDL,a}$	Effective diffusion coefficient of water vapor in the anode GDL [m <sup>2</sup> s <sup>-1</sup> ]
$D_M$	Diffusion coefficient of water in the MEA [m <sup>2</sup> s <sup>-1</sup> ]
$EW$	Equivalent weight of the ionomer [kg <sub>io</sub> mol <sub>SO<sub>3</sub><sup>-</sup></sub> <sup>-1</sup> ]
$F$	Faraday's constant (96485 C mol <sup>-1</sup> )
$I, i$	Cell current [A] and cell current density [A cm <sup>-2</sup> ]
$I_{min}, I_{max}$	Minimum and maximum of triangle shaped current profiles [A]
$\kappa_{GDL}^{eff}$	Effective thermal conductivity of the GDL [W m <sup>-1</sup> K <sup>-1</sup> ]
$\chi_1, \chi_2$	Regularization coefficients [mol m <sup>-2</sup> s <sup>-1</sup> ] and [∅]
$LHV_{H_2}$	Low Heating Value of hydrogen (242 × 10 <sup>3</sup> J mol <sup>-1</sup> )
$L_v$	Latent heat of vaporization of water (40.7 × 10 <sup>3</sup> J mol <sup>-1</sup> )
$\lambda_a, \lambda_c$	Water content at the anode and cathode interface of the MEA [mol <sub>H<sub>2</sub>O</sub> mol <sub>SO<sub>3</sub><sup>-</sup></sub> <sup>-1</sup> ]
$M_{H_2O}$	Molar mass of water (18 × 10 <sup>-3</sup> kg mol <sup>-1</sup> )
$N_{H_2}^{GDL,a}$	Molar flux density of hydrogen through the anode GDL [mol m <sup>-2</sup> s <sup>-1</sup> ]
$N_{O_2}^{GDL,c}$	Molar flux density of oxygen through the cathode GDL [mol m <sup>-2</sup> s <sup>-1</sup> ]
$N_{H_2O}^{GDL,a}, N_{H_2O}^{GDL,c}$	Molar flux density of water vapor through the anode and cathode GDL [mol m <sup>-2</sup> s <sup>-1</sup> ]
$N_{H_2O}^{MEA}$	Water molar flux density through the MEA [mol m <sup>-2</sup> s <sup>-1</sup> ]
$\phi_{MEA}$	Heat flux in the MEA [W]
$P_a, P_c$	Total pressure at the anode and cathode compartment [Pa]

$R_{MEA}^{diff}$	Diffusion resistance for water transfer through the MEA [ $s\ m^{-1}$ ]
$R_{GDL}^{th}$	Conductive thermal resistance of the compressed GDL [ $K\ W^{-1}$ ]
$\rho_{H_2O,l}$	Density of liquid water ( $10^3\ kg\ m^{-3}$ )
$\rho_{dry}$	Density of dry ionomer in the MEA [ $kg_{io}\ m_{io}^{-3}$ ]
$S_c$	Water saturation of cathode compartment [ $\emptyset$ ]
$S_{lim}$	Maximum water saturation of cathode compartment [ $\emptyset$ ]
$T_a, T_c$	Anode and cathode plate temperatures [K]
$T_{MEA}$	MEA temperature [K]
$t_{GDL}$	Thickness of the compressed GDL [m]
$t_{MEA}$	Thickness of the MEA [m]
$U$	Cell voltage [V]
$V_c$	Wettable volume of cathode compartment [ $m^3$ ]
$v$	Sweeping velocity of triangle current profiles [ $A\ s^{-1}$ ]
$\xi$	Electro-osmosis drag coefficient [ $\emptyset$ ]

# **General conclusions and outlooks**

The global energy system must rapidly move to a low-carbon model. Global warming is worsening and its consequences are becoming increasingly visible. Whether in the field of industry or mobility, the hydrogen carrier can contribute to the decarbonization of many activities. First of all, the activities for which it is already used must make a successful transition to low-carbon production methods such as water electrolysis. Other fields, such as mobility, must reinvent themselves to find alternatives to polluting modes of propulsion. Alongside the electric carrier, hydrogen must find its place, which seems to be in long-distance or heavy mobility.

Fuel cells are an essential tool for the hydrogen sector, as they allow its conversion into electricity and heat. Among the different technologies, PEM fuel cells offer compactness, efficiency and convenience of use. However, many degradations reduce their lifetime and performances. Even if aging is an inevitable mechanism, it must be reduced as much as possible to ensure the best possible longevity of the systems. Heat and water management are two levers that designers and operators can play on. Sufficient heat removal from a stack is essential to avoid overheating of components, which could lead to degradation. Also, the evacuation of the water produced during the generation of current is necessary, at the risk of drowning the cells and thus decreasing the performances and the lifespan. On the other hand, a cell that is too dry decreases efficiency, increases heat production and with it degradation. The modeling of water and heat transport phenomena allows a better understanding of the physical phenomena and thus an optimization of the designs and operating conditions. This work was the occasion to mix experiments and modeling in order to estimate crucial parameters for water and heat transport.

The modeling of water transport in the cell has been the subject of much research and many models have emerged. The transport of water vapor in porous layers is commonly modeled by molecular diffusion, to which convection can be superimposed. Here, the effective diffusion coefficient in the gas phase is crucial to correctly model the transfers. In the membrane, diffusive models were among the first to be developed. The differences in hydration of the membrane generate water fluxes which are managed by a diffusion coefficient. The two parameters mentioned here

have been the subject of estimations. An original design of experiments has been developed and implemented. A 1+1D model has also been developed to be coupled to the experiments. The results were found to be accurate and repeatable. Different MEAs were characterized and it was found that reinforced membranes have a lower diffusion coefficient than Nafion-based membranes only. However, the transfer resistances also depend on the thickness, which can compensate for these low diffusivities. Also, the catalytic layers did not show any influence on the estimated parameters. The sorption of liquid water by the membrane influences the water diffusion and two interpretations of Schroeder's paradox are discussed. Finally, the gas diffusion coefficients are correctly estimated. The expected ratio of water diffusion in hydrogen and air was not observed due to the contribution of other mechanisms that were not specifically modeled.

Even if the total amount of heat produced by a cell is an easily known quantity, the dissociation of the different contributions and their localization remains a difficulty of the modeling. The complexity of the transfers is even more important when the transport of water is coupled to that of heat. An important parameter for the modeling of heat transport is the thermal resistance between the MEA and the plates. Conduction is the main heat transport mechanism in GDLs and thus thermal conductivity is paramount. The original experiments that have been developed have allowed the estimation of this parameter, then called effective. Indeed, the estimates contain the contribution of conduction, but also the geometrical effects and the contact resistances. Thus, this parameter can be easily incorporated in a lumped heat transport model. The estimates made in this work are reproducible and consistent with literature values.

Finally, load cycle experiments were used to study the cell during a transient regime. In particular, water storage was investigated during increasing and decreasing current ramps. Water balances are performed in real time as well as current and voltage measurements. In addition, a current oscillation at 1 kHz is applied to the cell, allowing to obtain the resistance at this frequency. Although many contributions are involved in establishing this resistance value, it gives clues to the level of wetting of the MEA. The cell shows a different behavior for increasing and decreasing ramps. This is observed by the systematic presence of a voltage hysteresis but also by differences in

the resistance profiles. The integration of the water balances over time allows us to calculate the amount of water in the cell over time. These results are compared to a transient model of coupled water and heat transport. This model contains parameters that should be estimated with dedicated experiments. For the moment, it turns out that the model does not sufficiently represent the experiments performed.

Future work should allow for accurate modeling of coupled water and heat transport in an assembly, whether in steady state or transient. Each chapter presents possible improvements and openings to the work that has already been done. Water transport experiments could be improved and additional transport mechanisms such as Knudsen diffusion or sorption resistances could be considered. Estimations of thermal conductivity could be validated by the measurement of the MEA temperature and refined by the consideration of convection-diffusion in the GDLs. Finally, crucial parameters are still to estimate in the transient model. In the end, the development of reduced models together with the estimation of associated parameters can improve the control and design of fuel cells as well as the selection of key materials such as membranes, electrodes and porous layers.

## References

- [1] R. K. Pachauri, L. Mayer, et Intergovernmental Panel on Climate Change, Éd., *Climate change 2014: synthesis report*. Geneva, Switzerland: Intergovernmental Panel on Climate Change, 2015.
- [2] « Key World Energy Statistics 2020 », p. 81.
- [3] R. P. Allan *et al.*, « Summary for Policymakers », *Intergov. Panel Clim. Change*, vol. Sixth Assessment Report, n° WGI, p. 32, 2022, doi: 10.1017/9781009157896.001.
- [4] P. Shukla et J. Skea, « Summary for Policymakers », *Intergov. Panel Clim. Change*, vol. Sixth Assessment Report, n° WGIII, p. 53, 2022.
- [5] I. Staffell *et al.*, « The role of hydrogen and fuel cells in the global energy system », *Energy Environ. Sci.*, vol. 12, n° 2, p. 463-491, 2019, doi: 10.1039/C8EE01157E.
- [6] R. Sims et R. Schaeffer, « Chapter 8 - Transport », *Intergov. Panel Clim. Change*, vol. Fifth Assessment Report, n° WGIII, p. 72, 2014.
- [7] P. D. Lund, J. Lindgren, J. Mikkola, et J. Salpakari, « Review of energy system flexibility measures to enable high levels of variable renewable electricity », *Renew. Sustain. Energy Rev.*, vol. 45, p. 785-807, mai 2015, doi: 10.1016/j.rser.2015.01.057.
- [8] G. Gahleitner, « Hydrogen from renewable electricity: An international review of power-to-gas pilot plants for stationary applications », *Int. J. Hydrog. Energy*, vol. 38, n° 5, p. 2039-2061, févr. 2013, doi: 10.1016/j.ijhydene.2012.12.010.
- [9] S. E. Hosseini, « Hydrogen production from renewable and sustainable energy resources\_ Promising green energy carrier for clean development », *Renew. Sustain. Energy Rev.*, p. 17, 2016.
- [10] S. Singh *et al.*, « Hydrogen: A sustainable fuel for future of the transport sector », *Renew. Sustain. Energy Rev.*, vol. 51, p. 623-633, nov. 2015, doi: 10.1016/j.rser.2015.06.040.
- [11] K. Jiao *et al.*, « Designing the next generation of proton-exchange membrane fuel cells », *Nature*, vol. 595, n° 7867, p. 361-369, juill. 2021, doi: 10.1038/s41586-021-03482-7.
- [12] T. Alleau, P. Malbrunot, et J. Saint-Just, « Production d'hydrogène à partir des combustibles fossiles ». AFHYPAC, novembre 2019.
- [13] M. Hermesmann et T. E. Müller, « Green, Turquoise, Blue, or Grey? Environmentally friendly Hydrogen Production in Transforming Energy Systems »,

- Prog. Energy Combust. Sci.*, vol. 90, p. 100996, mai 2022, doi: 10.1016/j.pecs.2022.100996.
- [14] M. A. Laguna-Bercero, « Recent advances in high temperature electrolysis using solid oxide fuel cells: A review », *J. Power Sources*, vol. 203, p. 4-16, avr. 2012, doi: 10.1016/j.jpowsour.2011.12.019.
- [15] C. Santoro *et al.*, « What is Next in Anion-Exchange Membrane Water Electrolyzers? Bottlenecks, Benefits, and Future », *ChemSusChem*, vol. 15, n° 8, avr. 2022, doi: 10.1002/cssc.202200027.
- [16] G. Sdanghi, G. Maranzana, A. Celzard, et V. Fierro, « Review of the current technologies and performances of hydrogen compression for stationary and automotive applications », *Renew. Sustain. Energy Rev.*, vol. 102, p. 150-170, mars 2019, doi: 10.1016/j.rser.2018.11.028.
- [17] Agence internationale de l'énergie et Organisation de coopération et de développement économiques, *Energy technology perspectives: scenarios & strategies to 2050 : in support of the G8 Plan of action*. Paris: OECD, IEA, 2006.
- [18] R. Ramachandran, « An overview of industrial uses of hydrogen », *Int. J. Hydrog. Energy*, vol. 23, n° 7, p. 593-598, juill. 1998, doi: 10.1016/S0360-3199(97)00112-2.
- [19] J. R. Bartels, « A feasibility study of implementing an Ammonia Economy », Master of Science, Iowa State University, Digital Repository, Ames, 2008. doi: 10.31274/etd-180810-1374.
- [20] I. Dincer et Y. Bicer, « 3.2 Ammonia Production », in *Comprehensive Energy Systems*, Elsevier, 2018, p. 41-94. doi: 10.1016/B978-0-12-809597-3.00305-9.
- [21] Y. Wang, D. F. Ruiz Diaz, K. S. Chen, Z. Wang, et X. C. Adroher, « Materials, technological status, and fundamentals of PEM fuel cells – A review », *Mater. Today*, vol. 32, p. 178-203, janv. 2020, doi: 10.1016/j.mattod.2019.06.005.
- [22] D. H. Jung, C. H. Lee, C. S. Kim, et D. R. Shin, « Performance of a direct methanol polymer electrolyte fuel cell », *J. Power Sources*, p. 5, 1998.
- [23] A. Wojcik, H. Middleton, I. Damopoulos, et J. Van herle, « Ammonia as a fuel in solid oxide fuel cells », *J. Power Sources*, vol. 118, n° 1-2, p. 342-348, mai 2003, doi: 10.1016/S0378-7753(03)00083-1.
- [24] M. M. Mench, *Fuel cell engines*. Hoboken, N.J: John Wiley & Sons, 2008.
- [25] S. Mekhilef, R. Saidur, et A. Safari, « Comparative study of different fuel cell technologies », *Renew. Sustain. Energy Rev.*, vol. 16, n° 1, p. 981-989, janv. 2012, doi: 10.1016/j.rser.2011.09.020.

- [26] A. A. Kulikovskiy, « Modelling of fuel cell stacks », in *Analytical Modelling of Fuel Cells*, Elsevier, 2010, p. 193-272. doi: 10.1016/B978-0-444-53560-3.00010-1.
- [27] Q. Liu, F. Lan, C. Zeng, J. Chen, et J. Wang, « A review of proton exchange membrane fuel cell's bipolar plate design and fabrication process », *J. Power Sources*, vol. 538, p. 231543, août 2022, doi: 10.1016/j.jpowsour.2022.231543.
- [28] Q. Ding, H.-L. Zhao, Z.-M. Wan, Y.-R. Yang, C. Yang, et X.-D. Wang, « Performance of Parallel, Interdigitated, and Serpentine Flow Field PEM Fuel Cells with Straight or Wavelike Channels », *J. Energy Eng.*, vol. 146, n° 5, p. 04020054, oct. 2020, doi: 10.1061/(ASCE)EY.1943-7897.0000701.
- [29] A. Ozden, S. Shahgaldi, X. Li, et F. Hamdullahpur, « A review of gas diffusion layers for proton exchange membrane fuel cells—With a focus on characteristics, characterization techniques, materials and designs », *Prog. Energy Combust. Sci.*, vol. 74, p. 50-102, sept. 2019, doi: 10.1016/j.peecs.2019.05.002.
- [30] A. El-kharouf, T. J. Mason, D. J. L. Brett, et B. G. Pollet, « Ex-situ characterisation of gas diffusion layers for proton exchange membrane fuel cells », *J. Power Sources*, vol. 218, p. 393-404, nov. 2012, doi: 10.1016/j.jpowsour.2012.06.099.
- [31] J. Zhou, S. Shukla, A. Putz, et M. Secanell, « Analysis of the role of the microporous layer in improving polymer electrolyte fuel cell performance », *Electrochimica Acta*, vol. 268, p. 366-382, avr. 2018, doi: 10.1016/j.electacta.2018.02.100.
- [32] M. Xie *et al.*, « Preparation, Performance and Challenges of Catalyst Layer for Proton Exchange Membrane Fuel Cell », *Membranes*, vol. 11, n° 11, p. 879, nov. 2021, doi: 10.3390/membranes11110879.
- [33] H. Zhang et P. K. Shen, « Recent Development of Polymer Electrolyte Membranes for Fuel Cells », *Chem Rev*, p. 53, 2012.
- [34] B. Smitha, S. Sridhar, et A. A. Khan, « Solid polymer electrolyte membranes for fuel cell applications—a review », *J. Membr. Sci.*, vol. 259, n° 1-2, p. 10-26, août 2005, doi: 10.1016/j.memsci.2005.01.035.
- [35] A. Kraytsberg et Y. Ein-Eli, « Review of Advanced Materials for Proton Exchange Membrane Fuel Cells », *Energy Fuels*, vol. 28, n° 12, p. 7303-7330, déc. 2014, doi: 10.1021/ef501977k.
- [36] A. Kusoglu et A. Z. Weber, « New Insights into Perfluorinated Sulfonic-Acid Ionomers », *Chem. Rev.*, vol. 117, n° 3, p. 987-1104, févr. 2017, doi: 10.1021/acs.chemrev.6b00159.
- [37] J. Li, M. Pan, et H. Tang, « Understanding short-side-chain perfluorinated sulfonic acid and its application for high temperature polymer electrolyte membrane fuel cells », *RSC Adv*, vol. 4, n° 8, p. 3944-3965, 2014, doi: 10.1039/C3RA43735C.

- [38] A. Z. Weber *et al.*, « A Critical Review of Modeling Transport Phenomena in Polymer-Electrolyte Fuel Cells », *J. Electrochem. Soc.*, vol. 161, n° 12, p. F1254-F1299, 2014, doi: 10.1149/2.0751412jes.
- [39] J. Mainka, G. Maranzana, J. Dillet, S. Didierjean, et O. Lottin, « On the estimation of high frequency parameters of Proton Exchange Membrane Fuel Cells via Electrochemical Impedance Spectroscopy », *J. Power Sources*, vol. 253, p. 381-391, mai 2014, doi: 10.1016/j.jpowsour.2013.12.064.
- [40] A. Z. Weber et J. Newman, « Modeling Transport in Polymer-Electrolyte Fuel Cells », *Chem. Rev.*, vol. 104, n° 10, p. 4679-4726, oct. 2004, doi: 10.1021/cr020729l.
- [41] J. Ramousse, O. Lottin, S. Didierjean, et D. Maillet, « Heat sources in proton exchange membrane (PEM) fuel cells », *J. Power Sources*, vol. 192, n° 2, p. 435-441, juill. 2009, doi: 10.1016/j.jpowsour.2009.03.038.
- [42] R. Borup *et al.*, « Scientific Aspects of Polymer Electrolyte Fuel Cell Durability and Degradation », *Chem. Rev.*, vol. 107, n° 10, p. 3904-3951, oct. 2007, doi: 10.1021/cr050182l.
- [43] R. L. Borup *et al.*, « Recent developments in catalyst-related PEM fuel cell durability », *Curr. Opin. Electrochem.*, vol. 21, p. 192-200, juin 2020, doi: 10.1016/j.coelec.2020.02.007.
- [44] L. Dubau *et al.*, « A review of PEM fuel cell durability: materials degradation, local heterogeneities of aging and possible mitigation strategies », *WIREs Energy Environ.*, vol. 3, n° 6, p. 540-560, nov. 2014, doi: 10.1002/wene.113.
- [45] M. Bahrami *et al.*, « Modeling a Proton Exchange Membrane Fuel Cell Stack Cell by Cell: Illustration of a Mechanism for the Propagation of Degradations », *J. Electrochem. Soc.*, vol. 168, n° 9, p. 094507, sept. 2021, doi: 10.1149/1945-7111/ac2686.
- [46] P. C. Okonkwo, I. Ben Belgacem, W. Emori, et P. C. Uzoma, « Nafion degradation mechanisms in proton exchange membrane fuel cell (PEMFC) system: A review », *Int. J. Hydrog. Energy*, vol. 46, n° 55, p. 27956-27973, août 2021, doi: 10.1016/j.ijhydene.2021.06.032.
- [47] M. Robert *et al.*, « Effects of conjoint mechanical and chemical stress on perfluorosulfonic-acid membranes for fuel cells », *J. Power Sources*, vol. 476, p. 228662, nov. 2020, doi: 10.1016/j.jpowsour.2020.228662.
- [48] T. Ous et C. Arcoumanis, « Degradation aspects of water formation and transport in Proton Exchange Membrane Fuel Cell: A review », *J. Power Sources*, vol. 240, p. 558-582, oct. 2013, doi: 10.1016/j.jpowsour.2013.04.044.

- [49] M. Ji et Z. Wei, « A Review of Water Management in Polymer Electrolyte Membrane Fuel Cells », *Energies*, vol. 2, n° 4, p. 1057-1106, nov. 2009, doi: 10.3390/en20401057.
- [50] J. Wu *et al.*, « A review of PEM fuel cell durability: Degradation mechanisms and mitigation strategies », *J. Power Sources*, vol. 184, n° 1, p. 104-119, sept. 2008, doi: 10.1016/j.jpowsour.2008.06.006.
- [51] N. Macauley *et al.*, « Carbon Corrosion in PEM Fuel Cells and the Development of Accelerated Stress Tests », *J. Electrochem. Soc.*, p. 15, 2018.
- [52] L. Castanheira, W. O. Silva, F. H. B. Lima, A. Crisci, et L. Dubau, « Carbon Corrosion in Proton-Exchange Membrane Fuel Cells: Effect of the Carbon Structure, the Degradation Protocol, and the Gas Atmosphere », *ACS Catal*, p. 11, 2015.
- [53] G. Maranzana, A. Lamibrac, J. Dillet, S. Abbou, S. Didierjean, et O. Lottin, « Startup (and Shutdown) Model for Polymer Electrolyte Membrane Fuel Cells », *J. Electrochem. Soc.*, vol. 162, n° 7, p. F694-F706, 2015, doi: 10.1149/2.0451507jes.
- [54] Z. Zhao, L. Dubau, et F. Maillard, « Evidences of the migration of Pt crystallites on high surface area carbon supports in the presence of reducing molecules », *J. Power Sources*, vol. 217, p. 449-458, nov. 2012, doi: 10.1016/j.jpowsour.2012.06.016.
- [55] E. Guilminot *et al.*, « Membrane and Active Layer Degradation upon PEMFC Steady-State Operation », *J. Electrochem. Soc.*, vol. 154, n° 11, p. B1106, 2007, doi: 10.1149/1.2775218.
- [56] T. Ha *et al.*, « Experimental study of the effect of dissolution on the gas diffusion layer in polymer electrolyte membrane fuel cells », *Int. J. Hydrog. Energy*, vol. 36, n° 19, p. 12427-12435, sept. 2011, doi: 10.1016/j.ijhydene.2011.06.096.
- [57] J. Pauchet, M. Prat, P. Schott, et S. P. Kuttanikkad, « Performance loss of proton exchange membrane fuel cell due to hydrophobicity loss in gas diffusion layer: Analysis by multiscale approach combining pore network and performance modelling », *Int. J. Hydrog. Energy*, vol. 37, n° 2, p. 1628-1641, janv. 2012, doi: 10.1016/j.ijhydene.2011.09.127.
- [58] Y. Yin *et al.*, « Ionomer migration within PEMFC catalyst layers induced by humidity changes », *Electrochem. Commun.*, vol. 109, p. 106590, déc. 2019, doi: 10.1016/j.elecom.2019.106590.
- [59] T. Gaumont *et al.*, « Measurement of protonic resistance of catalyst layers as a tool for degradation monitoring », *Int. J. Hydrog. Energy*, vol. 42, n° 3, p. 1800-1812, janv. 2017, doi: 10.1016/j.ijhydene.2016.10.035.

- [60] T. Suzuki, « (Invited) Fuel Cell Stack Technology of Toyota », *ECS Trans.*, vol. 75, n° 14, p. 423-434, août 2016, doi: 10.1149/07514.0423ecst.
- [61] Q. Yan, H. Toghiani, et H. Causey, « Steady state and dynamic performance of proton exchange membrane fuel cells (PEMFCs) under various operating conditions and load changes », *J. Power Sources*, vol. 161, n° 1, p. 492-502, oct. 2006, doi: 10.1016/j.jpowsour.2006.03.077.
- [62] W. He, G. Lin, et T. Van Nguyen, « Diagnostic tool to detect electrode flooding in proton-exchange-membrane fuel cells », *AIChE J.*, vol. 49, n° 12, p. 3221-3228, déc. 2003, doi: 10.1002/aic.690491221.
- [63] A. P. Manso, F. F. Marzo, J. Barranco, X. Garikano, et M. Garmendia Mujika, « Influence of geometric parameters of the flow fields on the performance of a PEM fuel cell. A review », *Int. J. Hydrog. Energy*, vol. 37, n° 20, p. 15256-15287, oct. 2012, doi: 10.1016/j.ijhydene.2012.07.076.
- [64] T. Gaumont, « Résistance protonique d'électrodes de piles à combustible à membrane (PEMFC): effets de l'humidité et des dégradations », Université de Lorraine, LEMTA, 2017.
- [65] A. Thomas, G. Maranzana, S. Didierjean, J. Dillet, et O. Lottin, « Measurements of Electrode Temperatures, Heat and Water Fluxes in PEMFCs: Conclusions about Transfer Mechanisms », *J. Electrochem. Soc.*, vol. 160, n° 2, p. F191-F204, 2013, doi: 10.1149/2.006303jes.
- [66] A. Thomas, G. Maranzana, S. Didierjean, J. Dillet, et O. Lottin, « Thermal Effect on Water Transport in Proton Exchange Membrane Fuel Cell », *Fuel Cells*, vol. 12, n° 2, p. 212-224, avr. 2012, doi: 10.1002/face.201100100.
- [67] J. P. Owejan, J. E. Owejan, W. Gu, T. A. Trabold, T. W. Tighe, et M. F. Mathias, « Water Transport Mechanisms in PEMFC Gas Diffusion Layers », *J. Electrochem. Soc.*, vol. 157, n° 10, p. B1456, 2010, doi: 10.1149/1.3468615.
- [68] Y. Nagai *et al.*, « Improving water management in fuel cells through microporous layer modifications: Fast operando tomographic imaging of liquid water », *J. Power Sources*, vol. 435, p. 226809, sept. 2019, doi: 10.1016/j.jpowsour.2019.226809.
- [69] A. Lamibrac, J. Roth, M. Toulec, F. Marone, M. Stampanoni, et F. N. Büchi, « Characterization of Liquid Water Saturation in Gas Diffusion Layers by X-Ray Tomographic Microscopy », *J. Electrochem. Soc.*, vol. 163, n° 3, p. F202-F209, 2016, doi: 10.1149/2.0401603jes.
- [70] G. Zhang et S. G. Kandlikar, « A critical review of cooling techniques in proton exchange membrane fuel cell stacks », *Int. J. Hydrog. Energy*, vol. 37, n° 3, p. 2412-2429, févr. 2012, doi: 10.1016/j.ijhydene.2011.11.010.

- [71] H. Ju, H. Meng, et C.-Y. Wang, « A single-phase, non-isothermal model for PEM fuel cells », *Int. J. Heat Mass Transf.*, vol. 48, n° 7, p. 1303-1315, mars 2005, doi: 10.1016/j.ijheatmasstransfer.2004.10.004.
- [72] P.-Y. A. Chuang, M. A. Rahman, F. Mojica, D. S. Hussey, D. L. Jacobson, et J. M. LaManna, « The interactive effect of heat and mass transport on water condensation in the gas diffusion layer of a proton exchange membrane fuel cell », *J. Power Sources*, vol. 480, p. 229121, déc. 2020, doi: 10.1016/j.jpowsour.2020.229121.
- [73] T. E. Springer, « Polymer Electrolyte Fuel Cell Model », *J. Electrochem. Soc.*, vol. 138, n° 8, p. 2334, 1991, doi: 10.1149/1.2085971.
- [74] D. M. Bernardi, « A Mathematical Model of the Solid-Polymer-Electrolyte Fuel Cell », *J. Electrochem. Soc.*, vol. 139, n° 9, p. 2477, 1992, doi: 10.1149/1.2221251.
- [75] T. F. Fuller, « Water and Thermal Management in Solid-Polymer-Electrolyte Fuel Cells », *J. Electrochem. Soc.*, vol. 140, n° 5, p. 1218, 1993, doi: 10.1149/1.2220960.
- [76] M. Eikerling, « Phenomenological Theory of Electro-osmotic Effect and Water Management in Polymer Electrolyte Proton-Conducting Membranes », *J. Electrochem. Soc.*, vol. 145, n° 8, p. 2684, 1998, doi: 10.1149/1.1838700.
- [77] T. Colinart, « Gestion de l'eau et performances électriques d'une pile à combustible : des pores de la membrane à la cellule. », Université de Lorraine, LEMTA, 2008.
- [78] Y. Wang et C.-Y. Wang, « A Nonisothermal, Two-Phase Model for Polymer Electrolyte Fuel Cells », *J. Electrochem. Soc.*, vol. 153, n° 6, p. A1193, 2006, doi: 10.1149/1.2193403.
- [79] A. Z. Weber et J. Newman, « Coupled Thermal and Water Management in Polymer Electrolyte Fuel Cells », *J. Electrochem. Soc.*, p. 10, 2006.
- [80] R. Vetter et J. O. Schumacher, « Free open reference implementation of a two-phase PEM fuel cell model », *Comput. Phys. Commun.*, vol. 234, p. 223-234, janv. 2019, doi: 10.1016/j.cpc.2018.07.023.
- [81] A. Goshtasbi, B. L. Pence, et T. Ersal, « Computationally Efficient Pseudo-2D Non-Isothermal Modeling of Polymer Electrolyte Membrane Fuel Cells with Two-Phase Phenomena », *J. Electrochem. Soc.*, vol. 163, n° 13, p. F1412-F1432, 2016, doi: 10.1149/2.0871613jes.
- [82] A. Goshtasbi *et al.*, « A Mathematical Model toward Real-Time Monitoring of Automotive PEM Fuel Cells », *J. Electrochem. Soc.*, vol. 167, n° 2, p. 024518, févr. 2020, doi: 10.1149/1945-7111/ab6dd1.
- [83] A. U. Thosar, H. Agarwal, S. Govarthan, et A. K. Lele, « Comprehensive analytical model for polarization curve of a PEM fuel cell and experimental

- validation », *Chem. Eng. Sci.*, vol. 206, p. 96-117, oct. 2019, doi: 10.1016/j.ces.2019.05.022.
- [84] A. Z. Weber et M. A. Hickner, « Modeling and high-resolution-imaging studies of water-content profiles in a polymer-electrolyte-fuel-cell membrane-electrode assembly », *Electrochimica Acta*, vol. 53, n° 26, p. 7668-7674, nov. 2008, doi: 10.1016/j.electacta.2008.05.018.
- [85] L. M. Pant, S. Stewart, N. Craig, et A. Z. Weber, « Critical Parameter Identification of Fuel-Cell Models Using Sensitivity Analysis », *J. Electrochem. Soc.*, vol. 168, n° 7, p. 074501, juill. 2021, doi: 10.1149/1945-7111/ac0d68.
- [86] A. Goshtasbi, J. Chen, J. R. Waldecker, S. Hirano, et T. Ersal, « Effective Parameterization of PEM Fuel Cell Models—Part I: Sensitivity Analysis and Parameter Identifiability », *J. Electrochem. Soc.*, vol. 167, n° 4, p. 044504, févr. 2020, doi: 10.1149/1945-7111/ab7091.
- [87] R. Vetter et J. O. Schumacher, « Experimental parameter uncertainty in proton exchange membrane fuel cell modeling. Part II: Sensitivity analysis and importance ranking », *J. Power Sources*, vol. 439, p. 126529, nov. 2019, doi: 10.1016/j.jpowsour.2019.04.057.
- [88] N. Zamel *et al.*, « Experimental measurements of effective diffusion coefficient of oxygen–nitrogen mixture in PEM fuel cell diffusion media », *Chem. Eng. Sci.*, vol. 65, n° 2, p. 931-937, janv. 2010, doi: 10.1016/j.ces.2009.09.044.
- [89] L. Maldonado, J.-C. Perrin, J. Dillet, et O. Lottin, « Characterization of polymer electrolyte Nafion membranes: Influence of temperature, heat treatment and drying protocol on sorption and transport properties », *J. Membr. Sci.*, vol. 389, p. 43-56, févr. 2012, doi: 10.1016/j.memsci.2011.10.014.
- [90] R. C. Sellin, K. Mozet, A. Ménage, J. Dillet, S. Didierjean, et G. Maranzana, « Measuring electro-osmotic drag coefficients in PFSA membranes without any diffusion assumption », *Int. J. Hydrog. Energy*, vol. 44, n° 45, p. 24905-24912, sept. 2019, doi: 10.1016/j.ijhydene.2019.07.076.
- [91] J. T. Gostick, M. W. Fowler, M. A. Ioannidis, M. D. Pritzker, Y. M. Volfkovich, et A. Sakars, « Capillary pressure and hydrophilic porosity in gas diffusion layers for polymer electrolyte fuel cells », *J. Power Sources*, vol. 156, n° 2, p. 375-387, juin 2006, doi: 10.1016/j.jpowsour.2005.05.086.
- [92] O. Burheim, P. J. S. Vie, J. G. Pharoah, et S. Kjelstrup, « Ex situ measurements of through-plane thermal conductivities in a polymer electrolyte fuel cell », *J. Power Sources*, p. 8, 2010.
- [93] M. Arif, S. C. P. Cheung, et J. Andrews, « Different Approaches Used for Modeling and Simulation of Polymer Electrolyte Membrane Fuel Cells: A Review », *Energy Fuels*, vol. 34, n° 10, p. 11897-11915, oct. 2020, doi: 10.1021/acs.energyfuels.0c02414.

- [94] M. Eikerling, « Theory and Modeling of Fuel Cells: Extravaganza to Panacea? », *Fuel Cells*, vol. 16, n° 6, p. 663-668, déc. 2016, doi: 10.1002/fuce.201690010.
- [95] A. J. Bard et L. R. Faulkner, *Electrochemical Methods - Fundamentals and Applications*, Second Edition. John Wiley & Sons, 2000.
- [96] T. A. Zawodzinski, C. Derouin, S. Radzinski, R. Sherman, V. T. Smith, et T. E. Springer, « Water Uptake by and Transport Through Nafion<sup>®</sup> 117 Membranes », *J Electrochem Soc*, vol. 140, n° 4, p. 7, 1993.
- [97] M. Legras, Y. Hirata, Q. T. Nguyen, D. Langevin, et M. Métayer, « Sorption and diffusion behaviors of water in Nafion 117 membranes with different counter ions », *Desalination*, vol. 147, n° 1-3, p. 351-357, sept. 2002, doi: 10.1016/S0011-9164(02)00608-2.
- [98] Y. Li, Q. T. Nguyen, C. L. Buquet, D. Langevin, M. Legras, et S. Marais, « Water sorption in Nafion<sup>®</sup> membranes analyzed with an improved dual-mode sorption model—Structure/property relationships », *J. Membr. Sci.*, vol. 439, p. 1-11, juill. 2013, doi: 10.1016/j.memsci.2013.03.040.
- [99] L. Maldonado Sanchez, « Caractérisation expérimentale des propriétés de sorption de l'eau et de transport des membranes de piles à combustible », Université de Lorraine, 2012.
- [100] M. Safiollah, P.-E. A. Melchy, P. Berg, et M. Eikerling, « Model of Water Sorption and Swelling in Polymer Electrolyte Membranes: Diagnostic Applications », *J. Phys. Chem. B*, vol. 119, n° 25, p. 8165-8175, juin 2015, doi: 10.1021/acs.jpcc.5b00486.
- [101] J. T. Hinatsu, « Water Uptake of Perfluorosulfonic Acid Membranes from Liquid Water and Water Vapor », *J. Electrochem. Soc.*, vol. 141, n° 6, p. 1493, 1994, doi: 10.1149/1.2054951.
- [102] K. Chadha, S. Martemianov, et A. Thomas, « Estimation of the effective water diffusion coefficient in Nafion<sup>®</sup> membrane by water balance measurements », *Fuel Cells*, p. fuce.202000150, mars 2021, doi: 10.1002/fuce.202000150.
- [103] N. V. Trinh, X. L. Nguyen, Y. Kim, et S. Yu, « Characteristics of Water Transport of Membrane Electrolyte over Selected Temperature for Proton Exchange Membrane Fuel Cell », *Polymers*, vol. 14, n° 15, p. 2972, juill. 2022, doi: 10.3390/polym14152972.
- [104] D. A. Caulk, A. M. Brenner, et S. M. Clapham, « A Steady Permeation Method for Measuring Water Transport Properties of Fuel Cell Membranes », *J. Electrochem. Soc.*, vol. 159, n° 9, p. F518-F529, 2012, doi: 10.1149/2.016209jes.
- [105] Z. Peng, A. Morin, P. Huguet, P. Schott, et J. Pauchet, « In-Situ Measurement of Electroosmotic Drag Coefficient in Nafion Membrane for the PEMFC », *J. Phys. Chem. B*, vol. 115, n° 44, p. 12835-12844, nov. 2011, doi: 10.1021/jp205291f.

- [106] P. Berg, K. Promislow, J. St. Pierre, J. Stumper, et B. Wetton, « Water Management in PEM Fuel Cells », *J. Electrochem. Soc.*, vol. 151, n° 3, p. A341, 2004, doi: 10.1149/1.1641033.
- [107] H. Wu, « Mathematical Modeling of Transient Transport Phenomena in PEM Fuel Cells », University of Waterloo, 2009.
- [108] J. B. Duncan et H. L. Toor, « An experimental study of three component gas diffusion », *AIChE J.*, vol. 8, n° 1, p. 38-41, mars 1962, doi: 10.1002/aic.690080112.
- [109] F. A. Schwertz et J. E. Brow, « Diffusivity of Water Vapor in Some Common Gases », *J. Chem. Phys.*, vol. 19, n° 5, p. 640-646, mai 1951, doi: 10.1063/1.1748306.
- [110] R. B. Bird, W. E. Stewart, et E. N. Lightfoot, *Transport Phenomena*, 2nd éd. John Wiley & Sons, 1960.
- [111] R. Taylor et R. Krishna, *Multicomponent Mass Transfer*, John Wiley&Sons. USA, 1954.
- [112] J. G. Pharoah, K. Karan, et W. Sun, « On effective transport coefficients in PEM fuel cell electrodes: Anisotropy of the porous transport layers », *J. Power Sources*, vol. 161, n° 1, p. 214-224, oct. 2006, doi: 10.1016/j.jpowsour.2006.03.093.
- [113] M. M. Tomadakis et S. V. Sotirchos, « Ordinary and transition regime diffusion in random fiber structures », *AIChE J.*, vol. 39, n° 3, p. 397-412, mars 1993, doi: 10.1002/aic.690390304.
- [114] Y. Wang, S. Wang, S. Liu, H. Li, et K. Zhu, « Three-dimensional simulation of a PEM fuel cell with experimentally measured through-plane gas effective diffusivity considering Knudsen diffusion and the liquid water effect in porous electrodes », *Electrochimica Acta*, vol. 318, p. 770-782, sept. 2019, doi: 10.1016/j.electacta.2019.06.120.
- [115] P. Carrere, « Modélisation et simulation numérique du transfert de l'eau dans les piles à combustible de type PEMFC », Université de Toulouse, IMFT, 2019.
- [116] S. Chevalier *et al.*, « In operando measurements of liquid water saturation distributions and effective diffusivities of polymer electrolyte membrane fuel cell gas diffusion layers », *Electrochimica Acta*, vol. 210, p. 792-803, août 2016, doi: 10.1016/j.electacta.2016.05.180.
- [117] J. Eller, J. Roth, F. Marone, M. Stampanoni, et F. N. Büchi, « Operando Properties of Gas Diffusion Layers: Saturation and Liquid Permeability », *J. Electrochem. Soc.*, vol. 164, n° 2, p. F115-F126, 2017, doi: 10.1149/2.0881702jes.
- [118] T. Komiyama, T. Sasabe, H. Naito, K. Kawamura, T. Suzuki, et S. Hirai, « Investigation of Liquid Water Distribution under Temperature Gradient in PEFC

- Using in-situ X-ray Visualization », *ECS Trans.*, vol. 98, n° 9, p. 27-35, sept. 2020, doi: 10.1149/09809.0027ecst.
- [119] H. Naito, K. Ishikawa, T. Sasabe, S. Hirai, et T. Tanuma, « Investigation of effects of hydrophilic micro-porous layer on liquid water behavior by X-ray imaging », *J. Power Sources*, vol. 507, p. 230285, sept. 2021, doi: 10.1016/j.jpowsour.2021.230285.
- [120] H. Xu, M. Bührer, F. Marone, T. J. Schmidt, F. N. Büchi, et J. Eller, « Effects of Gas Diffusion Layer Substrates on PEFC Water Management: Part II. In Situ Liquid Water Removal via Evaporation », *J. Electrochem. Soc.*, sept. 2022, doi: 10.1149/1945-7111/ac94a2.
- [121] K. Jiao et X. Li, « Water transport in polymer electrolyte membrane fuel cells », *Prog. Energy Combust. Sci.*, vol. 37, n° 3, p. 221-291, juin 2011, doi: 10.1016/j.pecs.2010.06.002.
- [122] U. Pasaogullari et C. Y. Wang, « Liquid Water Transport in Gas Diffusion Layer of Polymer Electrolyte Fuel Cells », *J. Electrochem. Soc.*, vol. 151, n° 3, p. A399, 2004, doi: 10.1149/1.1646148.
- [123] G. A. Futter, P. Gazdzicki, K. A. Friedrich, A. Latz, et T. Jahnke, « Physical modeling of polymer-electrolyte membrane fuel cells: Understanding water management and impedance spectra », *J. Power Sources*, vol. 391, p. 148-161, juill. 2018, doi: 10.1016/j.jpowsour.2018.04.070.
- [124] M. A. Rahman, M. Sarker, F. Mojica, et P.-Y. A. Chuang, « A physics-based 1-D PEMFC model for simulating two-phase water transport in the electrode and gas diffusion media », *Appl. Energy*, vol. 316, p. 119101, juin 2022, doi: 10.1016/j.apenergy.2022.119101.
- [125] C. Si, G. Lu, X.-D. Wang, et D.-J. Lee, « Gas diffusion layer properties on the performance of proton exchange membrane fuel cell: pc-s relationship with K-function », *Int. J. Hydrog. Energy*, vol. 41, n° 46, p. 21827-21837, déc. 2016, doi: 10.1016/j.ijhydene.2016.07.005.
- [126] J. Zhou, D. Stanier, A. Putz, et M. Secanell, « A Mixed Wettability Pore Size Distribution Based Mathematical Model for Analyzing Two-Phase Flow in Porous Electrodes », *J. Electrochem. Soc.*, p. 18, 2017.
- [127] J. Zhou, A. Putz, et M. Secanell, « A Mixed Wettability Pore Size Distribution Based Mathematical Model for Analyzing Two-Phase Flow in Porous Electrodes », *J. Electrochem. Soc.*, p. 11, 2017.
- [128] A. Kulikovskiy, « The effect of Nafion film on the cathode catalyst layer performance in a low-Pt PEM fuel cell », *Electrochem. Commun.*, vol. 103, p. 61-65, juin 2019, doi: 10.1016/j.elecom.2019.05.003.
- [129] S. Cruz-Manzo et P. Greenwood, « Study of oxygen diffusion in the cathode catalyst layer and gas diffusion layer for polymer electrolyte fuel cells with EIS », *J.*

- Electroanal. Chem.*, vol. 892, p. 115270, juill. 2021, doi: 10.1016/j.jelechem.2021.115270.
- [130] J. Huang et M. Eikerling, « Modeling the oxygen reduction reaction at platinum-based catalysts: A brief review of recent developments », *Curr. Opin. Electrochem.*, vol. 13, p. 157-165, févr. 2019, doi: 10.1016/j.coelec.2019.01.004.
- [131] N. Nonoyama, S. Okazaki, A. Z. Weber, Y. Ikogi, et T. Yoshida, « Analysis of Oxygen-Transport Diffusion Resistance in Proton-Exchange-Membrane Fuel Cells », *J. Electrochem. Soc.*, vol. 158, n° 4, p. B416, 2011, doi: 10.1149/1.3546038.
- [132] T. V. Reshetenko et J. St-Pierre, « Separation Method for Oxygen Mass Transport Coefficient in Gas and Ionomer Phases in PEMFC GDE », *J. Electrochem. Soc.*, vol. 161, n° 10, p. F1089-F1100, 2014, doi: 10.1149/2.1021410jes.
- [133] A. A. Kulikovskiy, « A simple equation for in situ measurement of the catalyst layer oxygen diffusivity in PEM fuel cell », *J. Electroanal. Chem.*, vol. 720-721, p. 47-51, avr. 2014, doi: 10.1016/j.jelechem.2014.03.005.
- [134] V. Coeuriot, J. Dillet, G. Maranzana, O. Lottin, et S. Didierjean, « An ex-situ experiment to study the two-phase flow induced by water condensation into the channels of proton exchange membrane fuel cells (PEMFC) », *Int. J. Hydrog. Energy*, vol. 40, n° 22, p. 7192-7203, juin 2015, doi: 10.1016/j.ijhydene.2015.04.008.
- [135] C. Moyne, T. D. Le, et G. Maranzana, « Upscaled Model for Multicomponent Gas Transport in Porous Media Incorporating Slip Effect », *Transp. Porous Media*, vol. 135, n° 2, p. 309-330, nov. 2020, doi: 10.1007/s11242-020-01478-x.
- [136] R. Vetter et J. O. Schumacher, « Experimental parameter uncertainty in proton exchange membrane fuel cell modeling. Part I: Scatter in material parameterization », *J. Power Sources*, vol. 438, p. 227018, oct. 2019, doi: 10.1016/j.jpowsour.2019.227018.
- [137] E. N. Fuller, K. Ensley, et J. C. Giddings, « Diffusion of halogenated hydrocarbons in helium. The effect of structure on collision cross sections », *J. Phys. Chem.*, vol. 73, n° 11, p. 3679-3685, nov. 1969, doi: 10.1021/j100845a020.
- [138] M. M. Tellez-Cruz, J. Escorihuela, O. Solorza-Feria, et V. Compañ, « Proton Exchange Membrane Fuel Cells (PEMFCs): Advances and Challenges », *Polymers*, vol. 13, n° 18, p. 3064, sept. 2021, doi: 10.3390/polym13183064.
- [139] F. A. de Bruijn, V. a. T. Dam, et G. J. M. Janssen, « Review: Durability and Degradation Issues of PEM Fuel Cell Components », *Fuel Cells*, vol. 8, n° 1, p. 3-22, 2008, doi: 10.1002/fuce.200700053.

- [140] F. Nandjou, J.-P. Poirot-Crouvezier, M. Chandesris, et Y. Bultel, « A pseudo-3D model to investigate heat and water transport in large area PEM fuel cells – Part 1: Model development and validation », *Int. J. Hydrog. Energy*, vol. 41, n° 34, p. 15545-15561, sept. 2016, doi: 10.1016/j.ijhydene.2016.05.117.
- [141] E. Tardy, F. Courtois, M. Chandesris, J.-P. Poirot-Crouvezier, A. Morin, et Y. Bultel, « Investigation of liquid water heterogeneities in large area PEM fuel cells using a pseudo-3D multiphysics model », *Int. J. Heat Mass Transf.*, vol. 145, p. 118720, déc. 2019, doi: 10.1016/j.ijheatmasstransfer.2019.118720.
- [142] M. Bhaiya, A. Putz, et M. Secanell, « Analysis of non-isothermal effects on polymer electrolyte fuel cell electrode assemblies », *Electrochimica Acta*, vol. 147, p. 294-309, nov. 2014, doi: 10.1016/j.electacta.2014.09.051.
- [143] E. J. F. Dickinson et G. Smith, « Modelling the Proton-Conductive Membrane in Practical Polymer Electrolyte Membrane Fuel Cell (PEMFC) Simulation: A Review », *Membranes*, vol. 10, n° 11, p. 310, oct. 2020, doi: 10.3390/membranes10110310.
- [144] N. Zamel et X. Li, « Effective transport properties for polymer electrolyte membrane fuel cells – With a focus on the gas diffusion layer », *Prog. Energy Combust. Sci.*, vol. 39, n° 1, p. 111-146, févr. 2013, doi: 10.1016/j.pecs.2012.07.002.
- [145] P. K. Das, X. Li, et Z.-S. Liu, « Effective transport coefficients in PEM fuel cell catalyst and gas diffusion layers: Beyond Bruggeman approximation », *Appl. Energy*, vol. 87, n° 9, p. 2785-2796, sept. 2010, doi: 10.1016/j.apenergy.2009.05.006.
- [146] Y. Zhou, G. Lin, A. J. Shih, et S. J. Hu, « A micro-scale model for predicting contact resistance between bipolar plate and gas diffusion layer in PEM fuel cells », *J. Power Sources*, vol. 163, n° 2, p. 777-783, janv. 2007, doi: 10.1016/j.jpowsour.2006.09.019.
- [147] A. Higier et H. Liu, « Effects of the difference in electrical resistance under the land and channel in a PEM fuel cell », *Int. J. Hydrog. Energy*, vol. 36, n° 2, p. 1664-1670, janv. 2011, doi: 10.1016/j.ijhydene.2010.11.007.
- [148] S. Wu *et al.*, « A review of modified metal bipolar plates for proton exchange membrane fuel cells », *Int. J. Hydrog. Energy*, vol. 46, n° 12, p. 8672-8701, févr. 2021, doi: 10.1016/j.ijhydene.2020.12.074.
- [149] G. Karimi, X. Li, et P. Teertstra, « Measurement of through-plane effective thermal conductivity and contact resistance in PEM fuel cell diffusion media », *Electrochimica Acta*, vol. 55, n° 5, p. 1619-1625, févr. 2010, doi: 10.1016/j.electacta.2009.10.035.

- [150] P. J. S. Vie et S. Kjelstrup, « Thermal conductivities from temperature profiles in the polymer electrolyte fuel cell », *Electrochimica Acta*, vol. 49, n° 7, p. 1069-1077, mars 2004, doi: 10.1016/j.electacta.2003.10.018.
- [151] Q. Wang *et al.*, « Research progress of heat transfer inside proton exchange membrane fuel cells », *J. Power Sources*, vol. 492, p. 229613, avr. 2021, doi: 10.1016/j.jpowsour.2021.229613.
- [152] P. Roy Chowdhury, A. Vikram, R. K. Phillips, et M. Hoorfar, « Measurement of effective bulk and contact resistance of gas diffusion layer under inhomogeneous compression – Part II: Thermal conductivity », *J. Power Sources*, vol. 320, p. 222-230, juill. 2016, doi: 10.1016/j.jpowsour.2016.04.112.
- [153] R. Bock *et al.*, « Thermal Conductivity and Compaction of GDL-MPL Interfacial Composite Material », *J. Electrochem. Soc.*, vol. 165, n° 7, p. F514-F525, 2018, doi: 10.1149/2.0751807jes.
- [154] J. Ramousse, S. Didierjean, O. Lottin, et D. Maillet, « Estimation of the effective thermal conductivity of carbon felts used as PEMFC Gas Diffusion Layers », *Int. J. Therm. Sci.*, vol. 47, n° 1, p. 1-6, janv. 2008, doi: 10.1016/j.ijthermalsci.2007.01.018.
- [155] M. Khandelwal et M. M. Mench, « Direct measurement of through-plane thermal conductivity and contact resistance in fuel cell materials », *J. Power Sources*, vol. 161, n° 2, p. 1106-1115, oct. 2006, doi: 10.1016/j.jpowsour.2006.06.092.
- [156] Q. Wang *et al.*, « Numerical analysis of static and dynamic heat transfer behaviors inside proton exchange membrane fuel cell », *J. Power Sources*, vol. 488, p. 229419, mars 2021, doi: 10.1016/j.jpowsour.2020.229419.
- [157] S. Kim et M. M. Mench, « Investigation of Temperature-Driven Water Transport in Polymer Electrolyte Fuel Cell: Phase-Change-Induced Flow », *J. Electrochem. Soc.*, vol. 156, n° 3, p. B353, 2009, doi: 10.1149/1.3046136.
- [158] J. M. LaManna, D. S. Aaron, et M. M. Mench, « Architecture-Based Control of Temperature Gradient-Driven Water Transport in Polymer Electrolyte Fuel Cells », *J. Electrochem. Soc.*, vol. 167, n° 10, p. 104504, juin 2020, doi: 10.1149/1945-7111/ab8060.
- [159] A. D. Shum, D. Y. Parkinson, X. Xiao, A. Z. Weber, O. S. Burheim, et I. V. Zenyuk, « Investigating Phase-Change-Induced Flow in Gas Diffusion Layers in Fuel Cells with X-ray Computed Tomography », *Electrochimica Acta*, vol. 256, p. 279-290, déc. 2017, doi: 10.1016/j.electacta.2017.10.012.
- [160] P. Carrere et M. Prat, « Liquid water in cathode gas diffusion layers of PEM fuel cells: Identification of various pore filling regimes from pore network simulations », *Int. J. Heat Mass Transf.*, vol. 129, p. 1043-1056, févr. 2019, doi: 10.1016/j.ijheatmasstransfer.2018.10.004.

- [161] Jé. Bernard, S. Delprat, F. N. Buchi, et T. M. Guerra, « Fuel-Cell Hybrid Powertrain: Toward Minimization of Hydrogen Consumption », *IEEE Trans. Veh. Technol.*, vol. 58, n° 7, p. 3168-3176, sept. 2009, doi: 10.1109/TVT.2009.2014684.
- [162] P. Thounthong, S. Pierfederici, J.-P. Martin, M. Hinaje, et B. Davat, « Modeling and Control of Fuel Cell/Supercapacitor Hybrid Source Based on Differential Flatness Control », *IEEE Trans. Veh. Technol.*, vol. 59, n° 6, p. 2700-2710, juill. 2010, doi: 10.1109/TVT.2010.2046759.
- [163] F. Nandjou, J.-P. Poirot-Crouvezier, M. Chandesris, J.-F. Blachot, C. Bonnaud, et Y. Bultel, « Impact of heat and water management on proton exchange membrane fuel cells degradation in automotive application », *J. Power Sources*, vol. 326, p. 182-192, sept. 2016, doi: 10.1016/j.jpowsour.2016.07.004.
- [164] R. Lin, B. Li, Y. P. Hou, et J. M. Ma, « Investigation of dynamic driving cycle effect on performance degradation and micro-structure change of PEM fuel cell », *Int. J. Hydrog. Energy*, vol. 34, n° 5, p. 2369-2376, mars 2009, doi: 10.1016/j.ijhydene.2008.10.054.
- [165] J. Cho *et al.*, « Analysis of transient response of a unit proton-exchange membrane fuel cell with a degraded gas diffusion layer », *Int. J. Hydrog. Energy*, vol. 36, n° 10, p. 6090-6098, mai 2011, doi: 10.1016/j.ijhydene.2011.02.060.
- [166] J. Ramousse, J. Deseure, O. Lottin, S. Didierjean, et D. Maillet, « Modelling of heat, mass and charge transfer in a PEMFC single cell », *J. Power Sources*, vol. 145, n° 2, p. 416-427, août 2005, doi: 10.1016/j.jpowsour.2005.01.067.
- [167] P. A. García-Salaberri, G. Hwang, M. Vera, A. Z. Weber, et J. T. Gostick, « Effective diffusivity in partially-saturated carbon-fiber gas diffusion layers: Effect of through-plane saturation distribution », *Int. J. Heat Mass Transf.*, vol. 86, p. 319-333, juill. 2015, doi: 10.1016/j.ijheatmasstransfer.2015.02.073.
- [168] T. Schmitt, R. Bligny, G. Maranzana, et U. Sauter, « Rapid and Local EIS on a Segmented Fuel Cell: A New Method for Spatial and Temporal Resolution », *J. Electrochem. Soc.*, vol. 169, n° 9, p. 094504, sept. 2022, doi: 10.1149/1945-7111/ac9089.
- [169] G. S. Hwang et A. Z. Weber, « Effective-Diffusivity Measurement of Partially-Saturated Fuel-Cell Gas-Diffusion Layers », *J. Electrochem. Soc.*, vol. 159, n° 11, p. F683-F692, 2012, doi: 10.1149/2.024211jes.
- [170] T. Romero et W. Mérida, « Water transport in liquid and vapour equilibrated Nafion™ membranes », *J. Membr. Sci.*, vol. 338, n° 1-2, p. 135-144, août 2009, doi: 10.1016/j.memsci.2009.04.018.
- [171] S. Didierjean *et al.*, « Theoretical evidence of the difference in kinetics of water sorption and desorption in Nafion® membrane and experimental validation », *J. Power Sources*, vol. 300, p. 50-56, déc. 2015, doi: 10.1016/j.jpowsour.2015.09.053.

## **Abstract / Résumé**

Hydrogen is a promising energy carrier for the decarbonization of sectors such as industry and mobility. Its nature as a gas also makes hydrogen a suitable medium for storing renewable electricity. Fuel cells allow the production of electricity from hydrogen. Several technologies exist but PEM fuel cells offer efficiency, compactness and versatility. In addition to electricity, they produce heat and water as by-products and these must be properly managed to ensure proper operation of the systems. Too high temperature leads to premature aging of the materials. A membrane that is too dry decreases system performance and degrades more quickly. Conversely, if the cell contains too much water, the reactants can no longer carry out the electrochemical reactions and performance is reduced. The modeling of water and heat transport phenomena in PEM cells allows to improve their conception by a better design or the selection of better materials, as well as by an adapted piloting which preserves the cells from deleterious working conditions. These models contain parameters that must be estimated experimentally in order to make them as realistic as possible. This work, after having placed the role of hydrogen and fuel cells in the energy context, aims at estimating crucial parameters for water and heat transport in the cells. First, a water transport model is developed and design of experiment is set up to estimate the diffusion coefficients of water in the vapor and sorbed phases. Different methods and materials are compared, leading to results consistent with the literature. The influence of liquid water sorption by the membrane is also explored. Then, an original experiment allows to estimate the thermal resistance between the membrane-electrode assembly and the bipolar plates. The coupling between water transport and heat transport allows to estimate the temperature in the cell. An effective thermal conductivity is estimated. Finally, load cycle experiments are performed to study the water storage during a dynamic regime. Water balances are performed in parallel with impedance measurements and allow to explore the water storage in the cell. Preliminary experimental results are compared to a coupled transient model for water and heat transport.

L'hydrogène est un vecteur énergétique prometteur pour la décarbonation de secteurs tels que l'industrie ou la mobilité. Sa nature de gaz fait aussi de l'hydrogène un moyen adapté pour le stockage de l'électricité renouvelable. Les piles à combustible permettent de produire de l'électricité à partir d'hydrogène. Plusieurs technologies existent mais les piles à combustible PEM offrent efficacité, compacité et polyvalence. En plus de l'électricité, elles produisent de la chaleur et de l'eau comme sous-produits et ces derniers doivent être correctement gérés pour assurer le bon fonctionnement des systèmes. Une température trop élevée entraîne un vieillissement prématuré des matériaux. Une membrane trop sèche diminue le rendement du système et se dégrade plus rapidement. À l'inverse, si la cellule de pile contient trop d'eau, les réactifs ne peuvent plus assurer les réactions électrochimiques et les performances s'en voient diminuées. La modélisation des phénomènes de transport d'eau et de chaleur dans les piles PEM permet d'en améliorer leur conception par un meilleur design ou la sélection de meilleurs matériaux, ainsi que par un pilotage adapté qui préserve les cellules de conditions de travail délétères. Ces modèles contiennent des paramètres qu'il convient d'estimer expérimentalement afin de les rendre les plus réalistes possibles. Ce travail, après avoir placé le rôle de l'hydrogène et des piles à combustible dans le contexte énergétique, vise à estimer des paramètres cruciaux pour le transport de l'eau et de la chaleur dans les cellules. Tout d'abord, un modèle de transport de l'eau est développé et un plan d'expérience est mis en place afin d'estimer les coefficients de diffusion de l'eau en phase vapeur et adsorbée. Différentes méthodes et matériaux sont comparés, amenant à des résultats cohérents avec la littérature. L'influence de la sorption d'eau liquide par la membrane est aussi explorée. Ensuite, une expérience originale permet d'estimer la résistance thermique entre l'assemblage membrane-électrodes et les plaques bipolaires. Le couplage entre transport de l'eau et transport de la chaleur permet d'estimer la température dans le cœur de la cellule. Une conductivité thermique effective est estimée. Enfin, des expériences en cycles de charge sont réalisées afin d'étudier le stockage de l'eau lors d'un régime dynamique. Des bilans d'eau sont réalisés en parallèle de mesure d'impédance et permettent d'explorer le stockage de l'eau dans la cellule. Les résultats expérimentaux préliminaires sont comparés à un modèle transitoire couplé de transport d'eau et de chaleur.